EXTENSION OF THE FRINGE PROJECTION METHOD TO LARGE OBJECTS FOR SHAPE AND DEFORMATION MEASUREMENT

PAR

Anne-Isabelle DESMANGLES

physicienne diplômée de l'Université de Genève
de nationalité suisse et originaire de Klosters-Serneus (GR)

accaptée sur proposition du jury:

Prof. P. Jacquot, directeur de thèse
Prof. D. Cuche, rapporteur
Prof. O. Kölbl, rapporteur
Prof. Ph. Robert, rapporteur
Dr G. Tribillon, rapporteur

Lausanne, EPFL
2003

Acknowledgments

Abstract

There is a real need for methods to allow the measurement of the form and deformation of large objects. For example, for maintenance and production costs as well as for security. Even though there are many methods of measuring the form and deformation of small objects (up to $1m^2$), currently none of them are able to quickly measure larger objects (i.e. at a large number of points at the same time). Among the existing techniques, the fringe projection seem to us one of the most adequate to deal with these kinds of problems. In its classical form, this technique is very simple, since it consists of projecting equispaced rectilinear fringes on an object from one direction and of observing the scene from another with a CCD camera. The displacement of the fringes distorted by the object contains the desired shape information.

The phase shifting and phase unwrapping procedures allow automatic, rapid acquisition of an optical print (called a "phase map") of the object. In the case of small objects (the classical approach), the extraction of the shape information from this optical print is quite simple. A phase map of the object as well as a phase map of a reference surface plane is acquired. Then, basically, the desired shape information is obtained by subtracting these two maps from each other. For larger objects, this approach is not possible anymore. On the one hand, such a reference surface does not exist. On the other hand, in order to measure the whole surface at once, it must be fully illuminated. This suggests the use of interferometrically generated fringes, in divergent beams, which implies that the fringes are no longer rectilinear and equispaced. For these reasons the classical approach is no longer valid. It is therefore necessary to find another method to be able to extract the object shape information from the optical print.

In the frame of this work, three methods have been conceived and developed in order to extract the shape information of large objects from their optical print. The first two methods proposed here are dedicated to quasi-planar objects that are parallel to the imaging plane of the camera. These assumptions allow the simplification of the equations describing the system to "mimic" the classical approach, where the desired shape information is proportional to the difference between the measured and reference phase maps. The next step is to determine the parameters of the projection head. The first method is based on two coupled interferometers (of the Mach-Zehnder and Young's type), and the other uses least squares calculations with a small number of calibration points, aiming at minimizing the difference between the theoretical and measured phase at more than four calibration points. Finally, the desired reference phase map is artificially generated. These two techniques are simple but their application is limited only to planar object parallel to the imaging plane of the camera.

In the last technique, which is based on a new approach, the system is described by the interferometric equation and the central perspective equations. Solving them simultaneously allows the determination of the coordinates (x,y,z) of all measured points from the optical print. This approach is general and offers the advantage of allowing the measurement of the shape and deformation of large objects. In addition, it also makes the system more flexible.

In this report, these different techniques are presented and their feasibility is shown; examples of measurements give a first evaluation of their precision, and assess the new possibilities offered in terms of object shape and configuration of the measurement system, as well as their limitations. Finally, the three methods are compared one to another and advice for their optimization is proposed.

Résumé

Il existe actuellement dans l'industrie (génie civil, industries aéronautique, aérospatiale, navale, métallurgique, automobile,...) un besoin clair de méthodes permettant de mesurer la forme et la déformation d'objets de grande taille. Bien qu'il existe de nombreuses techniques pour mesurer les objets de petite taille (jusqu'à 1 m^2), aucune n'est directement applicable aux objets plus grands. Plus particulièrement, les conditions requises sont de pouvoir obtenir cette information de forme pour un grand nombre de points de la surface de l'objet (de l'ordre de 1 million), d'obtenir cette information rapidement - voire en une seule fois, tout en mesurant l'objet dans son environnement.

Parmi les techniques existantes, la *projection de franges* est intéressante car elle présente des caractéristiques permettant de résoudre ce problème. Le principe de base de cette technique, sous sa forme classique, est simple. Il s'agit de projeter des franges lumineuses rectilignes et équidistante sur l'objet dans une direction, et de les observer depuis une autre direction. Les franges sont déformées par l'objet et c'est ce déplacement des franges qui contient l'information de forme recherchée. Le matériel couramment utilisé consiste en une tête de projection pour créer et projeter les franges, et une caméra CCD connectée à un ordinateur, pour enregistrer des images et les traiter afin d'en extraire la forme de l'objet.

Dans le but d'étendre l'acquisition de cette information à l'espace entre les franges lumineuses, on utilise les techniques dites de *décalage de phase* et de *développement de phase*. Celles-ci permettent en outre d'obtenir rapidement et de manière automatique, une empreinte optique de l'objet appelée *carte de phase* à partir de franges projetées sur celui-ci. L'extraction de l'information recherchée à partir de cette carte de phase est simple. Il suffit d'enregistrer la carte de phase de l'objet ainsi que celle d'un plan de référence, puis de les soustraire l'une de l'autre: la forme de l'objet est proportionnelle à cette différence.

Or lorsque des objets plus grands que 1 m^2 sont considérés, cette approche classique n'est plus utilisable. D'une part, parce qu'un plan de référence correspondant à un objet de cette taille n'existe pas, et d'autre part, parce que pour mesurer un tel objet en une seule fois, il faut pouvoir éclairer toute sa surface, ce qui suggère l'utilisation de franges crées interférométriquement à partir de faisceaux divergents. Dans ce cas, les franges projetées sur l'objet sont courbes et non-équidistantes. Par conséquent, ces conditions de départ ne permettent plus d'appliquer le modèle classique, et une autre approche doit être trouvée.

Dans le cadre de ce travail, trois nouvelles techniques ont été conçues et développées, afin d'extraire la forme de l'objet à partir de son empreinte optique obtenue avec de telles franges. Les deux premières utilisent un modèle se rapprochant de la méthode classique. En effet, des hypothèses simplificatrices permettent d'exprimer à nouveau la forme de l'objet comme étant proportionnelle à la différence entre sa carte de phase et celle d'un plan de référence (généré artificiellement, ici). Ensuite, les paramètres du système sont déterminés en utilisant deux interféromètres couplés (première méthode), ou par un calcul de moindres carrés visant à minimiser la différence entre la phase mesurée et son expression théorique (deuxième méthode). Ces deux techniques sont intéressantes car simples, cependant leur utilisation est très limitée, puisqu'elles ne sont applicables qu'aux objets plans et à la configuration de mesure où la caméra et l'objet sont parallèles. C'est pourquoi une troisième méthode a été développée. De conception nouvelle, celle-ci repose sur une approche complètement différente où le système de mesure est décrit par les équations d'interférométrie (tête de projection) et de projection centrale (caméra). La résolution simultanée de ces équations donnent les coordonnées (x,y,z) de tout point de l'objet mesuré et codé dans l'empreinte optique. Différentes méthodes basées sur des calculs de moindres carrés permettent ensuite de déterminer les paramètres du système. Cette nouvelle approche donne désormais la possibilté de mesurer la forme et la déformation d'objets de grande taille et de forme quelconque. En outre elle rend le système plus flexible en permettant d'adapter sa configuration à l'objet et à l'environnement de mesure.

Dans ce travail, ces différentes techniques sont présentées et leur faisabilité démontrée. Ensuite, une première évaluation (précision, nouvelles possibilités offertes, limitations) en est faite à travers différents exemples de mesures, et elles sont comparées entre elles. Finalement, diverses pistes sont proposées en vue de les optimiser.

Table of Contents

Introduction

1. Context and motivation for measuring shape and deformation of large objects

Security, production-costs lowering, quality testing, surveillance, maintenance are sectors where shape and deformation measurements are applied, and that make them an important matter for industry (civil engineering, shipbuilding, automotive, aerospace,...). Indeed, people working in industry aim at designing, developing, producing and testing machines, vehicles and structures that must achieve acceptable levels of performance, reliability, and economy, while at the same time striving to guarantee that the item is both safe and durable. Shape and deformation measurements are necessary in the different steps of production, going from design to manufacturing in order to speed up and ensure product development and quality as well as to assess if it will satisfy its function properly [1-4].

Another concern for those type of measurements is at economy level. More particularly, degradation of infrastructures in terms of deformation and material fracture is of major economic importance, especially in the motor vehicle, aircraft and civil engineering sectors. Dowlings [4] mentions studies, led in the eighties's for the US and early nineties for Europe, estimating that the cost due to these damages[1], in all sectors of the economy, are on the order of 4% of the GNP in the US and in Europe. Indeed, the infrastructure in many countries of the world is aging and there is an increasing awareness of the need to assess the severity of the damage occurring to it. Limited resources preclude the replacement of all structures that need repairs or have exceeded their life

---

1. These costs include development of new machines, vehicles and structures, as well as techniques and tools, manpower and facilities. They also include repair, maintenance, replacement of parts, inspection of newly manufactured parts for flaws and of parts in service for developping cracks. Recalls, litigation, insurance costs were also considered

times. Methods to assess the amount and severity of failure and damage are crucial to implementing a systematic, cost effective approach to repair or replace the damaged structures. According to the same studies, two-third of the annual cost of material fracture could be eliminated by improved use of currently available technology, or by technology that could be developed in a reasonable time.

Furthermore, not only for production costs or economical reasons but also for safety measures and minimizing risk, assessment of the structure conditions and their monitoring must be considered as of utmost importance [5-6]. There is, generally, an increasing awareness amongst engineers that "standard" specimens (usually used for control and compliance testing prior to production or construction), although notionally of the same material, may misrepresent its true quality when it is used in a structure. Particularly in the civil engineering sector, with concern to large-scale structures of high risk potentials like multistoried buildings, TV-towers, wide spanned bridges, dams, containments of nuclear reactors, framework of cranes, heavy dredging equipment, ranks, etc., people realize that the usual methods (deterministic methods for predicting strain and stressing the design phase) are not sufficient to yield reliable information on the safety against failure and damage, ultimate load capacity and on the life span of such structures. Moreover, it must be checked whether changes in the utilization, time-dependent response of materials, fatigue, environmental conditions, etc. might influence the factor of safety of the structures and their stability. Shape and deformation measurements can be used to monitor the structure behavior (deflection, deformation, vibrations, creep...) under load testing [6-7] or under its own weight for large structures in order to prove their structural adequacy.

For all these reasons, the development of techniques and measurement systems for monitoring structures is an important matter. Not only will they allow to assess the security of existing structures (leading to their maintenance and repair if necessary), but also to better study and understand the deformation and fracture processes, in order to minimize their effects on newly developed items. A main challenge, however is to inspect existing structures under service conditions. This relies on a variety of technologies and techniques allowing in-situ and non-destructive evaluation of objects that are generally quite large. Among these, surface shape and deformation measurement techniques are particularly interesting for monitoring those large objects. Many shape measurement techniques on surfaces not exceeding 1 m^2 are proposed in literature and several are commercially available. But their application to shape and deformation measurement of larger surfaces up to several tens of square meters poses particular problems. We therefore come to the conclusion that there is a need for techniques allowing the measurement of large objects (shape and/or deformation). It is in this context that this project started, at the request of several groups, mainly from the civil engineering sector, who were looking for a method allowing them to perform such measurements.

2.   Before starting...

When reading the literature, a very unexpected, interesting and, at the same time, confusing aspect of shape measurement in general is its multi-disciplinarity and diversity. This is particularly true when considering its numerous fields of applications, the various existing systems and methods, and the great number of different technologies involved in this field. This is illustrated in

Table 1 which doesn't pretend to be exhaustive or precise, but just intends to give an idea of the sectors involved with regards to object sizes and the techniques used.

	Nanoscopic Objects	Microscopic Objects	Medium-size Objects	Large Objects	"Extra"-large objects
Spatial range (X, Y)	1 nm-100 μm	μm -mm	cm-m	m-hm	hm -...
Depth range (Z)	0.1 nm-100 μm	μm -mm	mm-dm	mm-m	m-km
Usual tools or methods					
• AFM	X				
• STM	X				
• SNOM	X				
• Stylus	X	X	X		
• Microscopes (confocal, fringe projection or interferometric)		X			
• Tomographic techniques			X	X	
• Whole-field optical techniques			X		
• Optical scanning techniques			X	X	
• Contact probes			X	X	
• Industrial photogrammetry				X	
• Theodolite				X	X
• Aeral, satellite Photogrammetry					X
• GPS					X
• Airborne laser scan					X
• SAR					X
Field of application					
• Research in physics, chemistry, biology	X	X			
• Medicine			X	X	
• Industry		X	X	X	
• Virtual reality			X	X	X
• 3-D vision				X	
• Archeology			X	X	
• Civil Engineering				X	X
• Architecture				X	
• Rural engineering					X
• Military sector					X

AFM: Atomic Force Microscope
STM: Scanning Tunnel Microscope
SNOM: Scanning Near Field Optical Microscope

GPS: Global Positioning System
SAR: Synthetic Aperture Radar

Table 1: Shape measurement methods or systems, and some of their fields of application [2, 10]

Considering just one field, industry for example, the objects sizes might range from micrometers (watch-making, micro-engineering) to meters (automotive) or tens of meters (aerospace, aircraft, shipbuilding). Many different technologies are employed for each of these sizes: scanning and tactile probe systems, or fringe projection microscopes for microscopic objects [2, 3, 8-10]; contact probes, whole-field or scanning optical techniques, for medium-sized [11] objects; and photogrammetry for large ones [12]. Conversely, a sole method can find an application in many different fields. Photogrammetry for example, is used not only for industry [13-14], but also for virtual reality [15-17], archeology [18], civil and rural engineering fields [19-20]. A consequence of this variety and multi-disciplinarity is complexity.

Indeed, people with numerous backgrounds needing to measure objects of different sizes and properties have developed independently and in parallel many different approaches, models and nomenclatures, leading to confusion. For example Besl [21] noticed that there were about fifteen different words to mean "shape measurement representation" depending on the context[1]. Furthermore, while people in industry speak about "depth" or "range", topometrists will say "height" or "elevation". For the latter, shape is strongly related to position in a given referential, while the former are principally interested in shape only. Moreover, sometimes the same measurement technique is called by several names; for example, industrial photogrammetry is also called close-range, non-topographic, or terrestrial photogrammetry. In addition, surfaces considered as large for micro engineers look small for people working in the civil engineering sector, and so on. No wonder that, according to Chen [1], professionals in the field complain of a lack of standards.

The aim here is not to present a standard, but to define certain basic notions as well as the scope of this work, before reviewing the techniques allowing the measurement of objects shape. First, we consider an *object shape representation* as a surface map representing the altitude of the points with regards to a given reference plane. Therefore, it can be written as a function $z = z\ (x,\ y)$, where x and y are the *in-plane or planimetric coordinates* belonging to the reference plane or object median plane [22], and z is the *height* or *depth (or altimetric coordinate)*. Then *out-of-plane deformation* of the object is considered as the variation with time of this altitude (z), upon loading, with regards to the reference plane (generally the median plane of the object). Note that it is different from the deformation as defined by mechanical engineers.

In addition, in the scope of this work, we will clearly focus on surface metrology, and more particularly of shape metrology, which differs from roughness that considers the microscopic aspect of an object surface. The objects considered are larger than 1 m^2 and their surface is mat. Finally, as for the desired technique, the requirements are the possibility to do the measurement at once, out of the lab environment, in a reasonably short period of time and with the highest achievable confidence level.

---

1. Range images are also known as: range map, depth map, range picture, range pic, 3-D image, 2.5-D image, digital terrain map (DTM), topographic map, 2.5-D primal sketch, surface profiles, xyz-point list, surface distance matrix, contour map, surface height map.

3. Reviewing the main existing methods

As seen earlier, there are a lot of different measurement methods, however here, we only consider those dealing with large objects (above 1 m^2). It is interesting to gather these
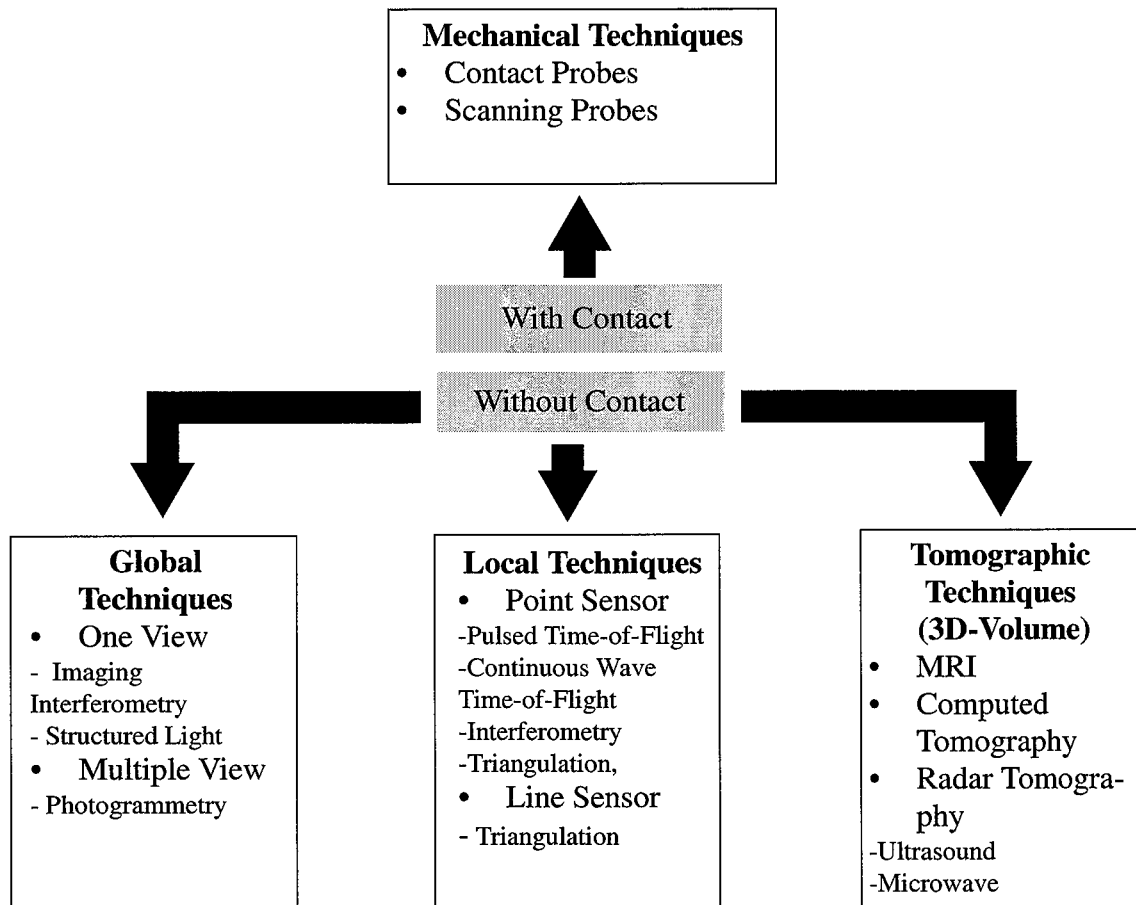
Figure 1: Overview of the most commonly used surface shape measurement techniques

measurement methods according to their "globality"[1] or whether they require contact or not. Indeed, these criteria give us a hint about the speed, the measurement volume and the flexibility of the method. Therefore, in the review below, which doesn't pretend to be exhaustive, the most commonly used methods (either among the commercially available systems or among those developed in research) will be grouped in two main families of 3D memorization systems: the ones with contact and the ones without contact, and then according to their "globality". This

---

1. A *global*, *whole-field* or *full-field* method allows to measure many points simultaneously while a *local* or *punctual* method measures only one point at a time and generally requires the measurement loop to be repeated in order to register more points

overview is summed up in Figure 1. A table in Appendix A gives an overview of the characteristics of different types of measurement systems.

3. 1.   Contact techniques

Contact techniques are the oldest and the most commonly used technique in industry (automotive, aerospace, industrial products), where they are well established and widely accepted, mostly for control purposes. They are based on mechanical probing of the surface, where the point-coordinates measurement is done through direct contact between the stylus tip (probe) and the object. The position information is acquired by the supporting structure (Co-ordinate Measuring Machines - CMM, mechanical or articulated arm,...) and then digitized. The measurement is either static or dynamic: trigger probes measure the coordinates of different points of a surface at regular intervals while scanning probes do continuous measurement of the surface. These techniques allow accuracies between 0.05 and 0.2 mm (see Appendix A), however they have slow measurement speeds because the tip must be positioned before each measurement. Different systems are provided by Faro [23], Romer [24] (mechanical arms), Renishaw [25] and Brown & Sharpe [26] (CMM). More recently, a system was developed where the probe position is determined by a set of cameras (AICON) [27].

3. 2.   Non-contact techniques

Non-contact techniques can be grouped in 3 sections: tomographic-based techniques, scanning techniques and whole-field techniques.

3. 2. 1   Tomography-based techniques [28-29]

These techniques were first developed for the medical field, and today, most of them have also reached the industrial field. In tomographic techniques, morphological information is acquired in a transversal thin slice (1 mm to a few cm) of the object by locally exposing it to a stimulus and registering the sample's reaction in the region considered. These raw data are then analyzed by data treatment algorithms which allows the display of 2D slice-images of the object, generally a patient. Basically the information is acquired slice by slice by moving the table upon which the patient lies, and then those 2-D slices can be further analyzed in order to stack them and reconstruct the 3-D surface [30]. Among tomographic techniques we find MRI also called MNR [31] (respectively Magnetic Resonance Imaging and Magnetic Nuclear Resonance), ultrasound echography [6, 29], and X-ray tomography (or Computer Tomography -CT- or Computer Assisted Tomography -CAT- scan) [6, 29, 32-35]. Different systems are provided by Siemens, General Electrics and Aracor.

3. 2. 2 Local techniques

The second type of non-contact techniques considered are the scanning techniques. The probes are local and thus the depth information is obtained locally, requiring a scan across the object in order to get the 3-D information on the whole surface. Thus the measurement as well as the data treatment must be repeated in order to generate the digitized 3D-surface. Several methods exist based on different principles, configurations and technologies.

3. 2. 2. a.   Point sensors

Basically, when using these systems, the depth information is acquired one point at a time. The 3-D range image is obtained after 2D-scanning the probe across the object surface. Several systems allow to derive this information, and the probe, sensor, configuration and measurement principle varies from one system to the other [36].

The first type of system considered is based on a triangulation configuration [37-38]. The probe is a laser beam projected on the object surface, producing a spot of light which is imaged by an optical sensor (CCD, CMOS,...) from another direction, as displayed in Figure 2. Knowing the geometry of the system (namely: the distance L and the angles θ and α) allows to retrieve the depth information (the range R) between any point of the surface and the sensor. A positioning system, generally composed of 2 mirrors fixed on galvanometers, is used to give two additional degrees of freedom in order to scan the object.
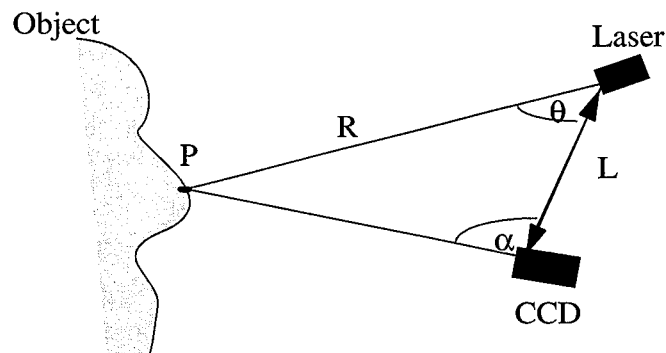
Figure 2: Basic principle of triangulation based-systems

The theodolite is another example of measuring technique based on triangulation. The basic principle of these systems is to aim for the same point P in the space with at least 2 theodolites, in a configuration similar to the one described in Figure 2. The position of the 2 lines materialized by the point P and the 2 theodolites (instead of laser and CCD, in Figure 2) allows to determine the 3D coordinates of P using triangulation. More recently automatized systems, namely distance-meter theodolites, have been developed. Basically, once aiming at a point, it is able to register the distance to this point as well as the angles. The object-coordinates of the measured point are computed from these data. The measurement is thereby simplified, since it does not require to work with two theodolites using the intersection method. The typical precision specified by the manufacturer is about ±1 mm (see Appendix A), however it can be improved when using specific

techniques, such as levelling. Initially this measurement technique was used in geodesy for position measurement and 3D digitalization and today, it is applied in the industrial sector (aerospace and automotive). The development of electronic theodolites has enhanced this trend thanks to their ease of use and to their ability to treat data automatically. One advantage of this technique is the possibility to digitize very large structures [39-40], by measuring a certain amount of points one after the other. Telemetric systems (also called imaging radars) are based on a coaxial position of the probe and sensor as displayed in Figure 3. Two main principles allow to retrieve the distance of each point on the surface to the system [41]: Pulsed Time-of-Flight (TOF) [42] and Amplitude Modulation [43] (also called phase-shift or Continuous Wave Time-of-Flight). The basic principle of TOF sensors is to measure the time taken by a wave-pulse to go from the transmitter to the receiver after being reflected by the object. This is done with a fast counter that acts like a chronometer. In phase-shift-based systems (CW), instead of exploiting a short laser impulsion emitted on the object to be digitized, the emission source is a continuous wave time-modulated at high frequencies. The phase-shift between the emitted and reflected signal is then measured and the distance R is given as a function of this phase shift.
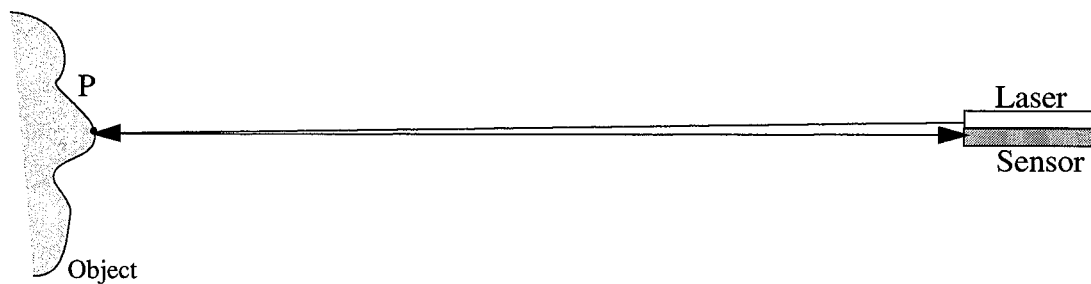
Figure 3: Basic principle of telemetry

3. 2. 2. b.   Line sensors

The principle of laser line sensors [44] is similar to that of laser point sensors, except that the probe is a line of light cast on the object surface generally obtained using cylindrical lenses in front of a laser diode. Theoretically, only one degree of freedom is necessary to scan a surface, but in practice, due to the limited length of the laser line, 2 degrees of freedom are necessary to extend the area to be digitized [45]. Two examples of systems are KLS 171 by KREON and Hyscan by HYMARC (see Appendix A). In surveying, this technique was used to measure tunnel profiles - mainly railway tunnels - and special devices were developed to determine the irregularities of road surfaces. Such systems can measure a width up to 4 m or even more, running with a speed of some 80 km/h [46].

3. 2. 3   Global techniques

Whole-field techniques are the last type of non-contact techniques considered. Typically, field-of-view or whole-field measurement systems measure the depth information in many points of the surface at the same time provided that they lie within a given field of view relative to a

single viewpoint or viewing direction. No scene motion or scan is required. This type of sensor creates a range image of the surface, directly, with either one or more cameras (resp. one view- or multiple view-systems).

3. 2. 3. a. Multiple-image whole-field technique: Industrial Photogrammetry[1] [13, 14, 47-51]

In industrial photogrammetry, the object to be measured is pictured by several cameras or with one camera from several view-points. Indeed, when using only one camera or a single view-point the object in 3-D is projected onto a 2D plane: the image plane. Information is thus lost and there is no way to reconstruct the depth dimension from only one picture. However, using two images (or more) taken from different positions allows to reconstruct the shape of the object in three dimensions. For this purpose, several calibration points are selected on the object. Their image-coordinates on each image together with the orientation parameters of the corresponding images define spatial bundles of rays (shown in Figure 4). By means of the triangulation of at least two different bundles of rays and using special data treatment algorithms (bundle adjustment), the different images are matched. This allows to determine the three-dimensional coordinates of the points of the object and to reconstruct the 3D shape of the object.
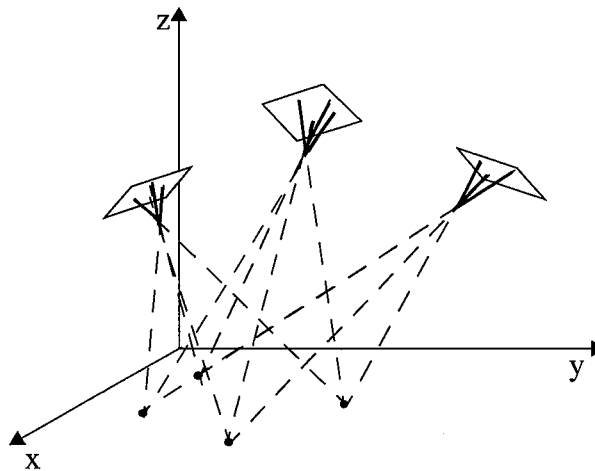
Figure 4: Basic principle of photogrammetry

Close-range photogrammetry is a very precise technique since it allows to measure the position of points on the surface of large objects with an accuracy of about 1/100 000 of the object size. It is also flexible since working distances and object sizes ranging from a fraction of mm to several hundred meters have been reported (basically, the principle of photogrammetry can be applied to larger objects, as shown by aerial photogrammetry). Photogrammetry is currently used for industrial applications (aircraft, aerospace, and ship building) [12-14, 39, 49-51] or geological

---

1. Industrial photogrammetry is also known as close range photogrammetry, non-topographic photogrammetry or terrestrial photogrammetry

applications such as mapping the geologic structures in mines. Several systems and measurement services are provided by Imetric [52] and Leica, for example.

3. 2. 3. b. Single- or one-view systems: whole-field optical methods

The basic principle of optical whole-field techniques is to project a light patterns on the object in such a way that the position of each point on the surface is coded in a unique way. From another position, a sensor (a CCD camera, for example) captures images of the object surface coded with the structured light. The reflected light-pattern acquired for the object is different from what would be obtained for a reference plane. Treating this information by adequate algorithms allows to retrieve the depth information for each point on the surface. Several whole-field methods exist (based on interferometry, fringe projection, holography, and speckles) and although a little bit different, they work on the same basic principle described above.Whole-field techniques applied to measure the shape or deformation of objects are currently used in different fields such as civil engineering [53-54], aircraft industry [55], medicine (orthopedic, reconstructive surgery,...), automotive industry. Several systems can be found on the market, such as Optotop by Breuckman [56], or Comet by Steinbichler, for example. The table in Appendix A shows that their height resolution is usually about 1/1000 of the largest object dimension. The measurement is carried out within a few seconds and the data treatment is achieved after a lap of time ranging from a few seconds to minutes. Interestingly, certain systems couple projection techniques with photogrammetry (e.g. Atos by GOM) by projecting structured-light pattern on the object and taking images with two cameras.

3. 3. Discussion

Contact techniques are very precise, however they present several drawbacks. First, the accessibility depends on the object and probe geometry. A second problem concerns the type of material considered: soft or hot materials are very difficult to digitize by contact. Finally, this method is fine for determining object shape on a relatively small scale (roughness or surface shape of small samples or thin films), but when it comes to very large objects of several meters width the method becomes time consuming and not flexible. As for tomographic-based techniques, their main advantage is the possibility to image the internal structure of the measured object. However, for our purpose here, this is of no use. Furthermore, the size of the object under investigation is limited by the system configuration itself. Because of these limitations in size of objects and of low speed, these two techniques are less interesting and will be left apart. We will rather examine the two last shape measurement techniques.

Local techniques are flexible and can measure objects of different sizes, since they have a large range of possible working distances. As for the accuracy, it varies from system to system and with the working distance, however, an acceptable measurement accuracy can be found using an adapted system. These techniques all share the common drawback of requiring a scan of the object to obtain a map of its shape. Therefore, they are intrinsically slow and need a relatively high measurement time.

Therefore whole-field measurement methods, namely industrial photogrammetry and structured light techniques, are potentially faster and thus more interesting for our purpose. The first one is

very powerful since it allows to measure objects of very various sizes, with a high precision. One drawback of industrial photogrammetry is that it requires specialists or trained operators, and specific material and equipment, which generally makes it a quite expensive method, up to date. Finally, the techniques based on projection of structured light are also interesting for our purpose. Indeed, in principle they allow the measurement of a large volume with a high point-density, being therefore intrinsically fast provided that the illumination is adapted to those large surfaces. As shown by the experiment, the measurement of the object takes a few seconds, giving data that are then treated in a few minutes. Generally, the height resolution of the method is about 1/1000 of the largest object size (empirical rule of thumb). There are mainly four different optical whole-field measurement techniques [57]: holographic and speckle interferometry [58-59], moiré [55,60-61] and fringe projection [62-64]. Holographic and speckle interferometry are particularly sensitive methods, and hence, they require the use of special material in order to isolate the measurement set-up from external vibration. Therefore, they are not really appropriate for our purpose. Instead, moiré and fringe projection are less sensitive to environmental perturbations and thus more interesting. In the moiré technique, a very thin fringe pattern is projected on the object and is observed from another direction through a reference grating. The projected fringes are deformed by the object and when observed through the observation grating, they form an interference moiré pattern related to the object shape. In the fringe projection method, there is no observation grating, and only the deformed projected-fringes are observed, from another direction. The displacement of the fringes is linked to the object shape.With a similar sensitivity, the fringe projection method is conceptually simpler and hence more practical to use and to calibrate. In contrast to moiré where a lot of projected light is lost by absorption (a great part of the light power is stopped by the projection and observation gratings), the fringe projection method offers the possibility to use interferometrically-created fringes, solving this problem. For these reasons, we think that fringe projection is a good candidate for our purpose, and we chose to focus on this method.

Both fringe projection and close-range photogrammetry are interesting to measure large objects, and even if both methods are currently used in the industry to do similar shape measurements (in particular, in the automotive industry), they are also complementary. In particular, fringe projection can be used advantageously in cases where the surface of the object under consideration has no visible texture ("natural marking points") - which is the case for many objects in civil engineering and industry - and where it is desirable to measure the object without prior preparation of its surface. Another advantage of the fringe projection is its inherent speed. Indeed, using active illumination (structured light projected on the object under consideration that is not only used as a marker, but also as a measurement "ruler") allows, in principle, to use only one camera (or camera position). This guaranties fast data acquisition and also a smaller data volume (compared to methods where several camera or camera positions are needed). Consequently the data treatment is also faster, and generally simpler. This may be particularly useful for deformation measurements where the data volume is critical.

4. Scientific problem, goal and main contribution

We saw that there is a need for methods allowing to measure the shape and deformation of large objects. These methods are desired to give the information on the largest number of points of

the surface measured at once. They are also required to be fast, flexible, and as precise as possible. According to us, the fringe projection method is a good candidate; however its application to large and deep surfaces for shape measurement is problematic. Indeed, fringe projection has been widely applied to shape and deformation measurement of small objects. Several set-ups are commercially available [65-67] but mainly due to calibration problems, very few people have applied this technique to larger surfaces (above 1 m^2) [1]. More precisely, in the case of small objects where the classical approach is employed, the projected fringes are straight, parallel and equispaced. This makes it easy to retrieve the shape, mainly by subtracting the optical print of a reference plane from the optical print of the object under investigation. In the case of large objects, the illumination cannot be parallel, and the large depth-of-field required suggests the use of interferometrically-created fringes. Moreover, a "once for all" calibration of the measurement volume becomes meaningless because both the observation and illumination positions have to be adapted to the object size and to the available space. Therefore, the classical approach cannot be used.

In this context, the main goal is to invent a novel approach and to develop new algorithms allowing to interpret the optical print of a large object, allowing thereby to extend the use of fringe projection to large objects for shape and deformation measurement. In this work, we propose several approaches allowing to extract the shape information from such optical prints. These methods are based on structured-light projection in divergent beams, where interferometrically-produced fringes are projected on a large surface. The intensity pattern is captured by a CCD camera and the evaluation of the phase in every image pixel allows the object shape to be coded in an "optical print" after procedures called "phase-shifting" and "phase-unwrapping". The results of all these operations is a continuous "phase surface" over the whole image, called phase map. At this stage, the next problem is to provide algorithms allowing to quantitatively determine the shape of the measured object by interpreting this phase map. In particular, these algorithms must take into account the features linked to the specific type of illumination. In a previous work done in our lab, Lehmann [68] proposed a first data treatment method based on the basic assumptions that the object is a plane and positioned parallel to the imaging plane of the camera. These basic assumptions allows to simplify the equations describing the system and to propose a model similar to the one used in the classical approach. The procedures for calibrating the system are simple and in particular, the calibration of the projection head (coherent-light projector; interferometer) is based on least square calculations used to artificially generate the phase map of the reference plane surface from the measured phase map of the object. However, in addition to the basic assumptions regarding the object shape (plane) and measurement configuration (object parallel to the imaging plane of the camera), this calibration procedure requires the object to lie in the plane $z = 0$, which may be problematic. In a first attempt to get rid of this additional requirement, two alternative methods for calibrating the projection head are proposed in the frame of this work. The first one relies on a projection head made of two mutually tuned interferometers - of Mach-Zehnder and Young types - set-up in series. The second proposed method also uses least squares calculations to calibrate the system, however this time, the least square calculation is performed on a few calibration points, for which physical coordinates as well as phase values are known. At this stage, due to the basic assumptions mentioned earlier, a problem still remains: the application of both methods are limited to plane objects and to a single measurement configuration where the object and camera are parallel. The last method conceived and implemented is based on a completely different approach. It relies on the description of the measurement system by the equations of interferometry and central perspective, and on the resolution of this set of non-linear equations at

once. Then calibration procedures allowing to determine the parameters describing the system are proposed.

The main contribution of this thesis is this original approach which allows to interpret, in a very general way, the optical print of large objects, and to extract the shape information from it. It is now possible to extend the fringe projection methods to large objects of general shape and to any measurement configuration of the system for shape and deformation measurements.

5. Plan of the thesis

In the first chapter, the fringe projection method and its basic principle will be presented. We will explain how the phase map of the object is obtained from images of the fringes projected onto the object, and how the height information is extracted from this optical print, using the classical approach. Then, we will see why it is not straightforward to extend the application of the fringe method technique to large objects and the problems arising when considering large surfaces will be clearly stated. First, in terms of illumination and material set-up; second, in terms of data treatment algorithms. A solution for the illumination based on interferometrically-created fringes of light will be proposed. As for the data treatment, several solutions will be presented in the four next chapters. Chapter 2 will deal with the particular case of flat objects positioned parallel to the imaging plane of the camera. These restrictions as regards the shape of the object and measurement configuration allow to describe the system with a relatively simple model similar to the one used in the classical approach. Calibration procedures are presented and in particular, three solutions for calibrating the projection head will be proposed. One done previously to this work is based on least squares applied to basically all the points of the object. In a first attempt to simplify and improve the flexibility of this calibration procedure, two alternative and original methods have been developed in the scope of this work. The first one relies on a projection head made of two consecutive interferometers allowing to geometrically calibrate it. The other method, also based on least square calculations, allows to calibrate the projection head using only a discrete number of calibration points. In Chapter 3, the feasibility of determining the shape of large objects using programs based on the two newly developed algorithms will be shown. Then all three data treatment methods will be tested on different objects, in order to do a first evaluation of their precision, and also to see what happens when they are used in conditions departing slightly from the basic conditions required for their application. This will allow us to compare them one to another, and to propose solutions for improving them. In Chapter 4, an original data treatment method allowing to measure large objects of general shape in any measurement configuration will be presented. This new approach is based on the description of the system by the interference equation and central projection equations, and on the determination of the analytical solution of this set of equations. Next, calibration procedures for determining the parameters of the system are proposed. Then, similarly to what was done for the three previous methods in Chapter 3, the feasibility of using this new method to determine the shape of objects is shown. Next, the method is tested on different objects, in order to conduct a first evaluation in terms of precision and the possibility to measure objects of general shape. Chapter 5 will present further examples showing the improved flexibility of the new method, and all the new measurement possibilities it offers. Finally, the conclusion will summurize the results and contribution of this work. Then, the

limitations of the newly developed methods as well as perspectives on possible improvements will be stated.

6. References

1. Chen F., Brown G. M., and Song M., *Overview of three-dimensional shape measurement using optical methods*, Optical Engineering, 2000, **39** (1), p. 10-22.

2. Stout K. J., *Three-Dimensional Surface Topography; Measurement, Interpretation and Applications: A survey and Bibliography*, 1994, Penton Press, London.

3. Whitehouse D. J., *Handbook of Surface Metrology*, 1994, Institute of Physics Publishing, London.

4. Dowling N. E., *Mechanical behavior of materials: Engineering Methods for Deformation, Fracture and Fatigue*, 1999, Prentice Hall, New Jersey.

5. Laerman K.-H., *Safety evaluation of large structures: Reality and perspectives*, in *Simulation and experiment in laser metrology. Proceedings of the international symposium on laser applications in precision measurements.*, Editors: Füzessy Z., Jüptner W., and Osten W., 1996, Akademie Verlag: Balatonfüred- Hungary, p. 15-24.

6. Bungey J. H. and Millard S. G., *Testing of concrete in structures*, 1996, Blackie Academic and Professional, London.

7. Moss R. M. and Matthews S. L., *In-service structural monitoring: a state-of-the-art review,*. Structural Engineer, 1995, **73** (2/17 January), p. 23-31.

8. Franz S., *et al.*, *Topograph for inspection of engine cylinder walls*, Applied Optics, 1999. **Vol. 38** (Nr. 36), p. 7375-7381.

9. Leonhardt K., Droste U., and Tiziani H. J., *Microshape and rough-surface analysis by fringe projection*, Applied Optics, 1994, **Vol. 33** (N0. 31), p. 7477-7488.

10. Whitehouse D. J., *Surface metrology*, Meas. Sci. Technol., 1997, **8**, p. 955-972.

11. Pryor T. R., Erf R. K., and Gara A. D., *Applications of Lasers to Production Metrology, Control, and Machine "Vision"*, SPIE Milestones Series: Selected Papers on Laser Distance Measurements, 1995, **Vol. 115**, p. 385-393.

12. Fraser C. S., *Deformation Measurement of a Rocket Thrust Structure*, Proceedings of the 6th International FIG-Symposium on Deformation Measurements, 1992, **Nr. 127**, p. 228-236.

13. Fraser, C.S., *A resume of some industrial applications of photogrammetry*. ISPRS Journal of Photogrammetry and Remote Sensing, 1993, **48**(3), p. 12-23.

14. Dold J., Godding R., and Uffenkamp V., *Applications of Photogrammetry and Image Processing in Industrial Measurements*, Proceedings of the 6th International FIG-Symposium on Deformation Measurements, 1992, **Nr. 127**: p. 170-180.

15. Sequeira V., *et al.*, *Hybrid 3D reconstruction and image based rendering techniques for reality modelling*, Proceedings of SPIE: Videometrics and Optical Methods for 3D Shape Measurement, 2001, **Vol. 4309**, p. 126-136.

16. Paquet E. et al., *The Virtual Boutique: a 3D Modelling and Content-based Management Approach to E-commerce*, Proceedings of SPIE: Videometrics and Optical Methods for 3D Shape Measurement, 2001, **Vol. 4309**, p. 137-147.

17.Xu B., Lin S., and Chen T., *3D measurement of human body for apparel mass-customization.* Proceedings of SPIE: Videometrics and Optical Methods for 3D Shape Measurement, 2001, **Vol. 4309**, p. 26-33.

18.Koelbl O., Cherradi F., and Hostettler H., *Conception of an integrated 3D-GIS for primary data acquisition and data management; Applied to an inventory of historic monuments,* International archives of Photogrammetry and Remote sensing, 2000, **XXXIII** (B5/1, Commission V), p. 445-452.

19.Koelbl O., *Photogrammétrie et système d'information du territoire,* 1990, Presses Polytechniques Romandes, Lausanne.

20.Gruen A. and Henricsson O., *TOBAGO and ARUBA - New Approaches for the Generation of Cybercity from Images,* Proceedings of the Second International Conference on Imaging Technologies: Techniques and Applications in Civil Engineering, 1997, p. 286-301.

21.Besl P. J., *Active optical range imaging sensors,* in *Advances in machine vision,* Sanz J. L., Editor. 1989, Springer-Verlag: New-York, p. 1-63.

22.Sherrington I. et al., *Modern measurement techniques in surface metrology: part II; Optical instruments,* Wear, 1988, **125**, p. 289-308.

23.*http://www.faro.com,* 2001, Faro.

24.*http://www.romer.com,* 2002, Romer.

25.*http://www.renishaw.com,* 2001-2002, Renishaw.

26.*http://www.brownandsharpe.com,* 2002, Brown & Sharpe.

27.Bösemann W. and Schneider C.-T., *Online 3D Measurement using Inverse Photogrammetry.* Proceedings of SPIE: Videometrics and Optical Methods for 3D Shape Measurement, 2001, **Vol. 4309**: p. 288-293.

28.*http://www.cs.uni-magdeburg.de/~nroeber/english/intern/intern.html,* 2000-12-14, Otto-von-Guericke Universität, Magdeburg.

29.Webster J. G., ed. *Medical Instrumentation: Application and Design,* Third Edition, 1998, John Wiley & Sons, Inc: New York, USA.

30.Blum A. and Régent D., *Scanner hélicoidal: Principes et modalités pratiques d'utilisation,* Collection d'imagerie radiologique, ed. Bléry M., 1995, Masson, Paris.

31.Hornak J. P., *The basics of MRI,* 1996-2002, Rochester Institute of Technology.

32.Roeber N., *Multidimensional Analysis and Visualization Software for dynamic SPECT,* 2000, Otto-von-Guericke Universität, Magdeburg.

33.*http://www.siemens.de,* 2000, Siemens.

34.*http://www.aracor.com,* 2002, ARACOR.

35.*http://www.gemedicalsystems.com/rad/ct/products/ebt/index.html,* 1997-2000, General Electrics.

36. Bosch T. and Lescure M., Eds., *Selected Papers on Laser Distance Measurements.* SPIE Milestones Series, 1995, **Vol. 115**, SPIE Optical Engineering Press: Bellingham, Washington USA. 1-720.

37.Pipitone F. and Marshall T. G., *A Wide-field Scanning Triangulation Rangefinder for Machine Vision,* in *Selected papers on Laser Distance Measurements,* Bosch T. and Lescure M., Editors, 1995, SPIE Optical Engineering Press: Bellingham, Washington USA, p. 394-404.

38.Rioux M., *Laser Range Finder based on Synchronized scanners,* in *Selected papers on Laser Distance Measurements,* Bosch T. and Lescure M., Editors, 1995, SPIE Optical Engineering Press, Bellingham, Washington USA, p. 425-432.

39.Lang M. and Welsh W., *Möglichkeiten und Grenzen von Theodolitmesssystemen bei der geometrischen Qualitätssicherung im Maschinenbau,* Proceedings of the 6th International FIG-Symposium on Deformation Measurements, 1992, **Nr. 127**, p. 436-449.

40. *http://www.leica-geosystems.com.*

41.Koskinen M., K. J., and Myllylä R., *Comparison of the continuous wave and pulsed time-of-flight laser range-finding techniques,* in *Selected papers on Laser Distance Measurements,* Bosch T. and Lescure M., Editors, 1995, SPIE Optical Engineering Press: Bellingham, Washington USA, p. 280-289.

42.Moring I., Heikkinen T., and Myllylä R., *Acquisition of three-dimensional image data by scanning laser range finder,* in *Selected papers on Laser Distance Measurements,* Bosch T. and Lescure M., Editors. 1995, SPIE Optical Engineering Press: Bellingham, Washington USA, p. 235-240.

43.Payne J. M., Parker D., and Bradley R. F., *Rangefinder with fast multiple range capability.* SPIE Milestones Series: Selected Papers on Laser Distance Measurements, 1995, **Vol. 115**: p. 257-262.

44.Asundi A., W.Z., *Unified calibration technique and its applications in optical triangular profilometry,* Applied Optics, 1999, **38**(16), p. 3556-3561.

45.Piazzini C., Plisson A., and Dennes S., *http://www.bordeaux.ensam.fr/enseignement/initiale/appro/proj31_99/projet5.html#deux* .

46. Matthias J., *Mitteilungen des Instituts für Geodäsie und Photogrammetrie,* ETHZ Nr. 55,1995, Zürich.

47.Koelbl O., *Cours de Photogrammetrie I et II,* 1984, Ecole Polytechnique Fédérale de Lausanne, Lausanne.

48.Dowman I.J., H. Ebner, and C. Heipke, *Overview of European developments in digital photogrammetric workstations,* Photogrammetric Engineering and Remote Sensing, 1992, **58**, p. 51-56.

49.El Hakim S.F., *Real-time image metrology with CCD cameras,* in *Photogrammetric Engineering and Remote Sensing,* 1986, vol.52, no.11, p. 1757-66.

50.Fraser, C.S., *Photogrammetric measurement to one part in a million compact range reflector,* in *Photogrammetric Engineering and Remote Sensing,* 1992, vol.58, no.3, p. 305-10.

51.Turek, D., J. Trimble, and W. North, *Test of close-range photogrammetry,* Experimental Techniques, 1989, **13**, p. 28-30.

52.*Imetric SA,Technopole, CH-2900 Porrentruy, http:\\www.imetric.com.*

53.Jacquot P. and Facchini M., *Interferometric imaging using holographic and speckle techniques II: Impact in civil Engineering,* in *Proceedings of the Second Internaltional Conference Imaging Technologies: Techniques and applications in Civil Engineering,* Frost J.D. and Mc Neil S., Editors, 1997, Davos.

54.Jacquot P. and Facchini M., *Interferometric imaging: involvement in civil engineering,* Journal of computing in civil engineering, 1999, **13**(2), p. 61-70.

55.Pirodda L., *Shadow and projection moiré techniques for absolute or relative mapping of surface shapes,* Optical Engineering, 1982. **21**(4), p. 640-649.

56. *http://www.breuckmann.com/english/index-prod.html,* 2002, Breuckmann GmbH.

57.Robinson D. W. and Reid G. T., Eds., *Interferogram analysis: digital fringe pattern measurement techniques,* First ed., 1993, Institute of Physics publishing: Bristol, Philadelphia.

58.Jacquot P. and Facchini M., *Interferometric imaging using holographic and speckle techniques I: Fundamental and basic characteristics,* in *Proceedings of the Second International*

Conference Imaging Technologies: Techniques and applications in Civil Engineering, Frost J.D. and Mc Neil S., Editors, 1997, Davos.

59.Vest C. M., *Holographic Interferometry*, John Wiley and sons, 1979, New York.

60.Kafri O. and Glatt I., *The physics of Moire metrology*, Wiley series in Pure and Applied Optics, 1989, ed. Goodman J. W., New York: Wiley.

61.Sciarammella C. A., *The moiré method: a review*, Experimental mechanics, 1982 (November), p. 418-433.

62.Dessus, B. and Leblanc M., *The 'fringe method' and its application to the measurement of deformations, vibrations, contour lines and differences of objects*, Opto Electronics, 1973, 5(5), p. 369-391.

63.Malacara D., Ed., *Optical shop testing*, 2nd ed, Wiley series in pure and applied optics, 1992, Wiley and Sons, Inc.: New York.

64.Vishnyakov, G.N., Levin G.G., and Naumov A.A., *Measurement of the Surface of 3-Dimensional Objects by the Method of Projection of Interference-Fringes*, Optics and spectroscopy, 1998, **85**(6), p. 933-937.

65.Breuckmann GmbH, *www.breuckmann.de*

66.Steinbichler Optotechnik GmbH, *www.steinbichler.de*

67.GOM, *http://www.gom.com/*

68.Lehmann M., Jacquot P., and Facchini. M., *Shape measurements on large surfaces by fringe projection*, Experimental Techniques, 1999, **23**(2), p. 31-35.

CHAPTER 1

Fringe projection: basic principle, method and problematic

Measuring the shape of any object using the fringe projection method is basically done in three steps: first, the creation of fringes and their projection on the object surface; second, the registration of the object optical print (called phase map); and third, the retrieval of the height information from this phase-map. In this chapter, we will review the basic principle of fringe projection, the method for acquiring the phase-map, and the classical method generally used for extracting the shape of small objects from the phase-map. Then, we will expose the problem arising when large surfaces are to be measured. Finally, we will consider more experimental aspects, presenting the set-up, the type of measured objects and an example of optical print acquisition.

1. 1. Basic principle of the fringe projection method[1-3]

The basic principle of fringe projection is quite simple and straightforward to understand. Plane parallel sheets of light are cast on the object to be measured from one direction, as illustrated in Figure 1.1.a). Observation of the scene from another direction gives an image of the object with superposed fringes. If the object is planar, the fringes will be straight and equispaced; however, if it is not planar, the fringes are distorted and their departure from straightness is related to the shape of the object. Indeed, as shown in Figure 1.1.b), the period of the fringes cast on the object is modified compared to the period that would be obtained if the structured pattern was projected on a plane. The shape of the surface is thus coded in this fringe pattern. Then, knowing the geometric parameters of the illumination and observation set-up the observer is able to deduce the relative height of each point on the measured surface. The surface shape is thereby extracted from the observed fringe pattern, where the height increment Δh is expressed by:

$$\Delta h = \frac{\Delta p}{\tan \alpha}$$
(1. 1)

where $\Delta p = p_p - p_a$ is the difference between the period p_p of the fringes projected on a planar surface and the apparent period p_a of the fringes projected on the object; and α is the angle between the incidence of light and the observation directions.

a)   b)
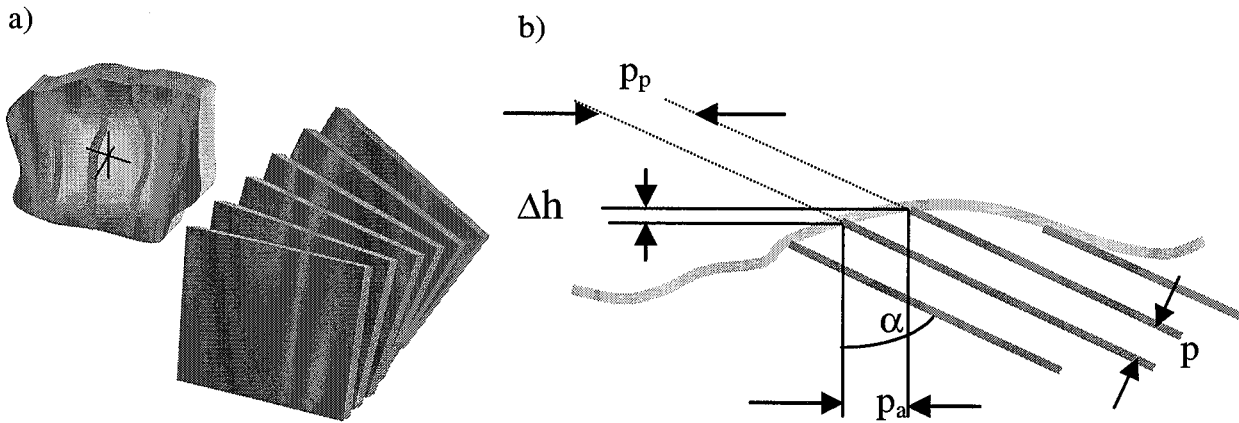
Figure 1. 1: Principle of the fringe projection method

Examples of resulting images are shown for a planar surface and for a face in Figure 1.2a) and b) respectively. The fringes projected on the plane are straight and equidistant; the fringes projected on the face follow its shape and enhance it.

a)   b)
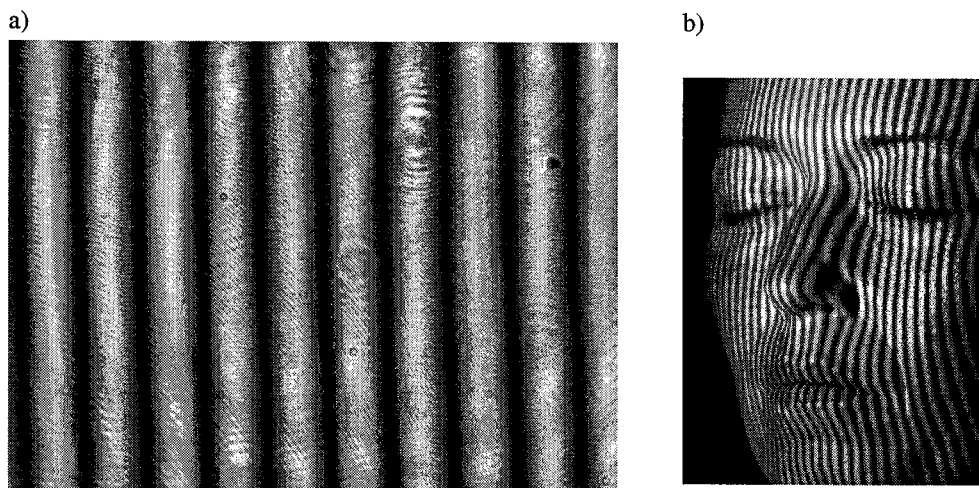
Figure 1. 2: Fringes projected a) on a plane and b) on a face

There are mainly two possibilities for creating a family of planar and parallel sheets of light: either with a white-light projector (slide projector, liquid crystal display) and a grating, either with a laser and an interferometer. When projected on the object, these fringes fill the volume

surrounding it. The basic measurement configuration of the system is sketched in Figure 1.3. The fringes are projected from one direction on the object and observed by a camera from another direction. Several images are taken and a data treatment allows to determine the phase-map according to the method described in the next section.
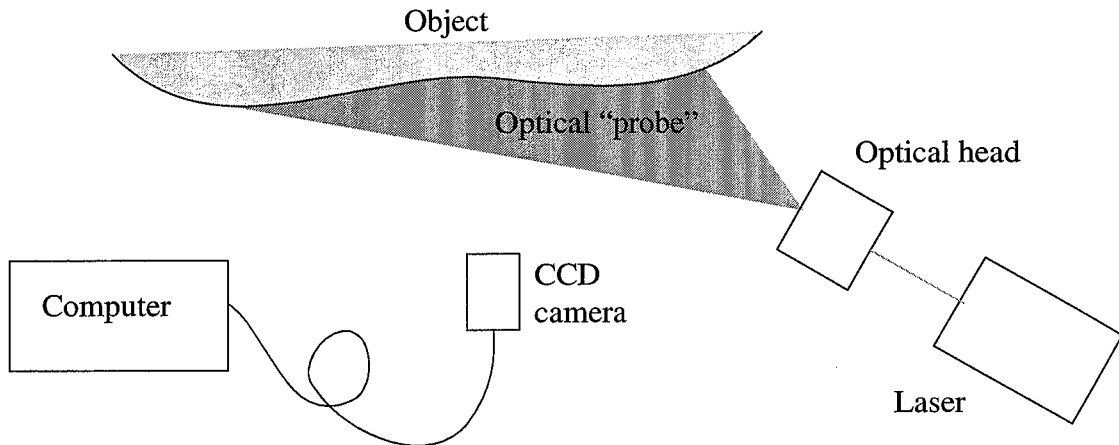
Figure 1. 3: Fringe projection system: basic configuration

1. 2.   Registration of the object optical print

1. 2. 1.   Using the phase map instead of the period of the fringes

In Section 1.1.1, we have seen that the height Δh is proportional to the difference between the projected fringe period p_p and the apparent fringe period p_a according to the equation (1.1). In this theoretical development, only the points located on the center of the bright (or dark) fringes (i.e. position of maximum - or minimum light intensity) were considered. Therefore in this case, the height information obtained is discrete. In order to extend the wanted height information to the space between the fringes, we relate it to the phase of the light instead of the fringe period. This approach offers the additional advantages to make the information acquisition and processing simpler, and more automatic.

Considering a surface illuminated by interference fringes, as illustrated Figure 1.4, the intensity I observed in any point (x, y, z) can be written as:

$$I(x, y, z) = I_0 + I_M \cdot \cos\varphi(x, y, z) \tag{1. 2}$$

where I_0 and I_M represent the background and modulation intensities, and $\varphi(x, y, z)$ is the phase difference between the two interfering beams. This equation shows that the physical quantity containing the height information is the phase.

Knowing that the phase varies linearly from 0 to 2π in one period p, and assuming that $\varphi(0, 0, 0) = 0$, a simple geometric calculation gives (see Figure 1.4):

$$\varphi(x, y, z) = \frac{2\pi}{p}(x \cdot \cos\alpha + z \cdot \sin\alpha) \qquad (1.3)$$

Hence, two points (x_0, y_0, z_0) and (x_1, y_1, z_1) centered on two consecutive fringes $(\Delta\varphi = 2\pi)$ are separated by the height:

$$z_1 - z_0 = \frac{p - (x_1 - x_0) \cdot \cos\alpha}{\sin\alpha} = \frac{(p_p - p_a)}{\tan\alpha} \qquad (1.4)$$

which is equivalent to Equation (1.1).
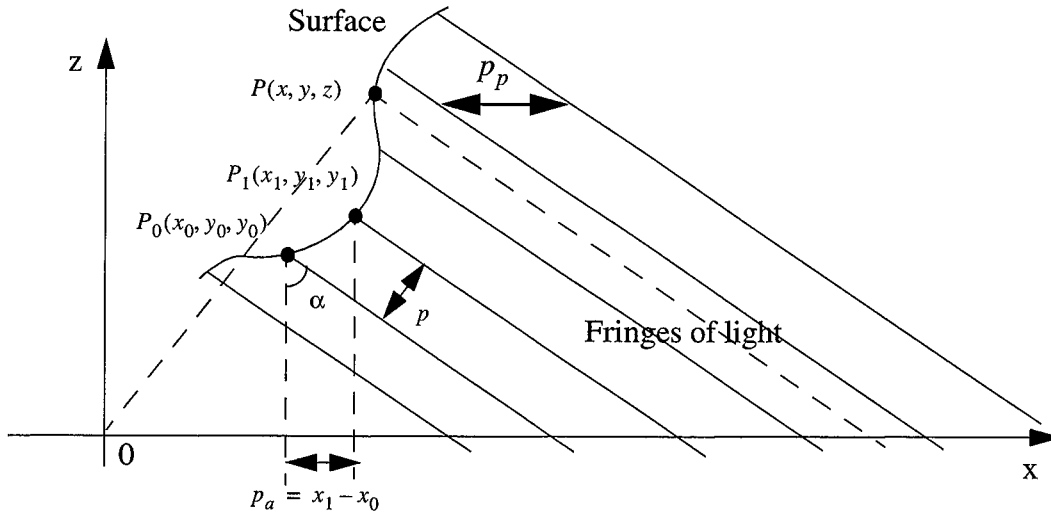
Figure 1. 4: Diagram showing the link between the two approaches using on the one hand, the phase and on the other hand, the period of the fringes of light

1. 2. 2. Getting the phase map[4]:"phase-shifting" and "phase unwrapping"

Robinson [4] reviews several methods to automatize the acquisition and processing of the fringe images, in order to obtain a coded image of the object under investigation. Some of the methods presented are based on the intensity of the captured light, and others on its phase. The method used in our work, namely phase-shifting, belongs to the latter category. Its principle consists in moving the fringes step by step on the whole surface, while at the same time acquiring images of these fringes for each step. From three different values of the intensity I_1, I_2, I_3 registered in each point (x, y, z) of the images, the value of the phase can be computed, as exposed in Figure 1.5. By doing the same for all the points on the images, we obtain the so-called "wrapped"-phase

map, where the value of φ is contained in an interval $[0, 2\pi]$. Another map, namely the modulation map, is also acquired.

a)

$$I_1(x,y,z) = I_0 + I_M \cdot \cos(\varphi(x,y,z))$$

$$I_2(x,y,z) = I_0 + I_M \cdot \cos(\varphi(x,y,z)+2\pi/3)$$

$$I_3(x,y,z) = I_0 + I_M \cdot \cos(\varphi(x,y,z)+4\pi/3)$$

$$\varphi = f(I_1, I_3, I_2) = \arctan\left(\sqrt{3}\ \frac{I_3 - I_2}{2I_1 - I_3 - I_2}\right)$$

b)

Phase-shifting   Phase map

Figure 1. 5: Principle of phase-shifting. a) Equation for one point (x,y,z); b) Diagram for a whole image

Figure 1. 6: Principle of phase unwrapping

It gives information on the modulation quality of the fringe, and can be useful to interpret the phase map. At least three images are necessary to perform the phase-shifting procedure, however algorithms using a greater number of images also exist (4-, 5-, 7-images algorithms). This redundancy of information allows to reach a better precision on the phase-map.

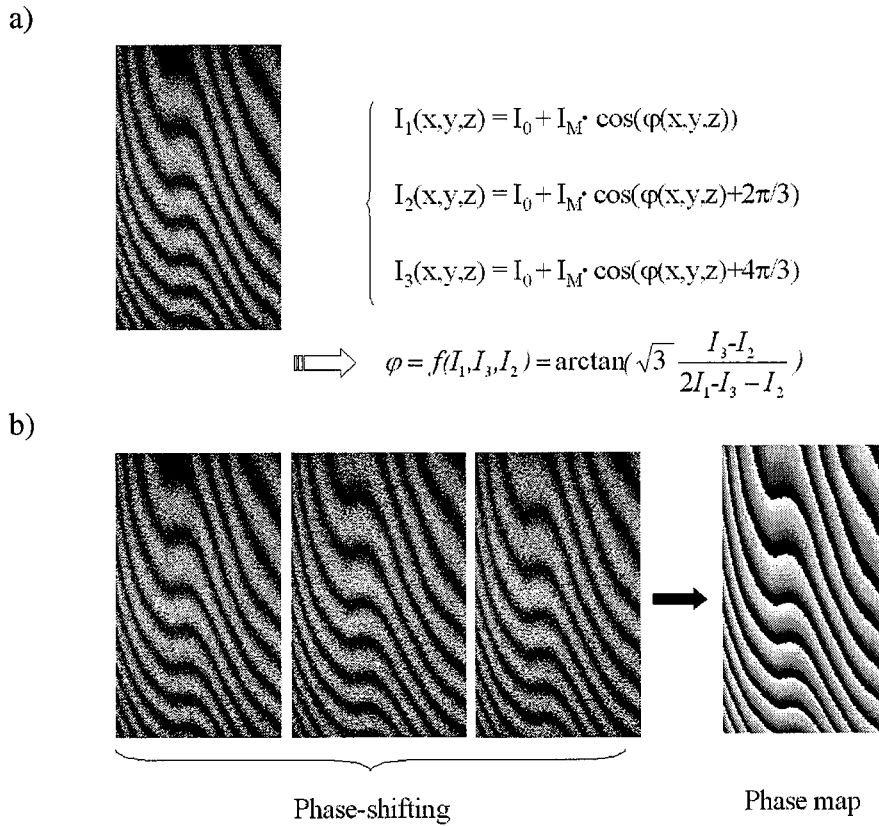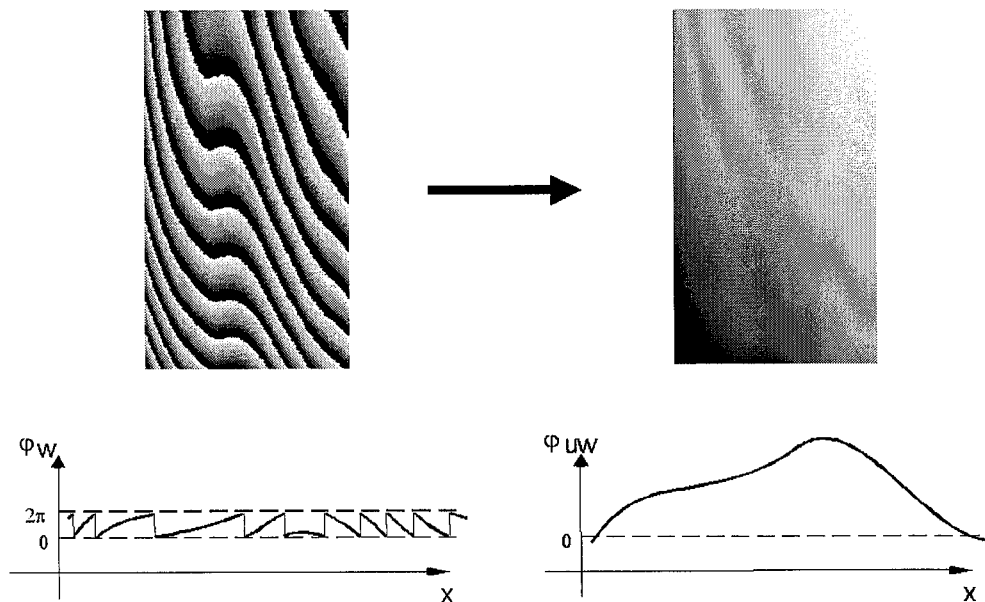Next, an operation called "phase-unwrapping" is carried out. It consists in developing the "wrapped"-phase obtained above, as shown in Figure 1.6. This unwrapped phase contains the signature of the measured object shape, and hence, the information we want. The procedure to extract this information from the phase-map is described in the next section. It is interesting to notice that there are several methods allowing to filter the measured phase map.

1. 3.   From the phase map to the height map: the classical method

In the previous section, we have seen that if the projected fringes are rectilinear and equispaced, then the fringe distribution on the object surface is directly related to the phase-map. According to this, the height can be expressed in terms of the phase $\varphi(x, y)$:

$$\Delta h = \Delta z = S \cdot \Delta \varphi \qquad (1.5)$$

where according to Equation (1.3):

$$S = \frac{p}{2\pi \cdot \sin \alpha} = \frac{p_a}{2\pi \cdot \tan \alpha} \qquad (1.6)$$

and

$$\Delta \varphi = \varphi_{obj} - \varphi_{ref} \qquad (1.7)$$

S is the sensitivity and is expressed here in [mm/rad], φ_{obj} is the measured phase map of the object and φ_{ref} is the measured phase map of a reference planar surface chosen such as $z = 0$. Hence, by registering the phase-map of the object and the reference plane and by determining the sensitivity S (depending on the set-up geometry, namely the period p of the fringes and the angle α between the projection and observation directions), the object height can be simply calculated. This method, called the classical method in this work, is applied to small objects. The whole measurement procedure is synthesized in Figure 1.7, in terms of system and model. In this model, the measurement system and the object are in the "system world". The measurements also take place there. Both the camera and the projection head (interferometer) are modeled in the mathematical "model world". The camera is modeled by a scaling transformation which is easily calibrated by calculating the correspondence between distance in meters and distance in pixels. For that purpose, a ruler is imaged and its length is measured in pixels on the monitor screen using a simple cursor. Then the ratio of distance in pixels and distance in meters is computed. This ratio allows to calculate the x and y object coordinates for each corresponding pixel.
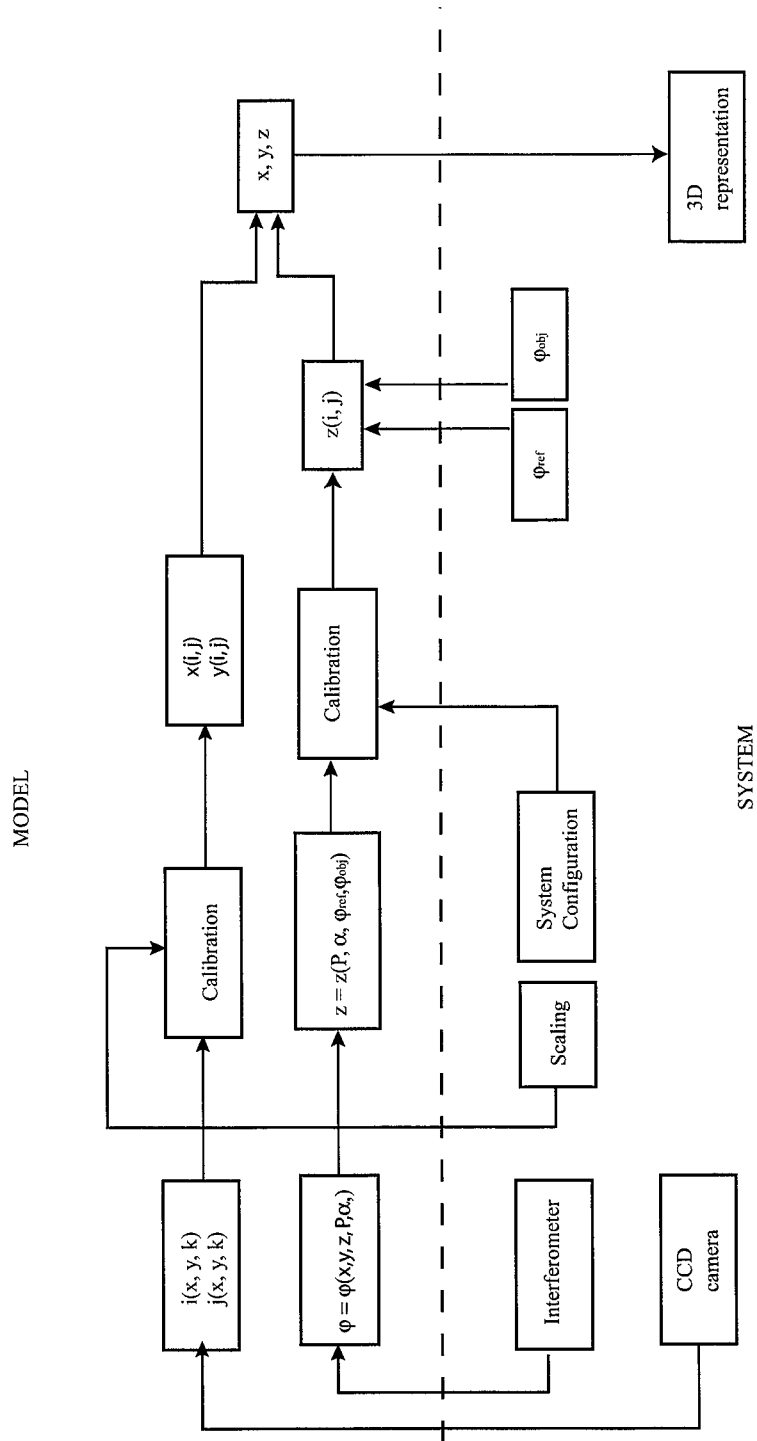
24

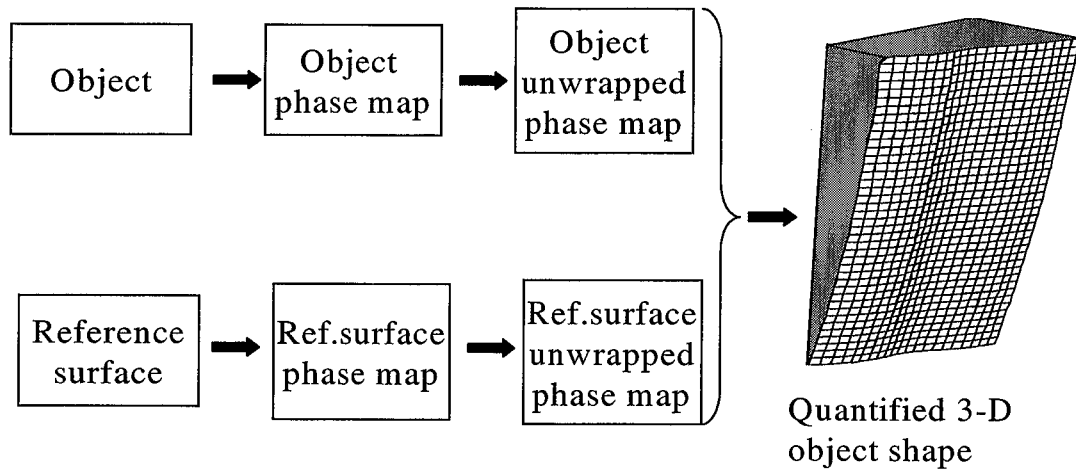**Figure 1. 7:** Synthesis of the classical approach

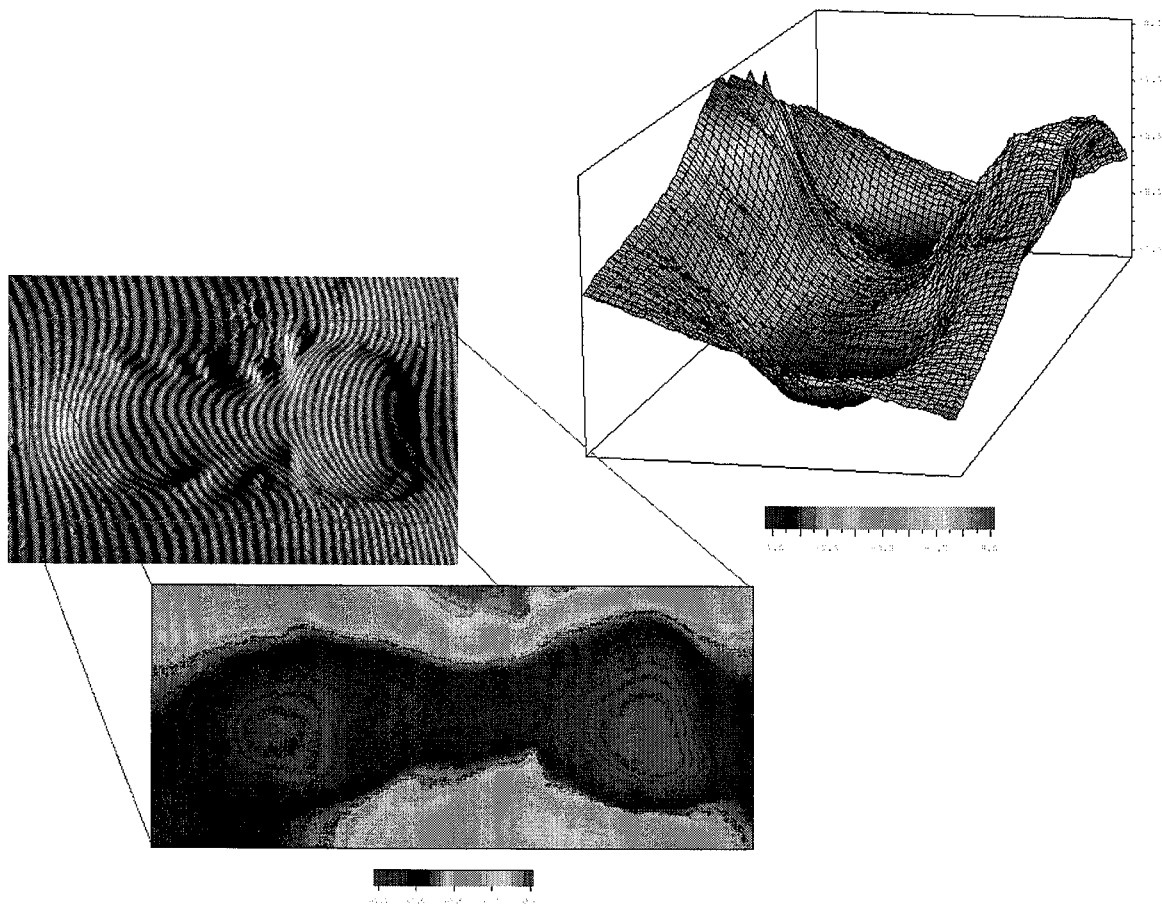*Figure 1. 8:* Fringe processing for small surfaces

Figure 1. 9: Measurement of a scar topography using the fringe projection technique.

As for the interferometer, it is modeled by Equation (1.3). From this, a simple calculation gives the expression of the height as a function of the period p, the angle α, and the measured phase maps of the object and reference plane (Equation (1.5)). Experimental measurements give the period p, the angle α, and an expression of z can be established which is only dependent on the two measured phase maps. Finally, the height z is determined in each pixel by subtracting the phase map of the reference plane from the phase map of the object, pixel by pixel, and multiplying this value by the sensitivity S. From the values obtained for x, y and z in each pixel, a quantitative 3D representation of the object can be reconstructed. Figure 1.8 illustrates in more detail how the 3D shape of the object is recovered from the measured phase map of the object and reference plane. An application of the fringe projection method for measuring the shape of small objects is shown in Figure 1.9. The measured surface is the silicon replica of a scar which was a few cm long and wide, and a few millimeter high. Its 3D representation is displayed on the right.

1. 4.   Problems arising when considering large objects

Fringe projection has been widely used for measuring the shape and deformation of small objects. Several set-ups (based on the classical method described above) are commercially available, however very few people have applied this technique to larger surfaces (above 1 m ^{2}) [5]. In this case, due to the large size of the object, the illumination cannot be parallel, and the depth of field suggests the use of interferometrically-created fringes. Furthermore, a "once-time" calibration of the measurement volume becomes useless because both the observation and the illumination positions have to be adapted to the object size and the available space. A different approach is therefore needed.

1. 4. 1.   The illumination

The first and more evident problem is to be able to illuminate the whole surface of the object (large and deep; several tens of meter square) at once, with a regular fringe pattern.

From a previous experience in our lab [6], we know that white-light projection is not optimum because of different types of problems: weight of a powerful white-light source, heating, limited depth of field, intensity profile and contrast (not possible to work in the daylight). Therefore we do not use white-light illumination but rather coherent light and an interferometer. Moreover since we are dealing with large objects, the illuminating beams must be divergent. Hence, the projected fringes are not parallel and equidistant anymore, as in the basic principle exposed above. Indeed, if the illumination is assumed to be achieved by two point sources, then $\varphi(x, y, z)$ is proportional to the difference between the distances from (x, y, z) to both sources:

$$\varphi(x, y, z) = \frac{2\pi}{\lambda} [\sqrt{(R_x + r_x - x)^2 + (R_y + r_y - y)^2 + (R_z + r_z - z)^2} - \sqrt{(R_x - x)^2 + (R_y - y)^2 + (R_z - z)^2}] \tag{1. 8}$$

where λ is the laser wavelength, $R = (R_x, R_y, R_z)$ the position of one point source, $r = (r_x, r_y, r_z)$ the separation vector of the two sources. Surfaces of equal phase difference $\varphi(x, y, z)$ are thus hyperboloids and consequently, the fringes created are curved and no more equidistant, as illustrated in Figure 1.10.

Here, it is important to discuss the choice of coherent light. Indeed, while solving problems in terms of illumination, coherent light presents an important drawback: the speckles [7]. These random grains of light act like noise in the fringe image and thus in the phase-map. They can be very disturbing for the measurement precision, especially when using small camera-objective apertures. In our case, we work with large camera-objective apertures. In particular, the latter aspect of the measurement set-up suggests that the speckles are not resolved and that their intensity is integrated and averaged when imaging the fringes projected on the object. Preliminary measurements showed that the resolution of 1/1000 of the object's largest dimension could be reached [8], which indicated that the measurement is not disturbed by speckles. However, in the future, especially if the system is to be optimized and calibrated, this feature should be investigated. Liu et al [9] studied the effect of speckles on optical triangulation measurement set-ups and proposed several solutions to decrease their influence.
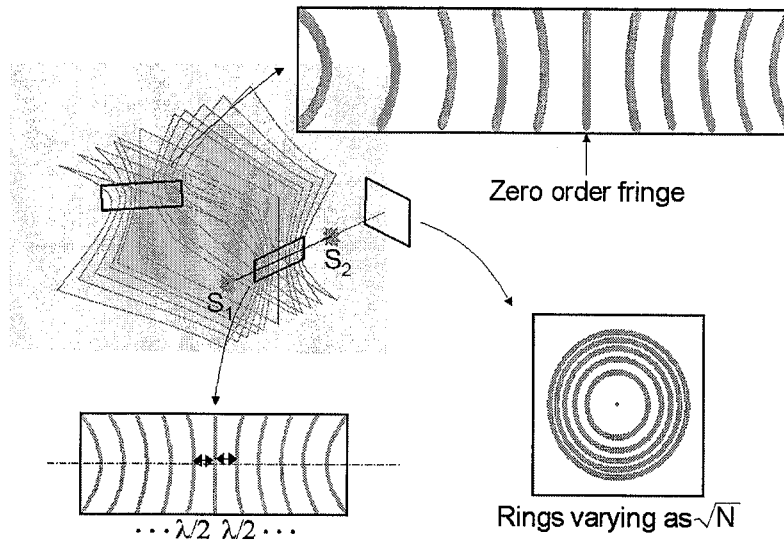
Figure 1. 10: Diagram of the hyperboloic interference fringes created by two point sources

1. 4. 2.   The data treatment

From the above illumination solution, another problem arises: the data treatment allowing to retrieve the height-map from the measured phase-map. Indeed, the classical approach modelled by Equation (1.6) is no longer valid since the fringes are neither rectilinear nor equispaced, and therefore cannot be used. As shown by Equation (1.8), the relation between the phase and the height is clearly not linear anymore, and considerably more complicated than Equation (1.7). Furthermore, even if this equation is linearized, there exist no physical reference plane as large as

the objects we are considering. This is illustrated in Figure 1.11. Therefore, another way for calculating z must be found, and another approach based on new algorithms must be developed.
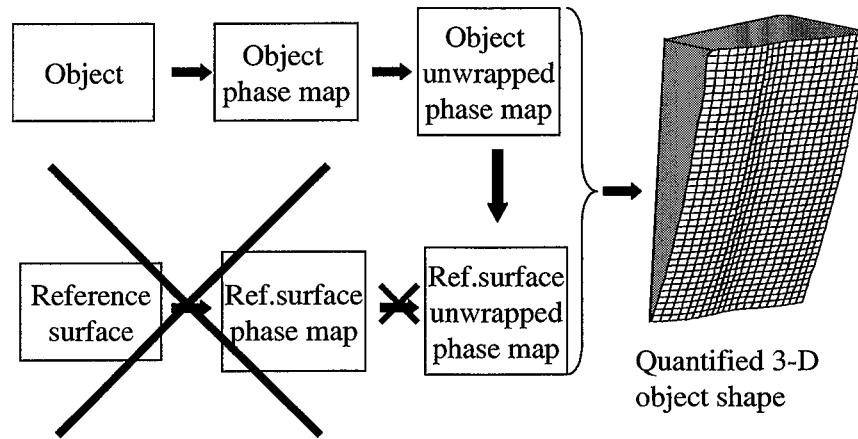
Figure 1. 11: Illustration of the problem generated by the absence of a reference plane

1. 5. Experimental aspects

1. 5. 1. The projection head

Since, in the long term, the measurements should take place out of the laboratory in more "adverse" environmental conditions, several basic requirements should be considered in the conception of the projection-head. A first study led us to conclude that the most important requirements of the projection-head are:
* sturdiness, so that it can be easily transported without having to do the adjustments each time
* compactness
* simple and fast adjustments
* easy phase-shifting
* easy variation of fringe pitch in order to adapt it easily to the object to be measured, and to the incidence angle
* a minimum influence of dust and aberrations

Several interferometers were evaluated and tested in a study previously done in our lab, and as a first step a Mach-Zehnder type interferometer was chosen for these measurements. It is sketched in Figure 1.12. The entering laser-beam is separated in two by the beam-splitter. The two beams are then reflected by two mirrors on the beam-splitter that recombines them. Then, the two slightly tilted laser beams enter the same microscope objective (40x) to create and project Young's fringes on the measured object. One of the two mirrors is fixed on a piezo that allows it to move perpendicularly to the reflecting surface, in order to perform the phase-shifting procedure described in Section1.2.2. The position and orientation of both mirrors can be changed in order to

adjust the position and angle of the two beams entering the microscope objective. This allows to adjust the relative position of the two point-sources S_1 and S_2, and thereby the spacing (period) and orientation of the fringes.
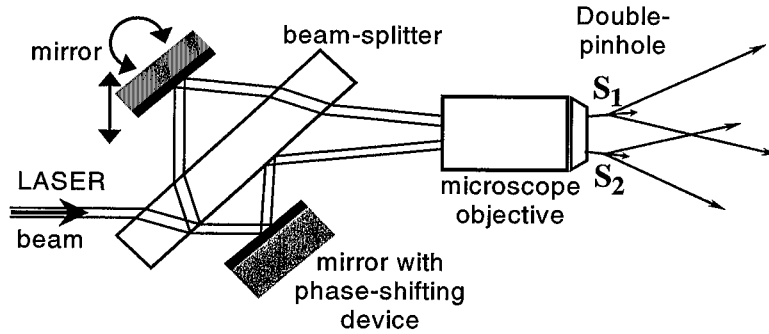
Figure 1. 12: Diagram of a modified Mach-Zehnder interferometer

1. 5. 2. The set up

The whole set-up is illustrated in Figure 1.13. The projection system is made of the laser and of the projection head shown in Figure 1.12. The observation system consists of a CCD-camera and an objective. Both the projection and observation systems are interfaced with a computer. More precisely, a Nd:Vanadate laser yielding green light (532 nm) is used as the source of light. Its power can go as high as 5 W, however in the frame of this work, we usually used 0.5 W. The projection head is placed at an angle α with respect to the surface normal (z-axis) at a distance **R** (usually a few meters), as illustrated in Figure 1.13. The distance between the two point-sources is about a few hundreds microns. The period of the fringes projected on the objects is about a few cm. The intensity profile is captured by a standard CCD camera (Sony XC-75 CE, 752 x 582 pixels, 8 bits, CCIR) and an 8 mm objective. The observation system is placed in front of the object along its normal (z-axis).

The computer is connected to the piezo and to the camera. It controls the piezo to carry out the phase-shifting procedure, while registering fringe images to produce the wrapped-phase map. After this acquisition procedure, it unwraps the phase-map in order to produce the unwrapped-phase map. A modified commercially-available program (Visilog 5.2) is used to perform the phase-shifting, the image acquisition and the phase map calculation. It also allows image filtering and analyses. In the frame of this work, a 4-image algorithm is used for the phase-shifting. The phase-maps used are not filtered.

As will be seen in more detail in Chapters 2 and 3, in order to retrieve the height information from the phase-maps, methods for calibrating the measurement system are needed. Towards this aim, we use a distance-meter theodolite to measure the position of the projection head and several points on the surface. Once aimed at a point, it is able to register the distance to this point as well as the angles of measurement. From these data it computes the object-coordinates of the measured point. This simplifies the measurement, since it does not require to work with two theodolites, by triangulation intersection. The accuracy announced by the provider was 1 mm. Furthermore, for the measurements done in the frame of this work, the object-coordinate system is set according to

the theodolite. Its vertical axis defines the y-axis, and the two other axes (x- and z-axis) are determined using a reference point to fix the theodolite orientation.
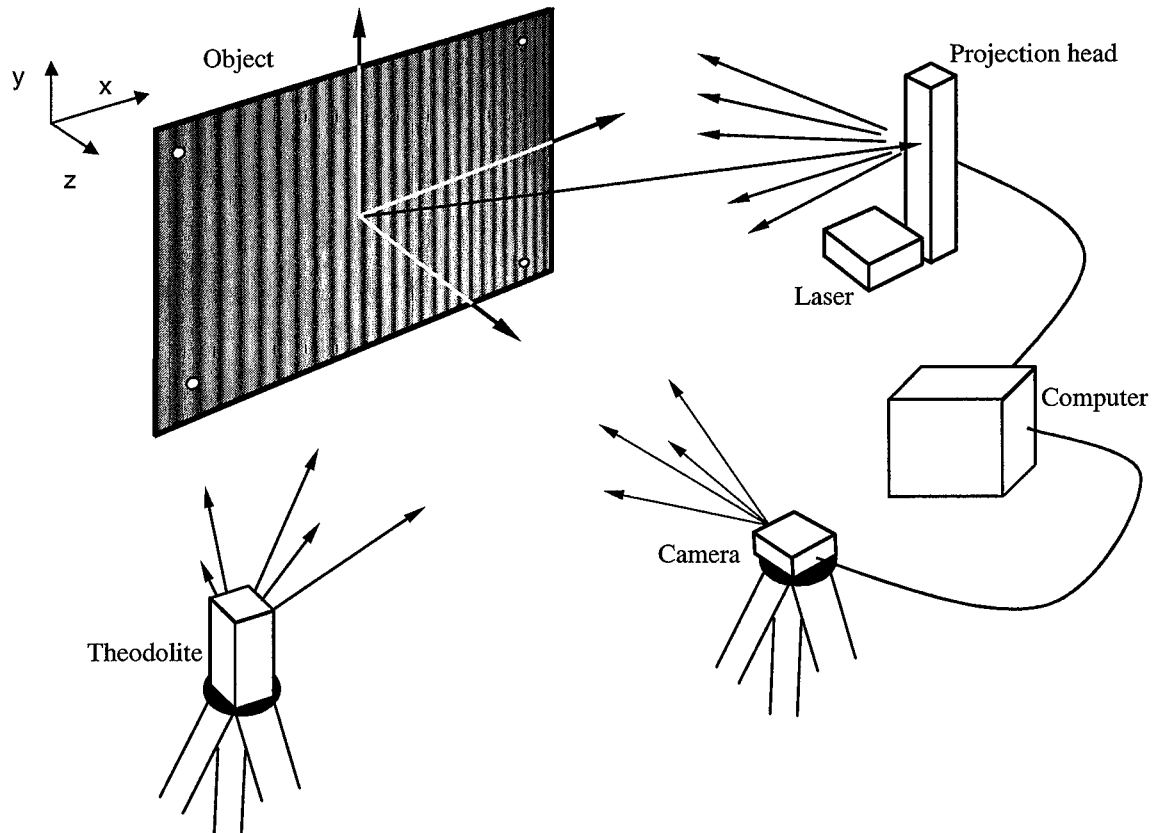
Figure 1. 13: Diagram of the set-up used to perform a fringe projection measurement on large objects

1. 5. 3. Objects measured

Several objects were measured to test the methods: a windsurf board, car part, portion of the lab wall and a beach umbrella. A common characteristic of all these object is that at least one of their dimension is systematically larger than 1 m. Furthermore, a calibration plate has been selected in the aim of testing the system. It is made of a composite aluminium-aluminium sandwich honeycomb structure, which is commonly used in the airplane industry. It represents the double advantages to be light-weight and rigid and its size is 1.5 x 2 m. Figure 1.14 shows a photograph of this plate and of its supporting structure. This was specially designed to fulfill certain requirements. Usually, the plate is used in a vertical configuration, however, in order to test the measuring system and its limitations, it is desirable to be able to lift the plate up and down, or to rotate it around a vertical or horizontal axis. Of course, the supporting structure must not deform the plate by applying constraints to it. A system of 3 contact points was used for this purpose. Furthermore, the whole system is fixed on a trolley with wheels allowing to move it easily from place to place.
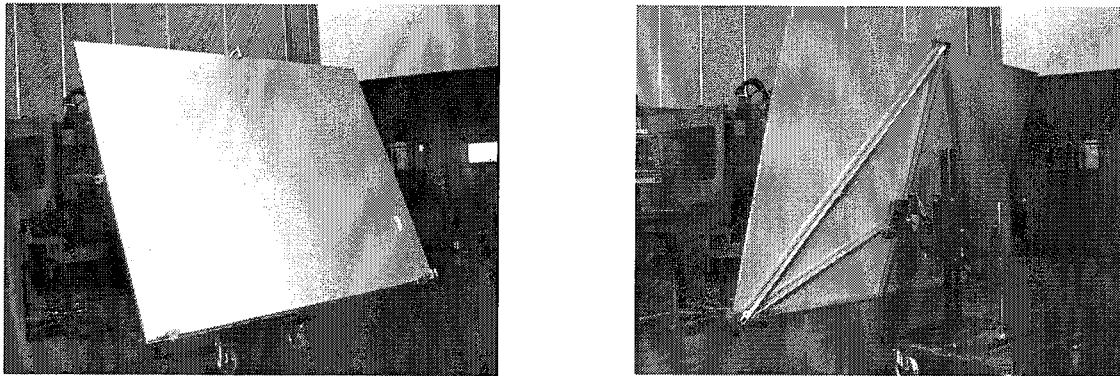
Figure 1. 14: Photograph of the calibrating plate and supporting frame with 5 degrees of freedom
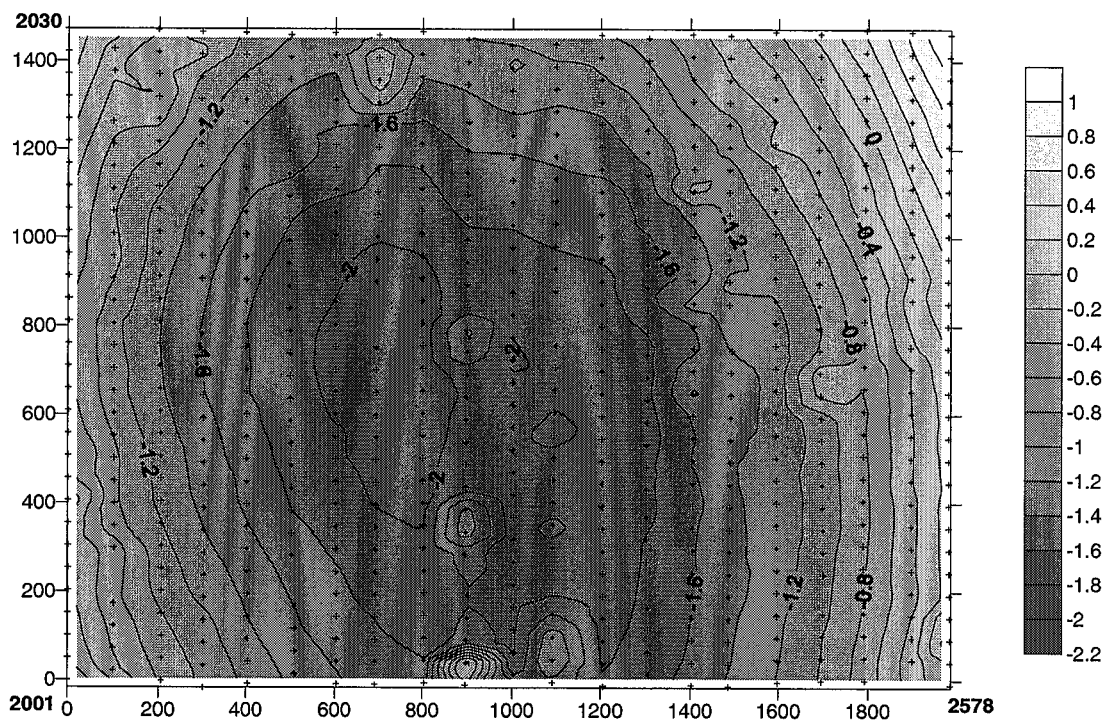
Figure 1. 15: Shape of the aluminium plate determined by photogrammetry, and represented relative to its median plane.

In order to know precisely the shape of the calibration plate, it was measured in a vertical position by photogrammetry. Since the plate has no visible texture, it had to be prepared first. For that purpose, 607 targets and markers distributed in 21 vertical lines were stuck on it, as well as scaling carbon bars. This phase of preparation took approximately 45 minutes. Then, 40 pictures (for

information redundancy) where taken: this step lasted about 20 minutes. Finally, adjustments were calculated using all the points and a best-fit about a plane. The distance from each point to the best-fit plane were also determined. The computation of the object coordinates of the points on the surface and the 3D reconstruction of the plate lasted about 10 minutes. The given precision in the x, y and z direction is 0.1 mm. The resulting shape relative to a median plane is displayed in Figure 1.15, and shows that the surface is planar within a few millimeters, with a small curvature in the middle.

1. 5. 4. Example of phase map acquisition

The phase-map of the object under investigation is acquired using the phase-shifting and phase-unwrapping procedures described in Section 1.2. As an example, Figure 1.16 illustrates the different measurement steps necessary for registering the optical print of the windsurf board:

- the image of the fringe pattern,
- the wrapped phase-map
- the modulation maps
- the unwrapped phase map.
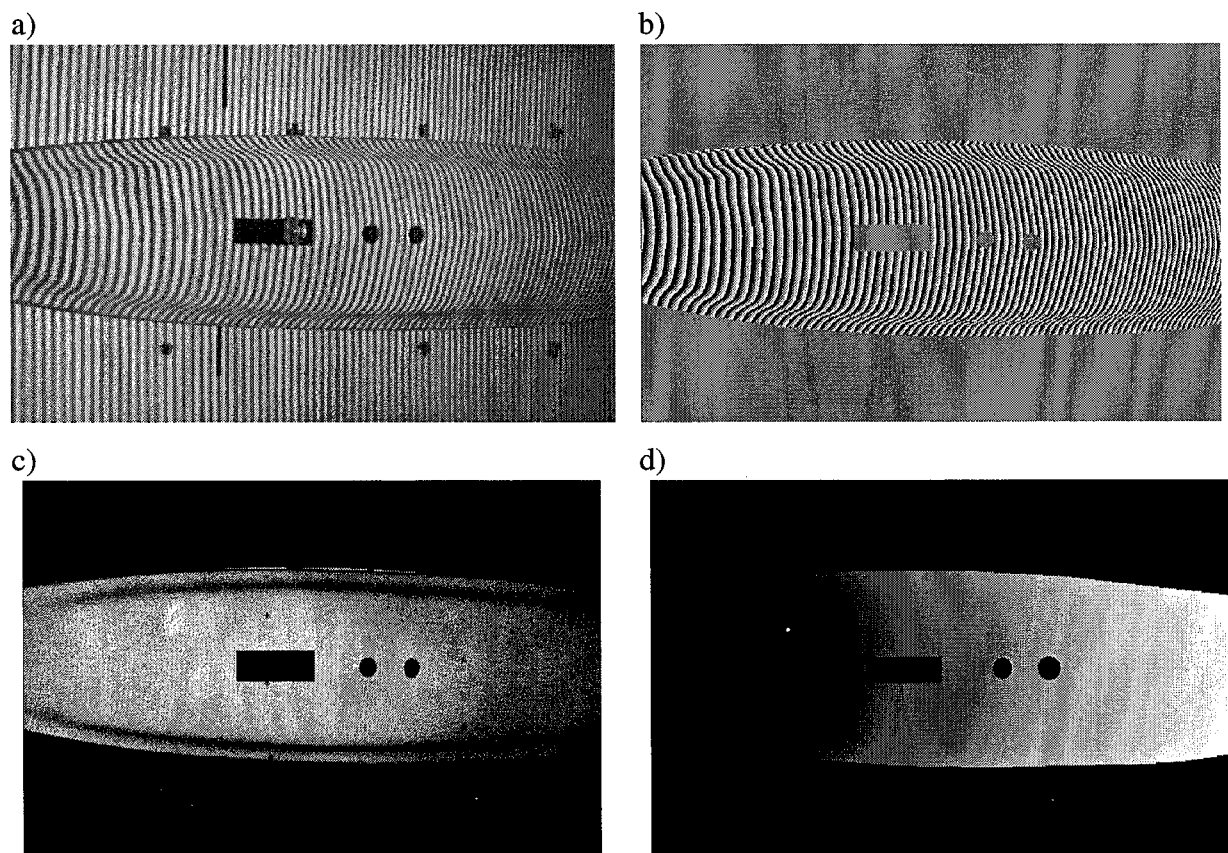
Figure 1. 16: Typical images of fringes projected on windsurf board (a), the subsequently measured wrapped phase-map (b) and modulation map (c). The last picture is the unwrapped phase map (d)

The four pictures are examples of: (a) an image of the fringes projected on the windsurf board, (b) the measured wrapped phase map, (c) the modulation map, and (d) the unwrapped phase map. The image was masked in order to select the region of interest to be submitted to the unwrapping program. The intensity is expressed in grey levels and usually varies between 0 to 256 grey levels in the fringe image, from -128 to 128 for the wrapped phase map (uses all the dynamic range of the acquisition board - 256 grey levels corresponding to the phase range going from 0 to 2π). The modulation map varies from 0 for the darker ones to 256 grey levels for the lighter shades. The unwrapped phase-map range of values corresponds to 256 multiplied by the number of fringes.

1. 6.   Conclusion towards new data treatment algorithms

An experimental solution has been found for illuminating the object: a divergent beam Mach-Zehnder type interferometer. The illumination system as well as the observation system used in this work are not fully optimized, nor characterized. Further studies should aim at improving and evaluating the illumination uniformity, the image dynamic, the characteristics of the camera, the fringe period and the sensitivity. The effect of the speckles and of the digital image treatment on the precision should also be assessed. However, clearly, this is not the aim of this work, since the problem we want to address is the interpretation of the object phase map. We consider that the measurement system is well enough developed to show the feasibility of phase-map interpretation.

As seen above, the illumination adopted in the frame of this work implies that the fringes are curved and not equispaced anymore, so that the classical approach for extracting the height information from the phase map cannot be used anymore. In the frame of this work, we will focus on finding new methods allowing to extract the height information from the optical print acquired. In that aim, we must solve different problems: the fringes shape and distribution, as well as the lack of a large plane reference surface. Original solutions are conceived and implemented. Finally, the feasibility of these methods as well as a first evaluation of their accuracy and limitation is done. All these results are presented in the four next chapters.

1. 7.   References

1. Dessus B., Leblanc M., *The 'fringe method' and its application to the measurement of deformations, vibrations, contour lines and differences of objects*, Opt Electronics, 1973, 5, p.369-91.

2. Vishnyakov G.N., Levin G.G., and Naumov A.A., *Measurement of the Surface of 3-Dimensional Objects by the Method of Projection of Interference-Fringes*, Optics and Spectroscopy, 1998, 85(6), p. 933-937.

3. Malacara D., Ed. *Optical shop testing*, 2nd ed. Wiley series in pure and applied optics, 1992, Wiley and Sons, Inc., New York.

4. Robinson D. W., Reid G. T., Eds. *Interferogram analysis: digital fringe pattern measurement techniques*, 1993, Institute of Physics publishing.

5. Chen F., Brown G. M., Song M., *Overview of three-dimensional shape measurement using optical methods, Optical Engineering,* 2000, **39**,p.10-22.

6. Oesch S., Sabri N., Pflug L., *Application de la technique des moirés à l'étude de la surface d'un revêtement routier*, Swiss Institute of Technology, Civil Engineering Department, Lausanne, December 1987, p.1-54.

7. Goodman J. W., *Introduction à l'optique de Fourier et à l'holographie*, 1972, Masson et Cie., Paris.

8. Lehmann M., Jacquot P., and Facchini M., *Shape measurements on large surfaces by fringe projection.* Experimental Techniques, 1999. **23**(2), p. 31-35.

9. Liu H., Lu G., Wu S., *Speckle-induced phase error in laser-based phase-shifting projected fringe profilometry*, J. Opt. Soc. Am. A, 1999, **16**, No. 6, p. 1484-149.

CHAPTER 2

The particular case of planar objects: methods

In the previous chapter, we described two problems that arise when applying the fringe projection method to large objects. The first problem is to illuminate the whole surface of those large objects in order to measure them at once. It can be solved by illuminating the object with interferometrically-generated fringes produced by divergent beams of coherent light. However, in that case, the projected fringes are not straight and equidistant, and the relation between the phase and the height is not linear. Therefore the classical data treatment method cannot be applied anymore. This leads to the second problem which is to extract the height information from the measured "optical prints" of large objects. Other approaches must be conceived and applied.

In this chapter, we address these problems in the particular case of planar objects. This limitation allows to simplify the equations describing the system. A key factor is the vector $r = (r_x, r_y, r_z)$ separating the two point-sources, whose components are unknown. In work previously done in our group, a first calibration procedure was developed in order to determine r. It is based on a least squares calculation minimizing the difference between the measured phase and the theoretical phase, for all the points of the surface that lie in the plane z = 0. Once r is determined, the shape of the object can be computed.

In a first attempt to calibrate r even if the measured surface does not lie in the plane z = 0, two alternative methods have been developed in the frame of this work. One of them is based on a projection-head made of two coupled-interferometers, where the distance separating the two illumination sources is determined physically, by construction. The other method is based on another least-squares calculation, similar to the one described above. However, this time, it is performed only on a few points of the surface, for which object-coordinates (z can have any value) and phases are known.

In this chapter, after considering the particularity of planar objects, the three methods are explained. Then a simulation studying the effects of a small variation of r_x, r_y, and r_z is presented.

2. 1. The special case of flat objects: linearization of the relation between the height and the phase [1]

A first approach to exploit the acquired "optical print" of large objects (i.e. their unwrapped phase-map) is to "mimic" the classical method used for small objects, by restoring a relation similar to Equation (1.5) between the height Δz and the phase difference $\Delta\varphi$. This is possible under certain assumptions that allow to linearize the expression of the phase φ in z, and to write the height as:

$$\Delta z = S(x, y) \cdot \Delta\varphi(x, y, z) \tag{2. 1}$$

where however, the sensitivity $S = S(x, y)$ is no longer a constant, but a function of x and y. The theoretical development is done below.

As described in Chapter 1; Section 1.5, we consider the object to be illuminated from the side under a large incidence angle (about 60° to 70°), by two points-sources of coherent light. This is sketched in Figure 2.1.

The following theoretical developments may in principle be adapted to any object surface, but for reasons related to the imaging of the object, we consider that:
*   the object is flat.
*   the object is almost parallel to the camera.
Furthermore, to simplify the calculation, we assume that:
*   the surface lies roughly in the (x, y, $z = 0$)-plane (vertical here),
*   the positive z-direction points toward the observation.

As seen in Chapter 1, Section 1.3, if the illumination is realized using two point-sources of coherent light, then the phase $\varphi(x, y, z)$ is proportional to the difference between the distances from any point (x, y, z) on the surface to both sources. This is expressed in Equation (2.2):

$$\varphi(x, y, z) = \frac{2\pi}{\lambda}[\sqrt{(R_x + r_x - x)^2 + (R_y + r_y - y)^2 + (R_z + r_z - z)^2} - \sqrt{(R_x - x)^2 + (R_y - y)^2 + (R_z - z)^2}] \tag{2. 2}$$

where λ is the laser wavelength, $R = (R_x, R_y, R_z)$ is the position of one of the two point-sources, and $r = (r_x, r_y, r_z)$ is the vector separating the two point-sources. Surfaces of equal phase difference $\varphi(x, y, z)$ are thus hyperboloids.

Since the distance R between the illumination sources and the origin (meters) is larger than the distance r between the two point-sources (few tenths of millimeter) by several orders of magnitude, $\varphi(x, y, z)$ can be approximated to the first-order of r, as given by Equation (2.3):

$$\varphi(x, y, z) = \frac{2\pi}{\lambda} \cdot \frac{((R_x - x)r_x + (R_y - y)r_y + (R_z - z)r_z)}{\sqrt{(R_x - x)^2 + (R_y - y)^2 + (R_z - z)^2}} \tag{2. 3}$$
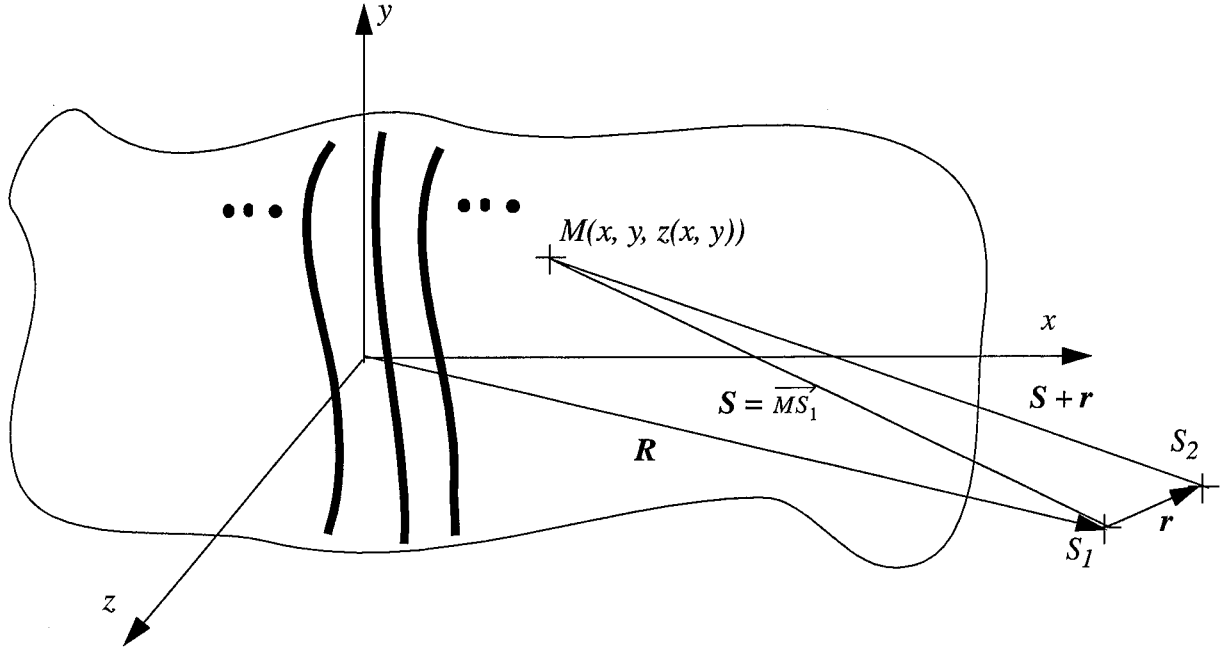
Figure 2. 1: Diagram illustrating the measurement configuration. The two point-sources, S_1 and S_2, are separated by a distance r.

Furthermore, when the height variation $z(x, y)$ is relatively small compared to the distance R to the sources (we have a flat or quasi-planar surface), $\varphi(x, y, z)$ can be written as first terms of a Taylor's series development, neglecting the high order terms (first-order expansion of Equation (2.3) in z):

$$\varphi_{meas} = \varphi(x, y, z= 0) + \frac{2\pi}{\lambda} \cdot z(x, y) \cdot \left[\frac{R_z \cdot ((R_x - x)r_x + (R_y - y)r_y + R_z r_z) - r_z \cdot ((R_x - x)^2 + (R_y - y)^2 + R_z^2)}{((R_x - x)^2 + (R_y - y)^2 + R_z^2)^{\frac{3}{2}}} \right] \qquad (2.4)$$

where $\varphi(x, y, z=0)$ is the phase of the reference plane at $z=0$. By reversing Equation (2.4), we obtain the height:

$$z(x, y) = \frac{(\varphi_{meas} - \varphi(x, y, z= 0))}{2\pi} \cdot \left[\frac{\lambda \cdot ((R_x - x)^2 + (R_y - y)^2 + R_z^2)^{\frac{3}{2}}}{R_z \cdot ((R_x - x)r_x + (R_y - y)r_y + R_z r_z) - r_z \cdot ((R_x - x)^2 + (R_y - y)^2 + R_z^2)} \right] \qquad (2.5)$$

According to Equation (2.5), the expression of the height z is similar to Equation (2.1). It is the product of a phase difference $((\varphi_{meas} - \varphi(x, y, z= 0)))$ and the sensitivity $S(x,y)$ (term in the square brackets). However, even though this equation looks like the expression of z given in

Chapter 1 (Equation (1.6)), there are some differences. Indeed, here the sensitivity is not constant, but is a function of x and y, and varies on the surface of the object. Furthermore, since for large objects there exist no reference plane, its phase-map $\varphi(x, y, z=0)$ cannot be measured, but has to be artificially generated.

In Equation (2.5), the wanted information is the height $z(x,y)$, the known or measured variables are the object-coordinates x, y and the phase φ_{meas}. The parameters r_x, r_y, r_z and R_x, R_y, R_z describe the set-up configuration and their determination is crucial to calibrate the system, and therefore, to solve our problem. Once their values are known, the phase-map $\varphi(x, y, z=0)$ of the reference plane and the sensitivity $S(x,y)$ are computed. And finally, from these values, the height $z(x,y)$ is calculated using these values, according to Equation (2.5).

The parameters R_x, R_y, R_z are easily measured using a ruler, a string or a theodolite. However, the components r_x, r_y, r_z of the vector r are more difficult to determine and methods to do so must be developed.

2. 2.   Calibration of the system by determining $r = (r_x, r_y, r_z)$

In the previous section, we have seen that under certain assumptions, the relation between height and phase can be simplified and is similar to the expression used to model the system in the classical approach (Chapter 1; Section 1.3). However, to be able to use this relation for calculating the height map of the object, the components of $r = (r_x, r_y, r_z)$ must be determined first. In this section, we present three methods to compute these parameters.

2. 2. 1.   LS1: the first least-squares method [1]

A first development, previously done in our group, aims at determining $r = (r_x, r_y, r_z)$ from the measured phase-map of flat objects. This methods uses least-squares calculations minimizing the difference between the measured phase of points lying in the plane $z = 0$, and their theoretical phase. This is expressed by Equation (2.6):

$$\varepsilon^2 = \sum \left(\varphi_{meas}(x_k, y_k) - \frac{2\pi}{\lambda} \cdot \frac{(R_x - x_k)r_x + (R_y - y_k)r_y + R_z r_z}{\sqrt{(R_x - x_k)^2 + (R_y - y_k)^2 + R_z^2}} - \varphi_0 \right)^2 \tag{2.6}$$

$\varphi_{meas}(x_k, y_k)$ is the phase measured at point (x_k, y_k) on the object surface (where it is assumed that $z_k = 0$). The second member in the parenthesis is the theoretical expression of the phase at points where $z = 0$, calculated according to Equation (2.3). φ_0 is an unknown phase offset mainly introduced by the phase unwrapping.

This method presents the advantage to be simple, but it also has a limitation. Indeed, it only works if the object theoretically lies in the plane $z = 0$, or if the experimenter knows exactly what points of the object belong to the plane $z = 0$. This initial assumption is technically difficult to realize, and therefore other approaches have been developed.

2. 2. 2. DPH: the double-pinhole method

The second proposed method aims at calibrating r geometrically. It is based on a projection head made of two mutually tuned interferometers set-up in series, namely a Mach-Zehnder and a Young interferometer. As in the projection head described in Chapter 1, Section 1.4, two slightly tilted laser beams enter the same microscope objective creating the two point-sources that project fringes of light on the measured object. The double-pinhole (i.e. the Young interferometer) is placed after the objective and then, the Mach-Zehnder interferometer is adjusted so that the two point-sources fit exactly the double-pinhole, as sketched in Figure 2.2 (left). Consequently, the distance between the two pinholes gives the spacing r between the two point-sources.

However, knowing r is not sufficient by itself to determine the vector components r_x, r_y, r_z of r. Therefore, we need additional information. For that purpose, we use the impact position of the two laser beams on a surface to evaluate the relative positions of the punctual sources S_1 and S_2. Indeed, if the double-pinhole is perpendicular to the bisector of the two beams, and if the microscope objective is well centered, the two laser beams will impinge on a surface at points P_1 and P_2 (after withdrawal of the microscope objective and double-pinhole), as sketched in Figure 2.3. Using the coordinates of these two points, we determine the position of point P_2', which is such that $\overrightarrow{S_2P_2'}$ and $\overrightarrow{S_2P_2}$ are colinear and that $\left\|\overrightarrow{S_2P_2'}\right\| = \left\|\overrightarrow{S_2P_1}\right\|$. To simplify, we make the approximation that, macroscopically, $S_1 \sim S_2 = S$. Finally, using the fact that $\overrightarrow{P_1P_2}$ is parallel to $\vec{r} = \overrightarrow{S_1S_2}$, by geometrical construction, we determine the vector r separating the two illumination point-sources. This method is justified by its simplicity and was corroborated by previous experiments measuring the orientation of r. Its advantage is that the vector r is now physically known.
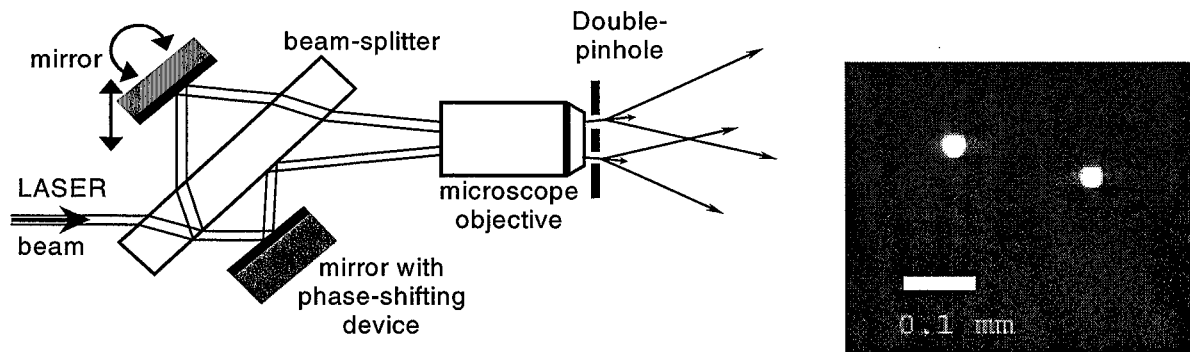
Figure 2. 2: On the left: diagram of the optical projection head built with two coupled interferometers (Mach-Zehnder and Young interferometer). On the right, microscope image of a double-pinhole

A typical double-pinhole is shown in Figure 2.2 (right). Several of them were made by "laser cutting" a thin stainless-steel sheet (0.1 mm) with different distances between the two holes and different hole diameters. This allows to adjust the fringes spacing by tuning the point sources, placing them closer or more remote. For this work, the distance between the holes was about 0.202 mm and their diameters about 0.025 mm, as measured with a high resolution microscope. The double-pinhole was fixed in a regular commercially available pinhole support.
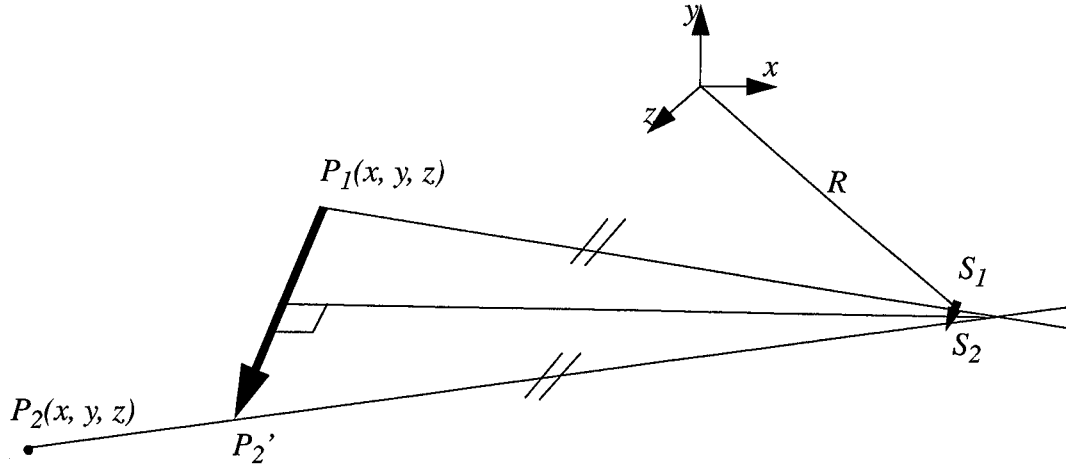
Figure 2. 3: Diagram of the measuring system when the microscope objective is taken off letting the two laser beam impinge on a surface at P_1 and P_2

2. 2. 3. LS2: the second least-squares method

Basically, the third method is based on a least-squares calculation similar to the one described in Section 2.2.1. However, here the calibration points considered for the calculation do not have to lie in the plane $z = 0$. Their object coordinates are measured with the theodolite. As for the phase, it is read on the unwrapped phase map, at the pixels corresponding to the calibration points (their positions are determined by displaying the image of the object on the monitor, and using a cursor). Knowing the object-coordinates of the calibration points, as well as their phase, we minimize the difference between the measured phase and the theoretical phase according to Equation (2.7):

$$\varepsilon^2 = \sum \left(\varphi_{meas}(x_k, y_k) - \frac{2\pi}{\lambda} \cdot \frac{(R_x - x_k)r_x + (R_y - y_k)r_y + (R_z - z_k)r_z}{\sqrt{(R_x - x_k)^2 + (R_y - y_k)^2 + (R_z - z_k)^2}} - \varphi_0 \right)^2 \tag{2.7}$$

This calibration method is described in more details in the following. As seen earlier, the phase can be written as:

$$\varphi(x, y, z) = \frac{2\pi}{\lambda} \cdot \frac{((R_x - x)r_x + (R_y - y)r_y + (R_z - z)r_z)}{\sqrt{(R_x - x)^2 + (R_y - y)^2 + (R_z - z)^2}} \quad \text{where} \quad r_x, r_y, r_z \text{ are to be determined.}$$

Knowing R_x, R_y, R_z by measuring them with the theodolite, considering n (n>4) calibration points (k=1 to n) and writing:

$$\begin{cases} a_{1k} = \dfrac{2\pi}{\lambda} \cdot \dfrac{(R_x - x_k)}{\sqrt{(R_x - x_k)^2 + (R_y - y_k)^2 + (R_z - z_k)^2}} \\[4mm] a_{2k} = \dfrac{2\pi}{\lambda} \cdot \dfrac{(R_y - y_k)}{\sqrt{(R_x - x_k)^2 + (R_y - y_k)^2 + (R_z - z_k)^2}} \\[4mm] a_{3k} = \dfrac{2\pi}{\lambda} \cdot \dfrac{(R_z - z_n)}{\sqrt{(R_x - x_k)^2 + (R_y - y_k)^2 + (R_z - z_k)^2}} \\[4mm] a_{4k} = 1 \end{cases} \tag{2.8}$$

where (x_k, y_k, z_k) is the kth calibration point, $\varphi(x_k, y_k, z_k)$ is the phase measured in the kth calibration point, one gets a set of linear equations:

$$\begin{cases} l_1 = a_{11} \cdot r_x + a_{12} \cdot r_y + a_{31} \cdot r_z + a_{41} \cdot \varphi_{offset} \\ l_2 = a_{12} \cdot r_x + a_{22} \cdot r_y + a_{32} \cdot r_z + a_{42} \cdot \varphi_{offset} \\ \qquad\qquad \dots \\ l_n = a_{1n} \cdot r_x + a_{2n} \cdot r_y + a_{3n} \cdot r_z + a_{4n} \cdot \varphi_{offset} \end{cases} \tag{2.9}$$

where φ_{offset} is an offset phase value artificially introduced by the phase unwrapping program. According to the theory, the least square method can be applied from n>4. In most of the cases treated below, we use at least 5 points (arbitrarily chosen).
Then, by writing:

$$l \equiv \begin{bmatrix} l_1 \\ l_2 \\ \dots \\ l_n \end{bmatrix}, \ X \equiv \begin{bmatrix} r_x \\ r_y \\ r_z \\ \varphi_{offset} \end{bmatrix} \ \text{and} \ A \equiv \begin{bmatrix} a_{11} & a_{21} & a_{31} & a_{41} \\ \dots & \dots & \dots & \dots \\ a_{1n} & a_{2n} & a_{3n} & a_{4n} \end{bmatrix} \tag{2.10}$$

the set of Equations (2.9) above can be simplified and written in a matricial form as:

$$l = A \cdot X \tag{2.11}$$

From this system of linear equations, we can write the equation of error:

$$V = A \cdot \hat{X} - l. \tag{2.12}$$

where l are the observations, $\hat{X}$ are the four unknown parameters (as they will be determined by the least square procedure), and V is the correction.

Then, the four unknown parameters $\hat{X}$ can be obtained by writing the condition of minimization:

$$V^T \cdot V = min = (A \cdot \hat{X} - l)^T \cdot (A \cdot \hat{X} - l) = \hat{X}^T A^T A \hat{X} - 2 l^T A \hat{X} + l^T l \tag{2.13}$$

The solution is given by:

$$\frac{\partial}{\partial X}(V^T \cdot V) = 2\hat{X}^T A^T A - 2l^T A = 0 \Rightarrow \hat{X} = (A^T A)^{-1} A^T l \tag{2.14}$$

Finally, r_x, r_y, r_z and φ_{offset} are determined.

2. 3.   Relation between the object-coordinates and the image-coordinates

An important aspect for the application of these three calibration methods is the relation between the observed image-coordinates and the object-coordinates, corresponding to the imaging. Indeed, in all the equations above, the coordinates considered are the object-coordinates x and y. However, what we actually measure with the CCD camera are the images-coordinates i and j (pixels). Consequently, in order to use the three calibration methods described above, we must first establish the relation between the image-coordinates (i, j) and the objects-coordinates. This relation is illustrated in Figure 2.4.

In order to be able to define a simple relation, the following assumptions are made (already stated in Section 2.1): the object is flat and almost parallel to the camera imaging-array. In addition, to simplify the calculation, we consider that the object lies roughly in the plane $(x, y, z = 0)$. In that case, a simple polynomial transformation allows to compute the object-coordinates (x, y) from the corresponding image-coordinates (i, j), and this transformation does not depend on $z(x, y)$. Pratt [2] uses a second order polynomial (called spatial warping polynomials):

$$\begin{cases} x = a_x + b_x \cdot i + c_x \cdot j + d_x \cdot i \cdot j + e_x \cdot i^2 + f_x \cdot j^2 + ... \\ y = a_y + b_y \cdot i + c_y \cdot j + d_y \cdot i \cdot j + e_y \cdot i^2 + f_y \cdot j^2 + ... \end{cases} \tag{2.15}$$

The first-order terms are related to translation, rotation and scaling between the object and its image. However there are no simple physical counterparts for higher-order terms. These are used to compensate for image deformation caused by the physical imaging system.

In our case, we consider that the imaging system does not deform the image, and neglect these terms. Thus, we have:

$$\begin{cases} x = a_x + b_x \cdot i + c_x \cdot j \\ y = a_y + b_y \cdot i + c_y \cdot j \end{cases} \tag{2.16}$$

Next, to take into account the effects of a slightly oblique observation or more generally, of a slight angle between the object and the imaging plane (causing a rectangular object to appear as a trapezoid on the image), additional terms are considered:

$$\begin{cases} x = a_x + b_x \cdot i + c_x \cdot j + D_x \cdot i \cdot j \\ y = a_y + b_y \cdot i + c_y \cdot j + D_y \cdot i \cdot j \end{cases}$$

(2. 17)

The coefficients of these equations are determined using at least four calibration points, for which the object-coordinates as well as image-coordinates are known. Finally, the general relation between the image-coordinates and the object-coordinates is known for any points on the object surface.
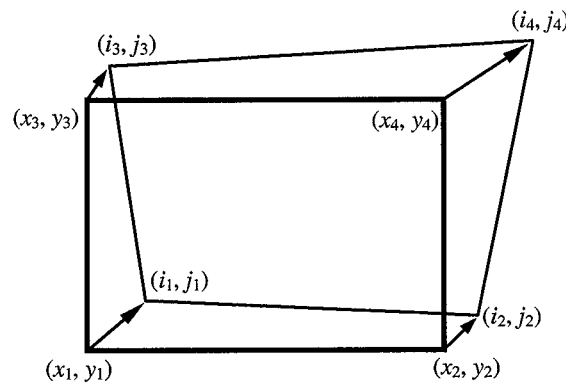
Figure 2. 4: In the case considered, at least 4 calibration points are necessary to determine the transformation between the object-coordinates (x, y) and the image-coordinates (i, j).

2. 4.   Methods

A typical measurement is done in the following way. The projection head (points-sources) and the camera are positioned relatively to the object as shown in Figure 1.13 or equivalently in Figure 2.1. At least four retro-reflective targets are placed on the object surface; they serve as calibration points. A theodolite is used to measure their object-coordinates, as well as the coordinates R_x, R_y, R_z of one of the two point-sources. An image of the object taken with the camera allows to measure the image-coordinates of the calibration points (retro-reflective targets). Finally, the fringes are projected on the object, and a phase-shifting procedure is carried out. A subsequent phase-unwrapping procedure yields the optical print of the measured object (unwrapped phase-map). If necessary, a binary mask is defined by selecting the areas of the object corresponding to points of the object where $z = 0$. The value 1 is attributed to the pixel corresponding to the points where $z = 0$ and the value 0 is attributed otherwise. All these data are used in the programs described in Section 2.4.1 and 2.4.2 to compute the desired height map (shape) of the measured object.

2. 4. 1. LS1 (first least-squares method) program

A program based on the first least-squares method (Section 2.2.1) was developed in order to determine the parameters r_x, r_y, r_z. Its front panel is displayed in Figure 2.5 a). As input data, we find the "Unwrapped-phase image" and a "Mask image". The latter allows us to delimit the area of the object lying in the $(x, y, z = 0)$-plane, where the least-squares calculation will be applied. The input parameters are the coordinates R_x, R_y, R_z of one of the illumination point-sources, a phase-scale allowing to convert the grey level units of the measured phase into the adequate radians units, and the laser light wavelength λ. The output data are the values of r_x, r_y, r_z, the reference plane phase-map, the sensitivity map and the height map. Furthermore, a scaling module (sub-routine) calculates the coefficients defining the transformation between the object-coordinates and the image-coordinates, using four calibration points. Its front panel is represented in Figure 2.5 b). The program works as follows. First, the experimenter enters the image-coordinates and the object-coordinates of four calibration points in the scaling module. Running it allows to determine the coefficients of Equations (2.17), and thus to compute the object-coordinates from the image-coordinates for any point of the surface measured with the camera.

a)   b)
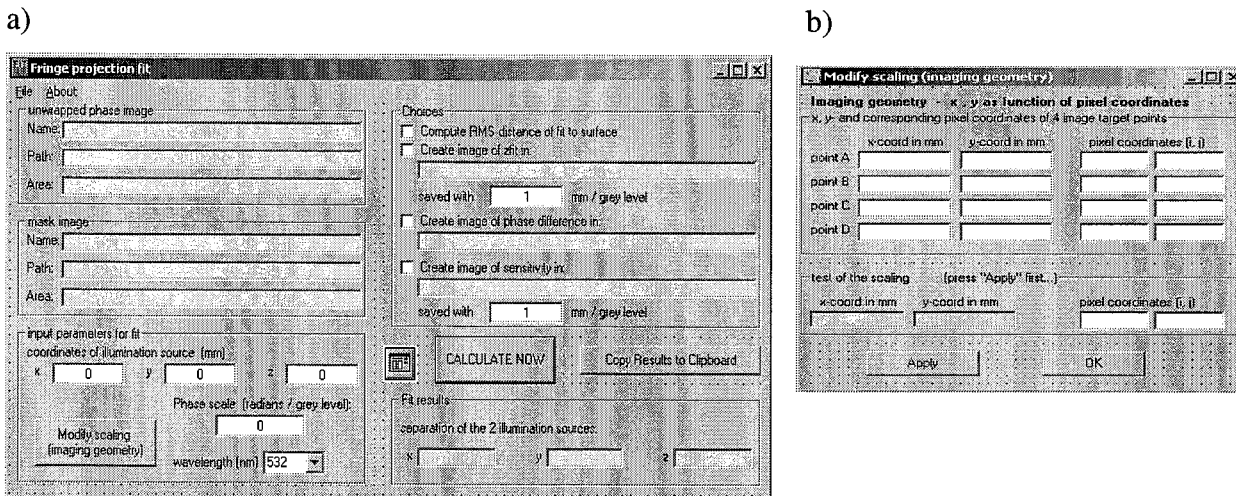
Figure 2. 5: a) Front panel of the program determining r_x, r_y, r_z by the LS1 method; b) Front panel of the scaling module

Then, the main module determines the parameters r_x, r_y, r_z the following way. For each pixel (i, j), the measured phase φ_{meas} is read in the input unwrapped-phase image. It is used for the least-squares calculation only if the test-value contained in the corresponding pixel of the mask-image is 1 (or if no mask is defined). Using the value of the measured phase φ_{meas}, the parameters R_x, R_y, R_z and the object-coordinates x and y corresponding to the pixel under consideration, the first least-squares method (LS1) is carried out using Equation (2.6), supplying the values of r_x, r_y, r_z.

Finally, using these values and all the input information mentioned above, the program computes and saves the reference phase-map, the sensitivity map and the height map, according to Equations (2.2) and (2.4).

2. 4. 2.   DPH (double-pinhole method) and LS2 (second least-squares method) program

A new program was implemented in order to compute the height map of the object, in the case where r_x, r_y, r_z is already known. Its front panel is displayed in Figure 2.6. It is inspired by the program described above, and similarly, the input data and parameters are the measured
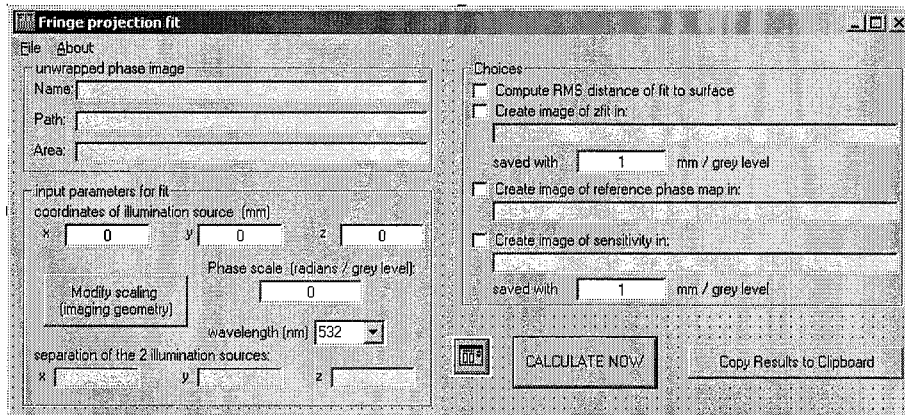
Figure 2. 6: Front panel of the program allowing the calculation of the sensitivity, the reference phase and the height maps using the double-pinholes method and second least-squares method

unwrapped phase-map, the coordinates of one of the illuminations sources R_x, R_y, R_z, a phase-scale allowing to convert the grey level units of the measured phase into the adequate radians units, and the laser light wavelength. The scaling module is exactly the same as the one described in the previous section. The main difference here, is that r_x, r_y, r_z are already known, since they are determined using separate procedures (DPH and LS2). Consequently, they are given as input parameters. In the case of the double-pinhole method (DPH), r_x, r_y, r_z are determined using the procedure described in Section 2.2.2. In the case of the second least-squares method (LS2), r_x, r_y, r_z are calibrated using Equation (2.7) and applying it to a small number of points. A set of calibration points with known image-coordinates are used in that purpose. Their measured phase $\varphi_{meas}(x_k, y_k)$ is read manually using a software for displaying images (Visilog 5.5).

In both cases, all these input data are used to compute the reference phase-map, the sensitivity map and the height map, according to Equation (2.2) and (2.4).

2. 4. 3.   Global overview

As for the classical method, this approach can be synthesized in terms of real and virtual worlds, as shown in Figure 2.7. The camera, projection head, measurement and results belong to the real world. Under the assumption that the object is planar and positioned parallel to the imaging plane of the camera (denoted 1 in the diagram), the latter can be modeled by the warping polynomials (2.17). These equations are calibrated using the pixel and object coordinates of the calibration points (this procedure is described at the beginning of this section). Finally, we obtain expressions giving the planimetric object coordinates (x and y) for any corresponding pixel (i, j).
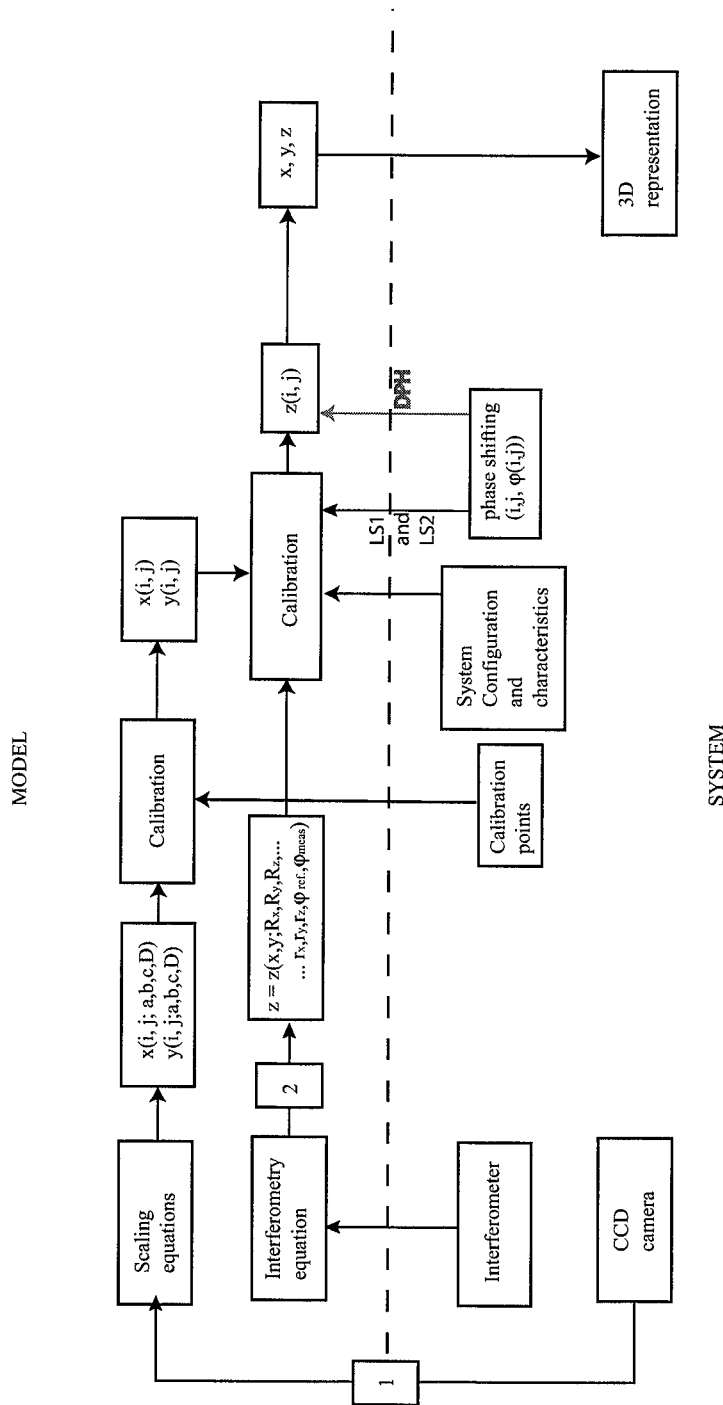
Figure 2. 7: Synthesis of the approach for planar objects

As for the projection head, it is modeled by the interferometric Equation (2.3). We have seen that under the assumption that $r \ll R$, the height z can be expressed by Equation (2.5), i. e. as a function of the measured phase map of the object φ_{obj}, the artificially generated phase map of the reference plane φ_{ref}, the parameters R_x, R_y, R_z, r_x, r_y, r_z and the planimetric object coordinates x and y.

Using the expression giving the planimetric coordinates x and y, and different calibration procedures described in Section 2.2.1 to 2.2.3, namely LS1, DPH and LS2, the expression of z as a function of the pixel position (i, j) only is established. Note that in the case of LS1, the measured phase map φ_{obj} is used for the system calibration (denoted by (3) in the diagram). Finally, using the measured phase map of the object and the expression giving the planimetric coordinates x and y, the height z is computed for every pixel (i, j). Knowing the object coordinates x, y and z corresponding to every pixel (i, j) allows to reconstruct the 3D shape of the object.

2.5. Preliminary testing

The first least-squares method (LS1) was tested on several objects larger than 1 m². The first example is a steel-concrete cantilever T-beam subjected to bending, as shown in Figure 2.8. The beam web undergoes buckling and is permanently deformed. The measurement was done after the buckling, and the measured area was about 1 m². The resulting map of deformations is presented in Figure 2.8 (right), and shows a maximum observed displacement of about 3 cm.
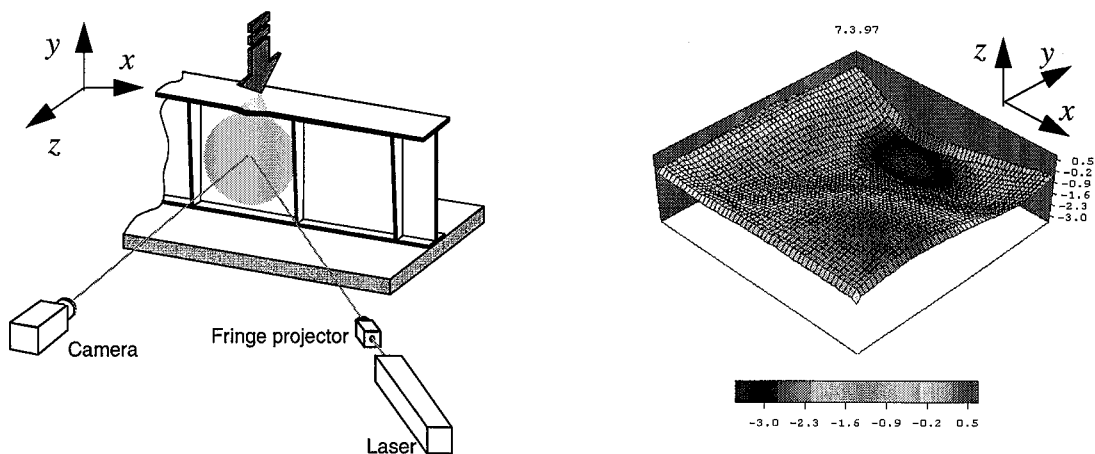
Figure 2. 8: Left: Diagram of the experimental set-up; and right: 3-D plot of the measurement result (the scale is given in grey level)
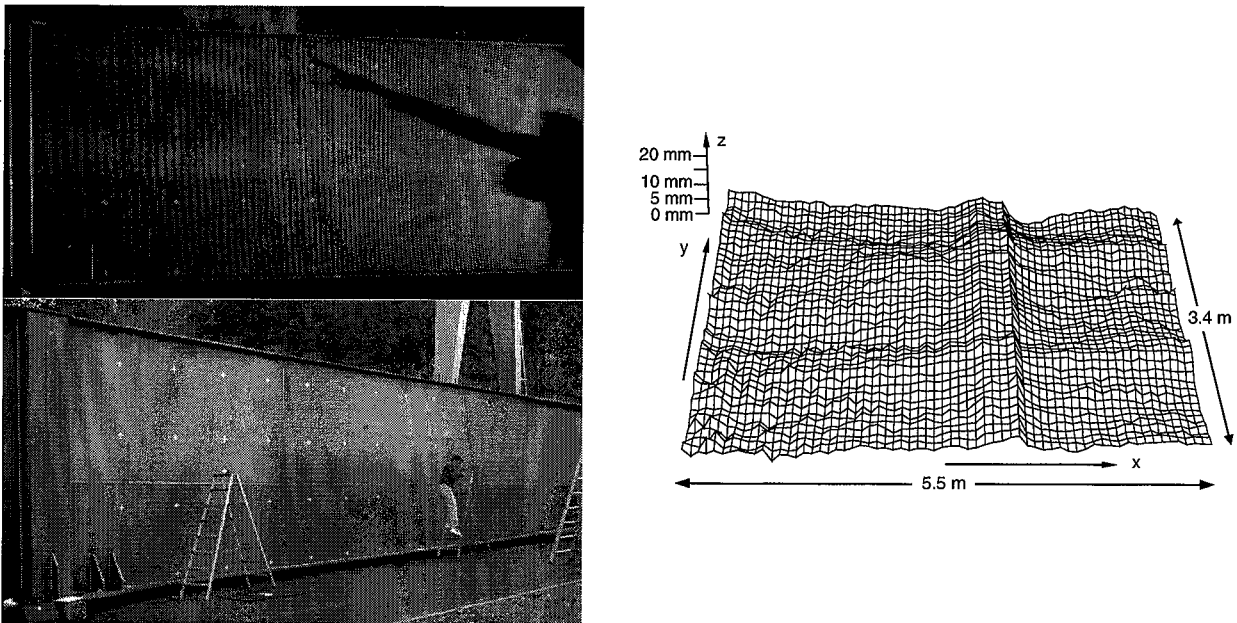
Figure 2. 9: Measurement of a bridge box girder using the first least-squares calibration method. Left (resp. top and bottom): picture of the bridge box girder with and without fringe projection; Right: result of the measurement

In the second example, the shape of a 6 x 20 m bridge box girder was assessed, using the same method (LS1). Figure 2.9 shows the fringe projection on those metallic walls during the measurement (upper left picture), and the results obtained for the 5.5 x 3.4 m portion (right). Unexpectedly, the effect of inner reinforcement bars (one vertical, and two horizontal ones, in the measured portion) welded on the back side of the box girder could be observed. For these measurements, the height resolution was estimated to be about 1 mm and the height variations including all errors (noise and systematic errors), remains within a z-interval of roughly 15 mm (over a total area of 7 x 4 m)[1].

Preliminary tests were also carried out for the double-pinhole method (DPH). The adjustment of the two point sources in front of the double-pinhole was shown to be feasible. The settings are quite easy, stable and reproducible after taking the pinhole off and putting it back. The system provides a direct determination of the separation of the two sources, within a few microns. A by-product of the double-pinhole is its filtering effect, as evidenced by Figures 2.10 and 2.11. It allows to significantly lower the noise due to imperfections and dust in the projection system as can be seen in Figure 2.11, and thereby to make $\varphi_{meas}(x, y)$ more accurate.

The preliminary testings presented above give encouraging results, and show the feasibility of measuring the shape of large and flat objects. However, the systematic errors or uncertainties are difficult to assess and a more quantitative evaluation of these methods is needed. Therefore, a first comparative evaluation of the three methods exposed above will be done and presented in the next chapter. But before this, it is interesting to see how an error or variation in the values of r_x, r_y, r_z affects the sensitivity and the reference phase-map, that means the height map.
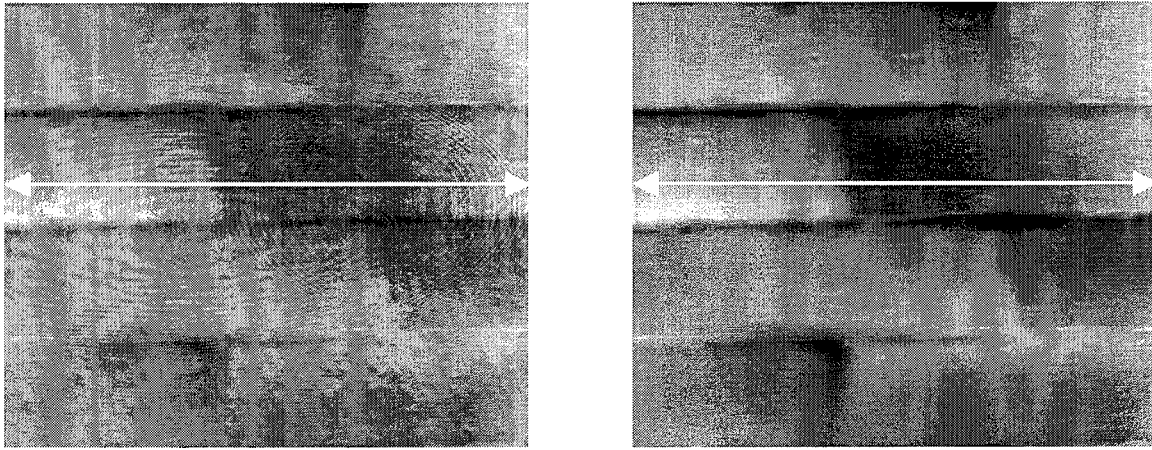
Figure 2. 10: Pinhole effect; phase image without pinhole(left), and with pinhole (right
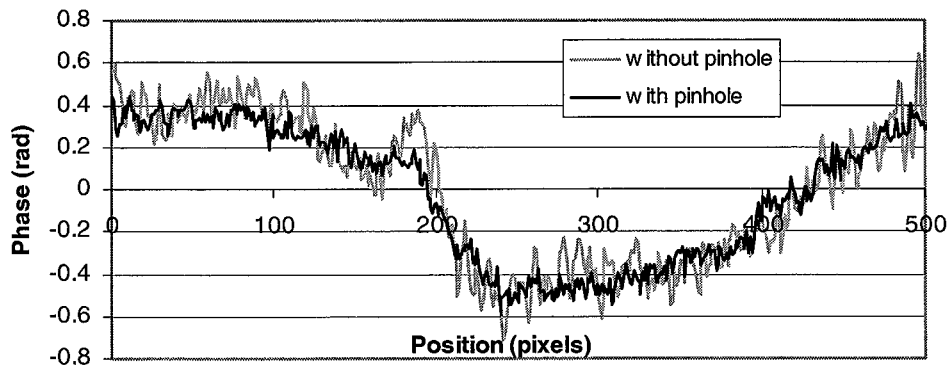
Figure 2. 11: Profile of the phase along the arrows drawn in the figures above

2. 6. Simulation of variations in r_x, r_y, r_z and of their effects on the phase and the sensitivity maps

The key factor in the three methods described above is the vector r separating the two point sources. Its modulus is generally about a few hundred microns and therefore, the precision in the determination of its coordinates is critical. A variation or small error in r (i.e. in r_x, r_y, r_z or r) induces a change in the orientation, spacing and curvature of the hyperbolic fringes. Thus it will affect the orientation, slope and curvature of the reference phase surface, and also the sensitivity. For example, it is well known from the theory [3] that the spacing p between to fringes is

approximately proportional to the distance between the sources and a point on the surface R and inversely proportional to r (p is taken perpendicularly to the fringes, spacing between two consecutive fringes near the fringe of order 0), according the following equation:

$$p \propto \frac{R}{r}$$
(2. 18)

Thus, when maintaining R constant, if r increases, p decreases and vice versa.

In the following, we study the effects of a small variation in r_x, r_y, r_z on the sensitivity and the reference phase-maps. This will also be useful to interpret the evaluation of the method exposed in the next chapter and to understand certain trends.

2. 6. 1. The reference phase-map

In this simulation, the sensitivity map and phase-map of a perfect reference artificial plane have been calculated for a value of $r_x = -0.06035mm$, $r_y = 0.002138$, $r_z = 0.187925mm$. Next, small variations $\Delta r_x = \pm 0.005mm$, $\Delta r_y = \pm 0.005mm$ and $\Delta r_z = \pm 0.005mm$ are introduced sequentially in the calculation[1]. The sensitivity and reference phase-maps are computed according to Eq. (2.2) and (2.4). Then, the profiles along two lines, one horizontal and one vertical crossing approximately at the center of the phase and sensitivity maps (see Figure 2.13c)), are observed. The results are shown in Figure 2.14 to 2.17.
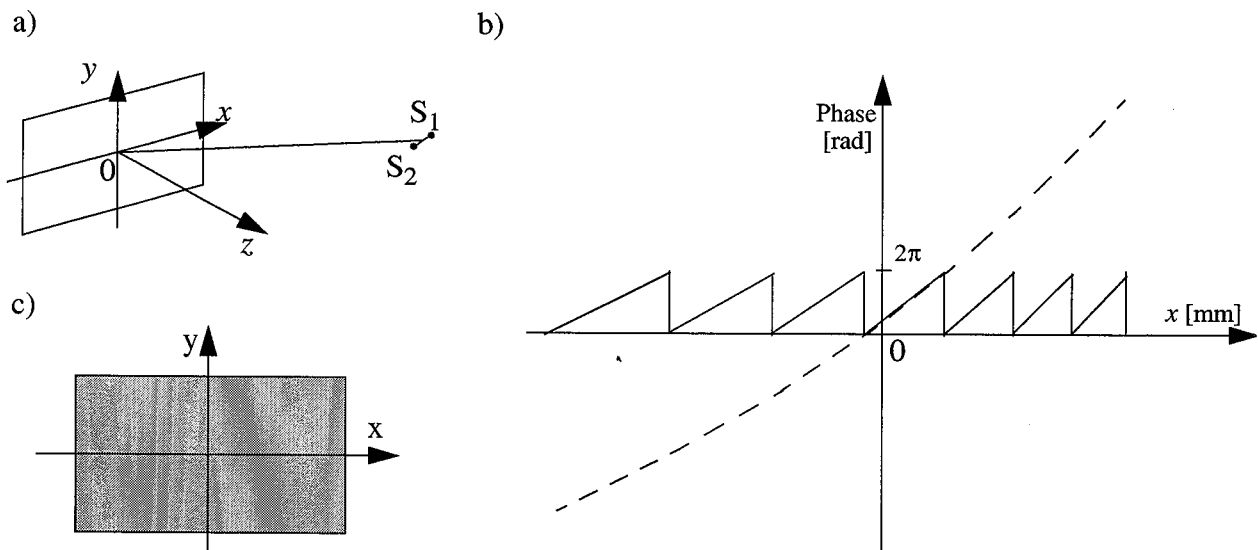
Figure 2. 12: a) Fringe projection configuration; b) Profile along a line taken across a wrapped and unwrapped phase map resulting from hyperbolic fringes.c) Diagram of the vertical and horizontal lines.

---

1. This values of r_x, r_y, r_z, and $\Delta r_x, \Delta r_y, \Delta r_z$ are chosen according to values commonly used or found in this work, i.e. for a punctual-sources separation of about 0.202 mm and a projection angle of about 70°.
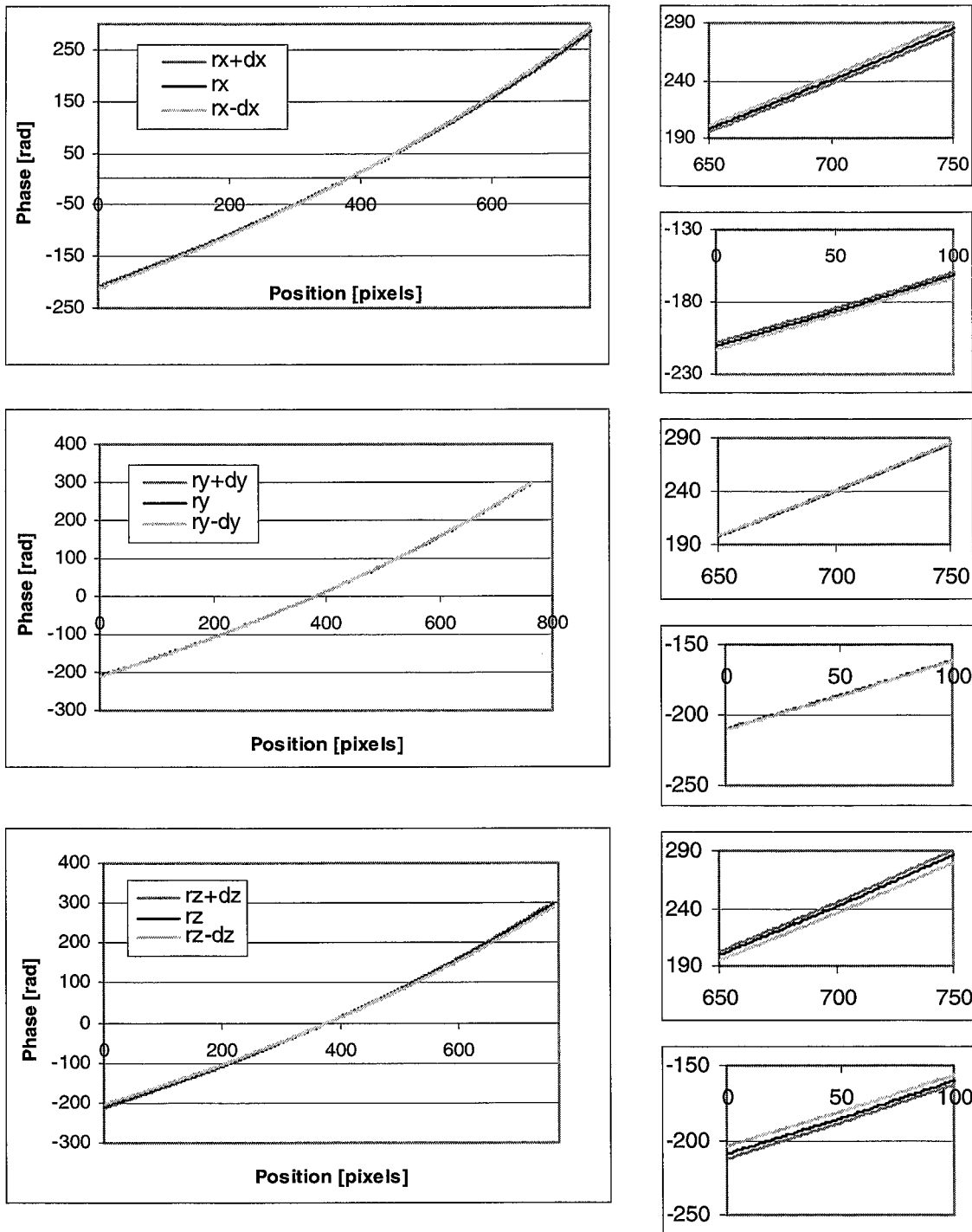
Figure 2. 13: Effect of a variation of r_x, r_y, r_z on the slope of the reference phase-map along a horizontal line.Upper right, details of the far right of the graphic; bottom right, details of the far left of the graphic.
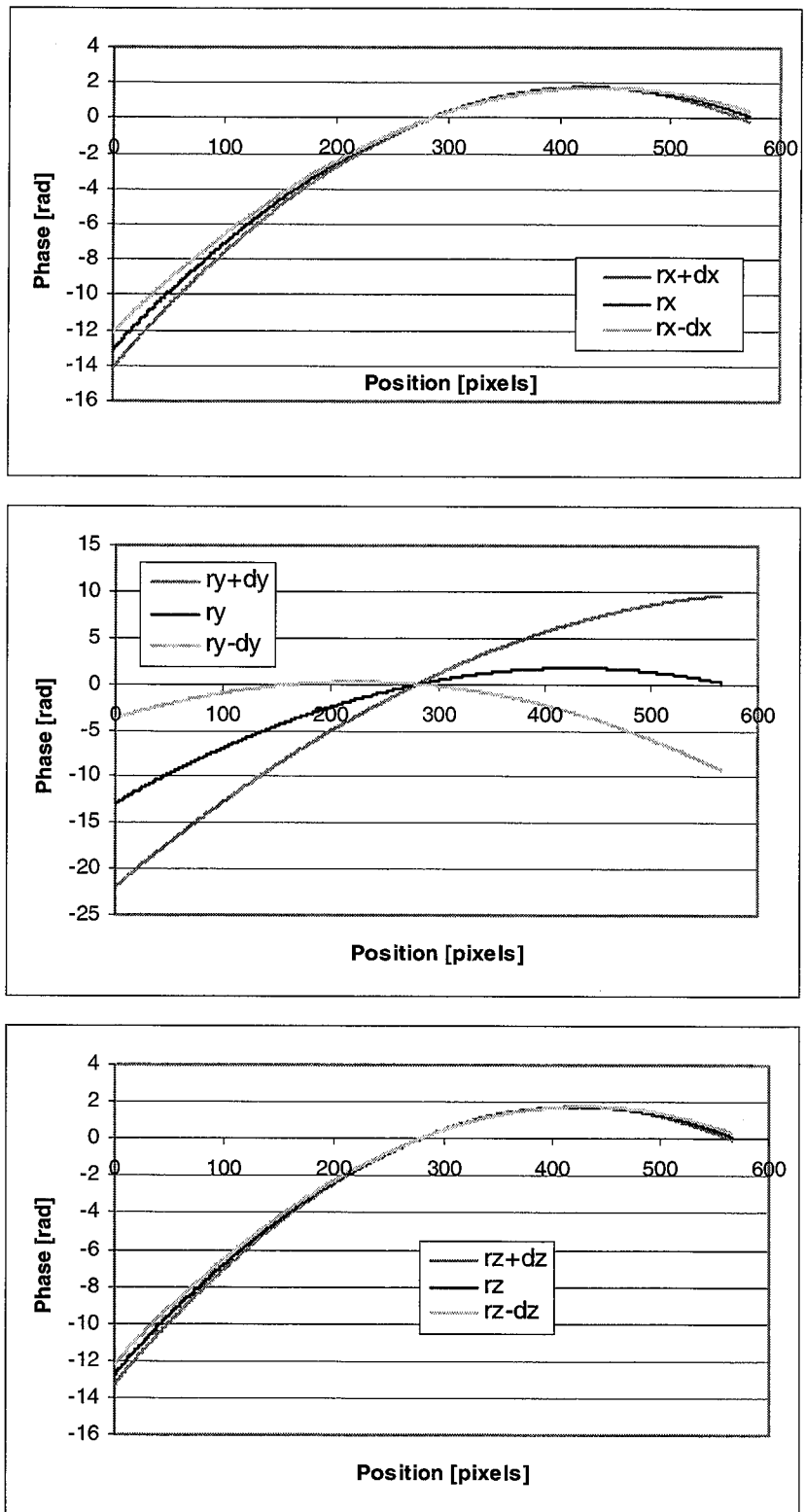
Figure 2. 14: Effect of a variation of r_x, r_y, r_z on the slope for the reference phase-map along a vertical line

The first observation is that the slope of the phase-map is not straight, but curved. For profiles along both vertical and horizontal lines, this is because the fringe interspace varies. For example, in this model, the fringes are projected from the right side of the object with an angle α of about 70° (Figure 2.13 a)). Therefore, the fringes are thinner on the right side of the object than on the left side. In that case, if a profile is taken along a line perpendicular to the fringes in a wrapped phase-map, then the profile observed looks like the one sketched in Figure 2.13 b). More precisely, the wrapped phase remains between 0 to 2π [rad], and the interspace decreases (from left to right). Thus, the local slope increases, from one fringe to another, and when the phase is unwrapped its global slope increases resulting in a curve Looking at Figure 2.14, we see that a variation of r_x, r_y, r_z leads to a tilt of the phase-map, implying a change in the slope. More precisely, a variation of r_x or r_z induces a tilt of the phase-map around a vertical axis, and have little effect on the vertical line profile, as shown by Figures 2.14 and 2.15.

At the opposite a change in r_y has very little effect on the horizontal profile of the phase-map, however, it influences perceptibly the vertical profile, showing a tilt about a horizontal axis. More specifically, when r_x decreases or r_z increases, the phase-map is tilted to the left around a vertical axis (Figure 2.14), and conversely. The change in the phase-map at the extremities of the graph reach approximately 5 to 10 rad.

As for the vertical profile, the effect of a variation of r_x or r_z influences more the curvature of the vertical profiles than their slope. The curvature of the vertical profile increases when r_x or r_z increase, and vice versa (Figure 2.15).

Apparently, the only effect of varying r_y is to tilt the vertical profile so that it varies of an amount of about 10 radians at 0 pixel for example. Furthermore, when r_y increases, the phase-map is tilted to the left, and conversely.

2. 6. 2. The sensitivity map

As for the sensitivity, the profiles along the vertical and horizontal lines are continuous curves and their values vary little: between 2.9 and 3.6 [mm/rad] along the horizontal line and between 3.1 and 3.3 [mm/rad] along the vertical line, so that it can be considered almost constant. Again, its variation doesn't depend the same way on the variation of r_x, r_y, r_z, in both profiles. It is almost invariant upon a variation of r_y. However, it is translated about 0.01 [mm/rad] up when r_x or r_z varies.
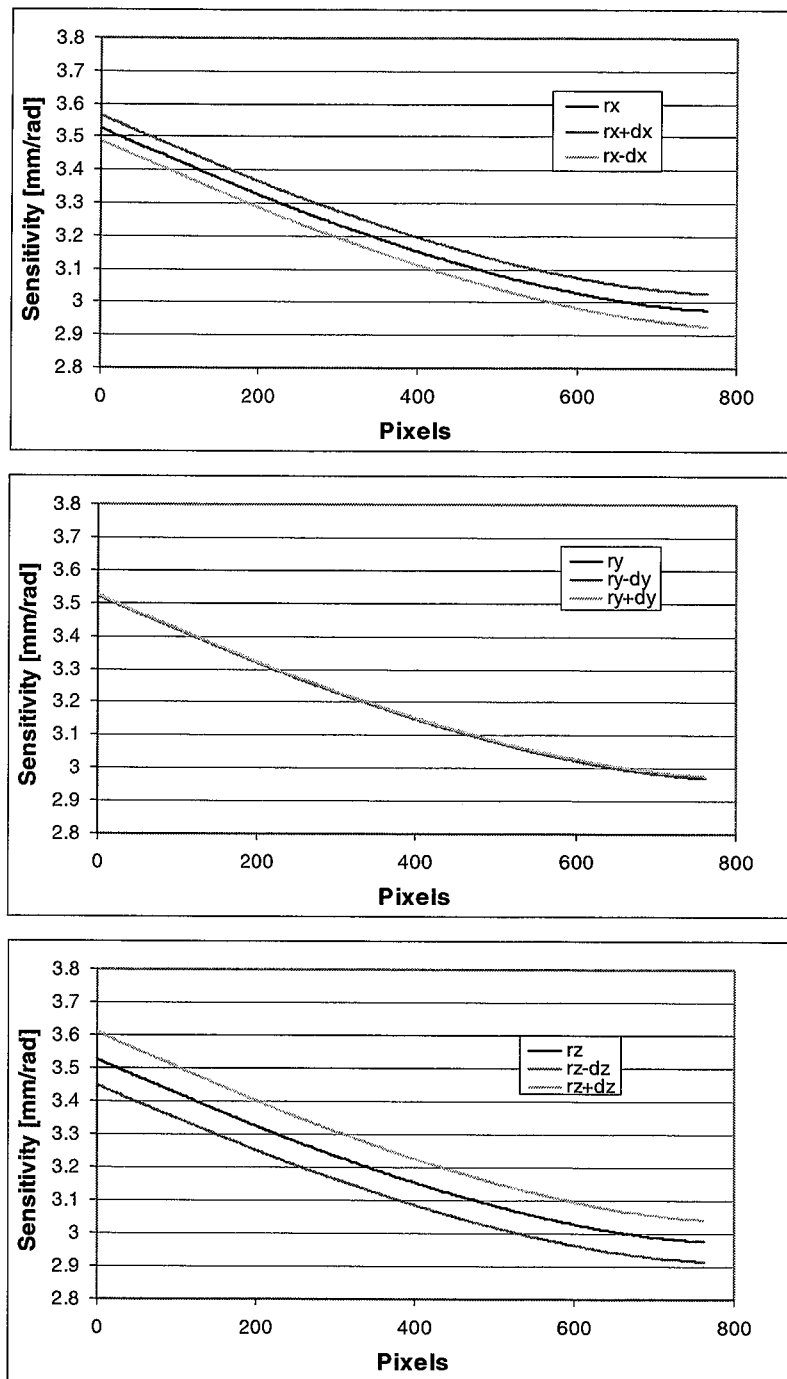
Figure 2. 15: Effect of a variation of r_x, r_y, r_z on the sensitivity along a horizontal line
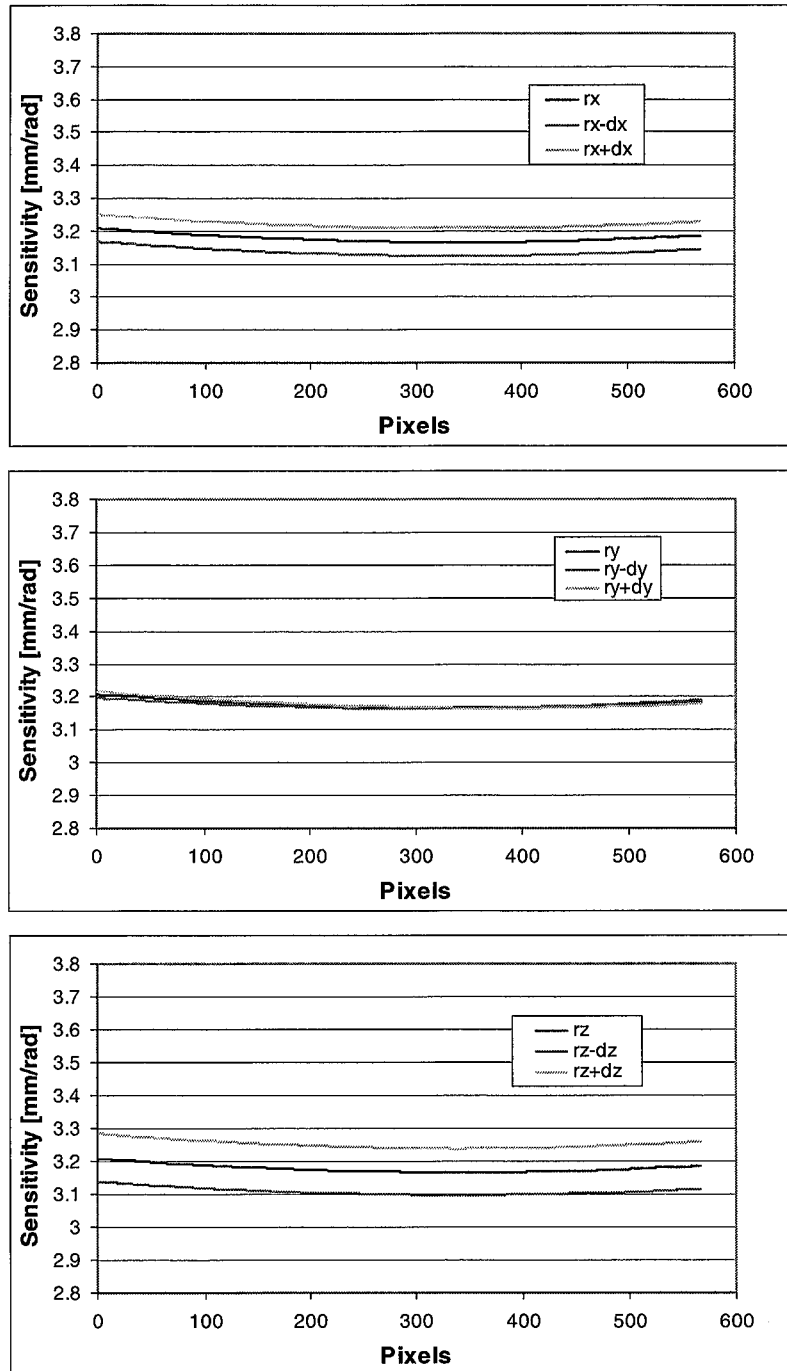
Figure 2. 16: Effect of a variation of r_x, r_y, r_z on the sensitivity along a vertical line

2. 6. 3.   Summary

The three calibration methods presented in this chapter, namely: LS1, DPH and LS2, give the components r_x, r_y, r_z of the vector separating the two point-sources. From these components, reference phase-maps and sensitivity maps can be computed and compared, in order to evaluate the calibration carried out by the different methods. This is what we will do in Chapter 3. Therefore, the aim here was to develop a simple model allowing us to understand the variations of the phase- and sensitivity-maps with the r_x, r_y, r_z determined by LS1, DPH and LS2. It could have been interesting to consider a more physical model studying the variations of the phase- and sensitivity-maps with the distance between the two point-sources and their orientation. Indeed, it would give more general trends, independently of the referential. However, since the referential chosen in this work is the same for all the measurements (see Chapter 3, Section 3.1), this model is sufficient to explain the trends observed in the next chapter. The more general model can be treated in the future.

In the vicinity of the values chosen for r_x, r_y, r_z in the model, the change in the slope of the phase along an horizontal and a vertical line was studied. The following observations are made:

- the slope of the phase taken along the horizontal line increases when r_x decreases or r_z increases, and vice versa. It is almost invariant when varying r_y. Consequently, this implies a rotation of the reference surface map around a vertical axis upon variation of r_x and r_z.

- the curvature of the phase taken along the horizontal line will decrease when r increases and vice versa.

- the slope of the phase taken along the vertical line increases with r_y, and vice versa. Consequently, this implies a rotation of the reference surface map around a horizontal axis upon a variation of r_y.

- the curvature of the phase along the vertical profile increases when r_x or r_z increases, and vice versa.

- the sensitivity is a positive almost constant quantity. Its value is slightly higher on the left side of the image then on the right side. It varies very little with a variation of r_x, r_y or r_z.

Since the method is complex, there are certainly other factors influencing the sensitivity or phase-map, however at this stage, we will only consider the conclusion of this model.

2. 7.   References

1. Lehmann M., Jacquot P., and Facchini. M., *Shape measurements on large surfaces by fringe projection.* Experimental Techniques, 1999. **23**(2), p. 31-35.

2. Pratt W. K., *Digital Image Processing,* 2nd Edition, 1991, J. Wiley - Interscience Publication, New York.

3. Steel W. H., *Interferometry,* 1983, Cambridge University Press,Cambridge.

CHAPTER 3

The particular case of planar objects: evaluation of the three methods

In the preceding chapter, we presented three different methods allowing to extract the height information (shape) from the phase-map of objects that are large and planar: two of these methods are partially based on least-square calculations (LS1 and LS2) and the last one is based on two coupled interferometers (DPH). In addition to the condition that the measured object is flat, these methods are based on the assumptions that the object should also be parallel to the imaging plane of the sensor. Furthermore, the calculation is simplified if the object-coordinate system is chosen so that the object roughly lies in the plane $z=0$ (see Section 2.3). In this chapter, we want to show the feasibility of the two newly conceived and developed methods (DPH and LS2), to do a first evaluation of their precision, to find their advantages and limitations, in order to compare them one to another and also to LS1, and to give recommendations for their optimization.

In this chapter, we will first present the measurements and evaluation procedures, before applying the three different data treatment methods to the measurements done on the objects. Then, we will analyse these first results, namely: the relation between the object-coordinates and image-coordinates, the values obtained for r_x, r_y and r_z determined using the three methods, and finally the height computed using all the measured or determined parameters, for a planar object parallel to the camera and also for a more general case.

3. 1.   Measurements and evaluation procedures

3. 1. 1.   Measurements

Two objects are used for this first evaluation of the methods allowing to calibrate the measurement system (LS1, DPH and LS2). One of them is the aluminium plate already presented

in Chapter 1 (see Figures 1.13 and 3.1). It is measured in two positions: once vertically and once rotated by 10 ° to the vertical axis, as shown in Figure 3.2. The inclined position is used to study the behavior of the three methods when the object is not parallel to the camera.
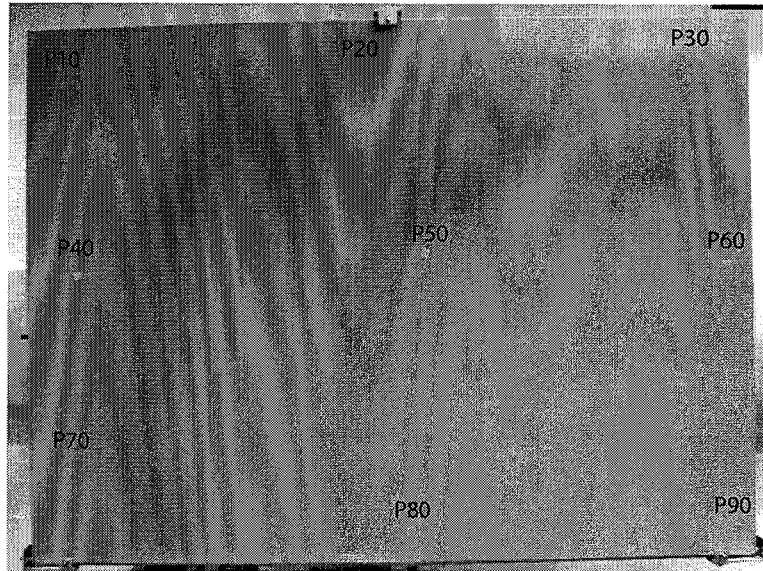
Figure 3. 1: Picture of the aluminium plate in vertical position. The calibration points are indicated.
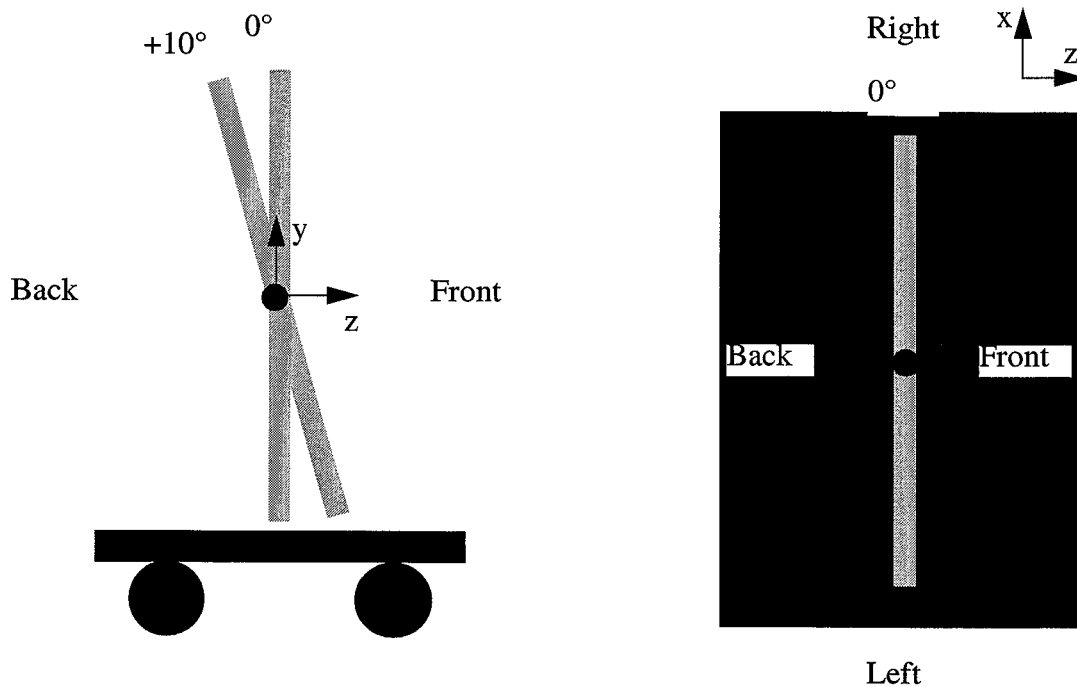
Figure 3. 2: Different measurement positions of the plate; side view (left); top view (right).

We also measure the wall of the lab (shown in Figure 3.3) on a portion representing a flat surface of about 2.5 x 1.75 m. It is interesting to include the wall in the experiment, in addition to the plate in vertical position, for two reasons. First, because it is larger than the plate, second, because when measuring the wall, it is more convenient to choose the measurement configuration in accordance to the initial assumptions described in Section 2.1 (object parallel to the imaging plane of the camera).
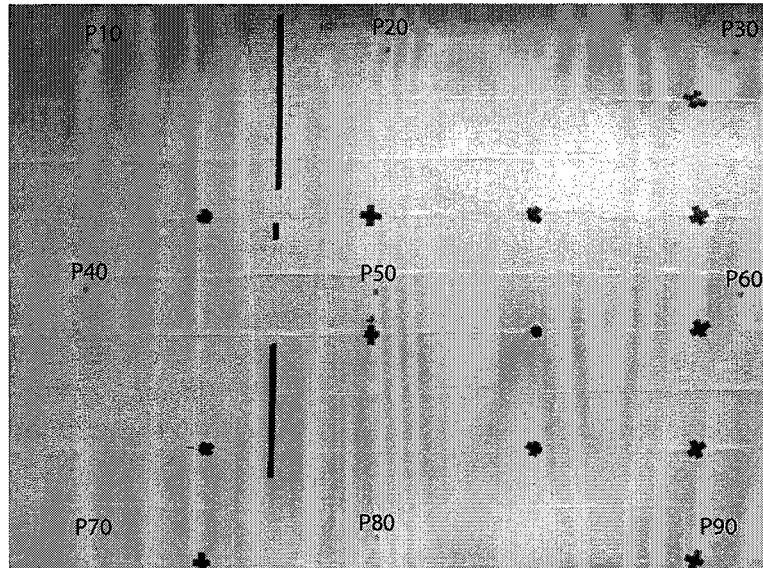
Figure 3. 3: Image of the wall where the calibration points are indicated. The black crosses and adhesive black tape stuck on the wall were placed there for another experiment and have nothing to do with this measurement

In each case, nine retro-reflective targets are fixed on the object surface, as shown in Figures 3.1 and 3.3. They represent reference points and are used either as calibration points, or as control points. In the following, they are generally called reference points, however when they serve for calibrating the system, they are called calibration points and when they serve for evaluating the system, they are called control points. The latter procedure is described in the next section.

For each object, the image- and object-coordinates of the calibration points, R_x, R_y, R_z are measured, and the phase-map is determined. All these values are used to calibrate the measurement system and then to compute the height map (shape) of the object under investigation.

More precisely, the measurements for each object are as follows. The object, projection head and camera, and theodolite are positioned. The measurement configuration is similar for all the experiments (see Figures 1.2 and 2.1): the camera is positioned at a distance of about 3 m from the object, and the projection head at about 6 m. The angle between the camera and projection axis direction is about 60°. For example, this configuration gives typical values of $R_x = 5367.41$ mm, $R_y = -250$ mm, $R_z = 3160.41$ mm in the case of the wall. For those measurements, the vertical axis of the object-coordinates system is given by the vertical axis of the theodolite (y-axis); the other axes (x- and z-axis) are determined using a reference point chosen in the lab (not on any object to be measured), setting the orientation of the theodolite once for all. The origin is fixed at point P50.

Then, the phase-map of the object under investigation is obtained using the phase-shifting and phase-unwrapping procedures described in Chapter 1; Section 1.2.

For the image measurement, the pictures are displayed on a computer screen. A simple cursor serves for the measurement of the image-coordinates by reading the pixel positions of the retro-reflective targets on the images of the measured object (wall or aluminium plate). In this way, the image-coordinates of the calibration points are obtained with a precision of ±1 pixel.

The parameters R_x, R_y, R_z and the object-coordinates of the calibration points are determined with the help of the distance-meter theodolite. Once aiming at a point, it is able to register the distance to this point as well as the angles. The object-coordinates of the measured points are computed from these data. The measurement is thereby simplified, since it doesn't require to work with two theodolites using the intersection method. As a first approximation of the precision, we consider the accuracy of the theodolite as specified by the manufacturer, which would be ±1 mm.

The values obtained for the object-coordinates of the reference points are presented in Tables 3.1 to 3.3, for the wall and the aluminium plate in vertical and inclined position respectively. The height (z) ranges from 0 mm to 2 mm for the wall, from -10 mm to 17 mm for the plate in vertical position, and from -86 mm to 128 mm for the inclined plate.

Additional measurements are required for the double-pinhole (DPH) and the second least squares (LS2) methods. The two impact points of the laser beams are determined using two retro-reflective targets and the theodolite for the DPH method (Chapter 2, Section 2.2). As for the LS2 method, the phase at each reference point is obtained from the measured unwrapped phase-map, by reading the phase value at the corresponding image-coordinates (pixels).

	$x_{theodolite}$ [mm]	$y_{theodolite}$ [mm]	$z_{theodolite}$ [mm]
P10	-962 ±1	839 ±1	2 ±1
P20	43 ±1	832 ±1	2 ±1
P30	1253 ±1	833±1	1 ±1
P40	-994 ±1	10 ±1	1 ±1
P50	0 ±1	0 ±1	0 ±1
P60	1258 ±1	-12 ±1	0 ±1
P70	-975 ±1	-889 ±1	1 ±1
P80	0 ±1	-848 ±1	0 ±1
P90	1184 ±1	-887 ±1	0 ±1

Table 3. 1: Wall. Object-coordinates of the reference points as measured with the theodolite

	$x_{theodolite}$ (mm)	$y_{theodolite}$ (mm)	$z_{theodolite}$ (mm)
P10	-999 ±1	474 ±1	11 ±1
P20	-98 ±1	576 ±1	-1 ±1
P30	842 ±1	605 ±1	-10 ±1
P40	-952 ±1	-62 ±1	13 ±1
P50	0 ±1	0 ±1	0 ±1
P60	832 ±1	-27 ±1	-7 ±1
P70	-983 ±1	-609 ±1	17 ±1
P80	-39 ±1	-765 ±1	6 ±1
P90	867 ±1	-762 ±1	-3 ±1

Table 3. 2: Plate in vertical position. Object-coordinates of the reference points as measured with the theodolite

	$x_{theodolite}$ (mm)	$y_{theodolite}$ (mm)	$z_{theodolite}$ (mm)
P10	-998 ±1	471 ±1	-83 ±1
P20	-122 ±1	547 ±1	-86 ±1
P30	843 ±1	596 ±1	-81±1
P40	-1029 ±1	7 ±1	-12 ±1
P50	0 ±1	0 ±1	0 ±1
P60	850 ±1	52 ±1	3 ±1
P70	-986 ±1	-599 ±1	83 ±1
P80	-82 ±1	-770 ±1	119 ±1
P90	863 ±1	-754 ±1	128 ±1

Table 3. 3: Inclined plate. Object-coordinates of the reference points as measured with the theodolite

Then the system is calibrated: the camera first, and then the projection head. More precisely, using four reference points as calibration points, generally (P10, P30, P70, P90), we determine the parameters defining the relation between the object- and image-coordinates given by Equations (2.10) in Chapter 2; Section 2.3. This allows us to determine the transformation formula for given values of x and y and the corresponding pixel (i, j). Next, the parameters r_x, r_y and r_z describing the

projection head are determined applying the three different methods (LS1, LS2, and DPH) described in Chapter 2; Sections 2.4.1 to 2.4.3. As for LS1, basically all measured points of the object are used as calibration points for the least squares calculation. As for DPH, the calibration is independent of the object, and for LS2, the nine reference points are used for the least squares calculation.

Finally, using r_x, r_y, r_z, R_x, R_y, R_z and the phase-map, the height z is calculated according to Equation (2.5).

3. 1. 2. Evaluation procedures

In order to evaluate the parameters r_x, r_y and r_z obtained by the three different methods (LS1, LS2, and DPH), we analyse the profiles of the phase-maps computed for the reference plane. More specifically, we use the values of r_x, r_y and r_z calculated using the three different methods (LS1, LS2, and DPH) to compute the phase-maps of the reference plane, according to Equation (2.3). Then we consider the profiles of these three phase-maps along a vertical line and a horizontal line crossing at the center of the image, as done in Chapter 2, Section 2.5. Finally, the profiles obtained for the three different methods are compared. Of course, the measurement conditions (object- and image-coordinates of the calibration points, R_x, R_y, R_z and the phase-map) and the measured objects used for this evaluation are the same for the three methods.

The object-coordinates x, y and z obtained by the three methods (LS1, LS2, and DPH) are evaluated at the calibration points. For that purpose, we consider the deviations between the coordinates measured with the theodolite ("reference") and the coordinates computed using the three calibration methods (LS1, LS2 and DPH). These deviations are represented in Figure 3.4 and are defined as follows:

- the "x-deviation": $d_x = x_{method} - x_{theodolite}$
- the "y-deviation": $d_y = y_{method} - y_{theodolite}$
- the "altimetric-deviation" (also called "z-" or "height-deviation"): $d_z = z_{method} - z_{theodolite}$

where d_x is the deviation between the x-coordinate as calculated using LS1, LS2 or DPH (x_{method}) and the x-coordinate as measured with the theodolite ($x_{theodolite}$). The deviations d_y and d_z are calculated in a similar way.

Two additional deviations are also considered:

- the "planimetric-" or "in-plane deviation": $\vec{d_{xy}} = d_x \cdot \vec{i} + d_y \cdot \vec{j}$, with

$$d_{xy} = \sqrt{(x_{method} - x_{theodolite})^2 + (y_{method} - y_{theodolite})^2} = \sqrt{d_x^2 + d_y^2}$$

- the "total deviation": $\vec{d} = d_x \cdot \vec{i} + d_y \cdot \vec{j} + d_z \cdot \vec{k}$, with

$$d = \sqrt{(x_{method} - x_{theodolite})^2 + (y_{method} - y_{theodolite})^2 + (z_{method} - z_{theodolite})^2} = \sqrt{d_x^2 + d_y^2 + d_z^2} = \sqrt{d_{xy}^2 + d_z^2}$$
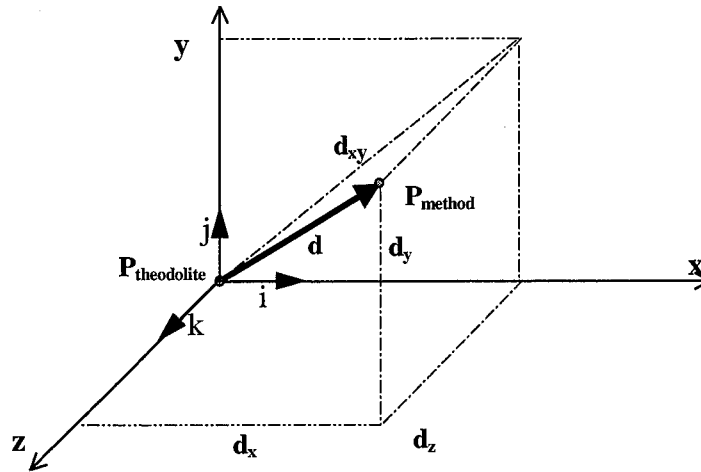
Figure 3. 4: Diagram showing the different deviations used for evaluating the computed object-coordinates

As said earlier the reference points serve either as calibration points or as control points. When they are used as calibration points, attention should be paid before also using them as control points. This is particularly true in the calibration of the camera in LS1, DPH and LS2. Indeed, since the set of Equations (2.17) contains four unknowns, at least four points are necessary for calibrating the camera. In our case, we only used four calibration points, which means that the number of calibration points and the number of unknowns are the same. Therefore there is no over-determination, and the four reference points used as calibration points cannot be used for evaluating the method. Other reference points must be used as control points.

As for the calibration of the projection head by LS1, DPH and LS2, the procedures are different. In LS1, basically all the points of the object, and in particular the reference points, are used as calibration points to carry out the first least squares calculation. Therefore the number of calibration points (about 0.5 millions pixels) is larger then the number of unknowns (four) as shown by Equation (2.6), and there is an over-determination. Hence, all the reference points can also be used as control points in the procedure for evaluating the method. Similarly, in LS2 we used all the nine reference points as calibration points to carry out the second least squares calculation. In that case again, the number of calibration points (nine) is larger than the number of unknowns (four), and there is over-determination. Hence the nine reference points can also be used as control points. In DPH, no reference points are used as calibration points and therefore, all of them can also be used as control points.

3. 2.   Planar object parallel to the imaging-plane of the camera

In agreement with the basic assumptions required for applying the three methods described in the Chapter 2; Section 2.1, the objects measured must be plane and parallel to the imaging plane of the camera. The first object chosen here is the wall, although it is not perfectly smooth. Indeed, it is the object that best allows to adjust the measurement configuration compared to the basic conditions required for applying LS1, DPH and LS2. Hence, among all the objects we measured, it best shows the feasibility of applying DPH and LS2 to determine the shape of a planar object. Then the measurement and evaluation procedures are performed as described in Sections 3.1.1 and 3.1.2. Of course, the same object's phase map was used to test the three different methods. The results are presented below.

3. 2. 1.   Evaluation of the relation between object- and image-coordinates
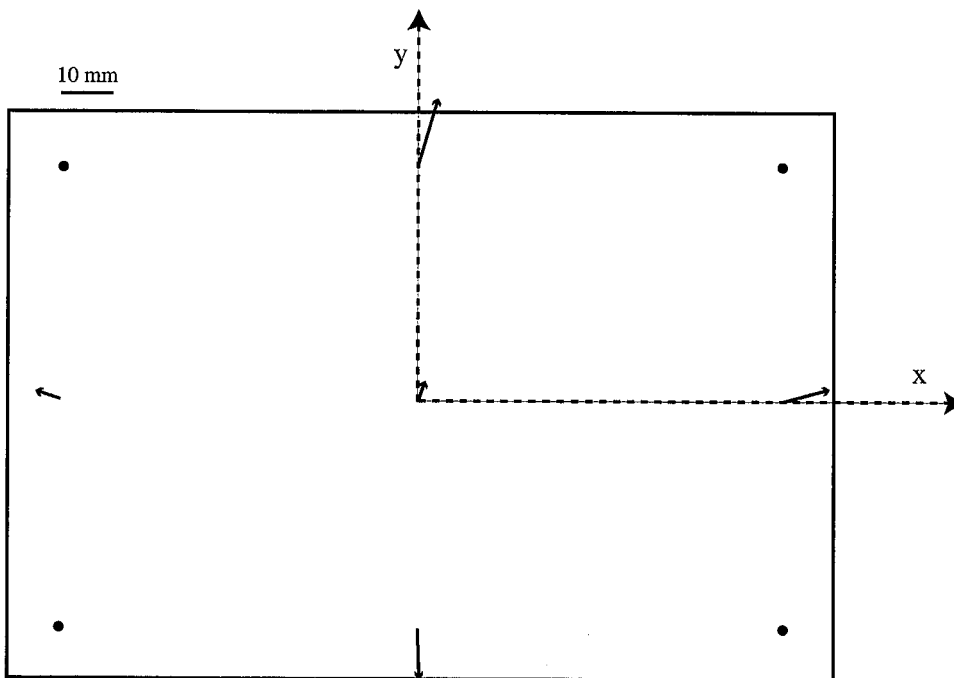
Figure 3. 5: Diagram showing the planimetric deviations (vectors) for each points of the wall

Here, the transformation between the object- and image-coordinates described in Section 2.3 allows to compute the planimetric object-coordinates x and y corresponding to each pixel position. This transformation is evaluated using the x- and y-planimetric deviation. Figure 3.5 represents the planimetric deviation $\overrightarrow{d_{xy}}$ of the control points on the wall. Typical values obtained range from 3.1 mm to 14.89 mm (mean: 8.30 mm; standard deviation: ±4.8 mm). Although there are not many measured points, we see that the values of d_{xy} are larger for the control points on the border of the

images (P20, P40, P60, P80) than for the one in its center (P50). Furthermore, we observe that the vectors $\overrightarrow{d_{xy}}$ point outward.

There are several causes for explaining these planimetric deviations d_{xy}. The most obvious is the reading error when determining the image-coordinates of the calibration points; it is approximated to ± 1 pixel. Another explanation is the limited spatial resolution of the camera (3.5 mm/pixel). A third one is the distortion coming from the imaging lens. This latter also explains why the planimetric deviations d_{xy} are larger on the border and why the vectors are directed to the periphery. Indeed a barrel aberration can be seen on the image of the aluminium plate in Figure 3.1. It is particularly visible on the plate periphery, where the upper and lower edges of the plate are slightly curved on the picture, but straight in reality. A simple calculus shows that this aberration generates a 30 mm "elongation" in the plate height and 15 mm in its width (median line).

3. 2. 2. Evaluation of the parameters r_x, r_y and r_z determined using the three methods

The components r_x, r_y, r_z found for the wall measurement using LS1, LS2 and DPH (see Chapter 2, Section 2.4) are presented in Table 3.4.

	r_x [mm]	r_y [mm]	r_z [mm]
First least-squares method (LS1)	-0.066	0.002	0.184
Double-pinhole method (DPH)	-0.063	0.000	0.191
Second least-squares method (LS2)	-0.063	0.002	0.187

Table 3. 4: Values of r_x, r_y, r_z, and r for the different methods applied to measure the wall.

These values of r_x, r_y, and r_z are used to artificially generate the reference phase map as well as the sensitivity map, according to Equations (2.3) and (2.5). Typical examples (here for LS1) of both maps are shown in Figure 3.6. These images are coded in grey levels and the darkest shade denotes the smallest value of the phase or the sensitivity.

The phase-maps of the reference plane were calculated using the three methods. Their profiles along horizontal and vertical lines are represented in Figures 3.7 and 3.8, where the measured phase-map of the wall is set as reference.

The differences between them, more clearly observable in the vertical profile shown in Figure 3.8, are explainable with the simulation made in Chapter 2; Section 2.5. In this figure, the curves vary between -10 rad to 5 rad and fit the profiles of the wall within a few radians. Looking at Table 3.4, we observe that: $r_x^{DPH} \approx r_x^{LS2} > r_x^{LS1}$ and $r_z^{LS1} < r_z^{LS2} < r_z^{DPH}$. Referring to the simulation, it is difficult to see a clear trend among the three cases at the same time, since the slope of the horizontal profile depends on two factors, r_x and r_z that have an opposite influence on the slope. However, it is possible to compare the results of DPH and LS2.

a)   b)
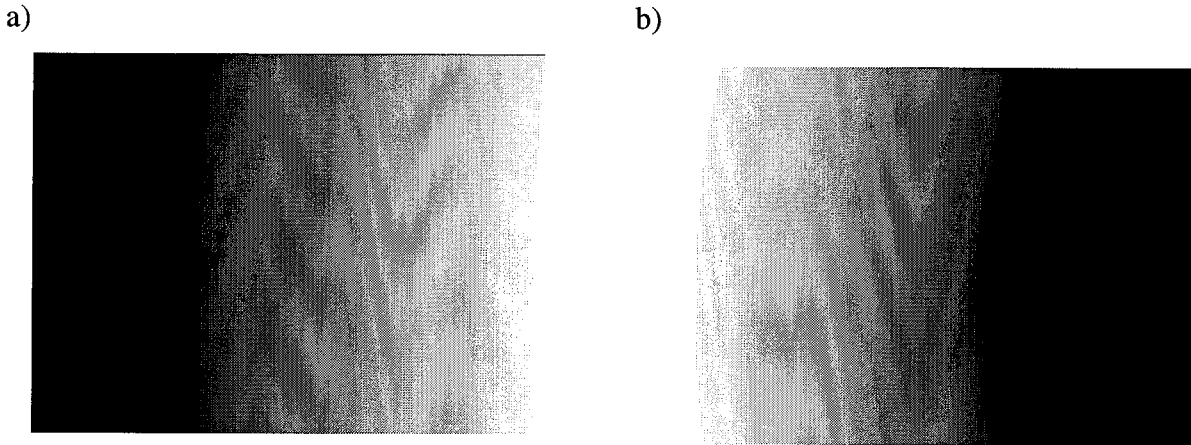
Figure 3. 6: Typical examples of a) a reference phase map and b) a sensitivity map.
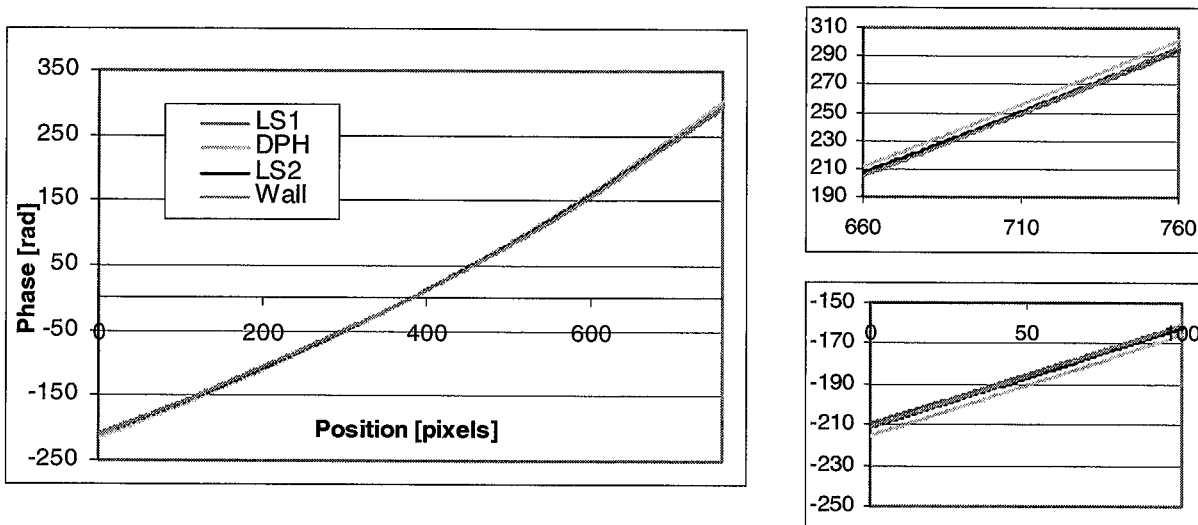
Figure 3. 7: Wall. Profile of the phase maps obtained by the different methods along a horizontal line.

According to the simulation, since $r_x^{DPH} \approx r_x^{LS2}$ and $r_z^{LS2} < r_z^{DPH}$, slope(DPH) > slope(LS2), which is exactly what we see in the horizontal profiles shown in Figure 3.7. As for LS1, the influences of r_x and r_z are opposite, and therefore it is difficult to compare it to the two other curves. It is easier to test the simulation on the vertical line profile represented in Figure 3.8. According to it, the effects of a variation in r_y has a stronger influence on the tilt of the vertical profile than a variation of r_x or r_z. Referring to the model if $r_y^{DPH} < r_y^{LS2} < r_y^{LS1}$, then $slope(DPH) < slope(LS2) < slope(LS1)$, which is exactly what is observed in Figure 3.8.

In conclusion, what can be seen from these profiles is that the best reference phase map is the one obtained by the LS1 method, since it is the closest curve to the measured phase map of the wall.

All the differences in the orientation and curvature of the reference phase-maps are due to the differences in the values of r_x, r_y, r_z found using the three methods. They are explained in terms of the simulation done in Chapter 2, Section 2.5.
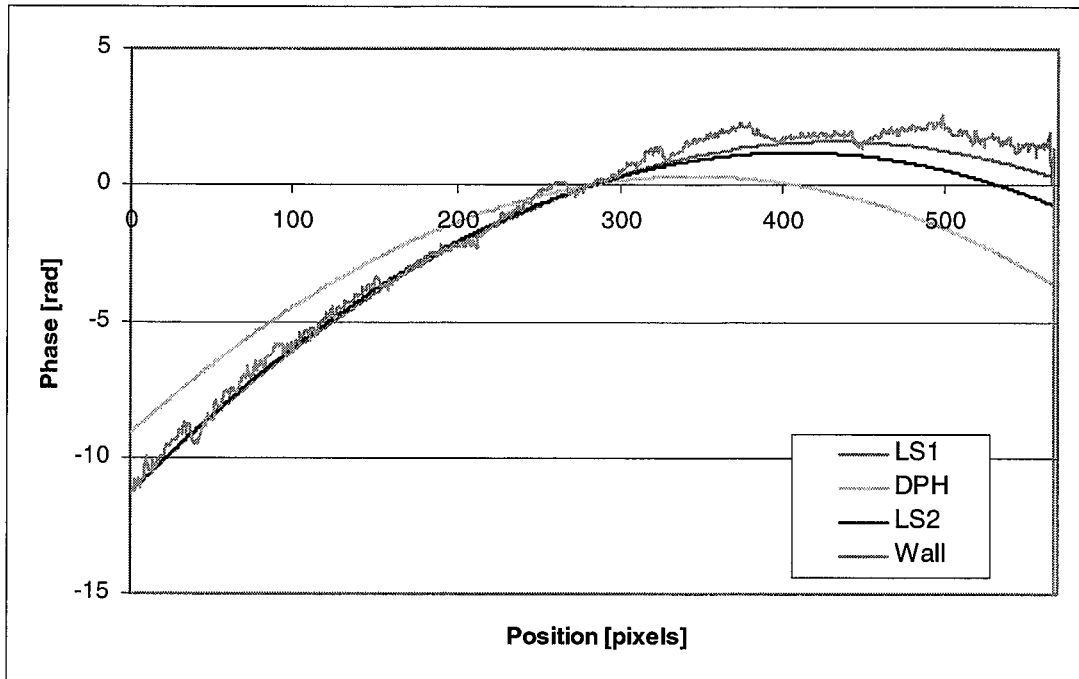
Figure 3. 8: Wall. Profile of the phase maps obtained by the different methods along a vertical line

3. 2. 3. Evaluation of the computed height

Using the relation between the image- and object-coordinates given by the set of Equations 2.17, the components r_x, r_y, r_z determined by LS1, DPH and LS2, and the parameters R_x, R_y, R_z, we compute the height z of each reference point used here as control points, according to Equation (2.5). Then, the z-deviations d_z of the control points are calculated according to the definitions given in Section 3.1.2. The results for LS1, DPH and LS2 are presented in Figure 3.9, 3.10 and 3.11 respectively.

The z-deviations d_z ranges from 0.06 mm to 10.54 mm for LS1 (mean: 3.12 mm, standard deviation: 3.18 mm), from 0.89 mm to 23.54 mm for DPH (mean: 11.65 mm; standard deviation: 7.9 mm), and from 1.3 mm to 6.22 for LS2 (mean: 2.87 mm; standard deviation: 1.50 mm). The values obtained for LS1 and LS2 are similar, however, they are significantly higher for DPH. No systematics is visible in the pattern of the arrows, except in the case of DPH, where they are orientated up on the right (positive d_z), and down on the left (negative d_z). Interestingly, we observe that in the case of LS1 (except for point 30) and LS2, the value founds for the height z fall within the 1/1000 of the depth-of-field resolution defined as a rule of thumb known in the field. It is also in accordance with the precision announced by Lehmann [1].

According to Equation (2.5), the z-deviation d_z has several origins. The first and most obvious one is the measured phase map. Indeed, local errors in the measured phase map (due for example to a bad modulation of the fringes) generate errors in the height. Another possible source of error is the reference phase map computed using the parameters r_x, r_y, r_z. More particularly, an error in the determination of r_x, r_y, r_z generates a global error in the computed reference phase map (Equation (2.3)), by causing a change in the orientation and curvature of the reference phase map as seen in the modelisation in Section 2.5, Chapter 2. This is shown in Figures 3.7 and 3.8. This variation in the orientation and curvature of the reference phase map causes a change in its position relative to the measured phase maps, and consequently a change in d_z. A third source of errors when determining z is the sensitivity map. However, this sensitivity map is generally a continuous surface whose z value varies very little from one point of the surface to another, as seen in Chapter 2. Therefore, we think that it is a less probable source of error. A last source of error in the height z evaluation is the planimetric deviation d_{xy}. As seen in the previous section, this is caused by several factors: the relatively low camera resolution, reading errors arising when calibrating the camera (a bad pixel (i,j) may be attributed to given object-coordinates (x,y)), camera lens distortions, or image deformations during the imaging process. All of these cause an error in the determination of the planimetric coordinates (x,y), and consequently an error when calculating the height z, because the phase value contained in the pixel is assigned to a wrong point of the object. In the case of LS1, the calibration point P30, has a higher height deviation than the other points, because of a "bad modulation problem". Indeed, this is confirmed by the modulation map where the upper-right side of the image is darker than the rest. This implies a poor quality of the wrapped phase at this place due to a low contrast of the fringes. Therefore, errors may arise in the unwrapped phase map at those points, causing errors in the height calculation at P30.
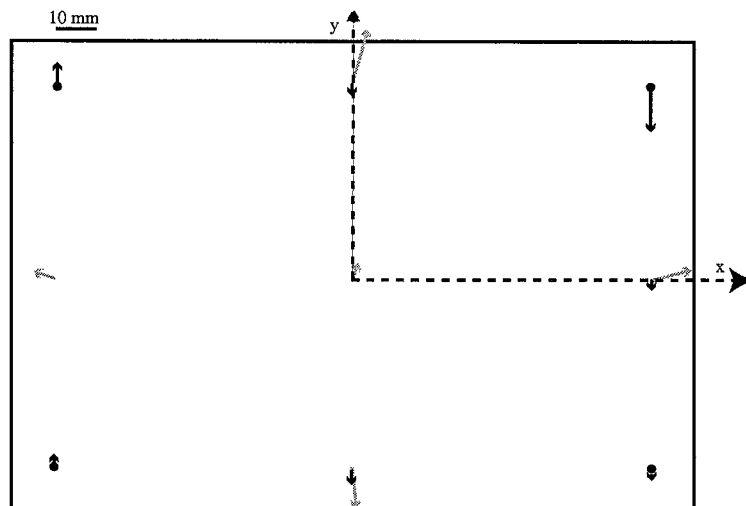
Figure 3. 9: Diagram of the z-deviations (black arrows) for the wall found using the LS1 method. When the z-deviation is positive, the arrows points up, and vice-versa. When the value of the z-deviation is smaller than 2 mm, it is not represented. The planimetric deviations (grey arrows) are represented as an additional information.
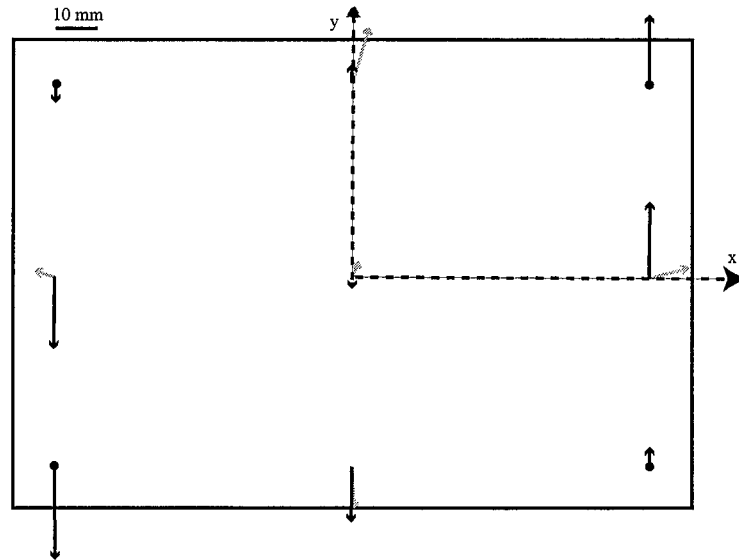
Figure 3. 10: Diagram of the z-deviations (black arrows) for the wall found using the DPH method. When the z-deviation is positive, the arrows points up, and vice-versa. When the value of the z-deviation is smaller than 2 mm, it is not represented. The planimetric deviations (grey arrows) are represented as an additional information.
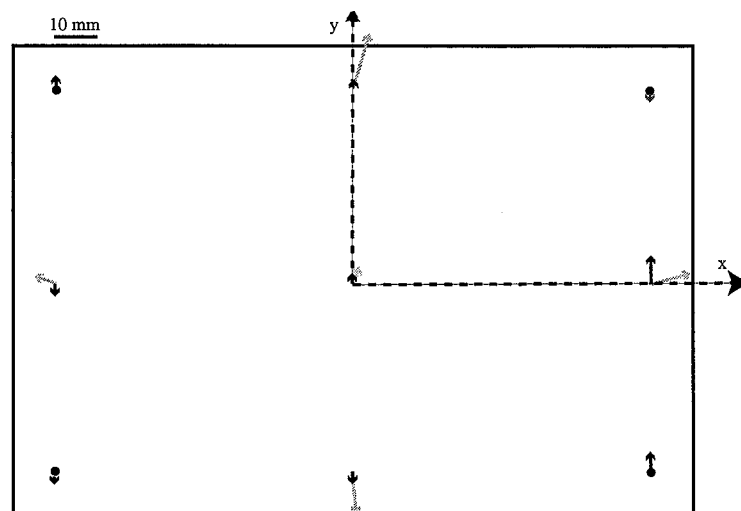
Figure 3. 11: Diagram of the z-deviations (black arrows) for the wall found using the LS2 method. When the z-deviation is positive, the arrows points up, and vice-versa. When the value of the z-deviation is smaller than 2 mm, it is not represented. The planimetric deviations (grey arrows) are represented as an additional information.
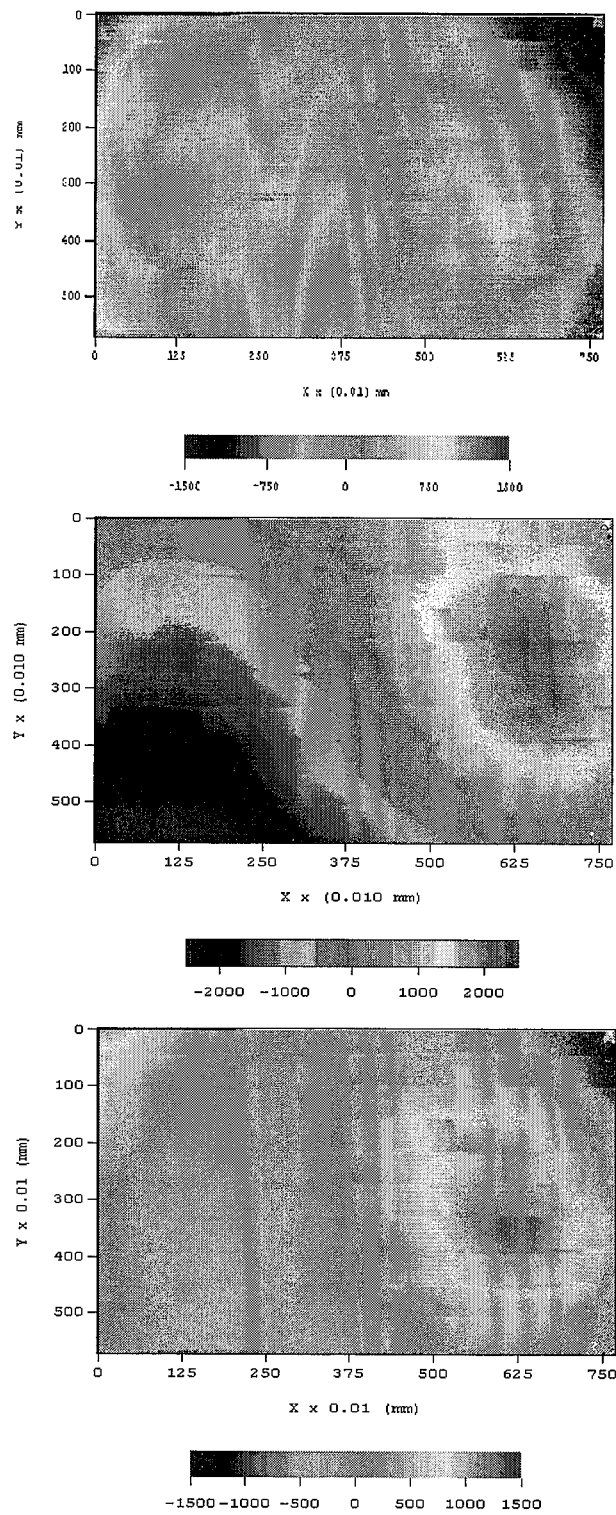
Figure 3. 12: Height map of the wall calculated by the LS1 (top), the DPH (middle) and the LS2 (bottom) methods; the greyscale gives the z-units (100 grey levels = 1 mm)

The differences between the z-deviations found by the three methods for the nine control points can be explained by the following. Among the four main factors influencing the height determination, the only one that varies from one method to another is the reference phase map. Indeed, as mentioned at the beginning of this section, the image-/object-coordinates transformation and the measured phase map are the same for all the methods. Furthermore, according to the modelisation (Section 2.5, Chapter 2), the sensitivity has little influence on the results since it varies very little over the whole map. Therefore, these three factors can be neglected here, and the differences between the height maps, or equivalently the height deviations, determined by the three different methods (LS1, LS2 and DPH) can be attributed to the differences between the reference phase maps (orientation and curvature) computed by these three different methods (see Figures 3.7 to 3.8).

Finally, an estimation of the overall error is given by the total deviation d, that has 2 components: the z-deviation d_z and the planimetric deviation d_{xy}. It ranges from 1.43 mm to 15 mm for LS1, from 3.22 mm to 23.54 mm for DPH, and from 1.82 mm to 14.95 mm for LS2. We see that the total deviations are quite large for DPH, but decrease by half when using LS1 and LS2.

For the four reference points: P10, P30, P70 and P90, used for calibrating the relation between the image- and object-coordinates, obviously $d=d_z$ and they are not used as control points. In order to give us a hint about the origins of the error and to understand what is happening with the other 500 000 points measured, we use the other reference points P20, P40, P50, P60 and P80. For these points, in the case of LS1 and LS2, generally $|d_z| \approx |d_{xy}|$, indicating that the main contribution to the error comes from the image-/object-coordinates transformation, more than from the depth determination. In the case of DPH, $d_z > d_{xy}$ in general, the errors in the height evaluation affect the determination of the distance d more than the spatial errors. This implies that the determination of r_x, r_y, r_z is not very good in this case, probably because of microscope-objective aberrations and centering problems. This is an area for further investigation.

The resulting image of the height map is displayed in Figure 3.12. The measurement is sufficiently precise for us to see the joints between the concrete blocks of the wall. Interestingly, according to this the wall is "deeper" on the right than on the left, and dark zones are observed on the far right side. The explanation for this is related to the bad modulation of the fringes at the upper right points (P90).

3. 3. First evaluation of the precision given by the three methods for flat-objects

The measurement tests done on the wall in the previous section show the feasibility of applying DPH and LS2 to determine the object-coordinates of points of the measured object. The aim here is not to fully characterize the system, since it must be further developed and optimized, but to do a first evaluation of the method's precision. For this purpose, we used the honey-comb aluminum-aluminium plate which was measured 20 times in the vertical position, in the configuration already described in Section 3.1. Each time, the measurement system (namely: the camera and projection head) was removed and placed back again; the phase-map was acquired,

and the object- and image-coordinates of the calibration points were measured. Then, the coordinates of each calibration points were computed using the three different methods (LS1, DPH and LS2), and the deviations (planimetric height- and total deviations) were evaluated. Finally, the means and the standard deviations were calculated for each method.

The planimetric and altimetric deviations (d_{xy} and d_z, resp.) were calculated for the three methods and the results are represented in Figure 3.13 and 3.14 respectively. The planimetric deviations are $0mm < |d_{xy}| < 12.19mm$ (mean: 8.33 mm, standard deviation: 3.61 mm). The z-deviation d_z is $0.62mm < |d_z| < 12.15mm$, $1.05mm < |\sigma_z| < 2.73mm$ (mean: 6.42 mm, standard deviation: 4.53 mm) for the first least squares method (LS1), $3.72mm < |d_z| < 15.98mm$, $1.05mm < |\sigma_z| < 3.34mm$ (mean: 9.25 mm, standard deviation: 4.26 mm) for the Double pinhole method (DPH), and $0.47mm < |d_z| < 4.42mm$, $0.72mm < |\sigma_z| < 2.58mm$ (mean: 1.40 mm, standard deviation: 1.25 mm) for the second least squares method (LS2).
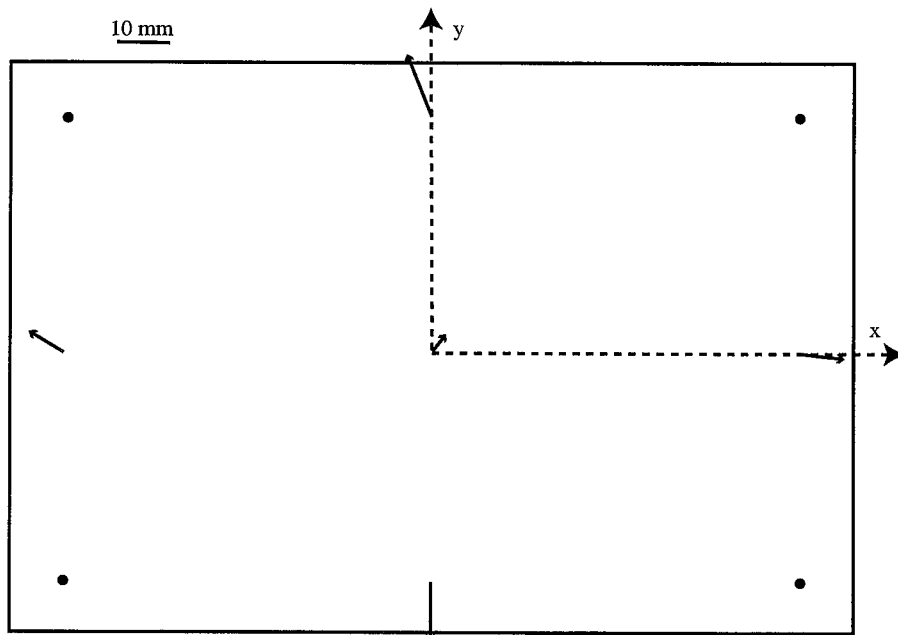
Figure 3. 13: Diagram showing the planimetric deviations for each points of the aluminium plate in vertical position

The total deviation is $0.80mm < |d| < 13.65mm$ (mean: 9.2 mm, standard deviation: 4.66 mm) for the first least squares method (LS1), $3.72mm < |d| < 15.33mm$ (mean: 10.31 mm, standard deviation: 4.17 mm) for the double-pinhole method (DPH), and $0.47mm < |d| < 12.34mm$ (mean: 5.12 mm, standard deviation: 4.63 mm) for the second least-squares method (LS2).

The mean values obtained here are similar to what was found for the wall measurement (Section 3.2), confirming these results. The total deviations (absolute value) found are generally rather large, since the means range from 5.12 mm (LS2) to 10.31 mm (DPH) with maximum values ranging from 12.34 (LS2) to 15.33 mm (DPH). In the case of LS1 and LS2, d_{xy} is generally smaller than d_z, which implies that errors on the determination of planimetric object coordinates have a greater contribution to the total deviation than errors on the determination of altimetric

object-coordinates. At the opposite, in the case of DPH, errors on the determination of altimetric object-coordinates have a greater contribution to the total deviation than errors on the determination of planimetric object coordinates, since d_{xy} is generally smaller than d_z. These deviations clearly come from systematic errors already discussed in the previous section, and the latter should be reduced by further optimization of the system.

Here again, the results obtained by the LS1 and LS2 methods are similar to each other and better than those found by the DPH method. For this latter, systematic errors seem to be more problematic.
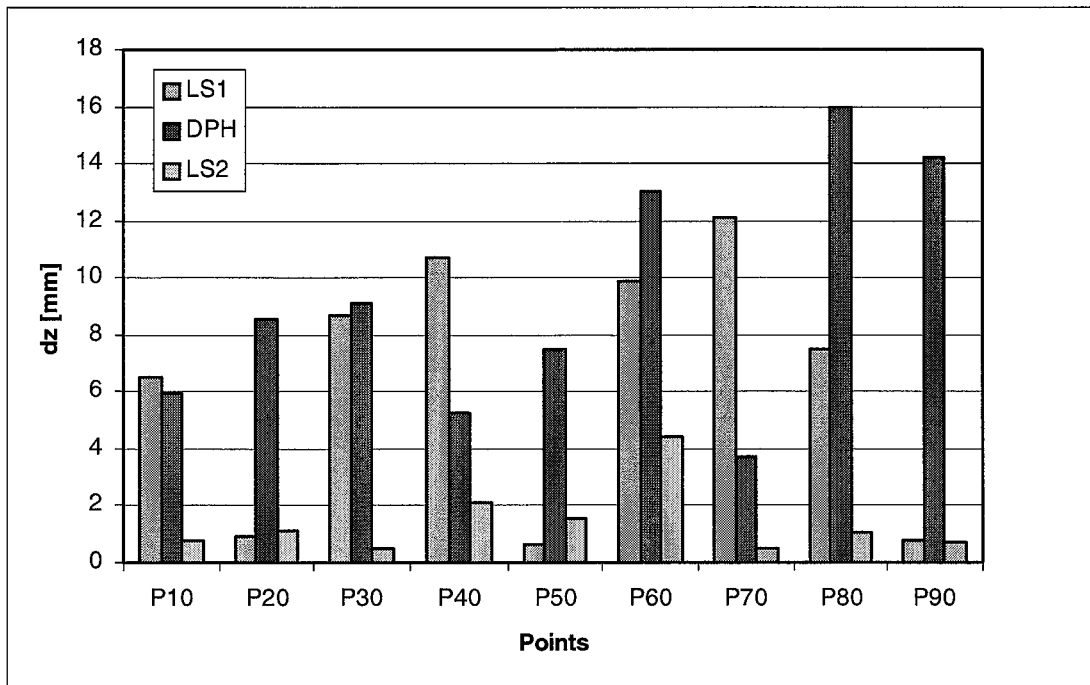
Figure 3. 14: Absolute value of the height deviation d_z for the three different method.

3. 4.   Planar object not parallel to the imaging plane of the camera

In Chapter 2, Section 2.3, we saw that two conditions were required to model the CCD camera with the image-/object-coordinates relation (Equation (2.17)). More precisely, the object must be planar and parallel to the imaging plane of the camera. In addition, to simplify the calculation, the object was chosen to lie the plane (x, y, $z = 0$). All this implies that the points of the object belong more or less to the plane (x, y, $z = 0$) that is parallel to the imaging plane of the camera. In the preceding section, we showed examples where these basic conditions were verified. In order to see what happens when the position of the object departs slightly from the position required by the basic assumption for applying LS1, LS2 and DPH, we consider the aluminium plate slightly rotated by 10° about its horizontal axis. The object was measured in a configuration similar to that of the previous measurements, and in particular, the origin of the object-coordinate

referential is set as P50, and the (x,y)-plane is taken parallel to the imaging plane of the camera. Then, the object coordinates were computed and evaluated according to the procedures described in Section 3.1. As in the previous cases, the same object's phase map is used for testing the three different methods.

3. 4. 1. Evaluation of the relation between object- and image-coordinates

The resulting planimetric deviations $\overrightarrow{d_{xy}}$ are represented in Figure 3.15. Their absolute values ranged between $0 < |d_{xy}| < 30.87$ (in more details, $0 < |d_x| < 14.5$ and $0 < |d_y| < 28.4$), and are obviously higher than in the case of objects parallel to the imaging plane of the camera (e.g. wall or plate in the vertical position).These results show that the transformation between the image- and object-coordinates given by Equation (2.17) does not work well when the measured object and the camera are not parallel.
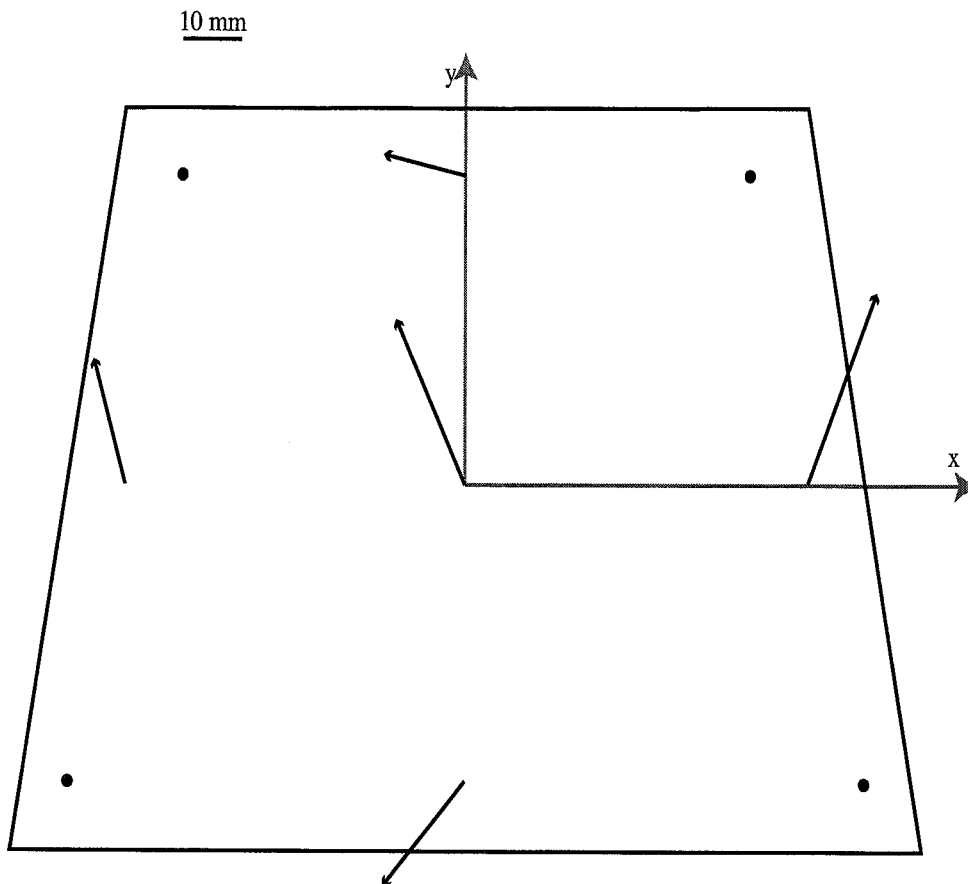
Figure 3. 15: Diagram of the planimetric deviations for each points of the aluminium plate inclined by 10° to the vertical axis

In order to check if these results were linked to the object-coordinate referential, we computed the planimetric deviations $\overrightarrow{d_{xy}}$ for another object-coordinate referential. The latter was chosen such that the $(x, y, z = 0)$-plane corresponds to the plate. Similar values of d_{xy} were found, which confirms that the "behavior" of the polynomials (2.17) do not depend on the referential chosen. Obviously, the first order terms in Eq. (2.17) are not sufficient to correct the deformation of the object on the image (trapezoidal on the image, but rectangular in reality) induced by the "non-parallelism" of the object and camera imaging-plane. Indeed, in order to decrease the planimetric deviations, higher order terms should be considered. However, in that case, more calibration points would be required to calibrate the imaging system, and consequently, the camera's calibration procedure would be longer and more complicated.

3. 4. 2. Evaluation of rx, ry and rz determined using the three methods

Similar to what was done for the wall in Section 3.2, we computed the value of the parameters r_x, r_y, r_z using the three different calibration procedures described in Chapter 2, Section 2.2 (LS1, DPH and LS2), and evaluated them (see Section 3.1.2). The results are presented in Table 3.5 and the profiles of the corresponding phase-maps (along horizontal and vertical lines) are shown in Figure 3.16.

	r_x [mm]	r_y [mm]	r_z [mm]
Least square method 1 (LS1)	-0.06971	-0.02591	0.17217
"Double pinhole" method	-0.06339	0.00013	0.191613
Least square method 2 (LS2)	-0.06028	0.002181	0.187876

Table 3. 5: Inclined aluminium plate. Coordinates of the vector giving the spacing between the two point-sources obtained by the different methods

Looking at Figures 3.16 a) and b), we observe that the profiles of the phase-maps computed with LS1 stick to the phase-map of the plate, which is not the case for the profiles of DPH and LS2. This is seen more clearly in Figure 3.16 b), where the vertical profiles of the phase obtained by DPH and LS2 vary in an interval (-10 rad to 5 rad) similar to what was obtained in the previous section for the wall (object observing the assumptions required to apply the three methods). As for the vertical profile of the phase obtained by LS1, it varies between 45 rad and 40 rad following the profile of the inclined plate. This difference in the behavior of the phase map's slope obtained by LS1 on the one hand, and LS2 and DPH on the other hand, show that LS1 is more influenced by the object position than DPH and LS2.

The most probable explanation for this is that the calculation procedures of DPH and LS2 are not based on the condition that the object lies in the plane $z = 0$ and do not depend on the transformation between image- and object-coordinate, conversely to LS1. Indeed, because the conditions required for applying LS1 are obviously not respected, two problems arise. First, as seen in the previous section, the relation between (x,y) and (i, j) doesn't work well since there is an angle between the object and the plane parallel to the imaging plane of the camera.

a)
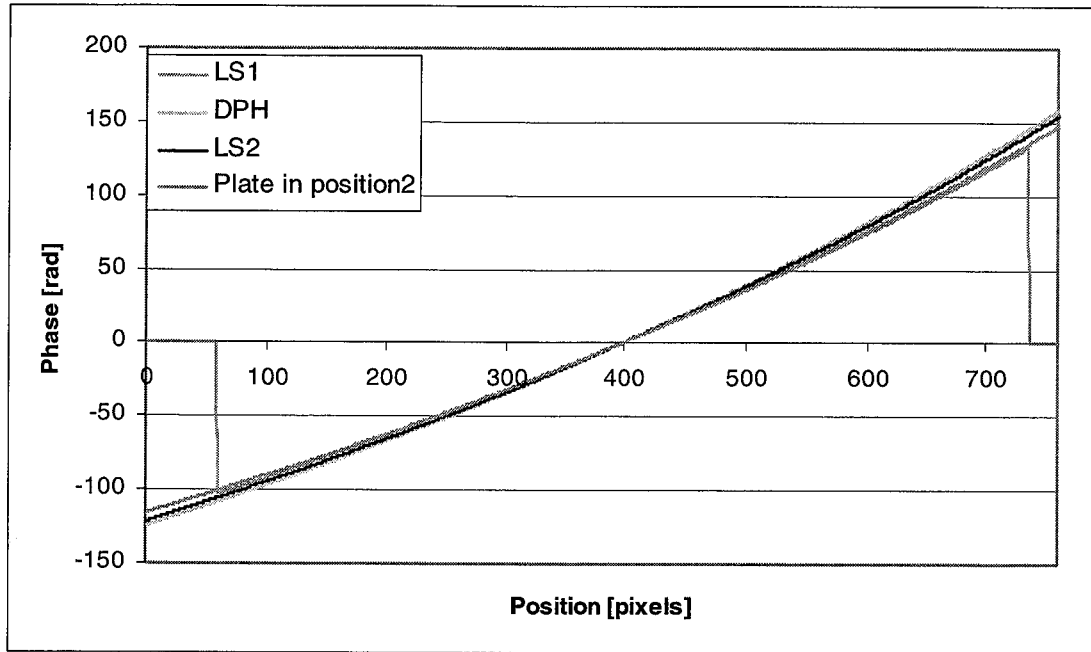
b)
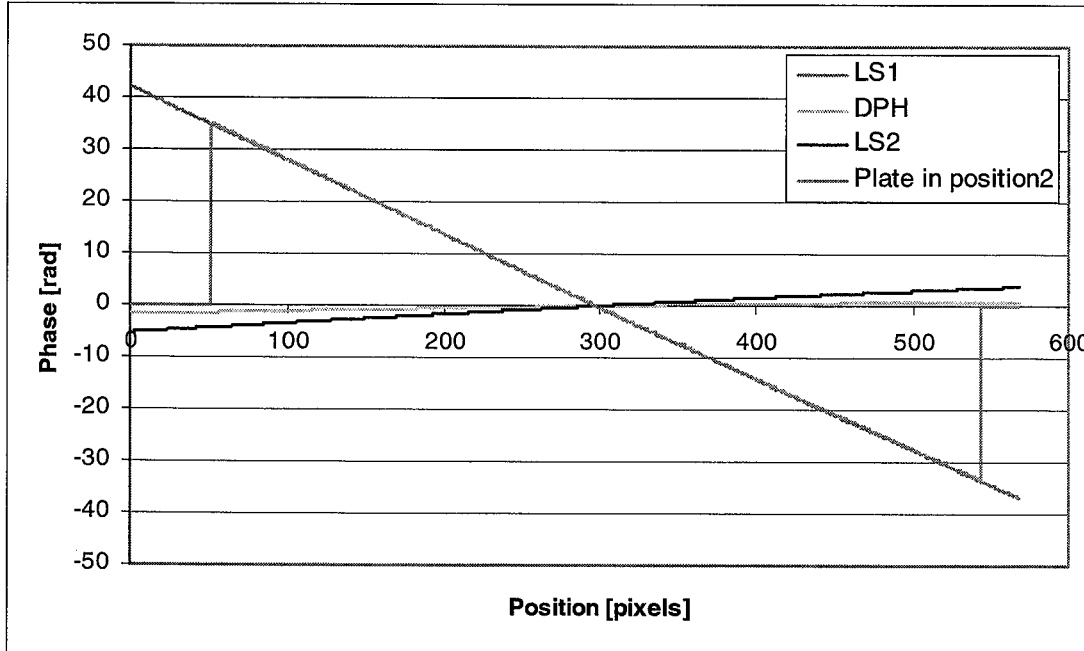
Figure 3. 16: Inclined aluminium plate. Comparison of the measured phase map and the reference phase map profiles obtained by the different methods (a) along a horizontal line and (b) along a vertical line.

Therefore, because the calibration procedure LS1 requires the use of this relation, conversely to DPH and LS2, an error is introduced in the determination of the parameters r_x, r_y, r_z. Second, to perform the LS1 procedure, we assumed that the object lies more or less in the plane $(x, y, z = 0)$. However, the height of the calibration points at the plate periphery range between 8 and 12 cm, which is obviously too large to be considered as points lying roughly in the (x,y, z=0)-plane (and parallel to the imaging plane of the camera). Therefore, the points that are too far from the plane $z = 0$ introduce an error in the values calculated for r_x, r_y and r_z when using LS1.

In conclusion, the DPH or LS2 methods allow to determine the parameters r_x, r_y, r_z independently of the object position and referential chosen, and thus to avoid this type of bias, giving better results. The height computed using these parameters are presented in the next section, and confirm the trends observed here.

3. 4. 3. Evaluation of the computed height

In this section, we evaluate the values obtained for the height z by the three methods (LS1, DPH and LS2), using Equation (2.5) and the parameters determined above. Towards this aim, we calculate the altimetric object-coordinate z and then, the altimetric deviations $\vec{d}_z$ (defined in Section 3.1) at the calibration points. The following results are found: $1.81mm < |d_z| < 128.07mm$ for the first least-squares method (LS1), $1.78mm < |d_z| < 17.24mm$ for the double-pinholes method (DPH), and $0.63mm < |d_z| < 5.22mm$ for the second least-squares method (LS2). From these intervals, as well as from Figure 3.17 a) to c), we see that $|d_z^{LS2}| < |d_z^{DPH}| \ll |d_z^{LS1}|$. The deviations found for LS1 are particularly large (one order of magnitude larger than the deviations found for DPH and LS2).These differences in the altimetric deviations result from the differences in the parameters r_x, r_y, r_z determined by the three methods (LS1, DPH, an LS2). This trend was already observed in the preceding section when considering the reference phase-maps. Clearly, the points belonging to the plate are too far from the plane $z = 0$, thus the determination of the parameters r_x, r_y, r_z using LS1 is biased. Consequently, this introduces errors in the calculated phase map, and thereby in the value of z (see Equation (2.5)). The position of the plate departs too much from the plane $z = 0$ to apply LS1. This trend is further confirmed by other measurements performed on non-plane objects or on measurement of the plate inclined by different angles relative to the vertical position. Their results were placed in Appendix C, for convenience and clarity of the text.

To obtain more reasonable values for the height z, in the case of the inclined aluminium plate, a partial solution is to do the calibration and object-coordinate calculation in the referential where the plane $(x, y, z = 0)$ coincides with the plate. This was done after rotating the referential in order to adjust the plane $(x\ y, z = 0)$ to the plate, then the object-coordinates $(x, y$ and $z)$ are transformed back in the initial referential for comparison with the other methods. The resulting z deviations are presented in Figure 3.18, where a clear improvement is observed.

This change of object-coordinate referential prior to calibrating the system with LS1 and computing the height z is only a partial solution. Indeed, both the calibration and height calculation depend on the relation between the image- and object-coordinates (Equations (2.17)). However, as seen in Section 3.4.1 and as observed when comparing the planimetric deviations in Figures 3.17 a) and 3.18, these relations do not work well when the object and camera imaging

plane are not parallel. Therefore, they will introduce errors in both calibration and height calculation.
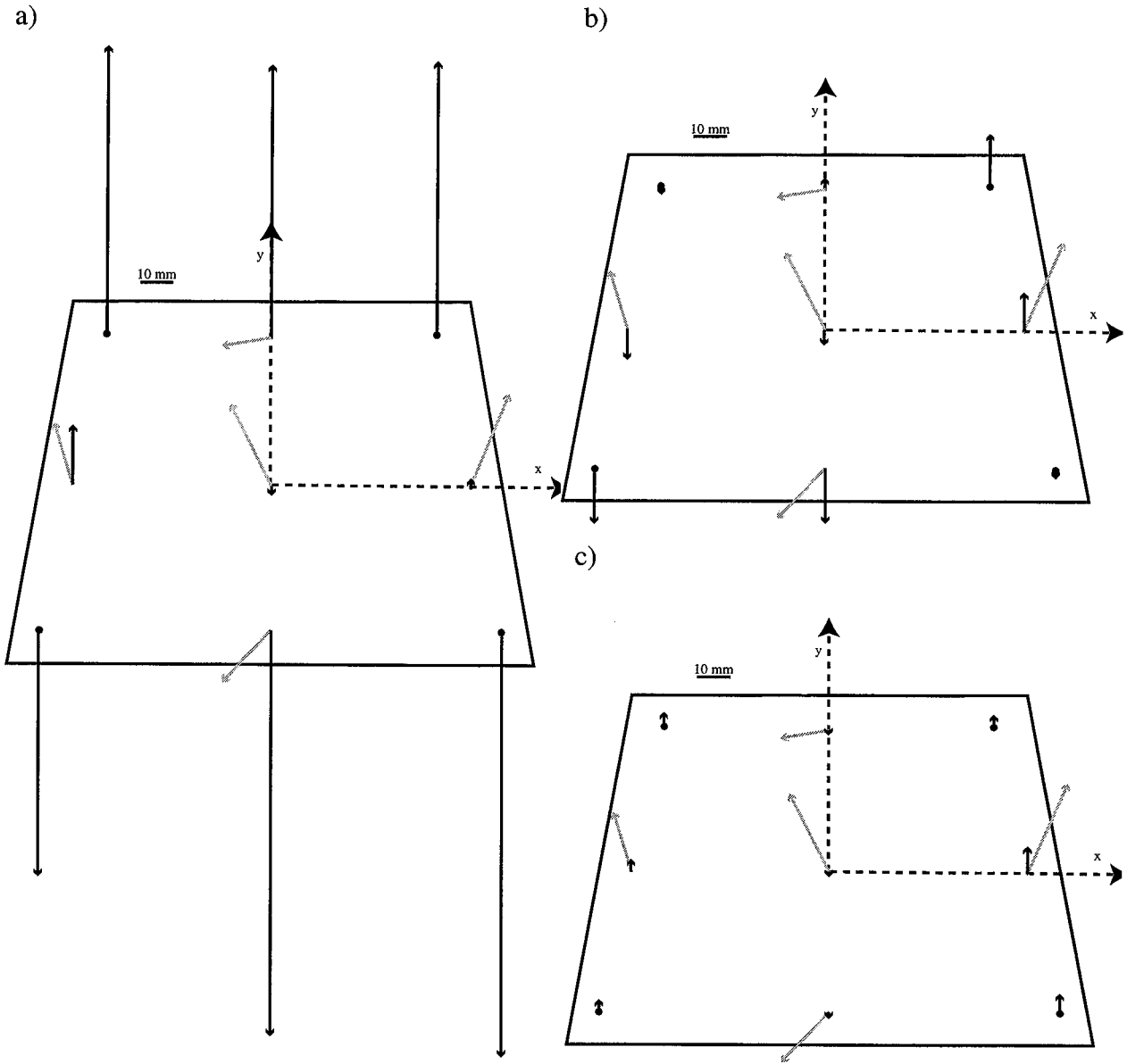
Figure 3. 17: Diagram of the planimetric (grey arrows) and z-deviation (black arrows) for the inclined aluminium plate found using LS1 (a), DPH (b), LS2 (c). If the z-deviation is positive, then the arrows points up, and vice-versa. If the value of the z-deviation is smaller than 2 mm, it is not represented.

Finally, looking at the absolute values of the total deviation, we observe the following results: $25.49mm < |d| < 128.07mm$ for the first least-squares method (LS1), $1.78mm < |d| < 32.96mm$ for the double-pinhole method (DPH), and $3.39mm < |d| < 31.58mm$ for the second least-squares method (LS2). Comparing the results of the three methods, we generally observe that $d_{max}^{LS1} > d_{max}^{DPH}$ and d_{max}^{LS2}, and

that $d_{max}^{DPH} > d_{max}^{LS2}$. This trend is further confirmed when considering the absolute value of the total distance d obtained by DPH and LS2 at each calibration point. The LS2 method gives better results than both the DPH (7 points over 9) and LS1 methods (9 points over 9), and the DPH method gives better results than the LS1 method (7 points over 9). Furthermore, since the transformation between image- and object-coordinates (see Equations (2.17)) is the same for the three methods, d_{xy} is the same at each point for the three methods. Hence, the differences observed in d between the three methods are mainly induced by the altimetric deviations d_z.
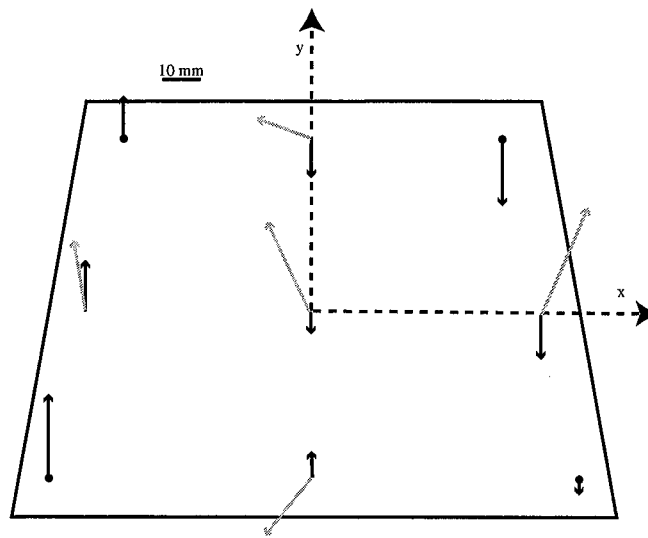
Figure 3. 18: Planimetric deviations obtained for the inclined plate using LS1, when the referential is rotated
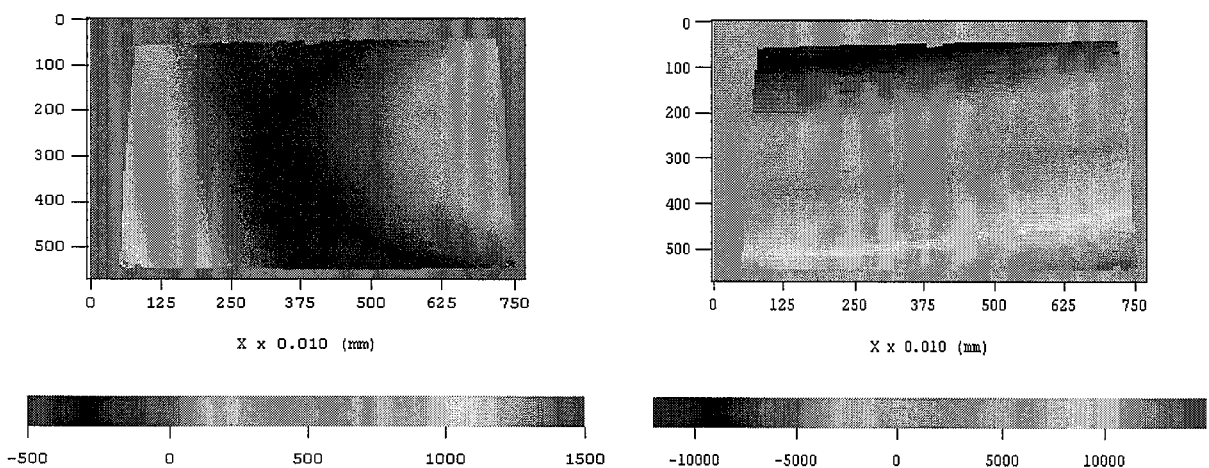
Figure 3. 19: Height map obtained for the plate in position 2 using thefirst least square method LS1 (left) and the "Double pinhole" method DPH (right). The greyscale gives the z-units (100 grey levels = 1 mm)
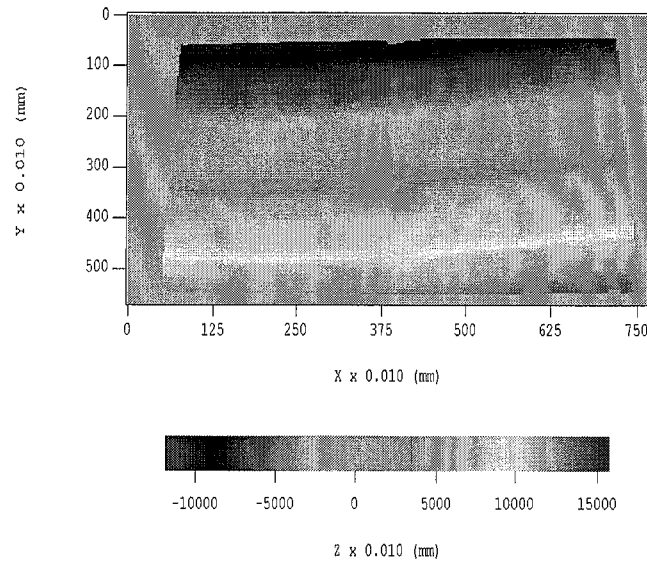
Figure 3. 20: Height map obtained for the plate in position 3 using the second least square method LS2. The greyscale gives the z-units (100 grey levels = 1 mm)

3. 5.   Discussion

The three different methods (LS1, DPH and LS2) were tested on different objects: the wall and plate in vertical position (plane objects parallel to the imaging plane of the camera, in accordance with the basic assumptions for applying the three methods) on the one hand, and the inclined plate (slight departure from these basic assumptions) on the other hand. Measurements (fringe projection, phase shifting and unwrapping) and calibrations procedures were carried out and using these, the coordinates of the measured point of the object were computed. Then the methods were evaluated in terms of planimetric and height deviations by comparing the computed coordinates of the calibration points with their coordinates as determined with the theodolite. A first evaluation of the methods was done, in term of precision and limitations.

As a first result, the feasibility of the double-pinhole (DPH) and second least squares methods (LS2) conceived and developed in the frame of this work (see Chapter 2) has been shown. As for the precision, globally the height deviations fell within a few millimeters for LS1 and LS2, but were larger for DPH (a few cm). The planimetric deviations were larger, ranging from a few millimeters to about one centimeter. Surprisingly, the LS2 method gave quite good results for planars object whether they are parallel or not to the imaging plane of the camera, despite the low number of calibration points used. Indeed, the height deviation was generally under 2 mm (reaching 5 mm for a few points), which is close to the z-resolution of 1/1000 of the object size commonly attributed to fringe projection systems. The double-pinhole method (DPH) is potentially interesting, however, it is strongly influenced by systematic errors and the height deviation ranges from 4-16 mm. Strong improvements are needed to solve these problems. As for the first least-squares method (LS1), it worked well for planar objects parallel to the imaging plane

of the camera. However its application to "deeper" objects (i.e. non planar objects or planar objects that are not parallel to the imaging plane of the camera) posed problems, as shown by the results obtained on the inclined plate. As suggested by other measurements performed on the plate rotated by different angles and other non-planar objects, we can say in a first step that LS1 is fine for objects that are plane and parallel "within 5 mm" to the imaging plane of the camera.

To summarize, the first least squares method (LS1) gave results similar to those obtained by the second least squares (LS2) method, for planar objects. The double-pinhole method (DPH) gave the worse results. In the case of the inclined plate, the second leasts square method (LS2) gave better results than both LS1 and DPH. These differences in height values calculated for reference points were studied and explained in terms of reference phase map differences due to a variation of r_x, r_y, r_z, according to the simulation developed in Chapter 2, Section 2.5. For computing the height map of this object using the LS1 method, a rotation of the referential must be carried out first, in order to adjust the plane $(x, y, z = 0)$ to the plate. This means that to be able to apply LS1 to deeper objects, an adjustment of the referential must be done first. In addition, if the object is not planar, this preliminary adjustment procedure is difficult to realize. For these reasons, the LS1 method is less user friendly than the other two (DPH and LS2).

Planimetric deviations common to the three methods were smaller in the center (a few mm) than in the periphery of the image (about 1 cm). This was explained in terms of lens distortions and of the relatively low camera resolution.

Possible improvements can be carried out at different levels of the method. To improve the determination of the height coordinates, several phase-maps of the object could be acquired, and then averaged and smoothed before using them for calibration (in the case of LS1) and determination of the height z. To further improve LS2, more calibration points could be considered, however, it would prolong the calibration procedure; therefore a trade off must be found between the number of calibration points required for good precision and the duration of the calibration procedure. In order to improve DPH, an effective way to guaranty the centering of the microscope's objective lens is required. In addition, an independent calibration procedure should be implemented in order to determine the unknown phase offset introduced by the unwrapping program, which was determined by the other methods in our work.

The determination of the planimetric coordinates can be improved by using a camera with higher spatial resolution (more pixels) and also by adding higher order terms in the equations giving the relation between pixel position and object-coordinates. This latter improvement is particularly important when measuring object that are not flat or parallel to the imaging plane of the camera, or to take into account the effect of lens distortion.

In conclusion, all three data treatment methods are relatively simple, however they suffer from a strong limitation due to the poor modelisation of the camera given by Equation (2.17), especially when considering "deep" objects. Indeed, considering that the transformation of (x,y) is independent of z is an overly simplistic model. The model used requires theoretical basic assumptions that are very restrictive in terms of object shape (flat) and configuration (to roughly lie in a plane that is as parallel as possible to the camera sensor). Therefore, these methods are inherently limited to quasi-planar objects that are parallel to the imaging plane of the camera. Since objects of general shape (without previous knowledge of its shape), and particularly deep "objects", do not respect at all the basic hypothesis of flatness, they poses particular problems to the methods considered in this chapter. Therefore in spite of improvements that may be brought to the method and to the system, another approach is clearly needed in order to make fringe

projection a more flexible measurement method in terms of object shape and measurement configuration.

3. 6.   References

1. Lehmann M., Jacquot P., and Facchini. M., *Shape measurements on large surfaces by fringe projection*. Experimental Techniques, 1999. **23**(2): p. 31-35.

CHAPTER 4

General method for measuring objects of any shape

For objects of general shape that are placed in any position, the data treatment methods used above are not applicable, since in their basic hypothesis (the object is flat, roughly lies in the plane $(x, y, z = 0)$ and is parallel to the imaging sensor) are not observed. Therefore another approach must be used. In the scope of this work, we propose novel algorithms that avoid such restrictive assumptions and make the measurement method more flexible. It is based on the modelization of the two point sources by the interferometry equation (2.2) and of the camera by the central perspective equations. This approach is more global and extends the application of fringe projection to more general cases.

In this chapter, the theory will first be exposed and then the calibration procedures allowing to determine the system parameters will be presented. Next, this new method will be applied to the case of the wall and the aluminium plate in a vertical position, and a first evaluation of its precision will be made. Finally, as for the two other methods in the preceding chapters, the measurement results for a plate in a 10° rotated position will be computed and commented.

4. 1.   Theoretical development

In Chapter 2, to cope with the problem of measuring large objects using fringe projection, we described the system with a simplified model based on three equations: one equation of the phase linearized in z (Equation (2.5)), and two polynomial equations (Equation (2.17)) corresponding to the imaging system. The first one gave a proportional relation between the height z and the phase. The two latter allowed to determine the planimetric object-coordinates x and y from pixel positions (i, j), independently of the height z.

The advantage of this model is its simplicity, particularly since the determination of the object-coordinates x and y is independent of the height z. The drawback is that its application is limited only to flat objects and to a single measurement configuration where the object is parallel to the imaging plane of the camera. These limitations arise mainly because of the simplified mathematical relation chosen to model the imaging device.

To extend the description of the camera for any object or measurement configuration, an adequate model is the central projection (also known as central perspective, in the literature [1]) defined by Equation (4.1), in correspondence with Figure 4.1:

$$\begin{cases} x = X_0 + (z - Z_0)\dfrac{r_{11}(\xi - \xi_0) + r_{12}(\eta - \eta_0) + r_{13}c}{r_{31}(\xi - \xi_0) + r_{32}(\eta - \eta_0) + r_{33}c} \\[2em] y = Y_0 + (z - Z_0)\dfrac{r_{21}(\xi - \xi_0) + r_{22}(\eta - \eta_0) + r_{23}c}{r_{31}(\xi - \xi_0) + r_{32}(\eta - \eta_0) + r_{33}c} \end{cases}$$

(4. 1)

where,

- (x, y, z): are the object-coordinates of any point P(x,y,z) of the object (in the object referential)
- (ξ, η): are the image-coordinates corresponding to point P(x,y,z), on the imaging plane (in the image referential)
- c: is the principal distance of the central projection (also known as camera constant). It is the distance between the image and the perspective center
- ξ_0, η_0: are the image-coordinates of the principal point (in the image referential)
- (X_0, Y_0, Z_0): are the object-coordinates of the perspective center (also known as projection center)
- r_{kl}: (k, l = 1 to 3) are the elements of the rotation matrix describing the orientation of the imaging plane with regard to the object-coordinates referential. They depend on the three rotation angles: ω, ϕ, κ, as shown by the following:

$$\rho = \begin{bmatrix} r_{11} & r_{12} & r_{13} \\ r_{21} & r_{22} & r_{23} \\ r_{31} & r_{32} & r_{33} \end{bmatrix} \Leftrightarrow \rho = \begin{bmatrix} \cos\phi\cos\kappa & -\cos\phi\sin\kappa & \sin\phi \\ \cos\omega\sin\kappa + \sin\omega\sin\phi\cos\kappa & \cos\omega\cos\kappa - \sin\omega\sin\phi\sin\kappa & -\sin\omega\cos\phi \\ \sin\omega\sin\kappa - \cos\omega\sin\phi\cos\kappa & \sin\omega\cos\kappa + \cos\omega\sin\phi\sin\kappa & \cos\omega\cos\phi \end{bmatrix}$$

(4. 2)

When considering the equations of central projection (4.1), one sees that the object-coordinates x and y now depend on the height z, which is the unknown we want to determine. Therefore these equations could not be used instead of Equations (2.17) in the model of Chapter 2 and 3, where it is assumed that x and y are determined independently of z. Therefore, in order to consider the most general cases, another approach is needed for data treatment, and the problem must be considered from another angle. This is illustrated by Figure 4.2 where the different elements present are the two point sources S1 and S2, the object, and the CCD camera. Any point P of the object surface is designated by its object-coordinates (x, y, z).

Fringes created by the two point sources S1,S2 of coherent light are projected on the object surface (operation P1).

The object and the fringes projected on its surface are imaged by the camera (operation P2). According to the central projection equation, a given point P(x, y, z) of the surface is projected on the imaging plane of the camera (e.g. a CCD pixel array) at a corresponding point (ξ, η). ξ and η are called the image-coordinates of point P.

When projecting the fringes of light on the object by operation P1, we add information, namely the phase $\varphi(x, y, z)$, at each point of the object surface, as shown by Equation (1.2). In addition, this information is physically related to the position of each point $P(x,y,z)$, since it is proportional to the difference of the distances between the point $P(x,y,z)$ and the two point sources S1,S2, as shown by Equation (1.8)).
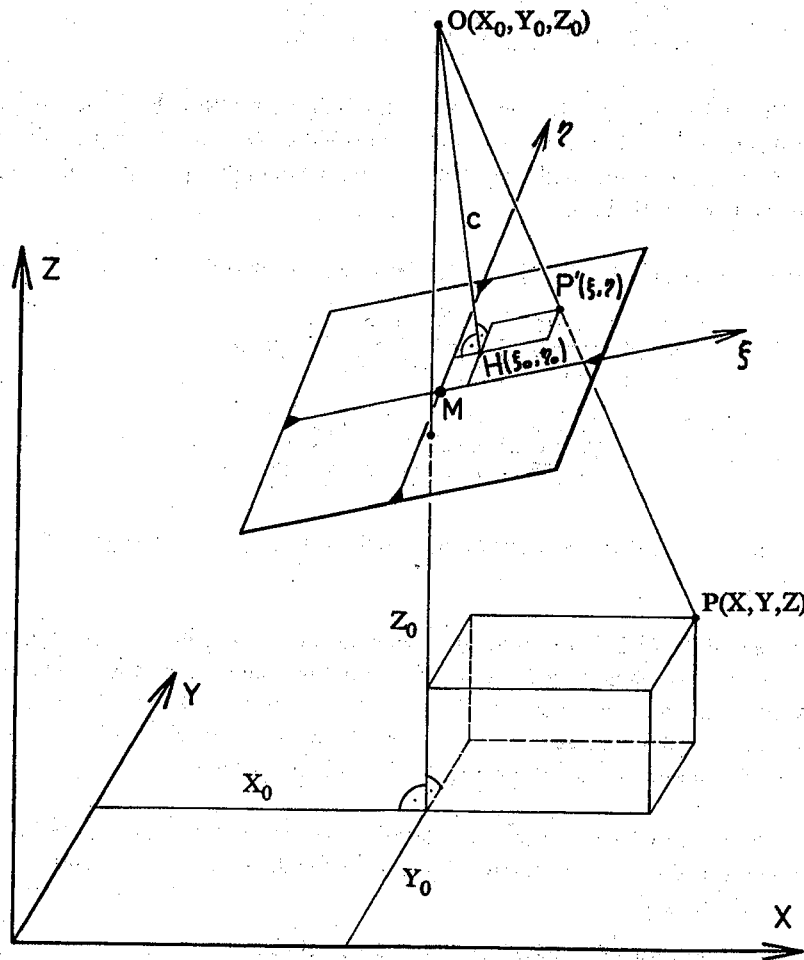
Figure 4. 1: relation between the image coordinates (ξ,η) and the object coordinates (x, y, z). Excerpt from[1].

Thus, after applying the operation P1, we can consider a mathematical "4D" space where each point P is coded in a unique way by its object-coordinates and the phase: $P(x, y, z, \varphi(x, y, z))$. When imaged by the camera (operation P2), this point P is projected at its corresponding point (ξ, η) of the imaging plane (e.g. CDD pixel array) with the information $\varphi(\xi, \eta)$. It can be considered as a point in another mathematical "3D" space, where each pixel corresponding to the image-coordinates (ξ, η) contains a phase value $\varphi(\xi, \eta)$.

Thus these two operations can be summed up by a composition of application $P_2 \circ P_1(x, y, z)$. Now if $(\xi, \eta, \varphi(\xi, \eta))$ are known and if the operations P1 and P2 are fully defined for a given measurement configuration and specification of the system, then the object coordinates can be

determined for each corresponding point (x, y, z). Hence, the object shape is known. This is what we do by using a model of the measurement system as illustrated by Figure 4.3.
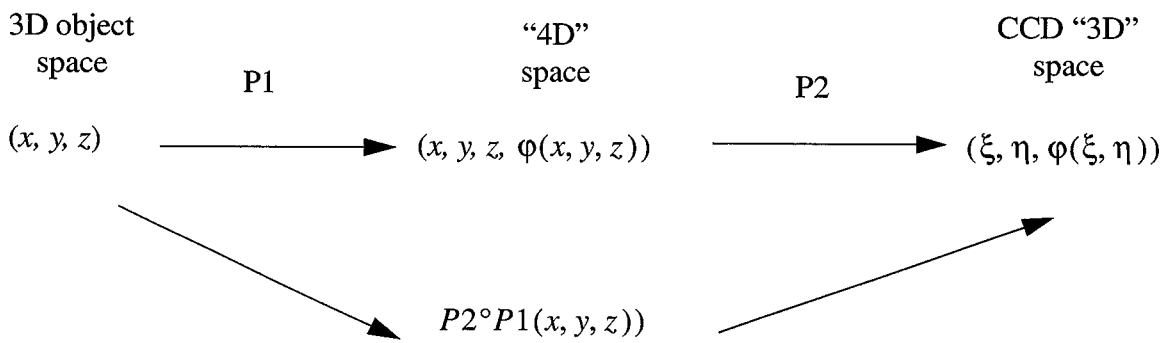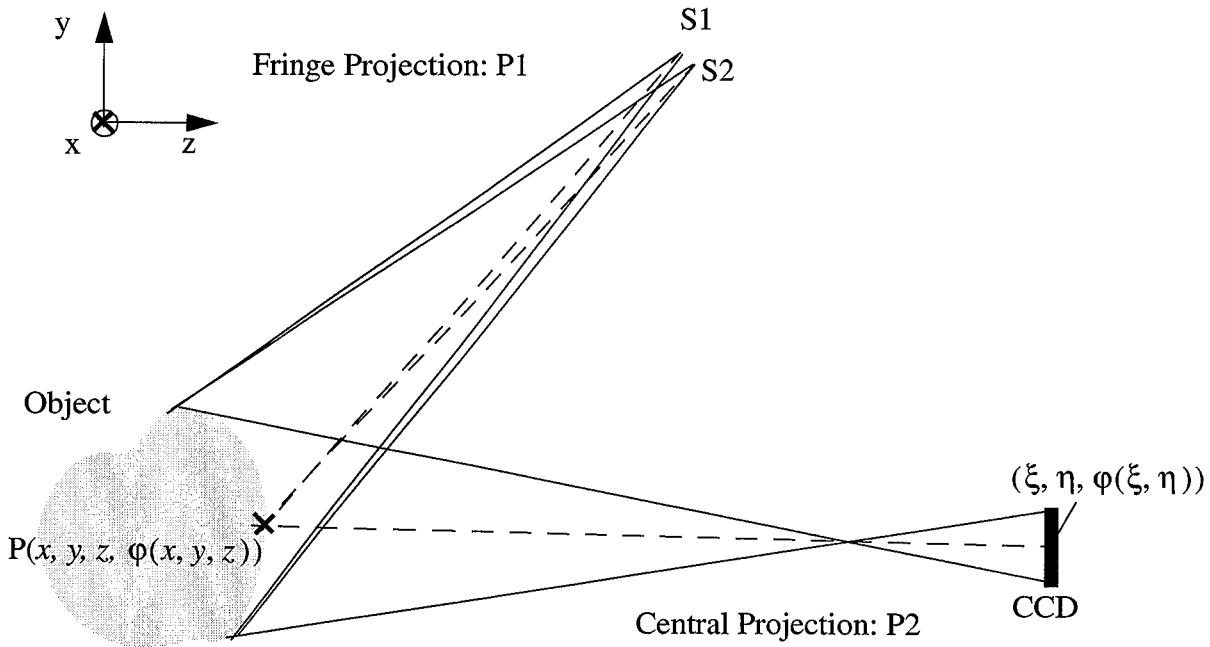
Figure 4. 2: Diagram of the fringe projection image acquisition

Figure 4.3 describes the modelization of the measurement system, and the procedures to recover the object-coordinates (x, y, z) of each measured point. The model in this approach is based on two levels: the system's world, where the system and the object exist and where the measurement takes place; and a model or abstract world. In the latter, the system, object and measurement are described by mathematical concepts. In particular, the measurement system is represented by the set of mathematical equations (4.3). The first equation describes the phase φ of the light and thus corresponds to the fringe projection (P1); since here the fringes are created by interferometry, we call it the interferometry equation. The two other equations correspond to the camera (P2); they are the central projection equations.

Thus the whole system can be described by the following set of equations:

$$\begin{cases} \varphi(x, y, z) = \dfrac{2\pi}{\lambda} \cdot \dfrac{((R_x - x)r_x + (R_y - y)r_y + (R_z - z)r_z)}{\sqrt{(R_x - x)^2 + (R_y - y)^2 + (R_z - z)^2}} \\[3mm] x = X_0 + (z - Z_0)\dfrac{r_{11}(\xi - \xi_0) + r_{12}(\eta - \eta_0) + r_{13} \cdot c}{r_{13}(\xi - \xi_0) + r_{23}(\eta - \eta_0) + r_{33} \cdot c} \\[3mm] y = Y_0 + (z - Z_0)\dfrac{r_{21}(\xi - \xi_0) + r_{22}(\eta - \eta_0) + r_{23} \cdot c}{r_{13}(\xi - \xi_0) + r_{23}(\eta - \eta_0) + r_{33} \cdot c} \end{cases} \qquad (4.3)$$

These equations depend on different parameters describing the system configuration and specifications. R_x, R_y, R_z, r_x, r_y, r_z describe the projection head, and since the fringes are interferometrically-created, they are called interferometric parameters; λ is the laser wavelength; ξ_0, η_0 and c are the interior orientation parameters of the camera; X_0, Y_0, Z_0 and ω, ϕ, κ are the exterior orientation parameters of the camera.

The desired object-coordinates x, y and z are the unknown. (ξ, η) are the image-coordinates and $\varphi(x, y, z)$ is the phase. These three latter variables correspond to point $P(x,y,z)$, and are determined by reading each pixel of the CCD camera 2D array.

This system of non-linear equations is solved giving general expressions of x, y, z, as follows:

$$\begin{cases} x \equiv x(\xi, \eta, \varphi; R_x, R_y, R_z, r_x, r_y, r_z, \lambda, \xi_0, \eta_0, X_0, Y_0, Z_0, \omega, \kappa, \phi) \\[2mm] y \equiv y(\xi, \eta, \varphi; R_x, R_y, R_z, r_x, r_y, r_z, \lambda, \xi_0, \eta_0, X_0, Y_0, Z_0, \omega, \kappa, \phi) \\[2mm] z \equiv z(\xi, \eta, \varphi; R_x, R_y, R_z, r_x, r_y, r_z, \lambda, \xi_0, \eta_0, X_0, Y_0, Z_0, \omega, \kappa, \phi) \end{cases} \qquad (4.4)$$

Calibration procedures (described in more detail later) give the value of the system parameters: R_x, R_y, R_z, r_x, r_y, r_z, ξ_0, η_0, c, X_0, Y_0, Z_0, ω, κ, ϕ. For this purpose, information about the system configuration and specifications and about the calibration points (phase, object- and image-coordinates) is used. Thus, expressions of x, y, and z specific to the system configuration and specifications (wavelength of the light, camera specifications, etc...) are obtained:

$$\begin{cases} x \equiv x(\xi, \eta, \varphi) \\[2mm] y \equiv y(\xi, \eta, \varphi) \\[2mm] z \equiv z(\xi, \eta, \varphi) \end{cases} \qquad (4.5)$$

As described above, a measurement is carried out through phase-shifting and phase unwrapping procedures giving a phase-map. This optical print of the object is an image in grey levels where each pixel (i, j) contains the phase information φ. Furthermore, each pixel (i, j) is related to the image-coordinates (ξ, η). Thus, reading a pixel (i, j) gives the information (ξ, η, φ). This allows to calculate the object-coordinates (x, y, z) of each point of the measured surface, by using the set of Equations (4.5). Once this is done for all the points of the object surface, a height map corresponding to the desired shape information can be represented using an adequate program.
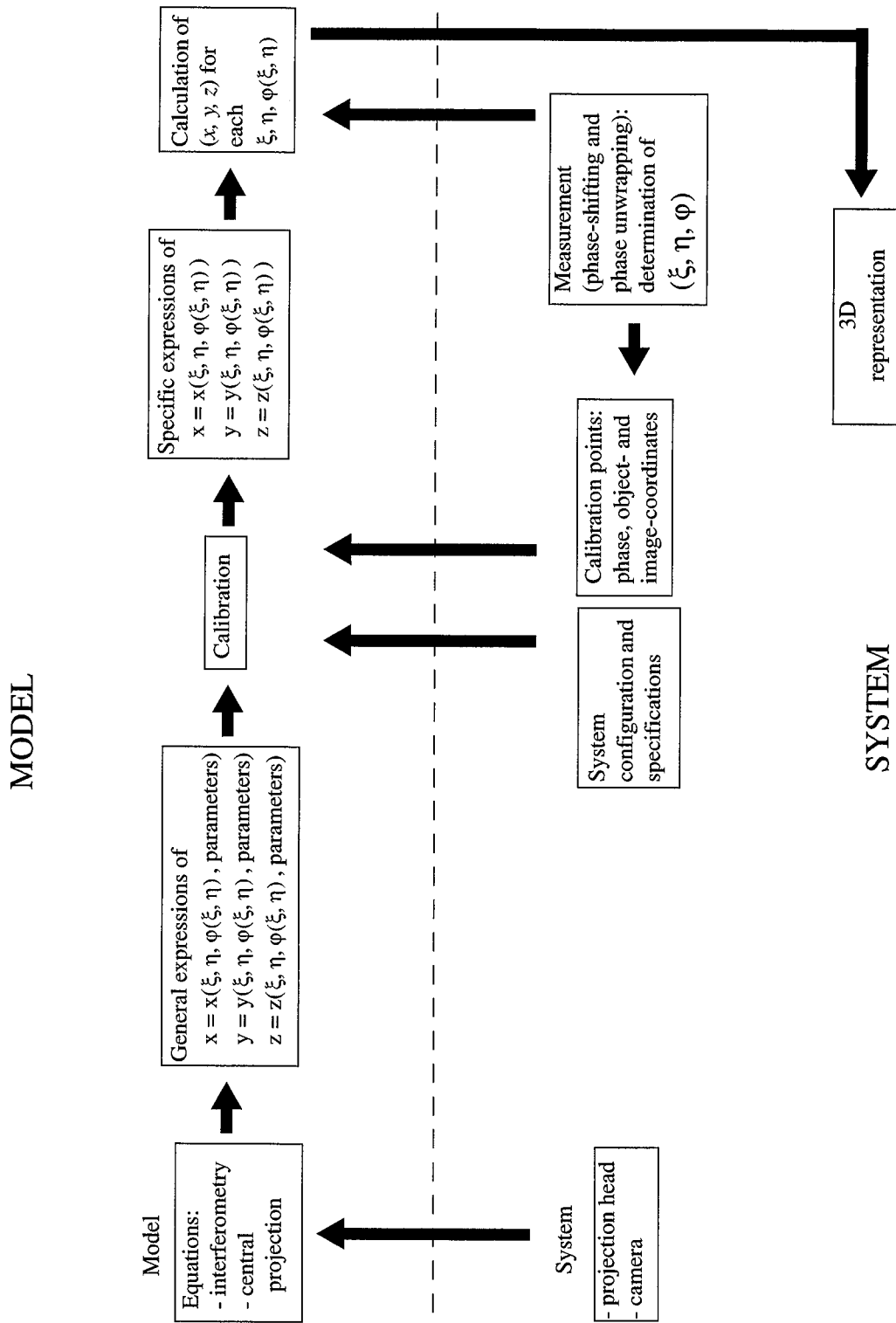
Figure 4. 3: Global description of the general method developed in the frame of this work

Several remarks can be made about the development above. First, the originality of this work is on the one hand to model the fringe projection measurement system by this set of non-linear equations, and on the other hand to solve these equations, determining the general solutions x, y, and z as functions of (ξ, η, φ). For convenience and readability, these general solutions are placed in Appendix D.

This method can also be applied to small objects, however in the cases where the distance between the object and projection head is small the original equation of phase (1.8) should be used. Indeed the condition $r \ll R$ for simplifying the phase equation might no longer be valid.

In most practical cases lens distortions are present and must be taken into account. For that purpose, the image-coordinates ξ and η must be corrected [2]:

$$\begin{cases} \xi' = \xi + \Delta\xi \\ \eta' = \eta + \Delta\eta \end{cases} \tag{4.6}$$

where $\Delta\xi$, $\Delta\eta$ are due to different factors [2]:
- radial symmetric lens distortion
- decentering distortion
- irregularities of the sensor elements spacing
- potential non-flatness of the sensor

In a first step, we consider only the distortions that bring the most errors:

$$\Delta\xi = (\xi - \xi_0)r^2 K_1 + (\xi - \xi_0)r^4 K_2 + \left(r^2 + 2(\xi - \xi_0)^2\right)P_1 + 2(\xi - \xi_0)(\eta - \eta_0)P_2 \tag{4.7}$$

$$\Delta\eta = (\eta - \eta_0)r^2 K_1 + (\eta - \eta_0)r^4 K_2 + 2(\xi - \xi_0)(\eta - \eta_0)P_1 + \left(r^2 + 2(\eta - \eta_0)^2\right)P_2 \tag{4.8}$$

where: $r = \sqrt{(\xi - \xi_0)^2 + (\eta - \eta_0)^2}$ \hfill (4.9)

K_1, K_2: are the first 2 parameters of radial symmetric distortion

P_1, P_2: are the first 2 parameters for decentering distortion

4.2. Determination of the system parameters

Once the expression of the x,y,z solutions are established, the parameters of the system that must be determined. The calibration procedure used are presented in Figure 4.4.

The interferometric parameters are R_x, R_y, R_z, and r_x, r_y, r_z. The parameters R_x, R_y, R_z, are measured using the theodolite. The parameters r_x, r_y, r_z are determined using calibration points for which the phase and object-coordinates are known and least squares calculations minimizing the difference between the measured phase values and theoretical phase values given by the interferometry equation (see Section 2.2.3). The wavelength λ is given by the laser specifications.

The interior orientation parameters (ξ_0, η_0, c) are determined by measuring a known object from different points of view with the camera and using bundle adjustment calculations [1]. Commercially available programs exist for this procedure, for example Photomodeler™ available from EOS Systems. This latter was used here.

The exterior orientation parameters are determined using calibration points, for which the image- and object-coordinates are known, and least squares calculations applied to the equations of central projection, after linearization. Approximate values of X_0, Y_0, Z_0, ω, κ, ϕ are entered in the program, and then optimized by iterations.

In this work, the interferometric, exterior and interior orientation parameters are determined separately using programs based on known least squares calculations. However, other approaches are also possible. For example, it is possible to determine the exterior and interior orientation parameters at the same time by using appropriate algorithms.

The procedures used are described in further details below in sections 4.2.2 to 4.2.4. In addition, based on the theoretical developments described hereafter, several programs were developed in MATLAB. However before performing the system calibration, the measured data must first be pre-treated.

```
                    ┌─────────────────────┐
                    │    Calibration      │
                    │      of the         │
                    │  system parameters  │
                    └─────────────────────┘
```

Interferometric parameters: theodolite measurement and least square calculations	Exterior orientation parameters: 1) linearisation of central equation projection 2) introduction of approximate values 3) least square calculations 4) iterations	Interior orientation parameters: Bundle adjustment calculations
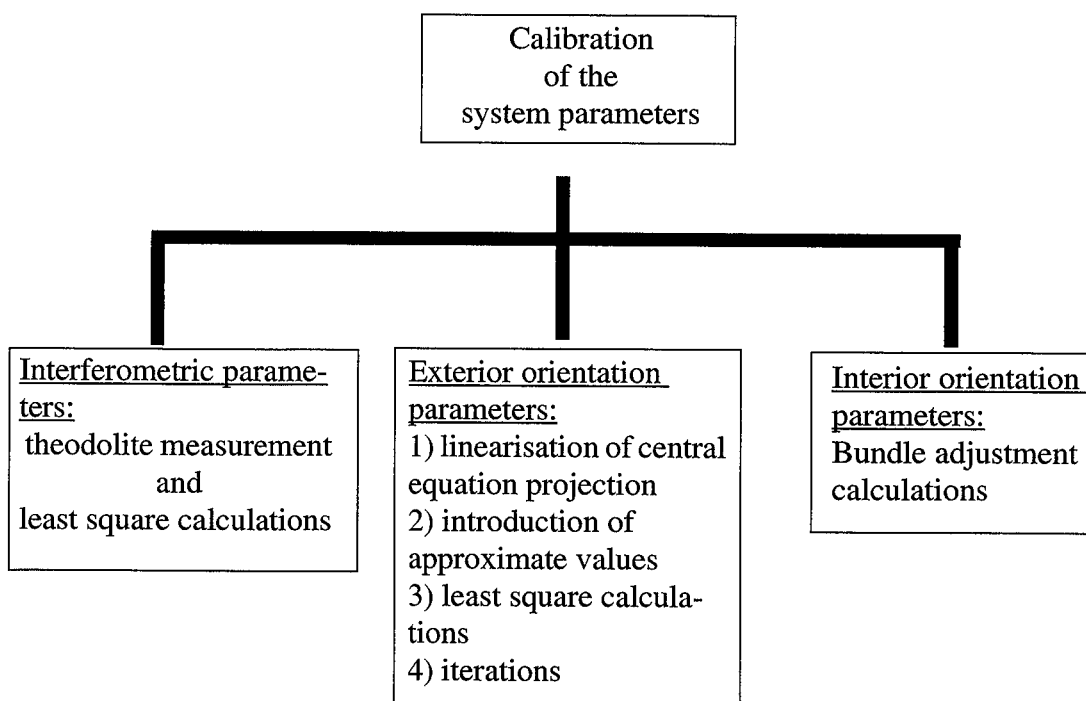
Figure 4. 4: Overview of the different type of system parameters to be determined and of the calibration procedures

4. 2. 1. Transformation of raw data

Figure 4.5 illustrates different procedures necessary to transform the raw data into usable data, expressed in the right units and referential, and corresponding to the mathematical equations developed. In particular, the phase measured directly from the phase map is expressed in grey

levels and must be transformed in radians to be suitable to the mathematical formula describing the phase. A linear relation between the phase expressed in grey levels and the phase expressed in radians allows to do the conversion represented in Figure 4.5(a):

$$\phi(x, y, z) = \frac{2\pi}{256}(\phi(\xi, \eta))$$

(4. 10)

where 256 is the number of grey levels linked to the camera dynamics (8 bits). Similarly, the object-coordinates of the calibration points and projection head as well as a first approximation of the object-coordinates of the perspective center must be transformed from the measurement referential (e.g. the theodolite referential) to the right object-coordinates referential, related to the central projection model. This is illustrated in Figure 4.5(b). The same is true for the pixel positions (*i*, *j*) of the reference points, initially expressed in integers (pixels). They must be expressed in units of length (e.g. mm), and transformed to suit the right image-coordinates referential (ξ, η) defined by the central projection model. This is represented in Figure 4.5(c). Several programs have been developed to carry out those transformations.

a) $\phi_{mes}(i, j)$ [grey level] ——▶ $\phi_{mes}(x, y, z)$ [rad]
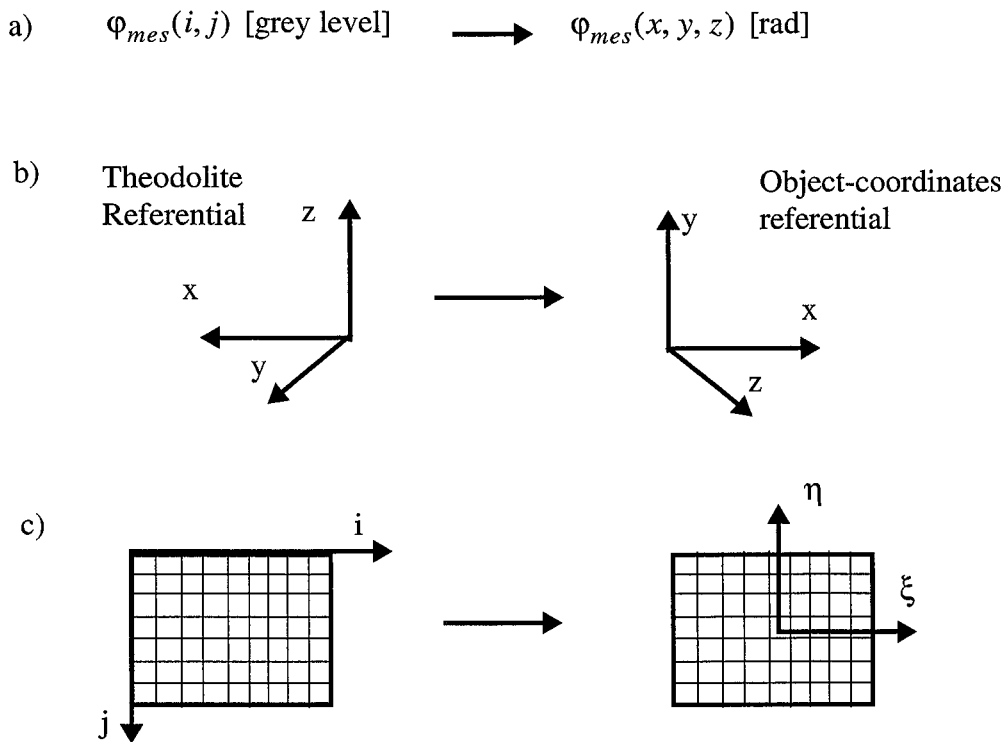
Figure 4. 5: Examples of raw data pre-treatment necessary prior to the application of the general method

4. 2. 2. Interferometric parameters

The interferometric parameters r_x, r_y, r_z are determined by a least squares method applied to Equation (2.3). It aims at minimizing the difference between the measured phase of the nine calibration points and their theoretical phase. This is expressed by

$$\varepsilon^2 = \sum \left(\varphi_{meas}(x_k, y_k) - \frac{2\pi}{\lambda} \cdot \frac{(R_x - x_k)r_x + (R_y - y_k)r_y + (R_z - z_k)r_z}{\sqrt{(R_x - x_k)^2 + (R_y - y_k)^2 + (R_z - z_k)^2}} - \varphi_0 \right)^2 \tag{4. 11}$$

This calibration method was described in more details in Chapter 2; Section 2.2.3.

4. 2. 3. Interior orientation parameters

The interior orientation parameters are determined by measuring a known object from different points of view with the camera as illustrated in Figure 4.6, and using the bundle adjustment method [1]. Commercially available programs exist for this procedure, for example Photomodeler^{TM} available from EOS systems which was used in the frame of this work. The front panel of the program is represented in Figure 4.7.

First, a pre-calibration procedure is carried out in order to give an approximate value of:

- the camera-objective focal length, the format size (c, in the theory above),
- the image size (Width W and height H),
- the principal point coordinates (noted X and Y in Photomodeler^{TM}, but corresponding to ξ_0, η_0 in the theory above)
- the image size in pixels

Then, pictures of the calibration object (here a poster with calibration pattern provided by Photo-modeler) are taken from different points of view, as displayed in Figure 4.6. These images are introduced in the program together with the pre-calibrated parameters mentioned in the previous paragraph. Then all these data are processed using bundle adjustment calculations to give the final calibrated interior parameters of the camera. An example of calibration results is displayed in Figure 4.7. In addition, this program also allows us to determine the size of the pixels (of the virtual camera), namely its width W and height H in mm, as well as the first order coefficients for the correction of lens aberration (K_1, K_2, P_1, P_2). These latter will be considered in the calculation of object coordinates in the next sections.

It is interesting to notice that the camera calibrated here is not the physical CCD camera used. Actually, it is a "virtual camera" which is equivalent to the set composed of the CCD camera, its objective, the frame grabber and the visualization program, as represented in Figure 4.8. Hence if one of these elements is changed, the calibration procedure must be carried out again. Therefore, great care must taken during the measurement in order not to change any of these elements. For the measurements carried out in this work, these elements were kept unchanged, and the determination of the interior orientation parameters were done once for all. The following values were found for the different parameters:

$$\xi_0 = -57.1 \cdot 10^{-3} \text{ mm}; \ \eta_0 = -106.2 \cdot 10^{-3} \text{ mm}; \ c = 7.66 \text{ mm}$$

$W = 5.89$ mm, $H = 4.43$ mm

$K_1 = 2.16 \cdot 10^{-3}$ mm, $K_2 = -1.04 \cdot 10^{-4}$ mm

$P_1 = 4.32 \cdot 10^{-5}$ mm, $P_2 = 2.06 \cdot 10^{-4}$ mm
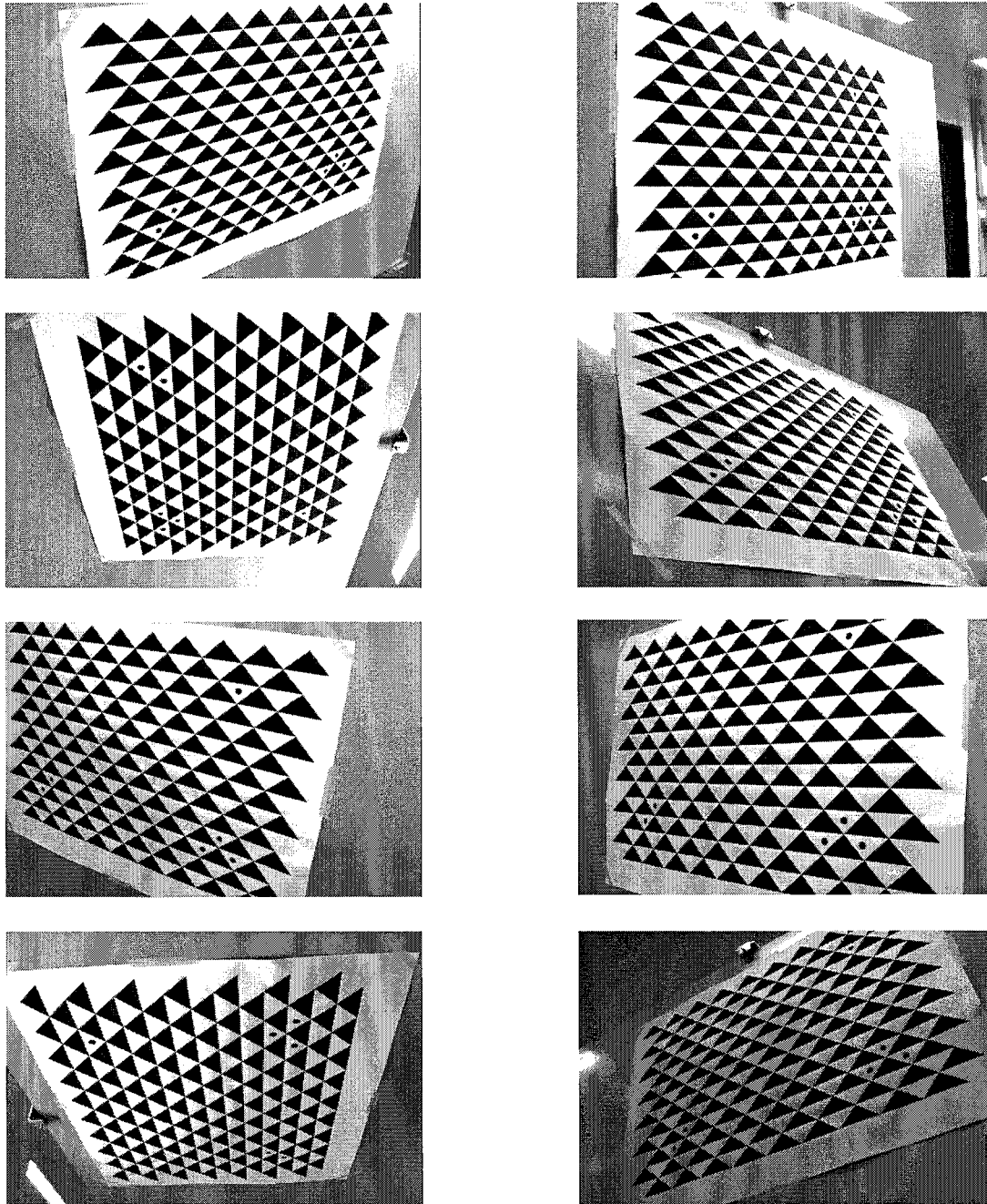
Figure 4. 6: Pictures of the calibration object (here a poster with known patterns provided with Photomodeler™ - Camera Calibrator) for determining the interior orientation parameters of the camera
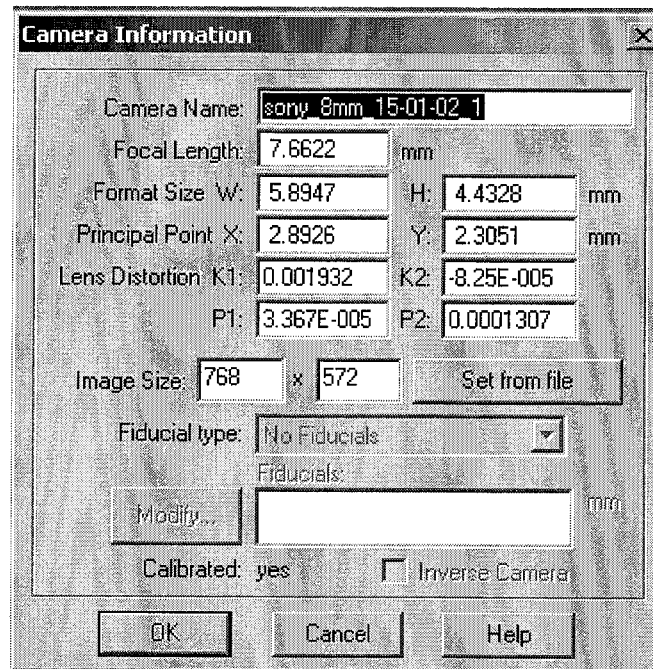
Figure 4. 7: Program for determining the interior orientation parameters
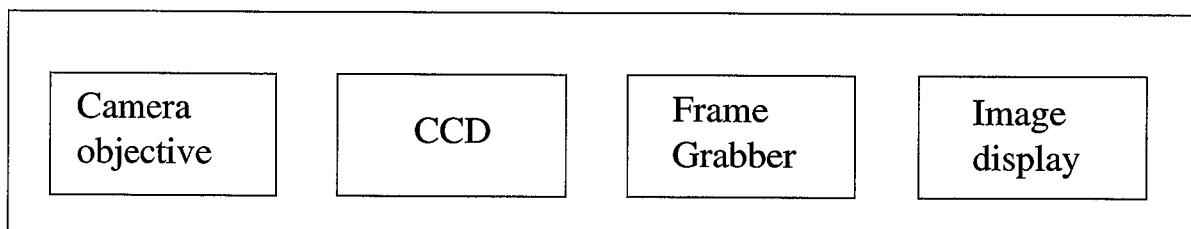
Figure 4. 8: Elements of the virtual camera

4. 2. 4. Exterior orientation parameters:

Once the interior orientation parameters of the camera are determined, we can consider the exterior orientation parameters. These were calibrated using the least squares procedures described in [1], the interior orientation parameters determined in the previous section and the image- and object-coordinates of the nine calibration points. Because here the lens distortion parameters were determined at the same time as the interior orientation parameters, as seen in the previous section, the effect of lens distortion must be taken into account when determining the exterior orientation parameters. This is done by considering the image-coordinates corrected for lens distortion, according to Equations (4.6) to (4.9) in Section 4.2:

$$\xi' = \xi + \Delta\xi \quad \text{and}$$
$$\eta' = \eta + \Delta\eta$$

where $\Delta\xi$, $\Delta\eta$ are deviations due to radial symmetric lens distortion and decentering distortion. For convenience, after the image-coordinates of the calibration points are corrected for aberration, we write ξ instead of ξ' in the development below.

Starting with the central projection equations, we thus have:

$$\begin{cases} \xi = \xi_0 - c\dfrac{r_{11}(x-X_0) + r_{21}(y-Y_0) + r_{31}(z-Z_0)}{r_{13}(x-X_0) + r_{23}(y-Y_0) + r_{33}(z-Z_0)} \\[4mm] \eta = \eta_0 - c\dfrac{r_{12}(x-X_0) + r_{22}(y-Y_0) + r_{32}(z-Z_0)}{r_{13}(x-X_0) + r_{23}(y-Y_0) + r_{33}(z-Z_0)} \end{cases} \qquad (4.12)$$

and writing:

$$\begin{cases} Z_\xi = r_{11}(x-X_0) + r_{21}(y-Y_0) + r_{31}(z-Z_0) \\ Z_\eta = r_{12}(x-X_0) + r_{22}(y-Y_0) + r_{32}(z-Z_0) \ , \\ D = r_{12}(x-X_0) + r_{22}(y-Y_0) + r_{32}(z-Z_0) \end{cases} \qquad (4.13)$$

the equations above become:

$$\begin{cases} \xi = \xi_0 - c \cdot \dfrac{Z_\xi}{D} \\[4mm] \eta = \eta_0 - c\dfrac{Z_\eta}{D} \end{cases} \qquad (4.14)$$

By developing the expression of ξ and η in a Taylor series around the approximation of the exterior orientation parameters, $C_0 = (\omega^0, \phi^0, \kappa^0, X_0^0, Y_0^0, Z_0^0)$, and considering only the first order terms one gets:

$$\begin{cases} \xi \cong \xi|_{C_0} + \dfrac{\partial\xi}{\partial\omega}\Big|_{C_0} d\omega + \dfrac{\partial\xi}{\partial\phi}\Big|_{C_0} d\phi + \dfrac{\partial\xi}{\partial\kappa}\Big|_{C_0} d\kappa + \dfrac{\partial\xi}{\partial X_0}\Big|_{C_0} dX_0 + \dfrac{\partial\xi}{\partial Y_0}\Big|_{C_0} dY_0 + \dfrac{\partial\xi}{\partial Z_0}\Big|_{C_0} dZ_0 \\[4mm] \eta \cong \xi|_{C_0} + \dfrac{\partial\eta}{\partial\omega}\Big|_{C_0} d\omega + \dfrac{\partial\eta}{\partial\phi}\Big|_{C_0} d\phi + \dfrac{\partial\eta}{\partial\kappa}\Big|_{C_0} d\kappa + \dfrac{\partial\eta}{\partial X_0}\Big|_{C_0} dX_0 + \dfrac{\partial\eta}{\partial Y_0}\Big|_{C_0} dY_0 + \dfrac{\partial\eta}{\partial Z_0}\Big|_{C_0} dZ_0 \end{cases} \qquad (4.15)$$

We define:

$$\begin{cases} a_2 = \dfrac{\partial \xi}{\partial X_0} = -\dfrac{C}{D^2}(r_{13} \cdot Z_\xi - r_{11} \cdot D) \\[2mm] a_3 = \dfrac{\partial \xi}{\partial Y_0} = -\dfrac{C}{D^2}(r_{23} \cdot Z_\xi - r_{21} \cdot D) \\[2mm] a_4 = \dfrac{\partial \xi}{\partial Z_0} = -\dfrac{C}{D^2}(r_{33} \cdot Z_\xi - r_{31} \cdot D) \\[2mm] a_5 = \dfrac{\partial \xi}{\partial \omega} = -\dfrac{C}{D}\left\{((Y-Y_0) \cdot r_{33} - (Z-Z_0) \cdot r_{23}) \cdot \dfrac{Z_\xi}{D} - (Y-Y_0) \cdot r_{31} + (Z-Z_0) \cdot r_{21}\right\} \\[2mm] a_6 = \dfrac{\partial \xi}{\partial \phi} = \dfrac{C}{D}\left\{(Z_\xi \cdot \cos\kappa - Z_\eta \cdot \sin\kappa) \cdot \dfrac{Z_\xi}{D} + D \cdot \cos\kappa\right\} \\[2mm] a_7 = \dfrac{\partial \xi}{\partial \kappa} = -\dfrac{C}{D}Z_\eta \end{cases} \qquad (4.\ 16)$$

$$\begin{cases} b_2 = \dfrac{\partial \eta}{\partial X_0} = -\dfrac{C}{D^2}(r_{13} \cdot Z_\eta - r_{12} \cdot D) \\[2mm] b_3 = \dfrac{\partial \eta}{\partial Y_0} = -\dfrac{C}{D^2}(r_{23} \cdot Z_\eta - r_{22} \cdot D) \\[2mm] b_4 = \dfrac{\partial \eta}{\partial Z_0} = -\dfrac{C}{D^2}(r_{33} \cdot Z_\eta - r_{32} \cdot D) \\[2mm] b_5 = \dfrac{\partial \eta}{\partial \omega} = -\dfrac{C}{D}\left\{((Y-Y_0) \cdot r_{33} - (Z-Z_0) \cdot r_{23}) \cdot \dfrac{Z_\eta}{D} - (Y-Y_0) \cdot r_{32} + (Z-Z_0) \cdot r_{22}\right\} \\[2mm] b_6 = \dfrac{\partial \eta}{\partial \phi} = \dfrac{C}{D}\left\{(Z_\xi \cdot \cos\kappa - Z_\eta \cdot \sin\kappa) \cdot \dfrac{Z_\eta}{D} - D \cdot \sin\kappa\right\} \\[2mm] b_7 = \dfrac{\partial \eta}{\partial \kappa} = \dfrac{C}{D}Z_\xi \end{cases} \qquad (4.\ 17)$$

and:

$$\begin{cases} l_\xi \equiv \xi_0 - \xi|_{C_0} \\[2mm] l_\eta \equiv \eta_0 - \eta|_{C_0} \end{cases} \qquad (4.\ 18)$$

Then, the equations (4.15) above can be written:

$$\begin{cases} l_\xi = a_2 \cdot dX_0 + a_3 \cdot dY_0 + a_4 \cdot dZ_0 + a_5 \cdot d\omega + a_6 \cdot d\phi + a_7 \cdot d\kappa \\[2mm] l_\eta = b_2 \cdot dX_0 + b_3 \cdot dY_0 + b_4 \cdot dZ_0 + b_5 \cdot d\omega + b_6 \cdot d\phi + b_7 \cdot d\kappa \end{cases} \qquad (4.\ 19)$$

By using a number n of calibration points, these n sets of equations may be written n times. Then,

$$l_\xi \equiv \begin{bmatrix} l_{\xi 1} \\ \cdots \\ l_{\xi n} \end{bmatrix} \text{ and } l_\eta \equiv \begin{bmatrix} l_{\eta 1} \\ \cdots \\ l_{\eta n} \end{bmatrix}$$

$$X \equiv \begin{bmatrix} dX_0 \\ dY_0 \\ dZ_0 \\ d\omega \\ d\phi \\ d\kappa \end{bmatrix} \text{ and } A \equiv \begin{bmatrix} a_{12} & a_{13} & \cdots & a_{17} \\ \cdots & & & \cdots \\ a_{n2} & & \cdots & a_{n7} \\ b_{12} & b_{13} & \cdots & b_{17} \\ \cdots & & & \cdots \\ b_{n2} & & \cdots & b_{n7} \end{bmatrix} = \begin{bmatrix} A_{11} & \cdots & A_{16} \\ \cdots & & \cdots \\ A_{(2n)1} & \cdots & A_{(2n)6} \end{bmatrix} \qquad (4.20)$$

The set of Equations (4.18) above can be simplified and written in a matricial form as:

$$l = A \cdot X \qquad (4.21)$$

From this system of linear equations, we can write the equation of error:

$$V = A \cdot \hat{X} - l. \qquad (4.22)$$

where l are the observations, $\hat{X}$ are the six unknown parameters[1], and V is the correction.

Then, the four unknown parameters $\hat{X}$ can be obtained by writing the condition of minimization:

$$V^T \cdot V = min = (A \cdot \hat{X} - l)^T \cdot (A \cdot \hat{X} - l) = \hat{X}^T A^T A \hat{X} - 2l^T A \hat{X} + l^T l \qquad (4.23)$$

The solution is given by:

$$\frac{\partial}{\partial X}(V^T \cdot V) = 2\hat{X}^T A^T A - 2l^T A = 0 \Rightarrow \hat{X} = (A^T A)^{-1} A^T l \qquad (4.24)$$

$$\qquad (4.25)$$

From this, we can get dX_0, dY_0, dZ_0, $d\omega$, $d\phi$, $d\kappa$ which will give the optimized values for

$$X_0, Y_0, Z_0, \omega, \phi, \kappa \text{ using } \hat{X} = C_0^{vrai} - C_0^{approx} \Rightarrow C_0^{vrai} = \hat{X} + C_0^{approx}. \qquad (4.26)$$

A MATLAB program has been developed in order to do these calculations. Initial approximate values must be entered, then this calculus is iterated until the values of X_0, Y_0, Z_0, ω, ϕ, κ do not vary anymore (until the 6th significative number, which is arbitrarily chosen).

---

1. X corresponds to the exact values of the parameters and $\hat{X}$ to the values as determined by the least square methods.

4. 2. 5. Testing programs

Two testing programs were written and used to do a first test of the values obtained for different system parameters, namely: the interferometric parameters and the camera interior and exterior orientation parameters. They were particularly useful to detect the origin of errors when developping the calibration procedures, and also when calculating the object-coordinates of the system. Indeed, as seen above there are fifteen parameters describing the system (6 for the projection head and 9 for the camera), and when the object-coordinates of the calibration points computed using Equations (4.5) are clearly wrong compared to the reference values measured with the theodolite, it is difficult to find the source of errors. These programs help us to determine if the errors arise because of the interferometric parameters or because of the camera parameters. The correction is thus easier.

The testing program for the interferometric parameters is based on the interferometric equation (first equation in the set of Equations (4.3)). Basically, theoretical values of the phase are computed at the calibration points using this equation and the interferometric parameters determined using the calibration procedure described in Section 4.2.2. Then, they are compared to the value of the phase measured at the calibration, according to:

$$d\varphi = \varphi^{calculated} - \varphi^{measured} \tag{4.27}$$

Similarly, the testing program for the camera parameters is based on the two last equations of the set (4.3). After calibration of the camera (interior and exterior orientation parameters), the planimetric object coordinates (x and y) are computed at the calibration points using these two equations and the altimetric object-coordinate z measured by theodolite. Then, the computed values of the planimetric object coordinates (x and y) are compared to the reference values of the planimetric object coordinates (x and y) given by the theodolite. This gives planimetric deviations d_x, d_y and d_{xy} that are similar to the planimetric deviations defined in Section 3.1; Chapter 3.

These phase and planimetric deviations allow us to detect whether the errors come from the interferometric or the camera parameters, or both.

4. 3. Summary of the measurement and calibration procedures

The object-coordinates of the points measured are computed using the general method and the calibration procedures presented in Section 4.1 and 4.2 respectively. In order to give a global view of the developments done above, Figure 4.9 (complementary to Figure 4.3) sums-up the different procedures necessary before being able to calculate the object-coordinates (x, y, z) of each measured point. As illustrated, the data acquisition 4.9(a) involves on the one hand fringe projection (by the projection head); image acquisition by the CCD camera, phase shifting procedure, and measurements using the theodolite (position of calibration points, of the camera and of one of the two point sources). On the other hand it involves a program (e.g. Photomodeler^{TM}) for measuring and determining data relative to the parameters describing the virtual camera (presented in Section 4.2.3), and the experimenter for performing all the

measurements. Most of the procedures carried out by the user can be automated using appropriate programs.

The data acquisition 4.9(a) leads to the production of raw data, namely: the wrapped phase map; the object-coordinates of the reference points, of the perspective center, and of one of the two light sources S1,S2 in the theodolite's referential; the interior orientation parameters (ξ_0, η_0, c); the image size (in millimeters and in pixels); the pixel positions (i, j) of the calibration points on images of the measured object; and a first approximation of the angles of the rotation matrix (ω, κ, ϕ).
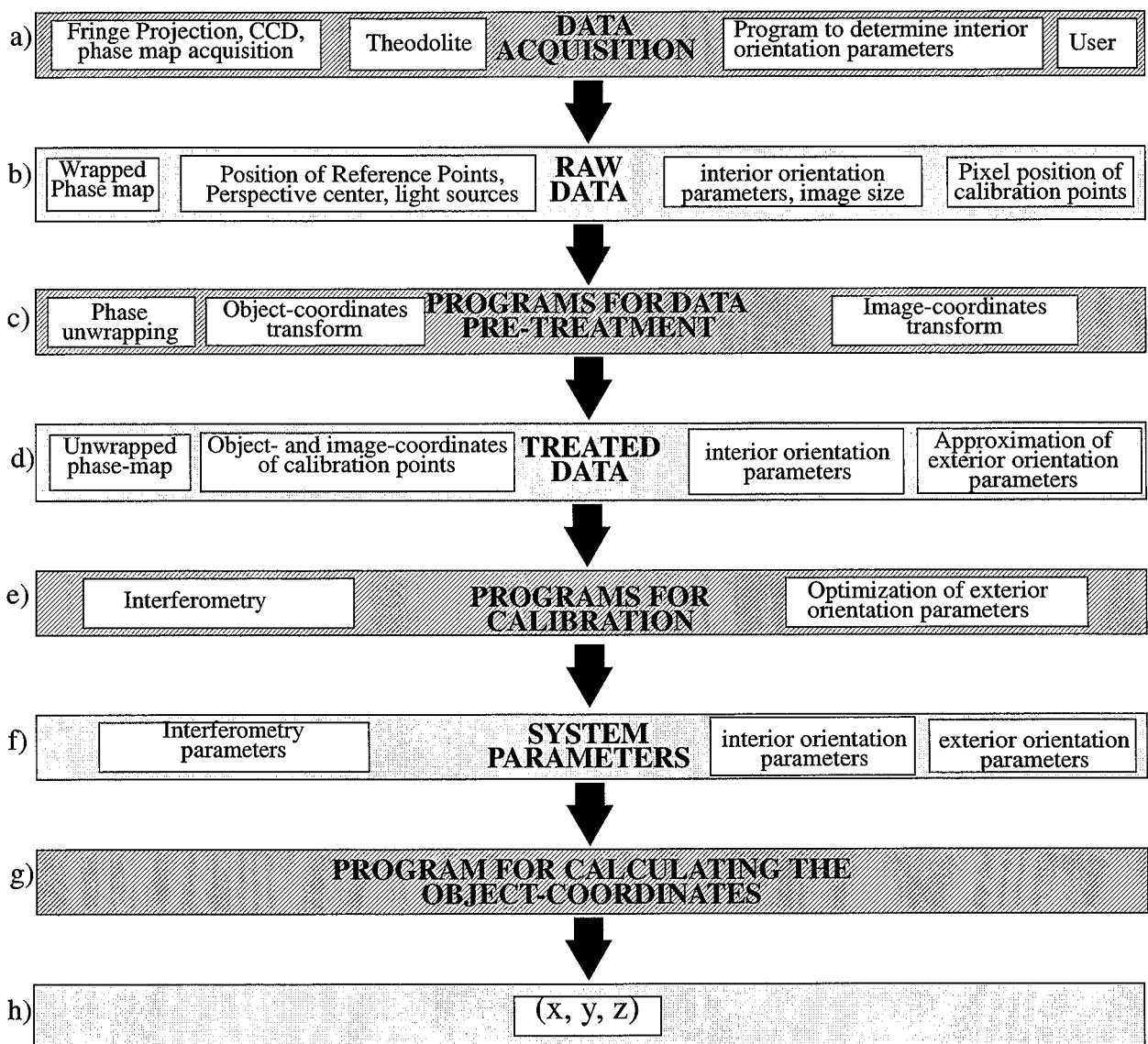
Figure 4. 9: Diagram giving a global view of the different steps necessary to apply the general method developed in the frame of this work

The raw data are supplied as illustrated in Figure 4.9(c) to programs for data pre-treatment, as illustrated in Figure 4.5(a). These programs carry out the phase unwrapping procedure and the transformation of the raw data (Section 4.2.1).

All this produces treated data as indicated in Fig. 4.9(d), namely the unwrapped phase map, the object- and image-coordinates $((x, y, z)$ and (ξ, η), respectively) of the calibration points, a first approximation of the perspective center position (X_0, Y_0, Z_0), and the coordinates (R_x, R_y, R_z) of one of the point sources S1, S2.

As illustrated in Fig. 4.9(e), the treated data is processed by programs for calibration determining the missing system parameters, namely: the interferometric parameters (r_x, r_y, r_z) and optimized values of the exterior orientation parameters $(X_0, Y_0, Z_0, \omega, \kappa, \phi)$. The calibration procedure used to determine all these parameters were presented in Section 4.2. At this stage, Fig. 4.9(f), all the system parameters are known: the interferometric parameters: $R_x, R_y, R_z, r_x, r_y, r_z, \lambda$, and the interior and exterior orientation parameters of the camera: $\xi_0, \eta_0, c, X_0, Y_0, Z_0, \omega, \kappa, \phi$.

Lastly, as indicated at Fig. 4.9(g) and 4.9(h), these parameters are used in programs based on the set of Equations (4.5) to determine the object-coordinates (x,y,z) of all the measured points of the object, and eventually to produce a quantitative 3D representation of the object.

4. 4. Application of the new data treatment method to the measurement of different objects

Similarly to what was done in Chapter 3, and for comparison, two objects are measured in order to do a first evaluation of the general method presented in this chapter: the wall and the aluminum plate in vertical and inclined positions. The measurement conditions, and hence the measured phase map, the object- and image-coordinates of the calibration points are the same as the ones considered in Chapter 3 (see Section 3.1.1) for further details). Only the data treatment procedure is changed here: we use the general method described in this chapter instead of LS1, DPH or LS2. In addition, the same evaluation procedure already described in Section 3.1.2; Chapter 3 is also used here. It is carried out at the nine reference points (used here as control points) previously measured with the theodolite and the comparison with the computed values are done using the same planimetric and altimetric deviations.

The results for the wall is presented in Section 4.4.1, and give an evaluation of the general method on planar objects parallel to the imaging plate of the camera. The results for the aluminium plate in vertical and inclined positions are presented in Sections 4.4.2 and 4.4.3, respectively. They give a first evaluation of the method's. In addition, they allow to assess the behavior of the method when the planar object is not parallel to the imaging plane of the camera.

4. 4. 1. Planar object parallel to the imaging plane of the camera: the wall

The first object measured is the wall. The object-coordinates of its calibration points as determined using the theodolite are given in Section 3.1.1; Chapter 3. The parameters of the measurement system (interferometric and camera orientation parameters) were determined using

the calibration procedures described in Section 4.2, and all nine calibration points (reported in Section 3.1; Chapter 3). We obtained the interferometric parameters: $r_x = -62.32 \cdot 10^{-3}$ mm, $r_y = 2.49 \cdot 10^{-3}$ mm, $r_z = 187.35 \cdot 10^{-3}$ mm. As for the interior orientation parameters, we found: $\xi_0 = -57.1 \cdot 10^{-3}$ mm; $\eta_0 = -106.2 \cdot 10^{-3}$ mm; $c = 7.66$ mm. Finally, the exterior orientation parameters are computed, and after 6 iterations we have: $X_0 = -4.69$ mm; $Y_0 = -20.71$ mm; $Z_0 = 3411.38$ mm; $\omega = -3 \cdot 10^{-3}$ rad; $\phi = -6.19 \cdot 10^{-3}$ rad; $\kappa = -2.78 \cdot 10^{-3}$ rad.

These values were tested with the testing programs described in Section 4.2.5, and the results are presented in Tables 4.1 and 4.2. The absolute values of the phase deviations $d\varphi$ are lower than 1 *rad* and range between *0.12* and *0.7 rad*. These values are commonly obtained in this work for other measurement (as shown by the experiment, values higher than 1 *rad* generally indicate a problem with the interferometric parameters). The phase deviations obtained seem to be random with no systematic in the determination of their value or sign. At this stage, nothing special can be said about them. These small deviations are probably due to the random errors in the measured phase map. They can be decreased by acquiring several phase maps and averaging them, for example.

	$\varphi^{measured}$ [rad]	$\varphi^{calculated}$ [rad]	$d\varphi$ [rad]
P10	321.64	321.95	0.31
P20	485.69	485.24	-0.45
P30	745.78	745.81	0.03
P40	324.07	324.02	-0.05
P50	487.04	487.60	0.54
P60	765.07	764.95	-0.12
P70	328.59	328.72	0.13
P80	489.20	488.50	-0.70
P90	743.08	743.44	0.35

Table 4. 1: Comparison between the phase values measured and calculated using the first equation in (4.4) (interferometry equation)

The camera orientation parameters are evaluated similarly (see Section 4.2.5), and the resulting deviations are presented in Table 4.2. The planimetric deviation $|d_{xy}|$ ranges from 1.34 to 9.53. Its origin is probably due to the same cause already considered in Chapter 3.2: the relatively low spatial resolution of the camera and the lens distortions. It is interesting to see that lens distortion remains in spite of the determination of its parameters by Photomodeler^{TM}. The calibration procedure is probably not precise enough, and it should be optimized in the future.

Finally, the object-coordinates are computed using the system of Equations (4.5) and the different deviations are then calculated (see Section 3.1; Chapter 3). For convenience, the values found are placed in Appendix E, Table 29.They are represented in Figure 4.10.

	x (mm)	y (mm)	d_{xy} (mm)	d_x (mm)	d_y (mm)
P10	-960.80	839.60	1.34	1.20	0.6
P20	41.87	841.46	9.53	-1.13	9.46
P30	1247.33	831.00	6.01	-5.67	-1.99
P40	-991.88	11.35	2.51	2.11	1.35
P50	-1.62	0.96	1.88	-1.62	0.96
P60	1261.61	-11.95	3.61	3.61	0.04
P70	-969.27	-889.5	5.75	5.72	-0.50
P80	-0.67	-855.87	7.89	-0.67	-7.87
P90	1180.37	-889.15	4.22	-3.63	-2.15

Table 4. 2: Comparison between the spatial coordinates (x, y) measured and calculated using the two last equations in (4.4) (central perspective equations)
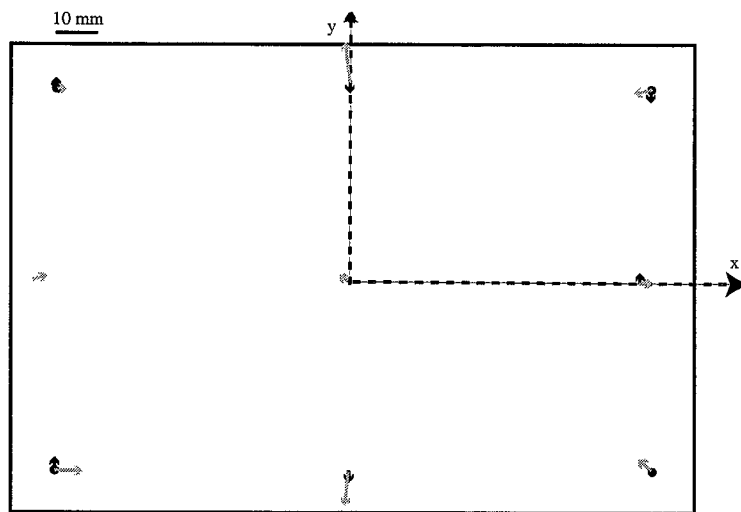
Figure 4. 10: Diagram of the z- and the in-plane deviations (resp. black arrows and grey arrows) for the wall using the general method. When the z-deviation is positive, the arrows point up, and vice versa. When the value of the deviation is smaller than 2 mm, it is not represented.

We observe that the total deviation d ranges between 2.59 and 10.52 mm (mean: *5.36 mm*; standard deviation: *3.07 mm*), the absolute value of the altimetric deviation d_z ranges from 0.72 mm to 3.85 mm (mean: 2.14; standard deviation 1.03 mm). The planimetric deviation d_{xy} varies from 1.73 to 6.41 mm (mean: 3.8 mm; standard deviation: 1.8 mm), d_x varies from 0.67 to 6.82 mm (mean: 2.77 mm; standard deviation: 1.92 mm) and d_y varies from 0.04 mm to 10.13 mm (mean: 2.81 mm; standard deviation: 3.79 mm).

For most of the points, $|d_z| < |d_{xy}|$ which means that the main contribution to the error in computing the coordinates of the points comes from the planimetric object-coordinates determination. Furthermore, for each point, the values of $|d_{xy}|$ obtained by x and y calculated with the solutions of the non-linear equations system (4.5) are of the same order of magnitude as the values of $|d_{xy}|$ obtained when calculating x and y with the central perspective equations (4.1), as can be seen by looking at Tables 4.2 and Figure 4.10. Thus, we can say that the behavior of the spatial distances being calculated using the solution of Equations (4.3) is similar to the one being calculated using the central projection equations (4.1). This indicated to us to think that the x and y expressions determined by using Equations (4.5) are more influenced by the parameters of the central projection, than by the phase (or equivalently by the optical parameters r_x, r_y, r_z). This was not obvious just by looking at the expressions displayed in the Appendix D. These deviations can be explained by residual lens distortions that could not fully be corrected by the lens distortion terms considered.

No similar link is observed between the depth distance d_z (calculated by the method developed in this chapter) and the phase deviations (calculated using the phase equation) when comparing Tables 4.1 and Figure 4.10.
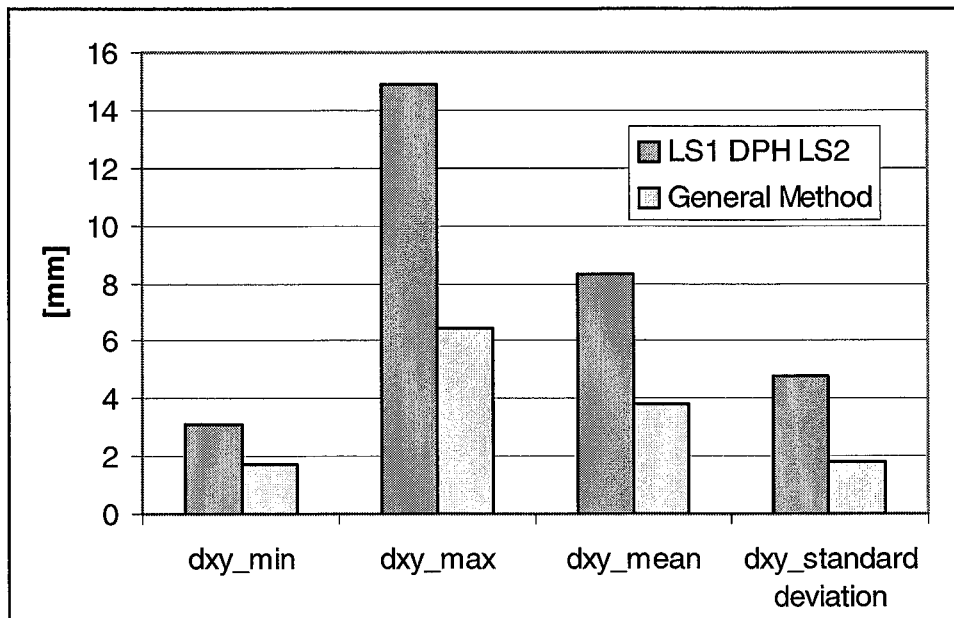
Figure 4. 11: Comparison of the planimetric deviations obtained for the wall by the four different methods: LS1, DPH LS2, and the general method.
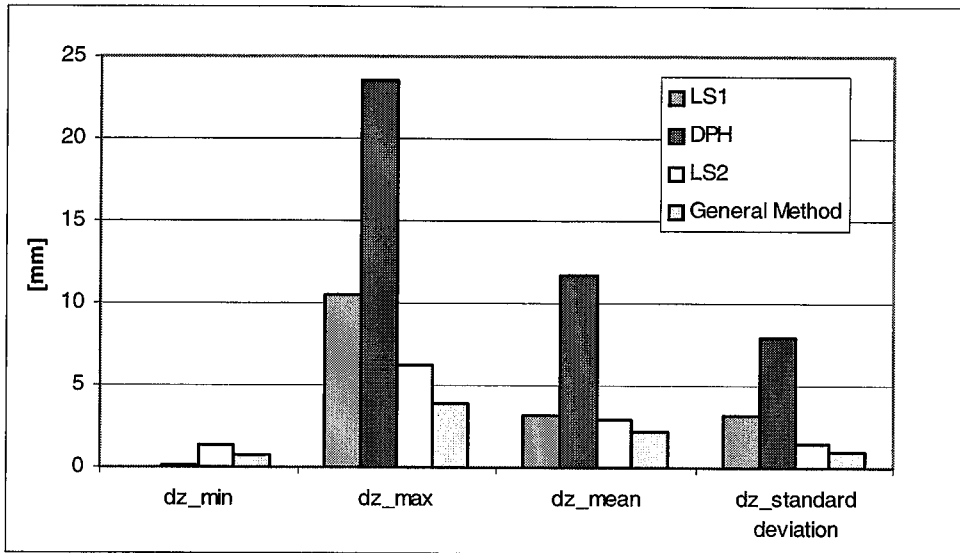
Figure 4. 12: Comparison of the altimetric deviations obtained for the wall by the four different methods: LS1, DPH LS2, and the general method.

In general, these values are slightly better than what was found for the wall using the first and second least squares methods LS1 and LS2 in Chapter 3; section 3.2.

4. 4. 2. First evaluation of the system precision: aluminium plate in vertical position

In this section, similarly to what has been done for the previous methods (LS1, DPH and LS2) in Section 3.3, Chapter 3, we used the aluminium plate in the vertical position to do a first evaluation of the general data treatment method presented in this chapter, in terms of precision. The measurement was repeated twenty times (the camera and projection head are moved each time) on the aluminium plate in the vertical position which is maintained immobile. The object coordinates of the calibration points as well as the planimetric, altimetric and total deviations were computed for each of the twenty measurement. Then, the means and standard deviations were calculated. This procedure is described in more details in Section 3.3, Chapter 3.

The results are represented in Figure 4.13. For convenience, the object-coordinates of the nine reference points considered are reported in Tables 30 and 31 in Appendix E. The results were calculated for the parameters using 5 calibration points, and are displayed in Figures 4.13 to 4.15. The same trends as those obtained for the wall were observed. In particular, the same order of magnitude is observed for the total deviation d ranging from 1.57 to 7.52 mm (mean: 4.41 mm; standard deviation: 2.12 mm); the absolute value d_z altimetric deviation ranges between 0.12 mm and 2.26 mm (mean: 1.01; standard deviation: 0.72 mm); the planimetric deviation d_{xy} ranges between 1.42 and 7.52 mm (mean: 4.21 mm; standard deviation: 2.18 mm); the absolute value d_x of the x-deviation ranges from 0.18 to 4.71 mm (mean: 2.48 mm; standard deviation: 1.45 mm) and finally, the absolute value d_y of the y-deviation ranges between 0.11 to 7.52 mm (mean: 2.59

mm; standard deviation: 1.45 mm). The planimetric deviation d_{xy} has a higher contribution to d than d_z since $|d_{xy}| > |d_z|$ for most of the points when considered one by one. The altimetric deviation d_z being generally small implies that the values of z are close to real values and that systematic errors on the determination of z are small. The arrow pattern has a radial distribution, which shows that as in the case of the wall, there are radial lens distortions, as already observed in Section 3.2.1, Chapter 3.
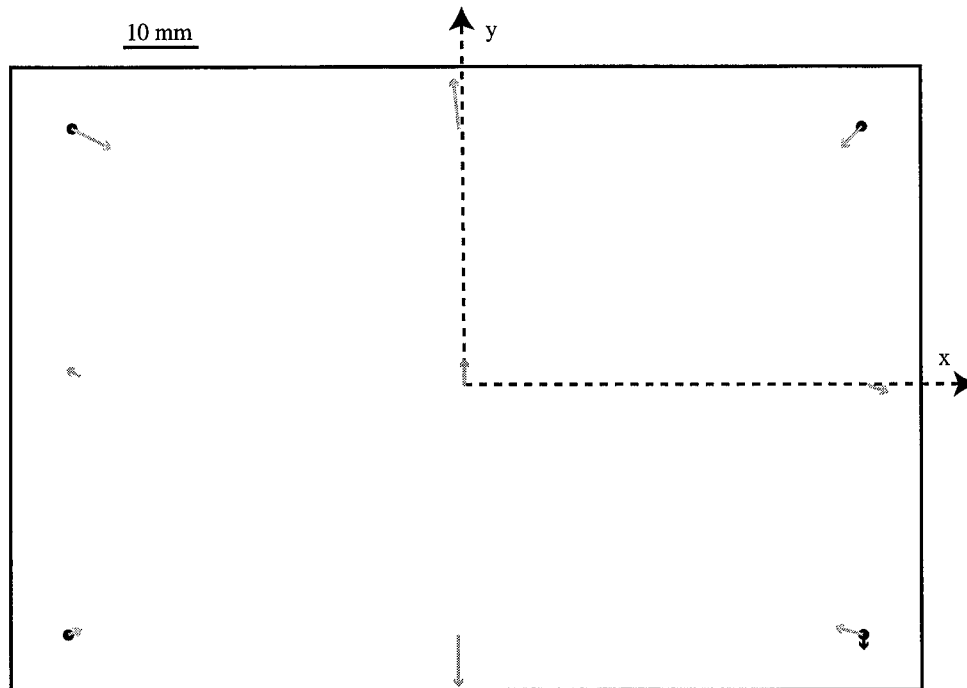
Figure 4. 13: Diagram of the z- and the in-plane deviations (resp. black arrows and grey arrows) for the plate in vertical position using the general method. When the z-deviation is positive, the arrows point up, and vice versa. When the value of the deviation is smaller than 2 mm, it is not represented.

The values observed here for d and d_{xy} are smaller than those found by LS1 and LS2 (approximately divided by two). As for the altimetric deviation d_z, their absolute values are even dramatically better compared to the previous methods: they are six times smaller than those found by LS1 and two times smaller than those found for LS2, as shown by Figure 4.15. Comparing the results of this method and the LS1 and LS2, we can say that the general method gives the best results.

Figure 4. 14: Comparison of the planimetric deviations obtained for the aluminum plate in vertical position by the four different method: LS1, DPH LS2, and the general method.

Figure 4. 15: Comparison of the altimetric deviations obtained for the aluminum plate in vertical position by the four different method: LS1, DPH LS2, and the general method.

4. 4. 3. Planar object not parallel to the imaging plane of the camera: the inclined aluminium plate

As done in Section 3.4; Chapter 3, we wish to see how the general method developed in this chapter works with objects that are planar, but not parallel to the imaging plane of the camera. For that purpose, we use the aluminium plate rotated by about 10° relative to the vertical position. The measurement method and evaluation procedures as well as the measured phase map are the same as those used in Chapter 3 (see Sections 3.1 and 3.4). The only thing that changes here is the data treatment method applied to extract the height information from the measured phase map. The calibration of the interferometric parameters on the one hand, and of the exterior orientation parameters on the other hand was done using all nine reference points. The object-coordinates of the calibration points as determined using the theodolite are given in Section 3.1.1; Chapter 3. The parameters of the measurement system (interferometric and camera orientation parameters) were determined using the calibration procedures described in Section 4.2, and all nine calibration points (reported in Section 3.1; Chapter 3). We obtained the interferometric parameters: $r_x = -60.16 \cdot 10^{-3}$ mm, $r_y = 2.21 \cdot 10^{-3}$ mm, $r_z = 187.82 \cdot 10^{-3}$ mm. As for the interior orientation parameters, we found: $\xi_0 = -57.1 \cdot 10^{-3}$ mm; $\eta_0 = -106.2 \cdot 10^{-3}$ mm; $c = 7.66$ mm. Finally, the exterior orientation parameters are computed, and after 6 iterations we have: $X_0 = -10.20$ mm; $Y_0 = -140.74$ mm; $Z_0 = 2945.56$ mm; $\omega = 0.55 \cdot 10^{-3}$ rad; $\phi = 45.29 \cdot 10^{-3}$ rad; $\kappa = 1.06 \cdot 10^{-3}$ rad.

We observe that the total deviation d ranges from 1.74 to 6.54 mm (mean: 3.92 mm; standard deviation: 1.82 mm); the absolute value of the altimetric deviation d_z ranges from 0.11 to 1.37 mm (mean: 0.88 mm; standard deviation:0.42 mm); the planimetric deviation d_{xy} ranges from 1.74 mm to 6.42 mm (mean:3.80 mm; standard deviation: 1.80 mm); the absolute value x-deviation d_x ranges from 0.42 mm to 5.17 mm (mean: 2.44 mm; standard deviation:1.75 mm); the absolute value of the y-deviation d_y ranges from 0.96 mm to 6.21 mm (meand: 2.51 mm; standard deviation:1.64 mm).These values are represented in Figures 4.16 to 4.18, and the values are reported in Table 32 in Appendix E.

These orders of magnitude are the same as for planar objects (wall and aluminium plate) parallel to the imaging plane of the camera. This shows that this method is not "disturbed" by the general shape of objects or the system configuration, as is the case for LS1, DPH and LS1. Furthermore, $d_{xy} > d_z$ and thus the higher contribution to the total error comes from the determination of planimetric object-coordinates x and y. This is probably because of the limited spatial resolution of the camera used here and to residual lens distortions.

In addition, when comparing the deviations, one by one (total, altimetric, planimetric, x- and y deviations, for each point, the general method presented in this chapter is better than the LS2 method (the best one for the rotated plate, as seen in Section 3.4, Chapter 3). This shows that the LS2 method is mainly limited by the poor quality of the camera model (scaling transformation), when considering non-planar objects.
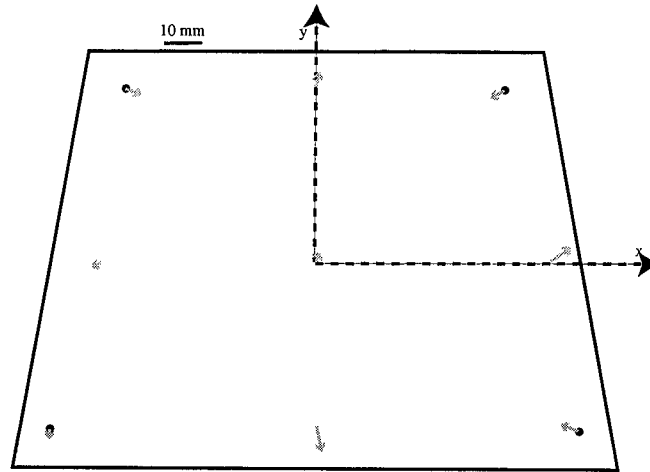
Figure 4. 16: Diagram of the z- and the in-plane deviations (resp. black arrows and grey arrows) for the inclined plate using the general method. When the z-deviation is positive, the arrows point up, and vice versa. When the value of the deviation is smaller than 2 mm, it is not represented.
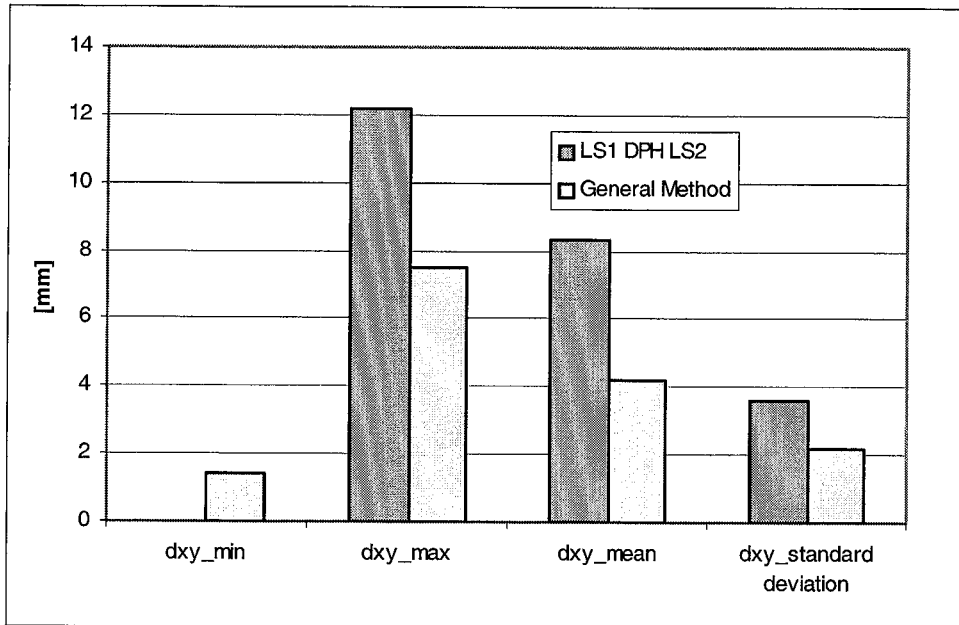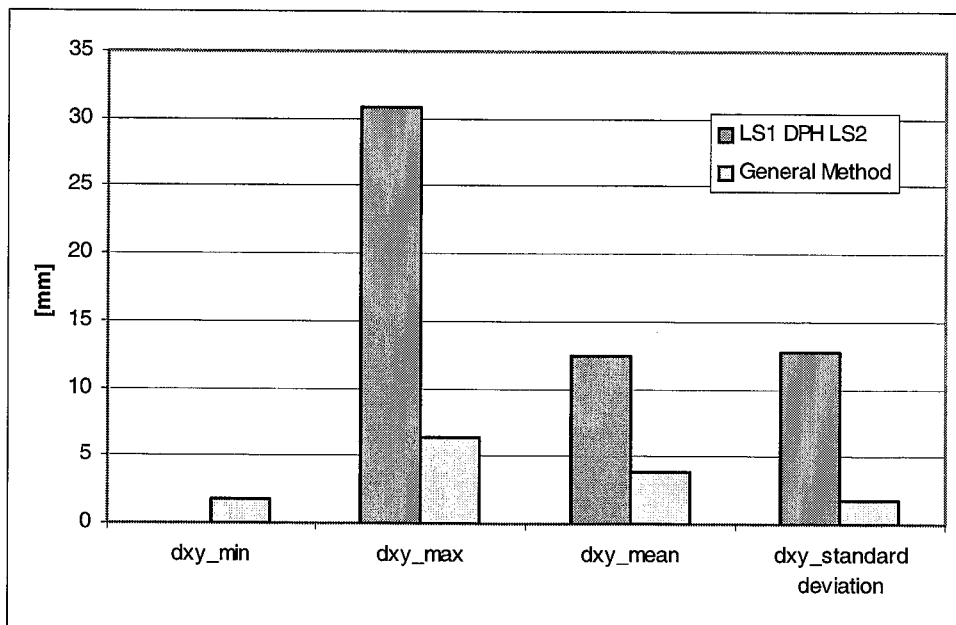

Figure 4. 17: Comparison of the planimetric deviations obtained for the inclined aluminum plate by the four different methods: LS1, DPH LS2, and the general method.
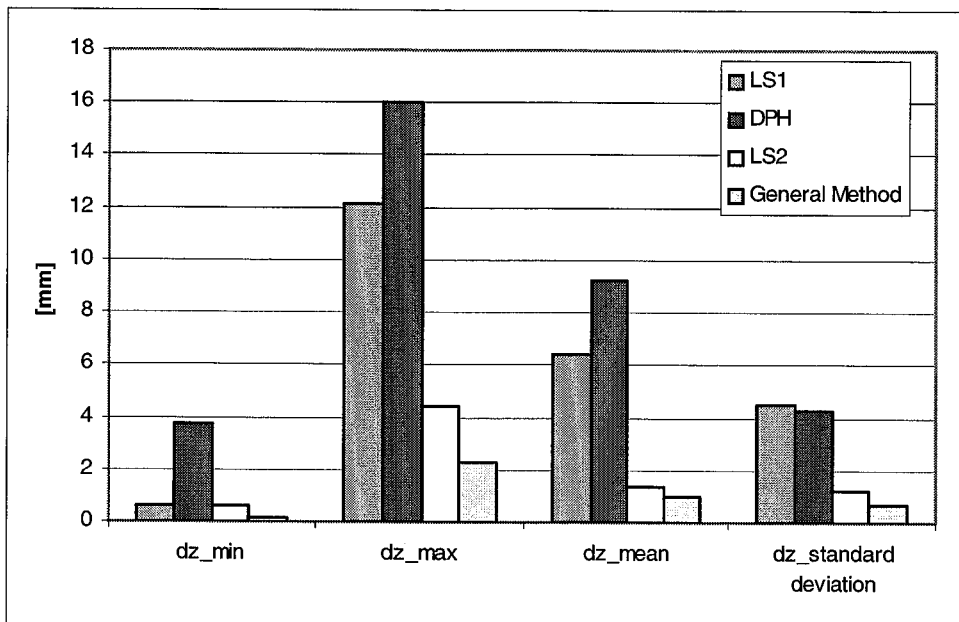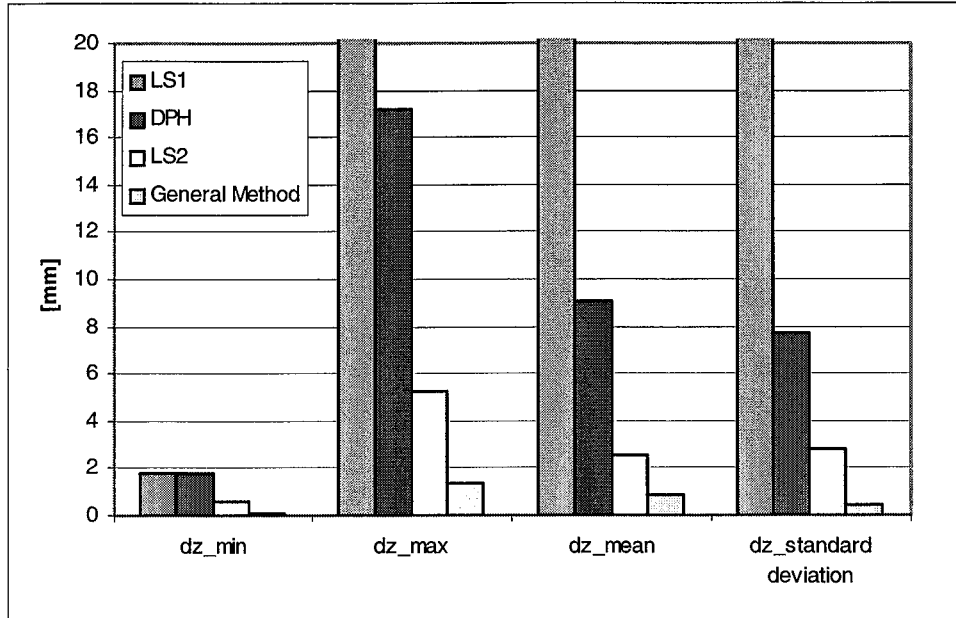
Figure 4. 18: Comparison of the altimetric deviations obtained for the inclined aluminum plate by the four different method: LS1, DPH LS2, and the general method.

4. 5.   Discussion

A new theoretical approach, as well as calibration procedures have been developed, in order to interpret the phase-map of large objects and extract the desired shape information. Its feasibility has been demonstrated and the first results obtained here show that this method is better than the ones previously developed (LS1, and LS2 for objects of general shape). The orders of magnitude found here range within millimeters, and in general, $|d_z| < |d_{xy}|$, which shows that the contribution to overall errors come from d_{xy} rather then from d_z. This, together with the fact that d_{xy} found by the general method is of the same order of magnitude as d_{xy} calculated using the testing procedures (see Section 4.2.5), implies that d is more influenced by the orientation parameters of the camera than by the value of the phase.

As for the testing procedure for the phase, we see that usually, $|d\varphi| < 1 rad$, however until now, no conclusions can be made about the relation between the values found for $d\varphi$ and the calculated z.

This method is general and not limited by the configuration of the measurement system with regard to the object or the shape of the object. It can be considered as a generalization of the others methods. In addition, it is not limited to large objects, but can also be applied for measuring the shape of small ones, provided that the interferometric hypothesis for using the interferometric equation is still valid. Otherwise it should be replaced by Equation (1.8) in the set of Equations (4.5).

Examples of measurement for objects of different shapes and with different measurement configurations of the system are presented in the next chapter.

4. 6.   References

1. Kraus K. and Waldhäusel P., *Manuel de Photogrammétrie*. 1998, Hermès, Paris
2. Beyer H., *Geometric and Radiometric Analysis of a CCD-Camera Based Photogrammetric Close-Range System*, in *Institut für Geodäsie und Photogrammetrie*. 1992, ETHZ: Zürich. p. 186.
3. Schreiber W. and Notni G., *Theory and arrangements of self-calibrating whole-body three-dimensional measurement systems using fringe projection technique*. Optical Engineering, 2000. **39**(1), p. 159-169.

CHAPTER 5

Examples of measurements: enhanced flexibility of the method

In Chapter 4 a new method allowing to extract the shape information from the phase map of large objects has been presented. Its feasibility has been shown and a first evaluation of its accuracy has been done. In addition, not only this method offers the possibility to measure plane object that are parallel to the imaging plane of the camera, but also those that are not.

In this chapter, the aim is to see more applications of this general method in terms of surface shape, system configurations and object deformation. It will be the occasion to see some of the new possibilities it offers as well as some of its limitations. The same presentation pattern will be used for all the measurements: a short description of the measurement, tables with object coordinates of the reference points as measured with the theodolite, and as calculated by the method exposed in Chapter 4. For a matter of clarity, the "intermediate" tables with the results of calibration evaluation are placed in the Appendix F.

5. 1.   Measurement of objects of general shape

In this section, we will consider objects of various shapes and made out of different materials.

5. 1. 1.   The windsurf board

- **Description of the measurement:**
    The windsurf board (3.2 x 1 m) is fixed vertically on the wall, as displayed by Figure 5.1. The camera is placed roughly parallel to the object, at a distance of about 3 m. The projection head

is positioned 6 m away on the right side, making a projection angle of about 60°, with regard to the observation direction. Eight retroreflective targets are fixed on the surface and define the reference points. Their position is measured with the theodolite, and they are used either as calibration either as control points. Then a fringe projection measurement is performed in order to capture the windsurf-board phase-map. Knowing the object- and image-coordinates of the reference points as well as the phase at their position allows us to calibrate the system parameters (the measurement procedure is described in more details in Section 3.1, Chapter 3).

After calibration, the following values are found:

*The interferometric parameters: $r_x = -0.060$ mm; $r_y = 0.002$ mm; $r_z = 0.188$ mm.

*The exterior orientation parameters: $X_0 = -364.27$ mm; $Y_0 = 103.65$; mm;

$Z_0 = 3278.27$ mm; $\omega = -4.94 \cdot 10^{-3}$ rad; $\phi = -32.16 \cdot 10^{-3}$ rad; $\kappa = 0.78 \cdot 10^{-3}$ rad found after 6 iterations and using the 8 calibration points.

*The interior orientation parameters used were: $c = 7.66$ mm, $\xi_0 = -0.057$ mm, $\eta_0 = -0.106$ mm

• **Comments on the results:**

As shown by Table 5.2, $0.71mm < |d| < 3.99mm$, $0.04mm < |d_z| < 1.11mm$, $0.67mm < |d_{xy}| < 3.81mm$. This is better than the values obtained for the wall and plate measured in the preceding chapter, probably because the reference points are quite centered here, and don't undergo the barrel distortion observed on P20 and P80 in both preceding examples. Of course, it is also better than results obtained by the least square methods exposed in chapter 2 and 3, for which the windsurf-board results were placed in Appendix B. Here, $|d_z| < |d_{xy}|$ for all the points, which indicates that in this measurement, the resolution is limited by the relatively low spatial resolution of the camera.
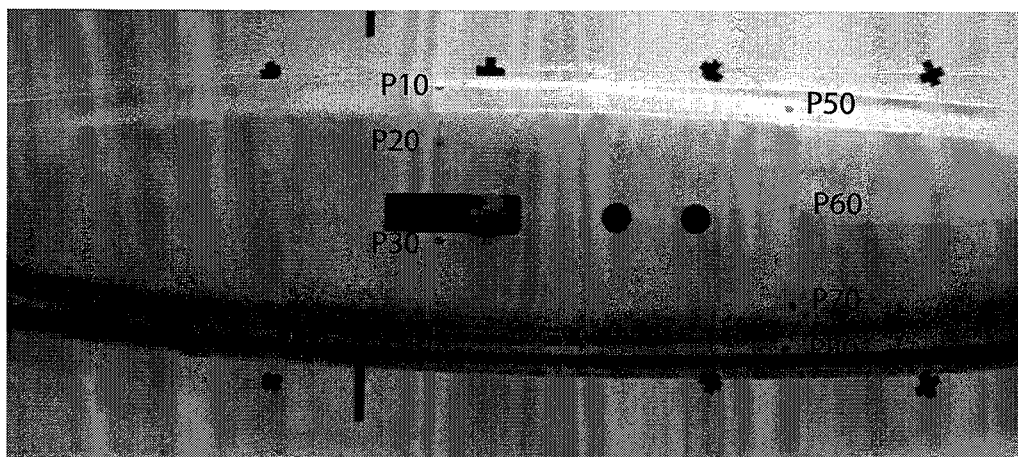
Figure 5. 1: Picture of the windsurf board fixed on the wall, and of calibration points

	$x_{theodolite}$ [mm]	$y_{theodolite}$ [mm]	$z_{theodolite}$ [mm]
P10	-432	330.5	-7
P20	-427	188.5	69
P30	-427	-46.5	75
P40	-417	-316.5	-15
P50	429	277.5	15
P60	423	35.5	88
P70	428	-206.5	59
P80	424	-323.5	-7

Table 5. 1: Windsurf-board. Object-coordinates of the reference points as measured with the theodolite

	x (mm)	y (mm)	z (mm)	d (mm)	d_z (mm)	d_{xy} (mm)
P10	-433.20	330.21	-6.77	1.25	-0.23	1.23
P20	-425.14	188.93	68.026	2.14	0.98	1.90
P30	-428.08	-44.24	75.27	2.52	-0.23	2.51
P40	-416.55	-318.07	-14.41	1.73	-0.59	1.63
P50	428.84	278.15	14.77	0.71	0.23	0.67
P60	421.23	33.78	87.96	2.47	0.04	2.47
P70	429.04	-209.78	58.08	3.57	0.92	3.45
P80	424.95	-319.78	-5.90	3.99	1.11	3.81

Table 5. 2: Windsurf board. Object-coordinates, total, altimetric and planimetric deviations as calculated using the method described in Chapter 4.

5. 1. 2. Car part

• **Description of the measurement:**

The car part (1.5 x 1 m) is fixed vertically on the wall, as displayed by Figure 5.2. The camera is placed roughly parallel to the object, at a distance of about 3 m. The projection head is positioned 6 m away on the right side (R_x = 4680.4 mm, R_y = -11.50 mm, R_z = 3015.4 mm), making a projection angle of about 60°, with regard to the observation direction. Eight

retroreflective targets are fixed on the surface and define the reference points. Their position is measured with the theodolite, and they are used either as calibration either as control points. Then a fringe projection measurement is performed in order to capture the car part phase-map. Knowing the object- and image-coordinates of the reference points as well as the phase at their position allows us to calibrate the system parameters (the measurement procedure is described in more details in Section 3.1, Chapter 3).

After calibration, the following values are found:

*The interferometric parameters: $r_x = -0.110\ mm$; $r_y = 0.009\ mm$; $r_z = 0.185\ mm$.

*The exterior orientation parameters: $X_0 = -55.89\ mm$; $Y_0 = -53.85$; mm; $Z_0 = 2535.5\ mm$; $\omega = 0.0015\ rad$; $\phi = -0.0095\ rad$; $\kappa = -0.0014\ rad$ found after 6 iterations and using the 8 calibration points.

*The interior orientation parameters used were: $c = 7.66\ mm$, $\xi_0 = -0.057\ mm$, $\eta_0 = -0.106\ mm$

• **Comments on results:**

As shown by Table 5.4, $0.31mm < |d| < 3.91mm$, $0.07mm < |d_z| < 1.11mm$, except for P10 where d = 57.55 mm, which is large. By looking at Table 30 in Appendix F displaying the spatial coordinates as calculated using the central perspective equations, we see that the value found for P10 is similar to the one found above. The most probable explanation for this is an error in determining the image coordinates of P10. This is further confirmed by the coincident high value of $d\phi$ at P10, as shown by Table 29 in Appendix F.
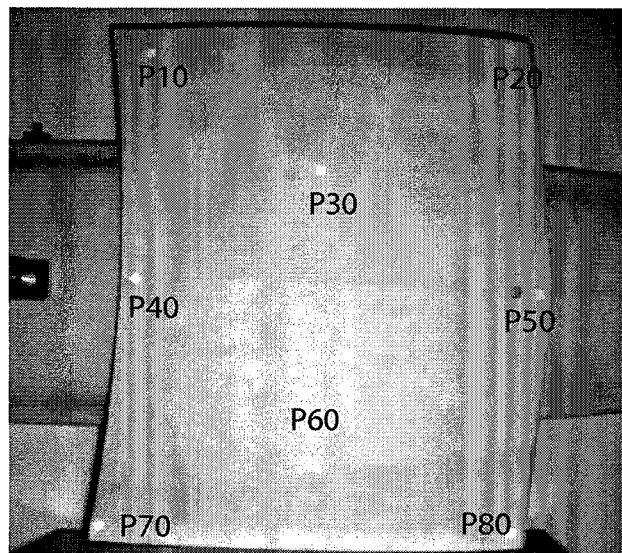
Figure 5. 2: Picture of the car part and of reference points

	$x_{theodolite}$ [mm]	$y_{theodolite}$ [mm]	$z_{theodolite}$ [mm]
P10	-374	553.50	49
P20	393	543.50	122
P30	-39	262.50	118
P40	-455	18.50	107
P50	455	-18.50	108
P60	-74	-238.50	154
P70	-541	-548.50	113
P80	377	-548.50	195

Table 5. 3: Car part. Object-coordinates of the reference points as measured with the theodolite.

	x (mm)	y (mm)	z (mm)	d (mm)	d_z (mm)
P10	-431.43	550.53	51.21	57.55	2.21
P20	391.77	541.68	120.84	2.48	1.16
P30	-39.76	265.82	118.07	3.41	0.07
P40	-455.41	19.77	106.79	1.35	0.21
P50	456.651	-18.19	109.54	2.28	1.54
P60	-74.13	-242.27	152.95	3.91	1.05
P70	-539.78	-547.52	114.11	1.91	1.11
P80	376.83	-548.33	194.81	0.31	0.19

Table 5. 4: Car part. Object-coordinates, total, altimetric and planimetric deviations as calculated using the method described in Chapter 4.

5. 2. Measurement with different configurations of the set-up

- **Description of the measurements:**

The aluminium plate is placed vertically and its position is kept fixed for all the following measurements. The projection head position is also kept fixed for all the measurements, at 6 m away on the right side (R_x = 5496.07 mm, R_y = -231 mm, R_z = 2544.2 mm). The measurements were done for different positions of the camera, as displayed by Figure 5.3. Five retroreflective

targets are fixed on the surface and define the reference points. Their position is measured with the theodolite, and they are used either as calibration either as control points. Then a fringe projection measurement is performed in order to capture the phase-map of the aluminum plate. Knowing the object- and image-coordinates of the reference points as well as the phase at their position allows us to calibrate the system parameters (the measurement procedure is described in more details in Section 3.1, Chapter 3).

• **Possibilities and limitations:**

These measurements show the increased flexibility of the system allowing to adapt its configuration to the object under investigation and to the site. One limitation is when the targets are too far from the camera: their visibility decreases, leading to error in the determination of the image coordinates for the calibration points.
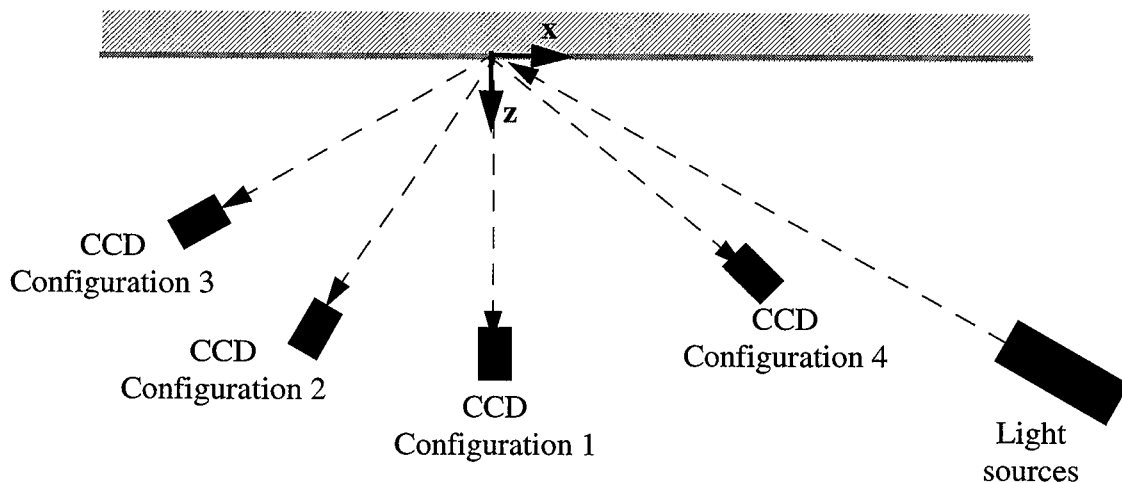
Figure 5. 3: Diagram of the different measurement configurations

5. 2. 1. Configuration 1

• **Camera position:**
  The camera is placed roughly parallel to the object, at a distance of about 3 m.

• **Parameters of the system:**
  After calibration, the following values are found:
  *The interferometric parameters: $r_x = -0.099$ mm; $r_y = 0.005$ mm; $r_z = 0.191$ mm.
  *The exterior orientation parameters: $X_0 = -23.10$ mm; $Y_0 = -206.88$; mm; $Z_0 = 2864.2$ mm;

  $\omega = 0.0163$ *rad;* $\phi = 0.012$ *rad;* $\kappa = 1.21 \cdot 10^{-3}$ *rad* found after 5 iterations and using the 5 calibration points.

*The interior orientation parameters used were: $c = 7.66$ mm, $\xi_0 = -0.057$ mm, $\eta_0 = -0.106$ mm.

• **Results:**

As shown by Table 5.5, $1.83mm < |d| < 2.65mm$, $0.25mm < |d_z| < 1.48mm$.

Figure 5. 4: Configuration 1. Picture of the aluminium plate and of the reference points

Object coordinates...	Point 1	Point 2	Point 3	Point 4	Point 5
... as measured with the theodolite (mm)	x = -1000 y = 472 z = 12	x = 841 y = 605 z = 16	x = 0 y = 0 z = 0	x = -983 y = -610 z = -14	x = 867 y = -761 z = -17
as calculated (mm)	x = -998.22 y = 471.65 z = 11.753	x = 840.86 y = 606.96 z = 16.317	x = 1.6846 y = 0.96301 z = 0.78595	x = -983.91 y = -611.86 z = -13.39	x = 865.1 y = -762.1 z = -18.485
Deviations (mm)	d = 1.83 d_z = 0.25	d = 1.99 d_z= 0.32	d = 2.09 d_z = 0.79	d = 2.16 d_z = 0.61	d = 2.65 d_z = 1.48

Table 5. 5: Configuration 1. Object-coordinates of the reference points as measured with the theodolite and calculated using the method descibed in Chapter 4.

5. 2. 2. Configuration 2

- **Camera position:**

    The camera is placed on the left of the object at a distance of about 3 m and slightly tilted (angle of about 20 °).

- **Parameters of the system:**

    After calibration, the following parameters values are found:

    *The interferometric parameters: $r_x = -0.098$ mm; $r_y = 0.005$ mm; $r_z = 0.192$ mm.

    *The exterior orientation parameters: $X_0 = -1095.9$ mm; $Y_0 = -209.38$ mm; $Z_0 = 2647.4$ mm;

    $\omega = 0.011$ rad; $\phi = -0.331$ rad; $\kappa = 1.62 \cdot 10^{-3}$ rad found after 5 iterations and using the 5 calibration points.

    *The interior orientation parameters used were: $c = 7.66$ mm, $\xi_0 = -0.057$ mm, $\eta_0 = -0.106$ mm

- **Results:**

    As shown by Table 5.6, $3.43mm < |d| < 6.38mm$, $0.20mm < |d_z| < 1.84mm$.
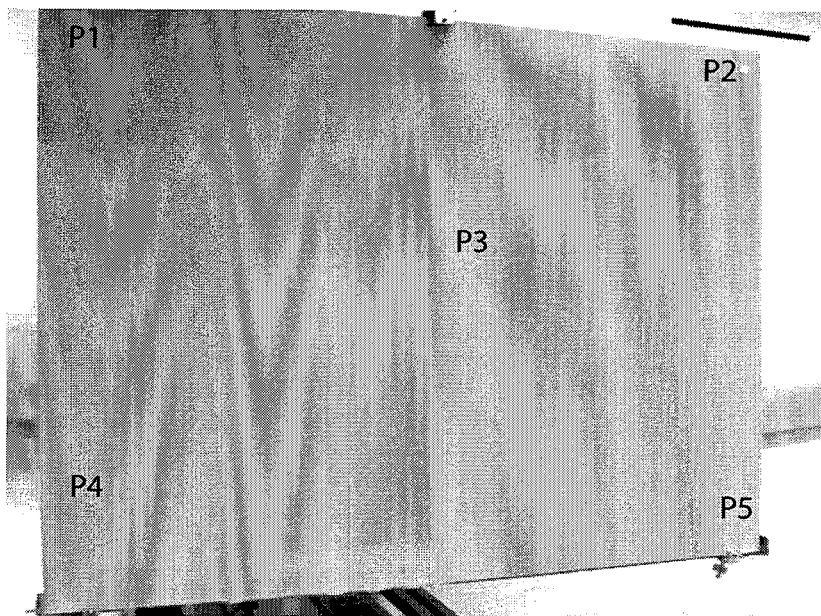
Figure 5. 5: Configuration 2. Picture of the aluminium plate and of the reference points

Object coordinates...	Point 1	Point 2	Point 3	Point 4	Point 5
... as measured with the theodolite (mm)	x = -1000 y = 473 z = 11	x = 841 y = 605 z = 16	x = 0 y = 0 z = 0	x = -983 y = -610 z = -15	x = 867 y = -761 z = -17
... as calculated (mm)	x = -998.17 y = 470.35 z = 9.8094	x = 840.19 y = 604.03 z = 16.52	x = 4.09 y = 4.54 z = 1.84	x = -987.30 y = -610.56 z = -14.80	x = 866.65 y = -759.91 z = -18.16
Deviations (mm)	d = 3.43 d_z = 1.19	d = 1.37 d_z = 0.52	d = 6.38 d_z = 1.84	d = 4.3451 dz = 0.19783	d = 1.62 d_z = 1.16

Table 5. 6: Configuration 2. Object-coordinates of the reference points as measured with the theodolite and calculated using the method described in Chapter 4.

5. 2. 3. Configuration 3

- **Camera position:**

The camera is placed on the left of the object at a distance of about 3 m and tilted with an angle of about 45 °.

- **Parameters of the system:**

After calibration, the following values are found:

*The interferometric parameters: r_x = -0.096 *mm;* r_y = 0.005 *mm;* r_z = 0.192 *mm.*

*The exterior orientation parameters: X_0 = *-2031.5 mm;* Y_0 = *-189.09 mm;* Z_0 = *2026.8 mm;* ω = *0.0024883 rad;* φ = *-0.65798 rad;* κ = *0.000945 rad* found after 12 iterations and using the 5 calibration points.

*The interior orientation parameters used were: c = *7.6622 mm,* ξ_0 = *-0.0571 mm,* η_0 = *-0.1062 mm*

- **Results:**

As shown in Table 5.7, $0.35mm < |d| < 9.76mm$, $0.33mm < |d_z| < 4.43mm$.

In this case, the exterior parameters are more difficult to obtain, as shown by the increased number of iterations.

Figure 5. 6: Configuration 3. Picture of the aluminium plate and of the calibration points

Object coordinates...	Point 1	Point 2	Point 3	Point 4	Point 5
... as measured with the theodolite (mm)	x = -1000 y = 473 z = 11	x = 841 y = 606 z = 17	x = 0 y = 0 z = 0	x = -983 y = -610 z = -15	x = 866 y = -761 z = -16
... as calculated (mm)	x = -1000.1 y = 472.93 z = 10.67	x = 836.43 y = 597.39 z = 16.46	x = 7.48 y = 2.60 z = 4.428	x = -987.73 y = -610.81 z = -14.579	x = 866.71 y = -752.86 z = -15.43
Deviations (mm)	d = 0.35 d_z = 0.33	d = 9.76 d_z = 0.54	d = 9.07 d_z = 4.43	d = 4.81 d_z = 0.42	d = 8.19 d_z = 0.57

Table 5. 7: Configuration 3. Object coordinates as measured with the theodolite and calculated using the method described in Chapter 4.

5. 2. 4.   Configuration 4

- **Camera position:**

    The camera is placed on the right of the object at a distance of about 3 m and tilted with an angle of about 40 °.

- **Parameters of the system:**

    After calibration, the following calibration values are found:

    *The interferometric parameters: r_x = -0.098 mm; r_y = 0.005 mm; r_z =0.191 mm.

    *The exterior orientation parameters: X_0 = 1848.4 mm; Y_0 = -191.15 mm; Z_0 = 2664.5 mm;

    ω = 4.3 · 10^{-3} rad; ϕ = 0.626 rad; κ = 5.37 · 10^{-3} rad found after 8 iterations and using the 5 calibration points.

    *The interior orientation parameters used were: c = 7.66 mm, ξ_0 = -0.057 mm, η_0 = -0.106 mm.

- **Results:**

    As shown in Table 5.8, $2.44m < |d| < 9.68mm$, $1.03mm < |d_z| < 8.59mm$. Here, the exterior parameters are more difficult to obtain, as shown by the increased number of iterations.
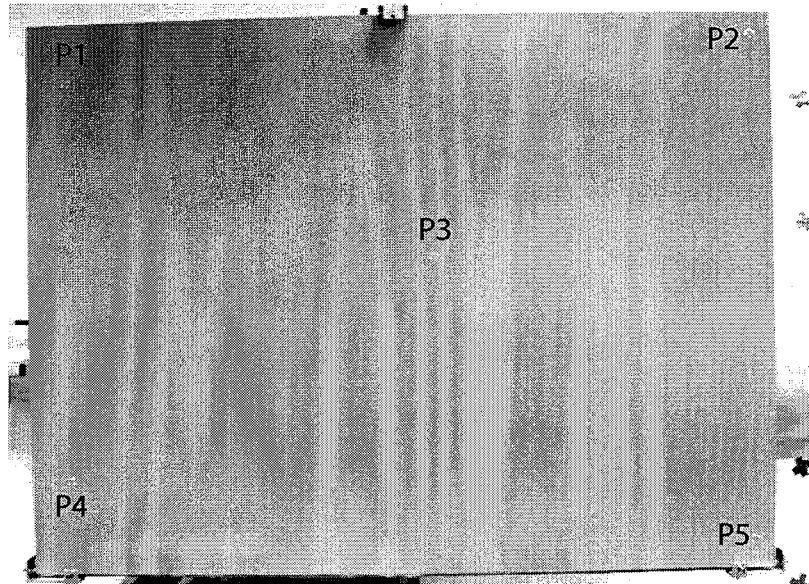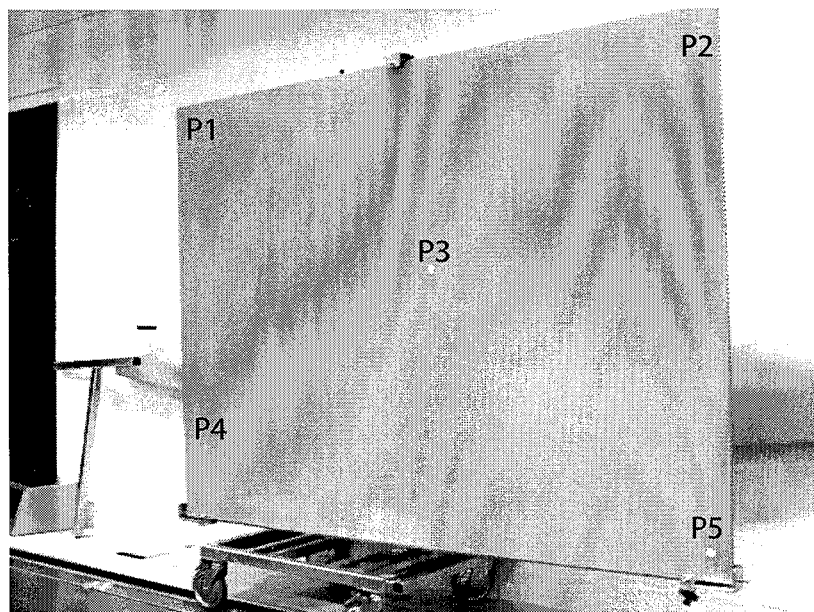

Figure 5. 7: Configuration 4. Picture of the aluminium plate and of the reference points

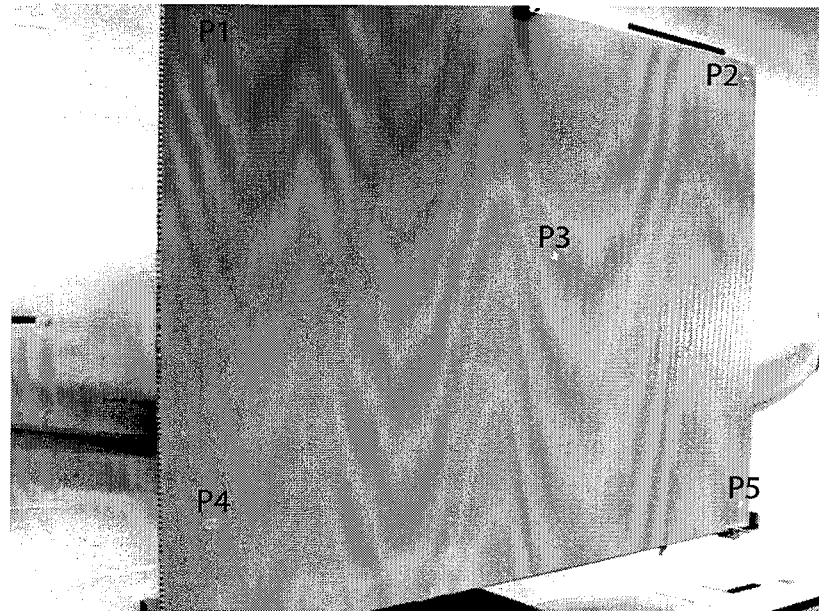| Object coordinates ...	Point 1	Point 2	Point 3	Point 4	Point 5
... as measured with the theodolite (mm)	x = -1000 y = 474 z = 13	x = 841 y = 605 z = 17	x = 0 y = 0 z = 0	x = -984 y = -609 z = -13	x = 866 y = -761 z = -17
... as calculated (mm)	x = -1002.4 y = 475.68 z = 10.896	x = 838.48 y = 604.45 z = 14.972	x = 5.7361 y = 3.9452 z = 2.9069	x = -983.91 y = -611.15 z = -11.856	x = 862.04 y = -763.71 z = -25.589
Distances (mm)	d = 3.5728 d_z = 2.1044	d = 2.7746 d_z = 1.028	d = 7.5443 d_z = 2.9069	d = 2.4412 d_z = 1.1435	d = 9.68 d_z = 8.5888

Table 5. 8: Aluminium plate, Configuration 4. Object coordinates as measured with the theodolite and calculated using the method described in Chapter 4.

5. 3. Measurement of the static out-of-plane deformation of an object

• **Description of the measurements:**

The object chosen here is a beach umbrella. It is placed vertically and its position is kept fixed for all the following measurements. The projection head position as well as the camera are also kept fixed. For all the measurements, the projection head is at 6 m away on the right side (R_x = 8973.60 mm, R_y = -190.50 mm, R_z = 1638.00 mm), and the camera is positioned slightly at the right of the umbrella making an angle a little bit larger than 90° with the projection direction. The measurements were done for different configurations of the beach umbrella, as displayed by Figure 5.8. Its initial position is fully open (its size is about 2 x 1.5 m), then for each following measurement, it is closed by step, sliding the supporting structure on the shaft, with about 30 cm between two measurements. Thirteen retroreflective targets are fixed on the surface and define the reference points (only twelve of them were considered for calibraion since the one in the bottom-middle was eliminated because it moved during the measurements and hence could not be used as a calibration point), and their position is measured with the theodolite. Then a fringe projection measurement is performed in order to capture the beach umbrella phase-map. Knowing the object and image-coordinates of the reference points as well as the value of the phase values at their position allows us to calibrate the system parameters. For each calibration procedure, the maximum number of points is used. For a matter of clarity and ease-to-read, only the tables displaying the object coordinates as measured with the theodolite and calculated using the method described in Chapter 4 will be kept here, the other ones being reported in the Appendix F. For the same reasons, only the information for 6 points (P1, P2, P6, P7, P10 and P12) will be reported here, the overall information being placed in Appendix F.

• **Possibilities and limitations:**

These measurements show the increased flexibility of the system allowing to adapt its configuration to the object under investigation and to the site, and to measure deformations of the object. As for the measurement with different system configurations (previous section), one limitation is when the targets are too far from the camera: their visibility decreases, leading to error in the determination of the image-coordinates of the calibration points. Another problem arising here is the shadow zones inherent to triangulation techniques and more particularly to the fringe projection technique. Furthermore, the immobility of the subject during the measurement is required. The theodolite and fringe projection measurements take about 15 minutes, up today.
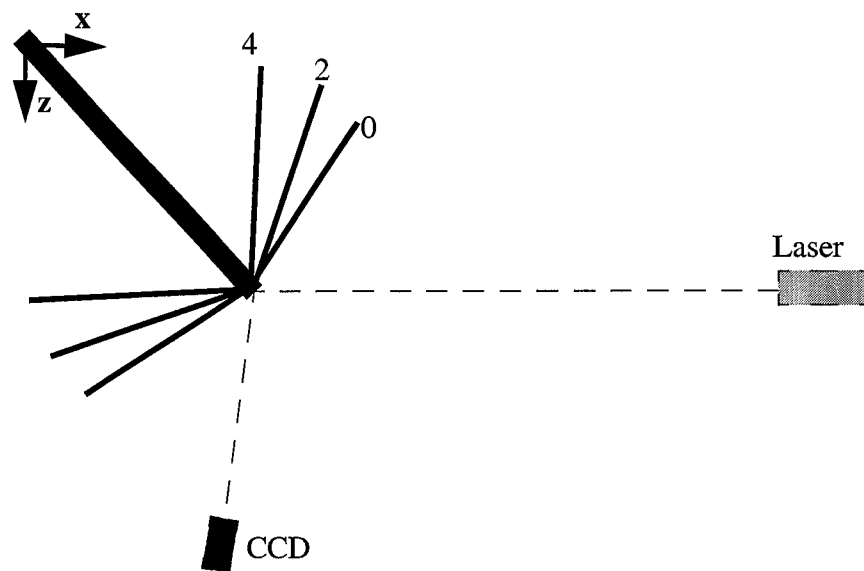
Figure 5. 8: Diagram of the different beach-umbrella configurations (numbers next to the umbrella)

5. 3. 1. Configuration 0

• **Parameters of the system:**

After calibration, the following values are found:

*The interferometric parameters: $r_x = -5.60 \cdot 10^{-3}$ mm; $r_y = -10.42 \cdot 10^{-3}$ mm; $r_z = 0.215$ mm.

*The exterior orientation parameters: $X_0 = 1422.8$ mm; $Y_0 = -40.19$ mm; $Z_0 = 3014.5$ mm;

$\omega = 3.32 \cdot 10^{-3}$ rad; $\phi = 0.448$ rad; $\kappa = -1.29 \cdot 10^{-3}$ rad found after 8 iterations and using all the calibration points.

*The interior orientation parameters used were: $c = 7.66$ mm, $\xi_0 = -0.057$ mm, $\eta_0 = -0.106$ mm.

- Results:

As shown by Table 5.9, $2.44m < |d| < 9.68mm$, $1.03mm < |d_z| < 8.59mm$.
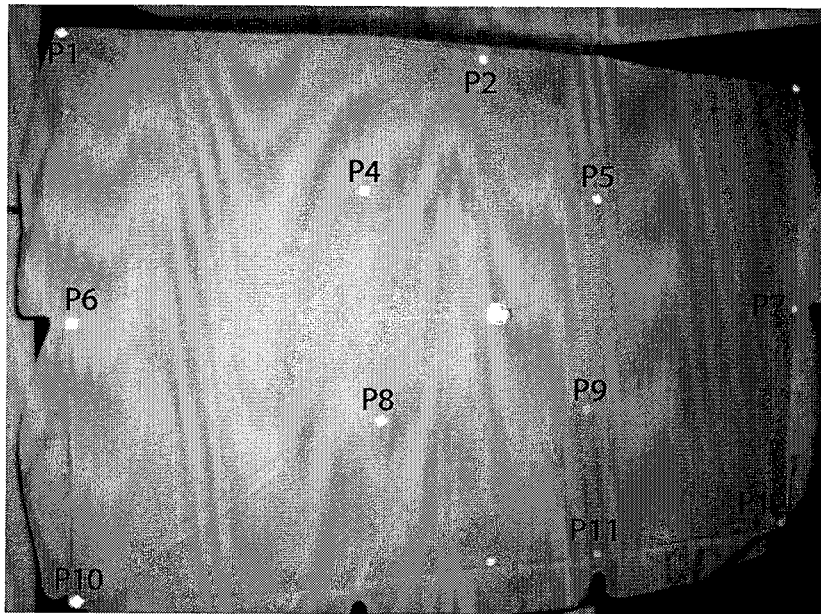
Figure 5. 9: Configuration 0. Picture of the beach umbrella and of the reference points

Object coordinates...	Point1	Point 3	Point6	Point 7	Point 10	Point 12
... as measured with the theodolite (mm)	x = -374.4 y = 657.5 z = 1141	x = 1073.6 y = 704.5 z = -381	x = -356.4 y = -28.5 z = 1108	x = 1063.6 y = 28.5 z = -401	x = -397.4 y = -704.5 z = 1057	x = 1020.6 y = -643.5 z = -463
... as calculated (mm)	x = 370.83 y = 653.4 z = 1141.20	x = 1067.8 y = 702.27 z = -383.76	x = -364.66 y = -27.80 z = 1106.60	x = 1064.7 y = 25.35 z = -398.15	x = -393.61 y = -700.08 z = 1058.2	x = 1018.6 y = -638.8 z = -463.91
Deviations (mm)	d = 5.44 d_z = 0.21	d = 6.81 d_z = 2.76	d = 8.41 d_z = 1.40	d = 4.38 d_z = 2.85	d = 5.9284 d_z = 1.15	d = 5.19 d_z = 0.90

Table 5. 9: Beach Umbrella; Configuration 0. Object coordinates as measured with the theodolite and calculated using the method described in Chapter 4

5. 3. 2. Position 2

- **System parameters:**

    After calibration, the following values are found:

    *The interferometric parameters: $r_x = 0.051$ mm; $r_y = -0.096$ mm; $r_z = 0.223$ mm.

    *The exterior orientation parameters: $X_0 = 1426.2$ mm; $Y_0 = -43.85$ mm; $Z_0 = 3004.4$ mm;

    $\omega = 4.77 \cdot 10^{-3}$ rad; $\phi = 0.451$ rad; $\kappa = -2.73 \cdot 10^{-3}$ rad found after 6 iterations and using all the calibration points.

    *The interior orientation parameters used were: $c = 7.6622$ mm, $\xi_0 = -0.0571$ mm, $\eta_0 = -0.1062$ mm.

- **Results:**

    As shown by Table 5.10, $2.44m < |d| < 9.68mm$, $1.03mm < |d_z| < 8.59mm$.
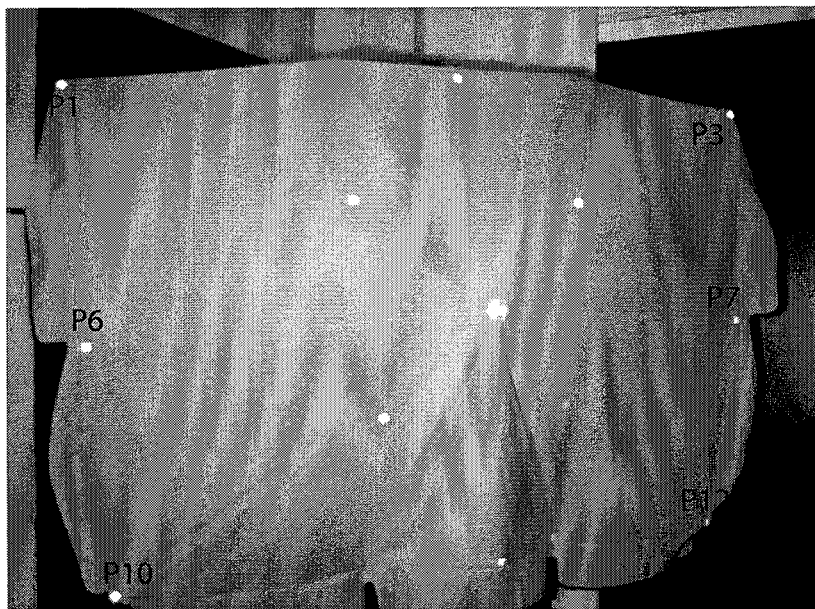
Figure 5. 10: Configuration 2. Picture of the beach umbrella and of the reference points

Object coordinates...	Point1	Point 3	Point6	Point 7	Point 10	Point 12
... as measured with the theodolite (mm)	x = -547.45 y = 595.5 z = 952.05	x = 867.55 y = 654.50 z = -542.95	x = -471.45 y = -86.50 z = 936.05	x = 880.55 y = -20.50 z = -509.95	*n.m.*	x = 784.55 y = -686.50 z = -546.95
... as calculated (mm)	x = -543.83 y = 592.89 z = 944.16	x = 867.96 y = 649.79 z = 529.71	x = -470.97 y = -87.951 z = 939.96	x = 876.57 y = -19.277 z = -521.00	*n.m.*	x = 777.88 y = -683.72 z = -552.12
Deviations (mm)	d = 9.07 d_z = 7.89	d = 14.05 d_z = 13.24	d = 4.20 d_z = 3.91	d = 11.81 d_z = 11.05	*n.m.*	d = 8.88 d_z = 5.17

Table 5. 10: Beach Umbrella; Configuration 2. Object coordinates as measured with the theodolite and calculated using the method described in Chapter 4; *n.m.* = *not measured*

5. 3. 3. Position 4

- **System parameters:**

    After calibration, the following values are found:

    *The interferometric parameters: $r_x = 0.009$ *mm*; $r_y = -0.012$ *mm*; $r_z = 0.218$ *mm*.

    *The exterior orientation parameters: $X_0 = 1450.7$ *mm*; $Y_0 = -44.801$ *mm*; $Z_0 = 2998.3$ *mm*;

    $\omega = 4.60 \cdot 10^{-3}$ *rad*; $\phi = 0.460$ *rad*; $\kappa = -1.61 \cdot 10^{-3}$ *rad* found after 8 iterations and using all the calibration points.

    *The interior orientation parameters used were: $c = 7.6622$ *mm*, $\xi_0 = -0.0571$ *mm*, $\eta_0 = -0.1062$ *mm*

- **Results:**

    As shown in Table 5.11, $3.74mm < |d| < 188.66mm$, $0.13mm < |d_z| < 182.74mm$.
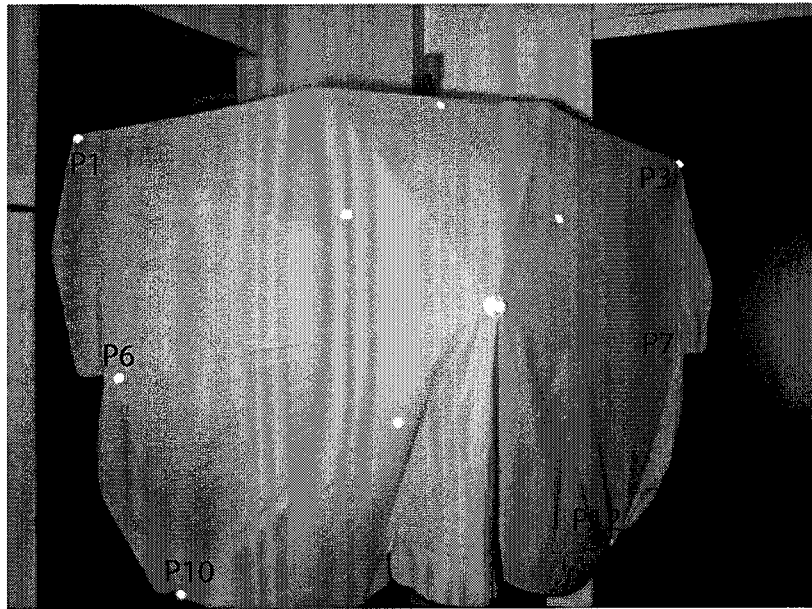
Figure 5. 11: Configuration 4. Picture of the beach umbrella and of the reference points

Object coordinates...	Point1	Point 3	Point 6	Point 7	Point 10	Point 12
... as measured with the theodolite (mm)	x = -679.45 y = 485.50 z = 760.05	x =683.55 y =512.50 z =-680.95	x =-538.45 y =-183.50 z =742.05	x = 684.55 y = -152.50 z = -565.95	n.m.	x = 482.55 y = -788.50 z = -526.95
... as calculated (mm)	x = -669.97 y = 483.53 z = 762.41	x = 718.67 y = 481.46 z = -498.21	x = -542.82 y = -185.37 z = 738.82	x = 703.34 y = -148.15 z = -481.42	n.m.	x = 474.43 y = -792.09 z = -553.45
Deviations (mm)	d = 9.97 d_z = 2.36	d = 188.66 d_z =182.74	d = 5.74 d_z = 3.22	d = 86.70 d_z = 84.53	n.m.	d = 27.95 d_z = 26.50

Table 5. 11: Beach Umbrella; Configuration 4. Object-coordinates as measured with the theodolite and calculated using the method described in Chapter 4; *n.m.* = *not measured*

5. 4. Discussion and comparison with the other methods presented in Chapter 3 (LS1 and LS2)

The results of this chapter show the enhanced flexibility of this method allowing to measure for objects of different shape and type of surface (diffusive). Furthermore, it is now possible to adapt the system configuration to the object under investigation and to the measurement site, to a certain extent. An additional advantage of the general method developed and presented in Chapter 4 is the new possibility to measure large out-of-plane deformations. Finally, in most of the cases treated here, the precision is better than for the other methods exposed in Chapter 2 and 3, as further demonstrated by results of Table 5.12. Indeed, this table presents a figure of merit used to discriminate the different methods according to their accuracy. For its calculation, we averaged the total, altimetric and planimetric deviations obtained for shape measurement of the wall, the plate in vertical position, the plate in position 1, 2 and 3, the windsurf board, at all the control points (a total of 53 points were considered for this calculation). This figure of merit was calculated for each method. Note that we only considered the two methods presented in Chapter 3 that gave the best results: namely LS1 and LS2.

	$<|d|>$ [mm]	$<|d_z|>$ [mm]	$<|d_{xy}|>$ [mm]	σ_d [mm]	σ_{d_z} [mm]	$\sigma_{d_{xy}}$ [mm]
LS1	51.47	46.9	8.25	51.26	48.68	4.82
LS2	9.79	2.71	8.25	5.2	1.03	4.82
General method	5.05	1.23	4.79	1.52	0.56	1.38

Table 5. 12: Comparison of the different methods using a figure of merits. LS1 and LS2: Least squares methods developed in Chapter 3 and 4. The general method is the one described in Chapter 4

Conclusion

In this work, several new data treatments have been proposed in order to extend the application of the fringe projection technique to large objects for shape and deformation measurement. The two first approaches are based on the assumptions that the object is quasi-planar and positioned parallel to the imaging plane of the camera. This allows to simplify the equations describing the system, and to mimic the classical approach used for measuring small objects. In the first proposed method, namely: the double-pinhole method (DPH), coupling two interferometers allows to physically calibrate the projection head. The basic principle of the second proposed method, namely the second least-squares method (LS2) relies on a least squares calculation minimizing the differences between the theoretical and measured phase value for a discrete number of calibration points whose object-coordinates are known. The result of both methods is to give the coordinates of the vector separating the two-point sources, which is the key parameter describing the projection head. From there, a reference phase-map and the sensitivity can be calculated, which in turn gives the desired height map.

The main contribution of this work is to propose a completely novel and more general approach. In this method, the measurement system is fully described using the interferometric equation together with the two equations of central perspective. Solving this set of non-linear equations at once gives the solution to interpret, in a very general way, the optical print of large objects obtained with interferometrically created fringes. Calibration procedures were also proposed.

After devising these methods, they were developed and implemented in programs that demonstrated their feasibility. Then they were evaluated and compared to a technique previously developed in our lab (based on least squares calculation and named LS1 in this work). The first method coping with a flat object (DPH) showed low precision and high dependence on systematic errors. It could be improved, however, considering its low measurement flexibility, we think that the time consumed to do so would not balance the benefits. The second method, based on least squares (LS2) is more interesting and flexible. From a limited number of calibration points, a depth resolution of about 1/1000 of the object size can be reached. However, it is limited only to

131

quasi-planar objects that are positioned parallel to the imaging plane of the camera, mostly because of the basic assumptions made. Indeed, the model used is too simple and induces large systematic errors when non-planar objects are considered. Finally, the most general method developed here allows to measure objects of general shape and deformation, and to make the measurement system more flexible, since now the system can be adapted, to a much larger extent than before, to the object under investigation and the measurement site. Here again, the 1/1000 depth resolution (rule of thumb known for fringe projection measurement systems) is reached, on planar as well as non-planar objects.

This work allowed to bring a new know-how in the lab, allowing to do real 3D measurements, since before, the type of measurements done in the lab was more 2D or 2.5D. This thesis brings general solutions independent of how deep the object under investigation is or the measurement configuration chosen. It also showed that the domain of validity of what has been developed before (the least square method LS1) is quite narrow, and that the "3D-measurement" problem is much more complex than what we thought at first. Finally, this work confirms the warning of colleagues from ETHZ that the announced performance and precision of commercially available shape measurement systems should be taken with great scepticism.

Several limitations arise, among which are the discontinuity of shape, the shadow zone and the "hidden" part problems that are inherent to optical triangulation techniques. This work also raises the question of the number of calibration points needed, in order to have a good precision and to be able to measure objects under deformation. Another limitation concerns the material used in our set-up, and particularly the observation device, which was chosen because it was the "on-the-shelf" material available at that time. More efficient material exists today. Therefore, the results found here are not the limits of the method, and the system can be improved in order to reach higher precision and better height and spatial resolutions.

Further optimizations should deal with other aspects of the imaging system, such as calibration of the internal orientation parameters, the external orientation parameters, and the lens distortions. Another improvement would consist of gathering all the programs together to make one single user-friendly program, automatization, and above all make the measurement method faster. An important programming work has been done in the frame of this project, reducing the data acquisition and treatment time from several hours (for the first measurements that were quite "manual") to thirty minutes. This time could be further reduced to a few minutes by automatizing the theodolite data acquisition and the reading of the calibration points image-coordinates, or by using wavelets for computing the unwrapped phase-map. Other studies should be led in order to determine the trade-off between the number of calibration points to consider for calibration and time to measure them. Another matter concerns the development of a program to do the 3D representation of the object. Actually, this step is not straightforward since the data does not consist of a simple height map $z(\xi, \eta)$, but rather of three sets of data: $x(\xi, \eta)$, $y(\xi, \eta)$ and $z(\xi, \eta)$, where the planimetric increments Δx and Δy are not constant over the image. The final aim is to represent the shape of the object $z(x, y)$ in three dimensions. Some developments have already been done in that direction and a first algorithm exists. Preliminary tests show encouraging results concerning the feasibility. However, further improvements are needed, particularly concerning the 3D image display. Some work is currently being done in that direction. Furthermore it would be the occasion to convert the proposed technique from physical coordinates measurement to real shape measurement, independent of any given referential. Finally, until now, the method has only been tested in the lab, and the method should be tested outdoors in order to evaluate the possibility of applying it for in situ measurements.

Appendix

1. 1. Appendix A: Review of the specifications of different commercially available shape or position measuring systems.

Type of system	System	Manufacturer	Resolution	Precision	Volume or distance and depth of field	Time for a measurement
Mechanical contact systems						
MMT	Cyclone Scanning machine	Renishaw [3]		50 μm	600x500x400 mm	
Mechanical arm	Microscribe 3DX	Immersion Corp.		0.23 mm	Sphere r = 1.27 m	a few seconds for each point
	Romer 3000i	Romer [4]		0.03 mm (2)	Sphere r = 3.6 m	
	Silver Series	Faro [5]		±0.076 mm		
Scanning Techniques						

Table 1: Review of the specifications of different commercially available shape or position measuring systems. Data from [1] and [2] and completed with different sources (cited in the table)

Laser Line Sensors (Triangulation)	Soisic	Mensi [6]	0.2 mm/m	0.3-0.8 mm σ	0.8 to 30 m	
	S10/S25	Mensi [6]	0.2 /0.35 mm	0.21/0.6 mm σ	0.8 to 10 m / 2-25 m	100 pts/s
	Bodygraph central		10 μm (3σ)	50 μm (3σ)	125x125x80	
	Cetim	Cetim	0.01 %	0.1 %	300x300x600 mm	
	OTP6M (probe for CMM)	Renishaw [3]		± 25 μm	36 mm (stand-off distance)	0.5-50 mm/ s?
Laser plane sensor	KLS 171	Kréon Ind. [3]	25 μm	0.1 mm	50 to 100 mm	8 pts/s
	Autoscan	Steinbichler [7]	8 μm	± 0.025 mm	150 ± 26 mm	
	Reversa 25H	3D scanners	25 μm	± 20 μm	80 to 110 mm	
	3030 RGB Hirez	Cyberware		0.1 mm		
	Surveyor 3200	Laser Design	0.001 mm	0.0127 mm (σ)	1016x1016x8 13 mm	
	Hyscan	Hymarc		± 0.025 mm (3σ)		
	HLS	Polhemus	0.5 mm	1mm to 200 mm	75 to 680 mm	
	LASCAN		4 μm	± 0.050 mm	65 mm	
	VI 700	Minolta	200x200x200 points		0.6 to 2.5 m	
	Digibot II	Digibotics		0.050 mm	diameter 380 x length 380 mm	
Time of Flight	Theta Scan	Polhemus		0.1 mm		
	Cyrax 2100 [4]	Cyratech		4 mm	0.5-100m	800 pts/s
	Fastrak	Polhemus		0.76 mm	762x762x762 mm	

Table 1: Review of the specifications of different commercially available shape or position measuring systems. Data from [1] and [2] and completed with different sources (cited in the table)

134

		Polhemus		0.1 mm	762x762x762 mm	
Laser Phase-shifting	CTB	Bertin		4 cm	75 m	
	TMF	Bertin	0.3 m to/at 2 m	0.5 mm	10 m	
Interferometry	SMART 310 - IMS	Leica [8]	1.26 μm	± 25 μm at /to 2.5 m	0.2-25 m	
Theodolithes	TPS 5000	Leica (1998 catalogue) [8]		0.05 mm	<120 m	3 s
Tomographic methods	ICT 2500	ARACOR [9]	3 mm	0.25 mm	2500 mm diameter	50-100 ms/ image
Whole-field methods						
Photogrammetry	V-Stars	Leica-IMS		0.05-0.1 mm		
	ICAM 6/28	Imetric [10]			1/30 000 - 1/ 200000	
Structured light	Comet 500	Steinbichler [7]	20 μm	± 0.2 mm (σ)	460x360x360 mm	
	Comet 100	Steinbichler [7]	5 μm	± 0.04 mm (σ)	85x65x80 mm	
	Comet Optotrack	Steinbichler [7]	10 μm	± 0.05 mm (2σ)	2.25 mm	
	SAS	Bertin	0.25 mm	0.05 mm	120x80x80 mm	
	Mini moiré	Eois	0.16 mm	± 0.10 mm	120x80x30 mm	
	Atos	GOM [11]	0.03 mm	0.04 mm/m	WD: 0.30-15 m 500x400 mm	20 s/mes 439296 pts/ mes

Table 1: Review of the specifications of different commercially available shape or position measuring systems. Data from [1] and [2] and completed with different sources (cited in the table)

A document giving information similar to this table and also complementary was just published [12]

1. 2. Appendix B: Coordinates and deviations computed by LS1, DPH and LS2 for the objects measured in Chapter 3

1. 2. 1. Planar object parallel to the imaging plane of the camera: the wall

	$x_{LeastSqr.1}$ [mm]	$y_{LeastSqr.1}$ [mm]	$z_{LeastSqr.1}$ [mm]	d [mm]	d_z [mm]	d_{xy} [mm]	d_x [mm]	d_y [mm]
P10	-962.00	839.00	7.34	5.34	5.34	0	0	0
P20	46.80	846.40	0.13	15.00	-1.87	14.89	3.80	14.40
P30	1253.00	833.00	-9.54	10.54	-10.54	0	0	0
P40	-997.80	11.60	1.06	4.12	0.06	4.12	3.80	1.60
P50	1.10	2.90	-0.52	3.14	-0.52	3.1	1.1	2.90
P60	1267.10	-9.70	-2.56	9.72	-2.56	9.39	9.10	2.30
P70	-975.00	-889.00	3.94	2.94	2.94	0	0	0
P80	0.50	-858.00	-2.81	10.40	-2.81	10.01	0.50	10.00
P90	1184.00	-887.00	-1.43	1.43	-1.43	0	0	0

Table 2: Values of the object-coordinates of the wall control points obtained by the first least square method (LS1)

	$x_{DoublePH}$ [mm]	$y_{DoublePH}$ [mm]	$z_{DoublePH}$ [mm]	d [mm]	d_z [mm]	d_{xy} [mm]	d_x [mm]	d_y [mm]
P10	-962.00	839.00	-3.44	5.44	-4.66	0	0	0
P20	46.80	846.40	6.66	15.6	4.66	14.89	3.80	14.40
P30	1253.00	833.00	17.87	16.87	16.87	0	0	0
P40	-997.80	11.60	-15.49	17.00	-16.49	4.12	3.80	1.60
P50	1.10	2.90	-0.89	3.22	-0.89	3.1	1.1	2.90
P60	1267.10	-9.70	18.88	21.08	18.88	9.39	9.10	2.30
P70	-975.00	-889.00	-22.54	23.54	-23.54	0	0	0
P80	0.50	-858.00	-13.45	16.77	-13.45	10.01	0.50	10.00
P90	1184.00	-887.00	5.44	5.44	5.44	0	0	0

Table 3: Values of the object coordinates of the wall control points obtained by the double-pinhole method (DPH).

	$x_{LeastSqr.2}$ [mm]	$y_{LeastSqr.2}$ [mm]	$z_{LeastSqr.2}$ [mm]	d [mm]	d_z [mm]	d_{xy} [mm]	d_x [mm]	d_y [mm]
P10	-962.00	839.00	3.20	3.69	3.69	0	0	0
P20	46.08	846.40	-2.28	14.95	1.3	14.89	3.80	14.40
P30	1253.00	833.00	-12.21	1.94	-1.94	0	0	0
P40	-997.80	11.60	0.23	4.65	-2.16	4.12	3.80	1.60
P50	1.10	2.90	1.20	3.80	2.19	3.1	1.1	2.90
P60	1267.10	-9.70	0.11	11.26	6.22	9.39	9.10	2.30
P70	-975.00	-889.00	3.09	1.82	-1.82	0	0	0
P80	0.50	-858.00	-1.34	10.38	-2.75	10.01	0.50	10.00
P90	1184.00	-887.0	0.63	3.72	3.72	0	0	0

Table 4: Values of the object coordinates of the wall control points obtained by the second least squares method (LS2).

1. 2. 2. First evaluation of the precision of LS1, DPH and LS2: the plate in vertical position

• The first least squares method (LS1):

	<x> (mm)	<y> (mm)	<z> (mm)	<d> (mm)	$<d_z>$ (mm)	$<d_{xy}>$ (mm)	$<d_x>$ (mm)	$<d_y>$ (mm)
P10	-999.00	474.00	4.48	6.52	-6.52	0	0	0
P20	-103.16	587.04	-1.93	12.22	-0.93	12.19	-5.16	11.04
P30	842.00	605.00	-1.33	8.67	8.67	0	0	0
P40	-957.68	-58.48	2.27	12.67	-10.73	6.68	-5.68	3.52
P50	1.26	3.08	-0.62	3.39	-0.62	3.33	1.26	3.08
P60	840.04	-27.78	2.85	12.77	9.85	8.08	8.04	-0.78
P70	-983.00	-609.00	4.85	12.15	-12.15	0	0	0
P80	-39.18	-776.40	-1.51	13.65	-7.51	11.40	-0.18	-11.4
P90	867.00	-762.00	-2.20	0.80	0.80	0	0	0

Table 5: Object-coordinates of the control points as calculated by the first least squares method (LS1)

	σ_x (mm)	σ_y (mm)	σ_z (mm)
P10	0	0	1.61
P20	6.82	1.82	2.13
P30	0	0	1.81
P40	1.86	0.76	2.20
P50	6.25	1.23	1.05
P60	0.84	1.50	2.53
P70	0	0	2.01
P80	4.51	0.99	1.61
P90	0	0	2.73

Table 6: Standard deviation calculated for LS1

- The Double pinhole method (DPH):

	<x> (mm)	<y> (mm)	<z> (mm)	<d> (mm)	$<d_z>$ (mm)	$<d_{xy}>$ (mm)	$<d_x>$ (mm)	$<d_y>$ (mm)
P10	-999.00	474.00	5.04	5.96	-5.96	0	0	0
P20	-103.16	587.04	9.51	14.87	8.51	12.19	-5.16	11.04
P30	842.00	605.00	0.88	9.12	9.12	0	0	0
P40	-957.68	-58.48	7.74	8.50	-5.26	6.68	-5.68	3.52
P50	1.26	3.08	7.50	8.20	7.50	3.33	1.26	3.08
P60	840.04	-27.78	6.03	15.33	13.03	8.08	8.04	-0.78
P70	-983.00	-609.00	13.28	3.72	-3.72	0	0	0
P80	-39.18	-776.40	0.015	12.87	-15.98	11.40	-0.18	-11.4
P90	867.00	-762.00	-17.21	14.21	-14.21	0	0	0

Table 7: Object-coordinates of the control points as calculated by the double-pinholes method (DPH).

	σ_x (mm)	σ_y (mm)	σ_z (mm)
P10	0	0	2.81
P20	6.82	1.82	2.96
P30	0	0	2.28
P40	1.86	0.76	0.74
P50	6.25	1.23	1.62
P60	0.84	1.50	1.00
P70	0	0	2.34
P80	4.51	0.99	2.58
P90	0	0	3.34

Table 8: Standard deviation calculated for the double-pinholes method (DPH).

- The second least squares method (LS2):

	<x> (mm)	<y > (mm)	<z> (mm)	<d> (mm)	<d_z> (mm)	<d_{xy}> (mm)	<d_x> (mm)	<d_y> (mm)
P10	-999.00	474.00	10.24	0.76	-0.76	0	0	0
P20	-103.16	587.04	-2.09	12.34	-1.09	12.19	-5.16	11.04
P30	842.00	605.00	-10.50	0.50	-0.50	0	0	0
P40	-957.68	-58.48	10.92	7.00	-2.08	6.68	-5.68	3.52
P50	1.26	3.08	1.52	3.71	1.52	3.33	1.26	3.08
P60	840.04	-27.78	-2.58	9.21	4.42	8.08	8.04	-0.78
P70	-983.00	-609.00	16.53	0.47	-0.47	0	0	0
P80	-39.18	-776.40	4.97	11.45	-1.03	11.40	-0.18	-11.4
P90	867.00	-762.00	-3.68	0.68	-0.68	0	0	0

Table 9: Object-coordinates of the control points as calculated by the second least squares method (LS2).

	σ_x (mm)	σ_y (mm)	σ_z (mm)
P10	0	0	1.27
P20	6.82	1.82	1.96
P30	0	0	1.31
P40	1.86	0.76	1.47
P50	6.25	1.23	1.53
P60	0.84	1.50	1.27
P70	0	0	1.68
P80	4.51	0.99	2.58
P90	0	0	0.72

Table 10: Standard deviation calculated for the second least squares method (LS2).

1. 2. 3. Planar object not parallel to the imaging plane of the camera: the inclined plate

	$x_{LeastSqr.1}$ [mm]	$y_{LeastSqr.1}$ [mm]	$z_{LeastSqr.1}$ [mm]	d [mm]	d_z [mm]	d_{xy} [mm]	d_x [mm]	d_y [mm]
P10	-998.00	471.00	3.56	86.56	86.56	0	0	0
P20	-136.50	544.40	-3.29	84.01	82.71	14.73	-14.50	-2.60
P30	843.00	596.00	1.31	82.31	82.31	0	0	0
P40	-1033.60	24.80	5.66	25.49	17.66	18.38	-4.60	17.80
P50	-12.00	24.60	-1.81	27.43	-1.81	27.37	-12.00	24.60
P60	862.10	80.40	5.00	30.43	2.00	30.87	12.10	28.40
P70	-986.00	-599.00	8.15	74.85	-74.85	0	0	0
P80	-96.20	-785.50	-3.37	124.16	-122.37	21.02	-14.20	-15.50
P90	863.00	-754.00	-0.07	128.07	-128.07	0	0	0

Table 11: Object coordinates of the control points as calculated by the least squares method 1 (LS1).

	x$_{DPH}$ [mm]	y$_{DPH}$ [mm]	z$_{DPH}$ [mm]	d [mm]	d$_z$ [mm]	d$_{xy}$ [mm]	d$_x$ [mm]	d$_y$ [mm]
P10	-998.00	471.00	-84.78	1.78	-1.78	0	0	0
P20	-136.50	544.40	-83.62	14.92	2.38	14.73	-14.50	-2.60
P30	843.00	596.00	-64.87	16.13	16.13	0	0	0
P40	-1033.60	24.80	-2167	20.77	-9.67	18.38	-4.60	17.80
P50	-12.00	24.60	-4.29	27.70	-4.29	27.37	-12.00	24.60
P60	862.10	80.40	14.54	32.96	11.54	30.87	12.10	28.40
P70	-986.00	-599.00	65.76	17.24	-17.24	0	0	0
P80	-96.20	-785.50	102.08	26.98	-16.92	21.02	-14.20	-15.50
P90	863.00	-754.00	126.07	1.93	-1.93	0	0	0

Table 12: Object coordinates of the control points as calculated by the Double-Pinhole method (DPH)

	x$_{LeastSqr.2}$ [mm]	y$_{LeastSqr.2}$ [mm]	z$_{LeastSqr.2}$ [mm]	d [mm]	d$_z$ [mm]	d$_{xy}$ [mm]	d$_x$ [mm]	d$_y$ [mm]
P10	-998.00	471.00	-79.1	3.9	3.9	0	0	0
P20	-136.50	544.40	-86.79	14.75	-0.79	14.73	-14.50	-2.60
P30	843.00	596.00	-77.61	3.39	3.39	0	0	0
P40	-1033.60	24.80	-9.18	18.60	2.82	18.38	-4.60	17.80
P50	-12.00	24.60	-0.63	27.38	-0.63	27.37	-12.00	24.60
P60	862.10	80.40	9.68	31.58	6.68	30.87	12.10	28.40
P70	-986.00	-599.00	86.59	3.59	3.59	0	0	0
P80	-96.20	-785.50	117.81	21.05	-1.19	21.02	-14.20	-15.50
P90	863.00	-754.00	133.22	5.22	5.22	0	0	0

Table 13: Object coordinates of the control points as calculated by the least squares method 2 (LS2).

1. 3.   Appendix C: The rotated plate and surfboard measured using LS1, DPH and LS2 described in Chapters 2 and 3

The plate was placed and measured in three different positions: once in the vertical position, and then rotated around its horizontal axis by angles of 10° and 20 °, as displayed in the following diagram. The fringe projection set-up configuration as well as the measurement procedures are the same as the ones described in Chapter 3. As before, the points used for calibrating the scaling

relations are P10, P30, P70 and P90. Each time, the origin of the object-coordinate system is fixed at P50. Then the measured data are treated using the first and second least squares methods (LS1 and LS2) and the double pinhole (DPH) method (see Chapter 2). The results are evaluated with the evaluation procedure described in Section 3.1.
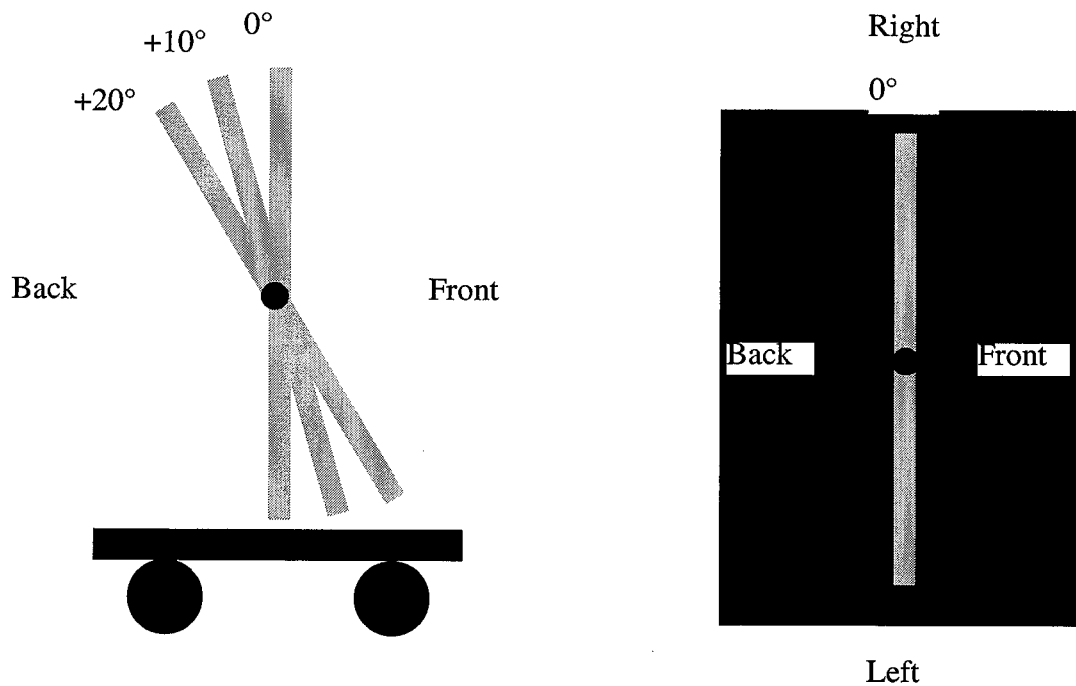
Figure 1: Different measurement positions of the plate; left: side view; right: top view.

For each configuration the following information computed with the three methods will systematically be given:
- the object-coordinates of the reference points as measured with the theodolite
- the coordinates r_x, r_y, r_z of the vector $\vec{r}$ separating the two point sources; these parameters describe the projection head
- the profiles of the phase, taken along a horizontal and a vertical line of the reference phase maps
- the height map of the measured object
- the coordinates of the reference points (used as control points) as calculated by LS1, DPH and LS2

We would like to underline that we did the measurement of the plate in the vertical position again, on purpose. Indeed, it allows to compare the results of this measurement to the results of the two other positions more easily, since the measurement configuration (object and set-up) remains unchanged for the three measurements. However, we will see that slight changes arise compared to the results for the vertical position obtained in the preceding chapter, and we will also see why.

1. 3. 1. Position 3: 0° rotation to the back around the horizontal axis

The object-coordinates of the reference points as measured with the theodolite are in Table 2. The values found for the parameters r_x, r_y, r_z using the three methods are displayed in Table 3. They were used to calculate the reference phase maps shown in Figure 2 and the height of the control points presented in Table 4 to 6. Height map of the object are shown in Figure 3 and 4. Tables 4 to 6 display the coordinates and deviations obtained for the control points by the three methods.

According to these, for the first least squares method (LS1), $2.44mm < |d| < 34.51mm$ and $2.44mm < |d_z| < 34.51mm$. The double pinholes method (DPH) gives $1.98mm < |d| < 22.17mm$ and $1.74mm < |d_z| < 14.93mm$, and the second least squares method (LS2), $0mm < |d| < 22.27mm$ and $0.1mm < |d_z| < 5.62mm$. For the three methods, $0 < |d_{xy}| < 21.55$ with $0 < |d_x| < 17.7$ and $0 < |d_y| < 12.3$.

Comparing the results of the three methods, we observe that generally $d_{max}^{LS1} > d_{max}^{DPH}$ and d_{max}^{LS2}, and that $d_{max}^{DPH} \approx d_{max}^{LS2}$. This trend is confirmed and refined by considering the total distance d point by joint. The LS2 method gives better results than both, the LS1 (8 points against 1) and DPH method (8 points against 1), and the double-pinholes method (DPH) gives better d then the first least squares (LS1) method (7 points against 2). Furthermore, since the scaling transformation is the same for the three methods, d_{xy} is the same at each point for the three methods. Hence, the differences observed in d between the three methods at each point come from d_z. As seen in the preceding chapter, this is mainly explained, by the difference in the reference maps, which can be observed in Figure 4 a) and b). Indeed, the LS1 calculation forces the reference map, which is supposed to correspond to z = 0, to "stick" to the measured phase-map. However, the measured phase map is not exactly in the plane z = 0, and in certain region, z > 10 mm or even 30 mm (see Table 2). Therefore, this introduces errors in the calculated reference phase map and thereby in the value of z. Conversely, using the DPH and LS2 methods allows to cast off the measured phase-map and thus to avoid this type of bias. Hence, these methods allow to compute values of z that are closer to reality. Figures 2 and 3 show more globally the differences in the height computed by the three methods.

As for d_{xy}, considering its intervals of values, we see that $|d_{xy}^{max}|$ obtained here is sensibly higher then the $|d_{xy}^{max}|$ computed for both the wall and the plate in the preceding chapter. Furthermore, considering the points P20, P40, P50, P60 and P80 again, we see that the correspondence between $|d_x| \geq |d_y|$ and $|x| \geq |y|$ is not so systematically observed here as in the preceding chapter. The most probable explanation for this discrepancy is that for most of the points chosen for calibrating the relation between the object- and image-coordinates (P10, P30, P70 and P90), the height z is sensibly further from 0 then in the case treated in the preceding chapter ($|z| > or \approx 10mm$ here, against $|z| < or \approx 10mm$). Hence, they introduce an error in the scaling transformation that cannot calculate x and y properly anymore. This seems to indicate that we are at the limits of the conditions allowing the application of the relation between the object- and image-coordinates as defined in Chapter 2. It is interesting to notice that a consequence of this error in the determination of x and y, is an additional error in the calculation of the reference phase map whatever the data treatment method used.

All these trends are more clearly seen in the next sections.

	$x_{theodolite}$ [mm]	$y_{theodolite}$ [mm]	$z_{theodolite}$ [mm]
P10	-998 ±1	476 ±1	3 ±1
P20	-122 ±1	553 ±1	17 ±1
P30	843 ±1	603 ±1	32 ±1
P40	-1027 ±1	5 ±1	-11 ±1
P50	0 ±1	0 ±1	0 ±1
P60	851 ±1	53 ±1	15 ±1
P70	-984 ±1	-607 ±1	-29 ±1
P80	-79 ±1	-780 ±1	-24 ±1
P90	865 ±1	-764 ±1	-10 ±1

Table 14: Object-coordinates of the reference points on the plate in position 3, as measured using the theodolite

	r_x [mm]	r_y [mm]	r_z [mm]
Least square method	-0.05784	-0.00777	0.17994
"Double pinhole" method	-0.06339	0.00013	0.191613
Corrected "Double-pinhole" method	-0.06018	0.002149	0.187904

Table 15: Interferometric parameters obtained by the different methods for the plate in position 3

a)
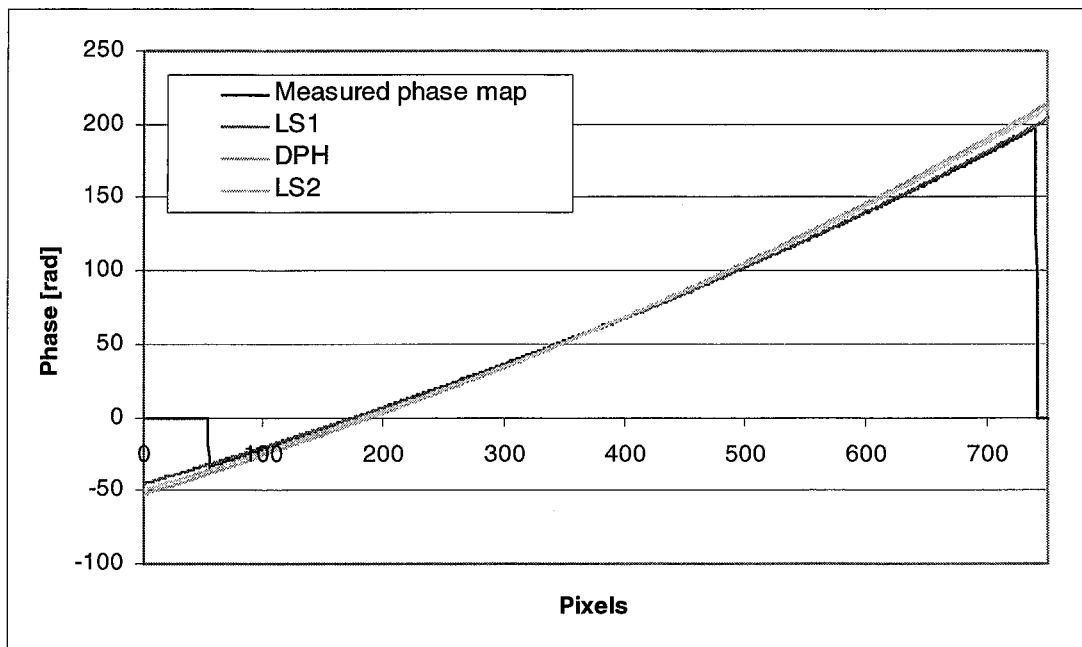
b)
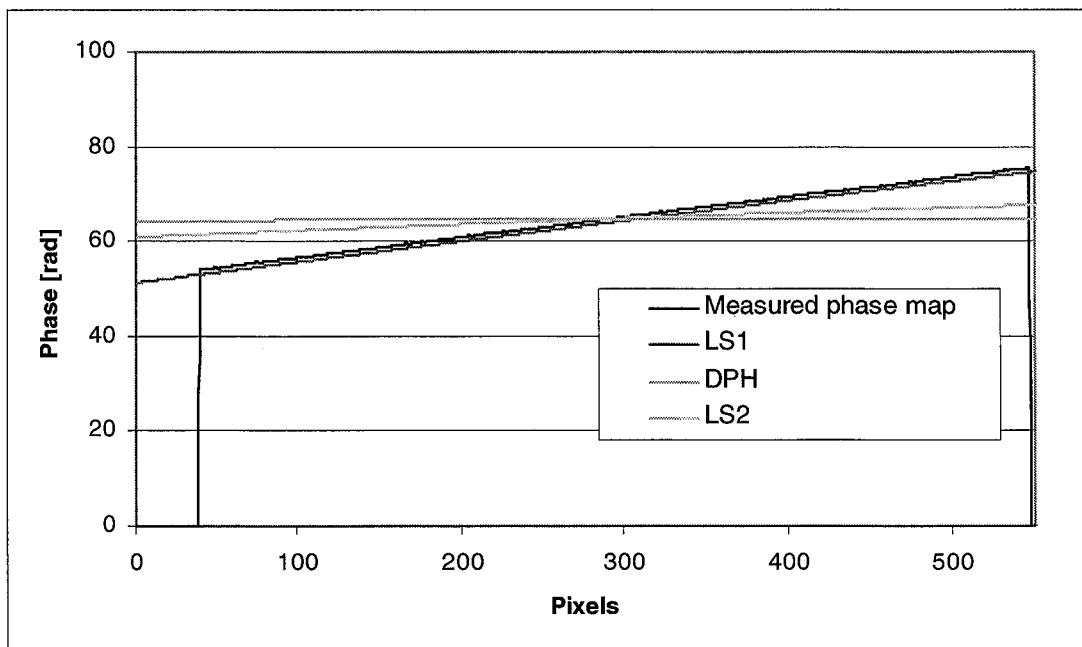
Figure 2: Plate in position 3. Comparison of the measured phase map to the reference phases map profiles obtained by different methods (a) along a horizontal line and (b) along a vertical line
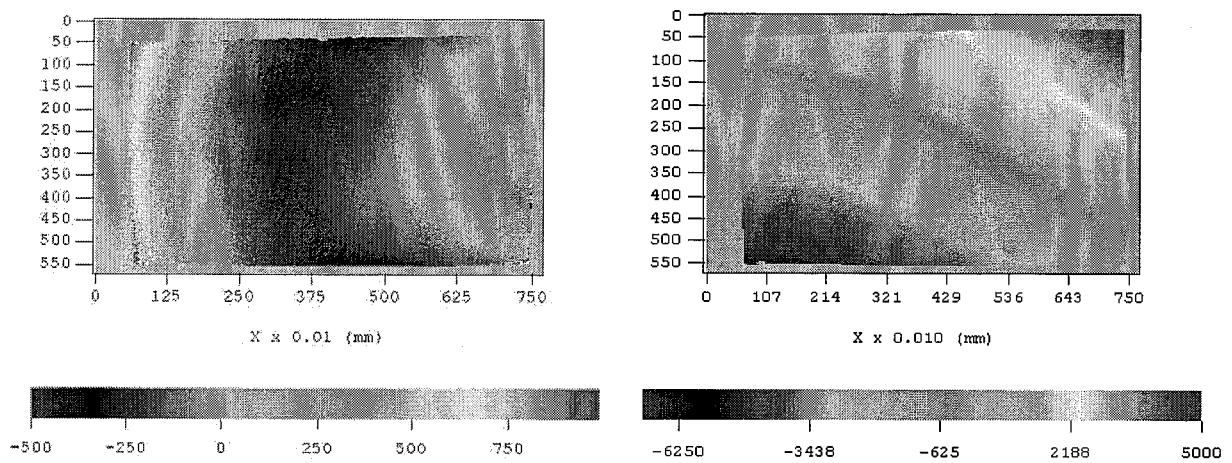
Figure 3: Height map obtained for the plate in position 3 using the LS1 (left) and the DPH method (right)
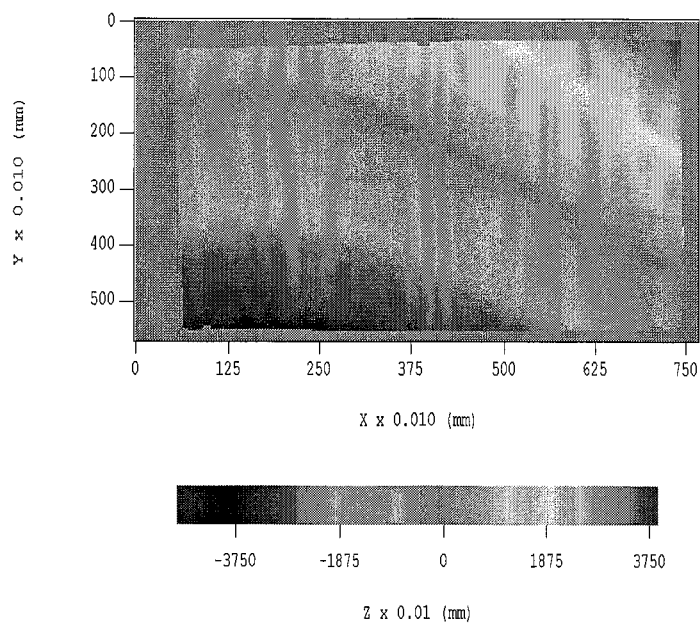
Figure 4: Height map obtained for the plate in position 3 using the second least squares method

	$x_{LeastSqr.1}$ [mm]	$y_{LeastSqr.1}$ [mm]	$z_{LeastSqr.1}$ [mm]	d [mm]	d_z [mm]	d_{xy} [mm]	d_x [mm]	d_y [mm]
P10	-998	476	5.44	2.44	2.44	0	0	0
P20	-139.7	565.3	-2.58	29.12	-19.58	21.55	-17.7	12.3
P30	843	603	1.06	30.94	-30.94	0	0	0
P40	-1027.2	5.3	5.32	16.323	16.32	0.36	-0.2	0.3
P50	-7.8	-2.1	-2.10	8.35	-2.1	8.08	-7.8	-2.1
P60	858.8	54.9	4.16	13.49	-10.84	8.03	7.8	1.9
P70	-984	-607	5.51	34.51	34.51	0	0	0
P80	-95.4	-785.3	-2.58	27.49	21.42	17.23	-16.4	-5.3
P90	865	-764	-0.09	9.91	9.91	0	0	0

*Table 16:* Object-coordinates of the control points as calculated by the first least squares method (LS1)

	$x_{DoublePH}$ [mm]	$y_{DoublePH}$ [mm]	$z_{DoublePH}$ [mm]	d [mm]	d_z [mm]	d_{xy} [mm]	d_x [mm]	d_y [mm]
P10	-998	476	-1.1	4.1	-4.1	0	0	0
P20	-139.7	565.3	15.26	21.62	-1.74	21.55	-17.7	12.3
P30	843	603	44.38	12.38	12.38	0	0	0
P40	-1027.2	5.3	-20.8	9.78	-9.78	0.36	-0.2	0.3
P50	-7.8	-2.1	-4.15	9.08	-4.15	8.08	-7.8	-2.1
P60	858.8	54.9	25.06	12.87	10.06	8.03	7.8	1.9
P70	-984	-607	-43.9	14.93	-14.93	0	0	0
P80	-95.4	-785.3	-38	22.17	-13.95	17.23	-16.4	-5.3
P90	-95.4	-785.3	-38	1.98	-1.98	0	0	0

Table 17: Object-coordinates of the control points as calculated by the "Double Pinhole" method (DPH)

	$x_{LeastSqr.2}$ [mm]	$y_{LeastSqr.2}$ [mm]	$z_{LeastSqr.2}$ [mm]	d [mm]	d_z [mm]	d_{xy} [mm]	d_x [mm]	d_y [mm]
P10	-998	476	2.98	0.02	-0.02	0	0	0
P20	-139.7	565.3	11.38	22.27475	-5.62	21.55	-17.7	12.3
P30	843	603	31.84	0.16	-0.16	0	0	0
P40	-1027.2	5.3	-11.61	0.70859	-0.61	0.36	-0.2	0.3
P50	-7.8	-2.1	-3.07	8.641464	-3.07	8.08	-7.8	-2.1
P60	858.8	54.9	18.51	8.761855	3.51	8.03	7.8	1.9
P70	-984	-607	-29.1	0.1	-0.1	0	0	0
P80	-95.4	-785.3	-28.62	17.84361	-4.62	17.23	-16.4	-5.3
P90	865	-764	-10.57	0.57	-0.57	0	0	0

Table 18: Object-coordinates of the control points as calculated by the second least squares method (LS2)

1. 3. 2. Position 1: 20 ° to the back around the horizontal axis

The object-coordinates of the reference points are in Table 7. The values found for the parameters r_x, r_y, r_z using the three methods are displayed in Table 8. They were used to calculate the reference phase maps shown in Figure 5 and the height of the points. Height maps of the object are presented in Figure 6 and 7. Tables 9, 10 and 11 display the object-coordinates and deviations obtained at the control points by the three methods. According to these, for the least squares method (LS1), $36.70mm < |d| < 237.77mm$ and $2.01mm < |d_z| < 238.02mm$. The double pinholes method (DPH) gives $3.58mm < |d| < 42.7mm$ and $0.42mm < |d_z| < 25.51mm$, and the corrected double pinholes method (LS2), $1.93mm < |d| < 43.32mm$ and $0.66mm < |d_z| < 5.93mm$. For the three methods, $0 < |d_{xy}| < 42.98mm$ with $0 < |d_x| < 13.2mm$ and $0 < |d_y| < 40.9mm$.

The results found for this position of the plate confirm more clearly the trends and interpretations found in the two previous sections, therefore we will not detail them here, but sum them up:

- $d_{max}^{LS1} > d_{max}^{DPH}$ and d_{max}^{LS2}, and that $d_{max}^{DPH} \approx d_{max}^{LS2}$. Since the relation between object- and image-coordinates is the same for all three methods, this is due to d_z.

- $|d_z^{LS1}| > |d_z^{DPH}| > |d_z^{LS2}|$ for most of the points considered one by one. This is because of differences in phase maps as displayed in Figure 5. The reference phase map determined by the first

least square method (LS1) has a strong bias because the assumption that the measured object lies in the plane $z = 0$ is clearly wrong now.

- $d_{xy}^{position1} > d_{xy}^{position2} > d_{xy}^{position3}$ because for the calibration points, $\left|z^{position1}\right| > \left|z^{position2}\right| > \left|z^{position3}\right| > 0$, contradicting the basic assumptions for applying the scaling transformation.

- Furthermore, $d_z^{position1} > d_z^{position2} > d_z^{position3}$ because for the calibration points,

$\left|z^{postion1}\right| > \left|z^{postion2}\right| > \left|z^{postion3}\right| > 0$ showing that the conditions for applying LS1 are not respected anymore.

	$x_{theodolite}$ [mm]	$y_{theodolite}$ [mm]	$z_{theodolite}$ [mm]
P10	-996 ±1	458 ±1	-151 ±1
P20	-120 ±1	528 ±1	-166 ±1
P30	845 ±1	573 ±1	-172 ±1
P40	-1029 ±1	10 ±1	-11 ±1
P50	0 ±1	0 ±1	0 ±1
P60	850 ±1	48 ±1	-7 ±1
P70	-989 ±1	-576 ±1	175 ±1
P80	-85 ±1	-743 ±1	234 ±1
P90	860 ±1	-730 ±1	238 ±1

Table 19: Object-coordinates of the reference points as measured by theodolite for the plate in position 1

	r_x [mm]	r_y [mm]	r_z [mm]
Least squares method 1 (LS1)	-0.110	-0.054	0.153
Double-pinhole method (DPH)	-0.063	0.000	0.192
Least squares method 2 (LS2)	-0.064	0.002	0.185

Table 20: interferometric parameters obtained by the different methods

a)
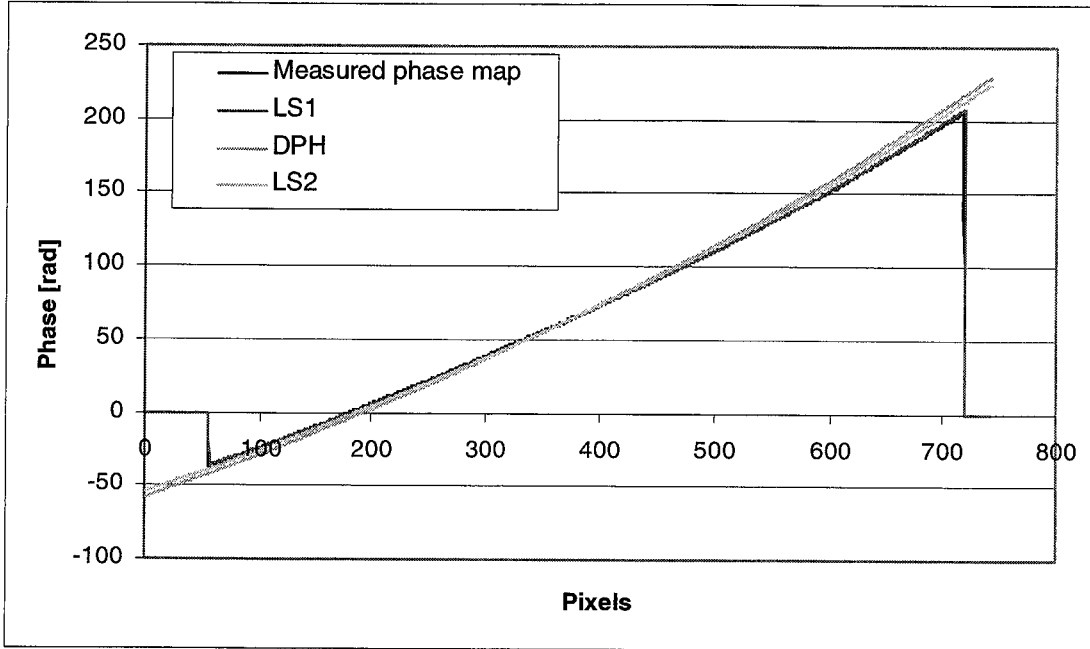
b)

Figure 5: Comparison of the measured phase map to the reference phases map profiles obtained by different methods (a) along a horizontal line and (b) along a vertical line

Figure 6: Height map obtained for the plate in position 1 using the LS1 method (left) and the DPH method (right)
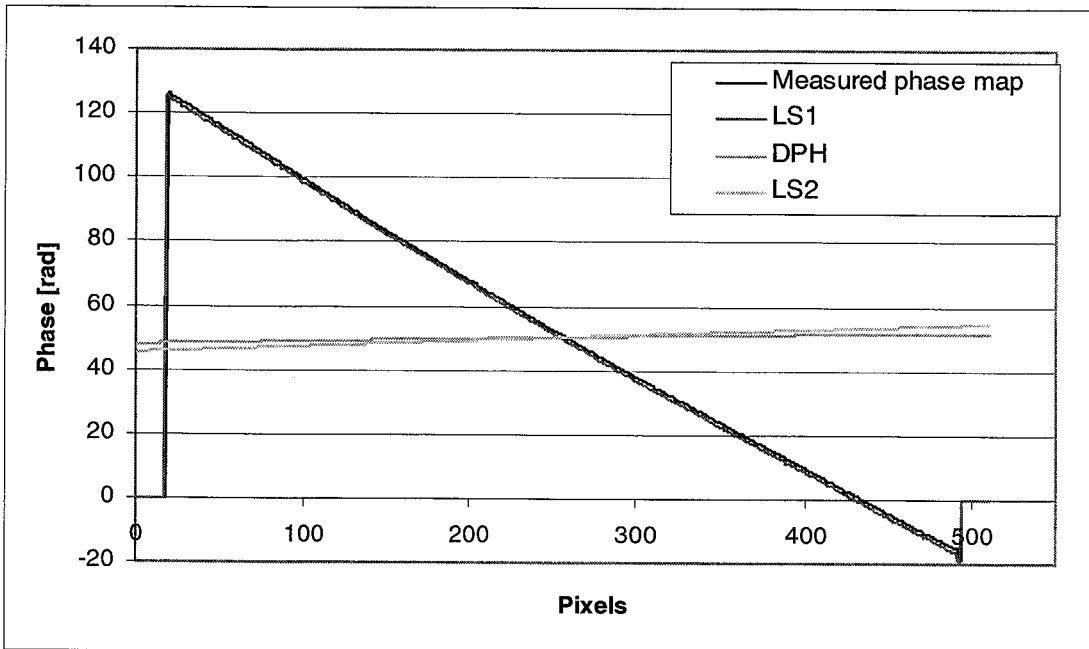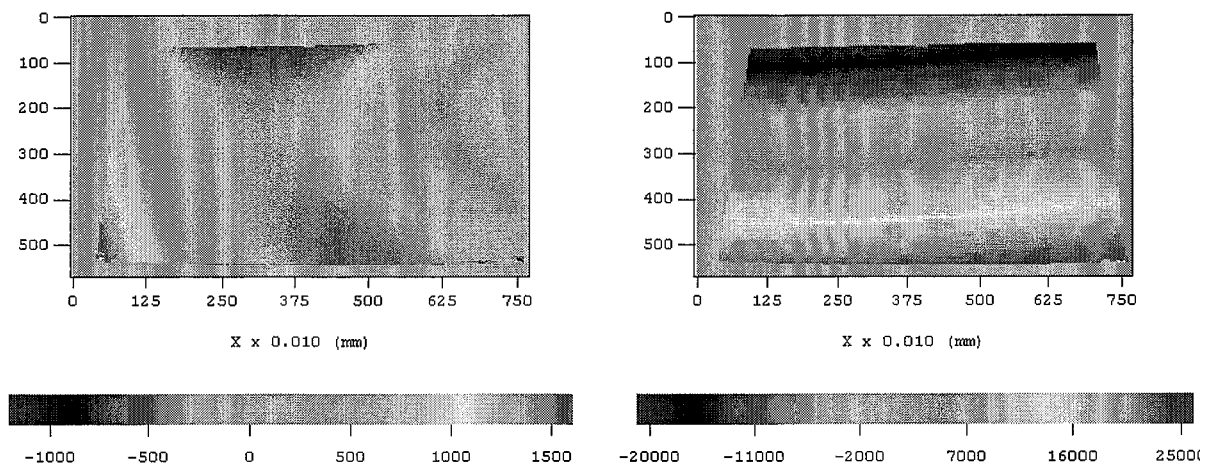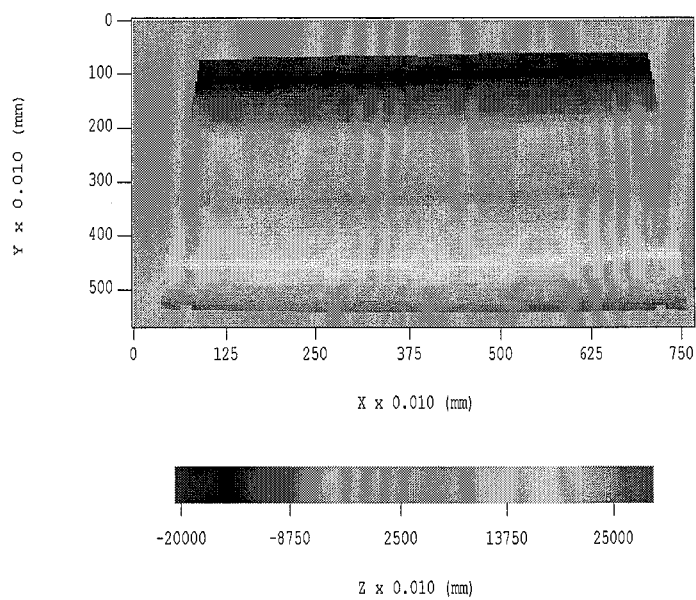

Figure 7: Height map obtained for the plate in position 1 using the LS2 method.

	$x_{LeastSqr.1}$ [mm]	$y_{LeastSqr.1}$ [mm]	$z_{LeastSqr.1}$ [mm]	d [mm]	d_z [mm]	d_{xy} [mm]	d_x [mm]	d_y [mm]
P10	-996	458	2.27	153.27	153.27	0	0	0
P20	-131.2	530.4	-5.11	161.30	160.89	11.45	-11.2	2.4
P30	845	573	4.65	176.65	176.65	0	0	0
P40	-1035.4	40.9	7.74	36.70	18.74	31.56	-6.4	30.9
P50	-6.5	41.3	-2.01	41.86	-2.01	41.81	-6.5	41.3
P60	863.2	88.9	7.66	45.41	14.66	42.98	13.2	40.9
P70	-989	-576	11.23	163	-163.77	0	0	0
P80	-89.5	-764.2	-4.02	239	238.02	21.67	-4.5	-21.2
P90	860	-730	0.23	237.77	-237.77	0	0	0

Table 21: Object-coordinates of the control points as calculated by the first least squares method (LS1)

	$x_{DoublePH}$ [mm]	$y_{DoublePH}$ [mm]	$z_{DoublePH}$ [mm]	d [mm]	d_z [mm]	d_{xy} [mm]	d_x [mm]	d_y [mm]
P10	-996	458	-156.27	5.27	-5.27	0	0	0
P20	-131.2	530.4	-165.58	11.46	0.42	11.45	-11.2	2.4
P30	845	573	-155.11	16.89	16.89	0	0	0
P40	-1035.4	40.9	-27.09	35.42	-16.09	31.56	-6.4	30.9
P50	-6.5	41.3	-8.67	42.70	-8.67	41.81	-6.5	41.3
P60	863.2	88.9	4.55	44.5	11.55	42.98	13.2	40.9
P70	-989	-576	150.51	25.51	-25.51	0	0	0
P80	-89.5	-764.2	213.17	30.06	-20.83	21.67	-4.5	-21.2
P90	860	-730	234.42	3.58	-3.58	0	0	0

Table 22: Object-coordinates of the control points as calculated by the "Double pinhole" method (DPH)

	$x_{LeastSqr.2}$ [mm]	$y_{LeastSqr.2}$ [mm]	$z_{LeastSqr.2}$ [mm]	d [mm]	d_z [mm]	d_{xy} [mm]	d_x [mm]	d_y [mm]
P10	-996	458	-149.07	1.93	1.93	0	0	0
P15	-131.2	530.4	-169.08	11.86113	-3.08	11.45	-11.2	2.4
P20	845	573	-169.87	2.13	2.13	0	0	0
P25	-1035.4	40.9	-11.77	31.56522	-0.77	31.55	-6.4	30.9
P30	-6.5	41.3	-4.57	42.0574	-4.57	41.81	-6.5	41.3
P35	863.2	88.9	-1.53	43.32402	5.47	42.98	13.2	40.9
P40	-989	-576	176.84	1.84	1.84	0	0	0
P45	-89.5	-764.2	233.34	21.68238	-0.66	21.67	-4.5	-21.2
P50	860	-730	243.93	5.93	5.93	0	0	0

Table 23: Object-coordinates of the control points as calculated by the second least squares method (LS2)

In a general way, in the cases where the plate is inclined (position 1 and 2), the second least squares method (LS2) gives better results than double pinhole method (DPH), which in turn gives better results than the first least squares method (LS1). This bad results for LS1 arise mainly because the basic conditions for applying it are not observed anymore (the object lye in the plane (x, y, z = 0)) and a therefore, its reference phase map is wrong. When the plate is positioned closer to the plane $z=0$, LS1 gives better evaluation of their height than the double pinhole method. In this case however, the LS2 method remains the best, showing thereby the potential of the double-pinholes method.

1. 3. 3.   Surfboard

The same measurement and evaluation procedures where done on a object that is positioned parallel to the imaging plane of the camera, but is not plane: a windsurf board of about 1 x 3.2 m. Here, the reference points P10, P40, P50 and P80 are used for calibrating the relation between the object- and image-coordinates. The origin of the object-coordinate system is chosen approximately in the middle of the image and belongs to the median plane of the windsurf board. This measurement confirms the results found above for the inclined plane as regards the effect of calibration points departing from the plane (z = 0) on the calibration of the projection head. The object-coordinates of the reference points as measured with the theodolite are presented in Table 12. The values found for the parameters r_x, r_y, r_z using the three methods are displayed in Table 13. They were used to calculated the reference phase maps shown in Figure 9 and the height of the control points. Height maps of the object are shown in Figure 10. Tables 14 to16 present the object-coordinates of the control points and deviations obtained by the three methods.
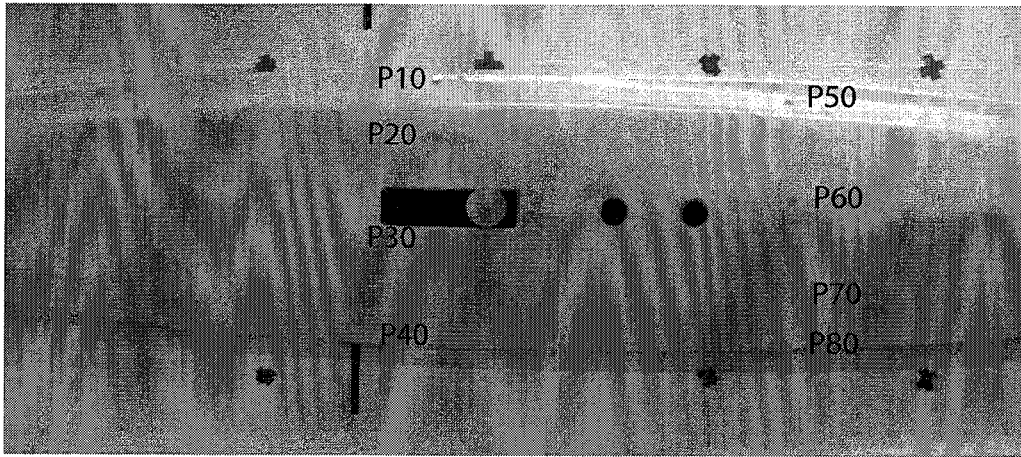
Figure 8: Image of the surfboard and positioning of the reference points

	$x_{theodolite}$ [mm]	$y_{theodolite}$ [mm]	$z_{theodolite}$ [mm]
P10	-432	330.5	-7
P20	-427	188.5	69
P30	-427	-46.5	75
P40	-417	-316.5	-15
P50	429	277.5	15
P60	423	35.5	88
P70	428	-206.5	59
P80	424	-323.5	-7

Table 24: Object-coordinates of the reference points as measured by theodolite for the surfboard

	r_x [mm]	r_y [mm]	r_z [mm]
Least squares method 1 (LS1)	-0.264	0.008	0.060
Double-pinhole method (DPH)	-0.063	0.000	0.192
Least squares method 2 (LS2)	-0.060	0.002	0.188

Table 25: lObject-nterferometric parameters obtained by the different methods

a)
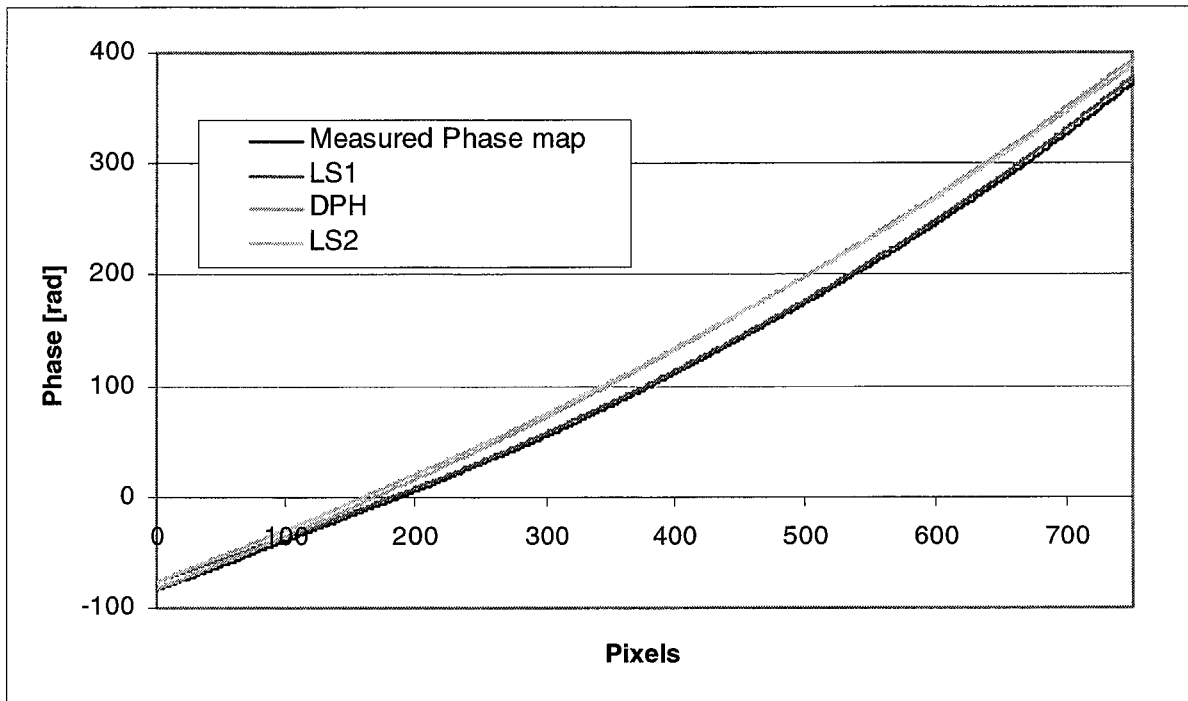
b)

Figure 9: Windsurf board. Profile of the phase map along a (a) horizontal ad (b) vertical line.
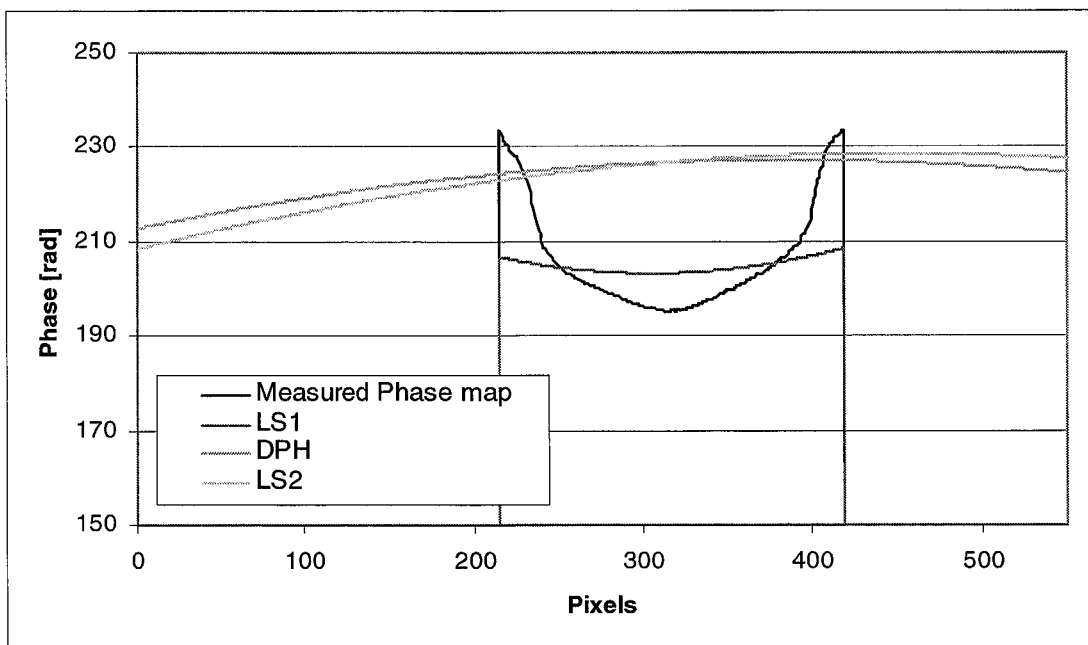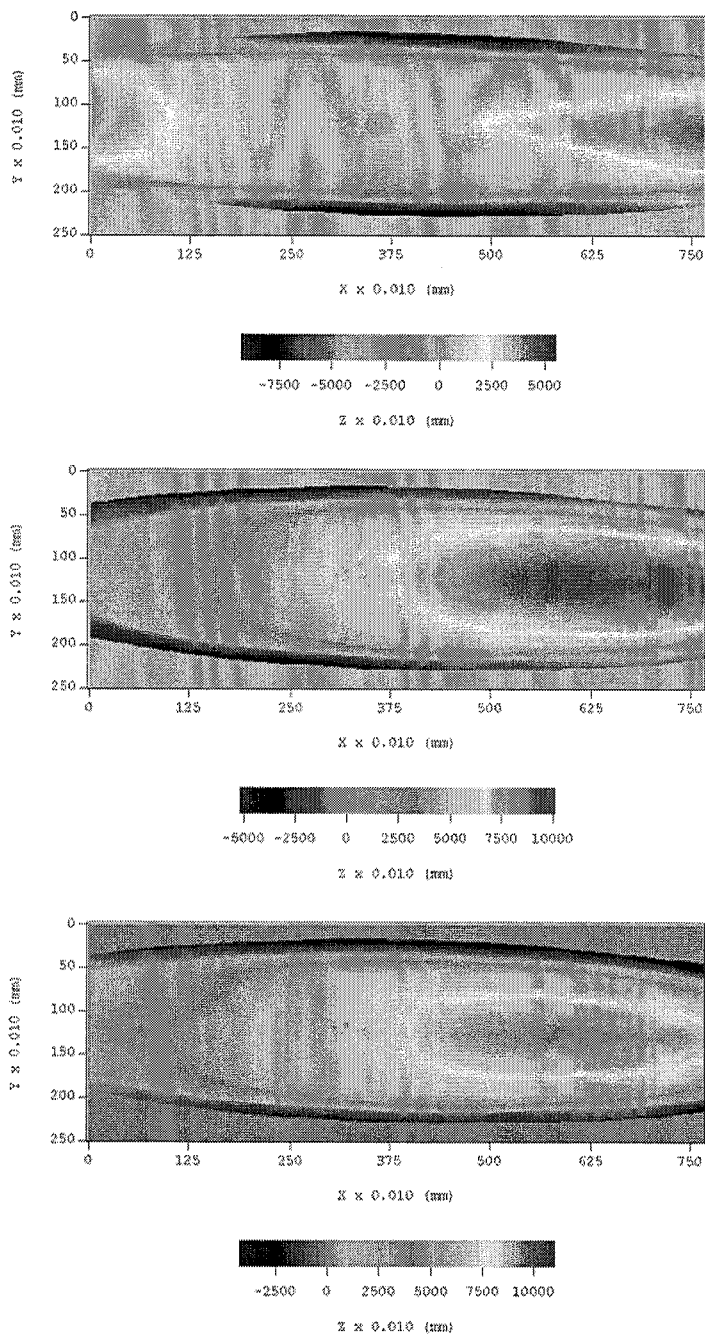
Figure 10: Height map obtained for the windsurf board using the LS1 (top), DPH (middle) and the LS2 (bottom) methods

	$x_{LeastSqr.1}$ [mm]	$y_{LeastSqr.1}$ [mm]	$z_{LeastSqr.1}$ [mm]	d [mm]	d_z [mm]	d_{xy} [mm]	d_x [mm]	d_y [mm]
P10	-432	330.5	-59.9	52.9	-52.9	0	0	0
P20	-425.8	191.2	9.33	59.74311	-59.67	2.95	1.2	2.7
P30	-429.6	-47.7	10.39	64.67343	-64.61	2.86	-2.6	-1.2
P40	-417	-316.5	-75.4	60.4	-60.4	0	0	0
P50	429	277.5	-42.69	57.69	-57.69	0	0	0
P60	440.9	29	27.5	63.42641	-60.5	19.04	17.9	-6.5
P70	443	-219.6	-1.3	63.50354	-60.3	19.91	15	-13.1
P80	424	-323.5	-66.42	59.42	-59.42	0	0	0

Table 26: Object- coordinates of the control points as calculated by the first least squares method (LS1)

	$x_{DoublePH}$ [mm]	$y_{DoublePH}$ [mm]	$z_{DoublePH}$ [mm]	d [mm]	d_z [mm]	d_{xy} [mm]	d_x [mm]	d_y [mm]
P10	-432	330.5	-16.85	9.85	-9.85	0	0	0
P20	-425.8	191.2	54.45	14.84697	-14.55	2.95	1.2	2.7
P30	-429.6	-47.7	59.05	16.20501	-15.95	2.86	-2.6	-1.2
P40	-417	-316.5	-29.76	14.76	-14.76	0	0	0
P50	429	277.5	14.27	0.73	-0.73	0	0	0
P60	440.9	29	95.81	20.58291	7.81	19.04	17.9	-6.5
P70	443	-219.6	61.44	20.06399	2.44	19.91	15	-13.1
P80	424	-323.5	-11.08	4.08	-4.08	0	0	0

Table 27: Object- coordinates of the control points as calculated by the "Double pinhole" method (DPH)

	$x_{LeastSqr.2}$ [mm]	$y_{LeastSqr.2}$ [mm]	$z_{LeastSqr.2}$ [mm]	d [mm]	d_z [mm]	d_{xy} [mm]	d_x [mm]	d_y [mm]
P10	-432	330.5	-11.06	4.06	-4.06	0	0	0
P20	-425.8	191.2	63.54	6.208188	-5.46	2.95	1.2	2.7
P30	-429.6	-47.7	71.19	4.766141	-3.81	2.86	-2.6	-1.2
P40	-417	-316.5	-16.77	1.77	-1.77	0	0	0
P50	429	277.5	7.95	7.05	-7.05	0	0	0
P60	440.9	29	94.72	20.19451	6.72	19.04	17.9	-6.5
P70	443	-219.6	62.42	20.20659	3.42	19.91	15	-13.1
P80	424	-323.5	-10.31	3.31	-3.31	0	0	0

Table 28: Object- coordinates of the control points as calculated by the second least squares method (LS2)

1. 4.   Appendix D: Solutions of the non-linear set of equations

The set of equations to be solved is:

$$\left\{ \begin{array}{l} \varphi(x,y,z) = \dfrac{2\pi}{\lambda} \cdot \dfrac{((R_x - x)r_x + (R_y - y)r_y + (R_z - z)r_z)}{\sqrt{(R_x - x)^2 + (R_y - y)^2 + (R_z - z)^2}} \\[3mm] x = X_0 + (z - Z_0)\dfrac{r_{11}(\xi - \xi_0) + r_{12}(\eta - \eta_0) + r_{13} \cdot c}{r_{13}(\xi - \xi_0) + r_{23}(\eta - \eta_0) + r_{33} \cdot c} \\[3mm] y = Y_0 + (z - Z_0)\dfrac{r_{21}(\xi - \xi_0) + r_{22}(\eta - \eta_0) + r_{23} \cdot c}{r_{13}(\xi - \xi_0) + r_{23}(\eta - \eta_0) + r_{33} \cdot c} \end{array} \right. \qquad (1)$$

By defining:

$$c_1 = \frac{r_{11}(\xi - \xi_0) + r_{12}(\eta - \eta_0) + r_{13}c}{r_{31}(\xi - \xi_0) + r_{32}(\eta - \eta_0) + r_{33}c}$$

$$c_2 = \frac{r_{21}(\xi - \xi_0) + r_{22}(\eta - \eta_0) + r_{23}c}{r_{31}(\xi - \xi_0) + r_{32}(\eta - \eta_0) + r_{33}c}$$

$$c_4 = \left(\frac{2\pi}{532 \cdot 10^{-6}}\right)^2,$$

the set of Equation (1) can be written:

$$\left\{ \begin{array}{c} \{\varphi(x,y,z)\}^2 \cdot \{(R_x - x)^2 + (R_y - y)^2 + (R_z - z)^2\} = c_4 \cdot \{(R_x - x)r_x + (R_y - y)r_y + (R_z - z)r_z\} \\[2mm] x = X_0 + (z - Z_0) \cdot c_1 \\[2mm] y = Y_0 + (z - Z_0) \cdot c_2 \end{array} \right. ,$$

which is solved analytically. There are two analytical solutions due to the squared terms in the first equation. These are related with the symmetrical distribution of the fringes relative to the zero order fringes. These two set of solutions are presented in Figure 11.

Figure 11: Solutions of the set of Equations (1) describing the system in the model developed in the general method.

1. 5.   Appendix E: Coordinates and deviations computed by the general method for the objects measured in Chapter 4

1. 5. 1.   Planar object parallel to the imaging plane of the camera: the wall

	x (mm)	y (mm)	z (mm)	d (mm)	d_z (mm)	d_{xy} (mm)	d_x (mm)	d_y (mm)
P10	-960.26	839.12	3.91	2.59	1.91	1.74	1.74	0.12
P20	41.90	842.13	-0.63	10.52	-2.63	10.19	-1.10	10.13
P30	1248.85	831.80	-2.16	5.64	-3.16	4.67	-4.52	-1.20
-991.59	-991.60	11.34	2.00	2.93	1.00	2.85	2.41	1.34
P50	-1.62	0.96	0.72	2.02	0.72	1.88	-1.62	0.96
P60	1260.92	-11.96	1.88	3.47	1.88	2.92	2.92	0.04
P70	-968.17	-888.52	4.86	7.86	3.86	6.84	6.83	0.48
P80	-0.67	-856.54	-2.73	8.99	-2.73	8.56	-0.67	-8.54
P90	1180.85	-889.51	-1.40	4.26	-1.40	4.03	-3.15	-2.51

Table 29: Object-coordinates of the control points on the wall calculated by the general method described in Chapter 4

1. 5. 2.   First evaluation of the precision of the general method: the plate in vertical position

	<x> (mm)	<y > (mm)	<z> (mm)	<d> (mm)	<d_z> (mm)	<d_{xy}> (mm)	<d_x> (mm)	<d_y> (mm)
P10	-994.29	471.67	12.00	5.49	1.00	5.40	4.71	-2.63
P20	-99.34	583.32	-0.79	7.45	0.21	7.45	-1.34	7.32
P30	838.58	607.16	-11.78	4.42	-1.78	4.04	-3.42	2.16
P40	-953.70	-60.88	12.51	2.10	-0.49	2.04	-1.70	1.23
P50	2.99	-0.11	1.38	3.30	1.38	3.00	2.99	-0.11
P60	834.65	-28.55	-5.81	3.30	1.18	3.08	2.66	-1.55
P70	-981.63	-608.60	17.66	1.57	0.66	1.42	1.37	0.40
P80	-38.82	-772.52	5.87	7.52	-0.12	7.52	0.182	-7.52
P90	863.02	-761.49	-5.26	4.60	-2.26	4.01	-3.98	0.51

Table 30: Plate in vertical position. Average of the calibration-points object coordinates and of the different distances

	σ_x (mm)	σ_y (mm)	σ_z (mm)
P10	0.88	0.84	0.69
P20	1.31	1.05	1.32
P30	1.16	1.47	0.97
P40	1.32	0.29	1.03
P50	1.99	0.98	1.33
P60	0.39	1.27	0.74
P70	0.68	10.6	1.00
P80	1.47	1.06	1.33
P90	0.58	0.96	0.60

Table 31: Standard deviation of the calibration-points physical coordinates

1. 5. 3. Planar object not parallel to the imaging plane of the camera: the inclined plate

	x (mm)	y (mm)	z (mm)	d (mm)	d_z (mm)	d_{xy} (mm)	d_x (mm)	d_y (mm)
P10	-993.79	469.60	-81.89	4.57	1.07	4.43	4.20	-1.40
P20	-120.84	550.16	-85.01	3.51	0.98	3.37	1.16	3.16
P30	840.07	594.09	-82.37	3.75	-1.37	3.49	-2.92	-1.90
P40	-1030.45	7.96	-11.88	1.74	0.11	1.74	-1.45	0.96
P50	0.69	1.64	0.76	1.94	0.76	1.78	0.69	1.64
P60	855.17	55.72	4.19	6.48	1.19	6.37	5.17	3.72
P70	-985.58	-601.05	82.65	2.12	-0.35	2.09	0.42	-2.04
P80	-83.63	-776.20	117.72	6.54	-1.28	6.42	-1.63	-6.20
P90	858.73	-752.46	127.21	4.61	-0.79	4.54	-4.27	1.54

Table 32: Object-Objectcoordinates and distances calculated for the plate in position 2 using the general method described in Chapter 4

1. 6. Appendix F: The rotated plate measured using the general method:

1. 6. 1. position 3: 0° rotation:

	$x_{theodolite}$ (mm)	$y_{theodolite}$ (mm)	$z_{theodolite}$ (mm)
P10	-998 ±1	476 ±1	3 ±1
P20	-122 ±1	553 ±1	17 ±1
P30	843 ±1	603 ±1	32 ±1
P40	-1027 ±1	5 ±1	-11 ±1
P50	0 ±1	0 ±1	0 ±1
P60	851 ±1	53 ±1	15 ±1
P70	-984 ±1	-607 ±1	-29 ±1
P80	-79 ±1	-780 ±1	-24 ±1
P90	865 ±1	-764 ±1	-10 ±1

Table 33: Object- coordinates of the control points on the plate in position 3, as measured using the theodolite

- **System parameters:**
  After calibration using all the nine reference points, the values found are:

*Interferometric parameters: r_x = -0.060 mm; r_y = 0.002 mm; r_z = 0.188 mm

*Exterior orientation parameters:

X_0 = -37.22 mm; Y_0 = -145.38 mm; Z_0 = 2920.10 mm; ω = 9.70 · $10^{-3} rad$;

ϕ = 38.20 · $10^{-3} rad$; κ = 1.45 · $10^{-3} rad$. This values were determined after 6 iterations.

*Interior orientation parameters:

ξ_0 = -57.1 · 10^{-3} mm; η_0 = -106.2 · 10^{-3} mm; c = 7.66 mm

- **Results:**
The following object-coordinates were calculated for the reference points used as control points using the general method:

	x (mm)	y (mm)	z (mm)	d (mm)	d_z (mm)	d_{xy} (mm)	d_x (mm)	d_y (mm)
P10	-997.66	471.93	3.12	4.09	0.12	4.08	0.34	-4.07
P20	-125.98	560.89	16.08	8.88	-0.92	8.83	-3.98	7.88
P30	840.60	599.00	30.91	4.79	-1.08	4.67	-2.40	-4.00
P40	-1027.63	5.92	-11.74	1.34	-0.74	1.11	-0.63	0.92
P50	5.86	-1.21	1.70	6.22	1.70	5.98	5.86	-1.21
P60	855.15	55.71	17.01	5.35	2.01	4.95	4.15	2.71
P70	-982.38	-604.93	-28.72	2.64	0.27	2.63	1.62	2.07
P80	-81.19	-784.41	-23.71	4.93	0.29	4.92	-2.19	-4.41
P90	862.38	-763.86	-11.64	3.10	-1.64	2.62	-2.62	0.14

Table 34: Object-coordinates and distances calculated for the plate in position 3, using the general method described in Chapter 4.

	$\varphi^{measured}$ [rad]	$\varphi^{calculated}$ [rad]	$d\varphi$ [rad]
P10	-48.080	-48.087	-0.007
P20	36.596	36.776	0.180
P30	159.412	159.326	-0.086
P40	-44.840	-45.006	-0.165
P50	59.667	59.544	-0.123
P60	171.144	171.292	0.148
P70	-33.305	-33.364	-0.059
P80	60.869	61.216	0.347
P90	186.533	186.313	-0.220

Table 35: Phase calculated for the plate in position 3, using the first equation of the set of Equations (4.3)

163

	x (mm)	y (mm)	d_{xy} (mm)	d_x (mm)	d_y (mm)
P10	-997.70	471.95	4.056	0.30	-4.04
P20	-125.95	560.65	8.62	-3.95	7.65
P30	840.27	598.72	5.08	-2.73	-4.28
P40	-1027.38	5.88	0.96	-0.38	0.88
P50	5.88	-1.12	5.99	5.88	-1.12
P60	855.76	55.85	5.55	4.76	2.85
P70	-982.47	-604.97	2.543	1.53	2.03
P80	-81.19	-784.47	4.98	-2.19	-4.47
P90	861.87	-763.51	3.16	-3.13	0.49

Table 36: Planimetric object-coordinates calculated for the plate in position 3, using the two last equations of the set of Equations (4.3)

1. 6. 2. Position 2: 10° rotation

	$\varphi^{measured}$ [rad]	$\varphi^{calculated}$ [rad]	$d\varphi$ [rad]
P10	-5.38	-5.46	-0.08
P20	89.82	90.04	0.22
P30	223.63	223.56	-0.07
P40	-28.53	-28.37	0.16
P50	78.34	78.53	0.19
P60	197.57	197.21	-0.36
P70	-51.11	-51.28	-0.17
P80	30.84	30.58	-0.26
P90	153.51	153.87	0.35

Table 37: Phase calculated for the plate in position 2, using using the first equation of the set of Equations (4.3))

	x (mm)	y (mm)	d_{xy} (mm)	d_x (mm)	d_y (mm)
P10	-992.78	468.86	5.64	5.21	-2.14
P20	-120.90	553.30	6.39	1.10	6.30
P30	838.25	593.19	5.52	-4.75	-2.81
P40	-1030.56	7.94	1.82	-1.56	0.94
P50	1.75	3.50	3.92	1.75	3.50
P60	855.46	56.10	6.83	5.46	4.10
P70	-985.13	-600.98	2.16	0.87	-1.98
P80	-83.80	-778.72	8.91	-1.80	-8.76
P90	857.73	-752.59	5.452	-5.27	1.41

Table 38: Planimetric object-coordinates calculated for the plate in position 2, using the two last equations of the set of Equations (4.3)

1. 6. 3. Position 1: 20° rotation

	$x_{theodolite}$ (mm)	$y_{theodolite}$ (mm)	$z_{theodolite}$ (mm)
P10	-996 ±1	458 ±1	-151 ±1
P20	-120 ±1	528 ±1	-166 ±1
P30	845 ±1	573 ±1	-172 ±1
P40	-1029 ±1	10 ±1	-11 ±1
P50	0 ±1	0 ±1	0 ±1
P60	850 ±1	48 ±1	-7 ±1
P70	-989 ±1	-576 ±1	175 ±1
P80	-85 ±1	-743 ±1	234 ±1
P90	860 ±1	-730 ±1	238 ±1

Table 39: Object-coordinates of the reference points as measured by theodolite for the plate in position 1

- **System parameters:**
  After calibration using all the nine reference points, the values found are:

*Interferometric parameters: $r_x = -0.057$ mm; $r_y = 0.002$ mm; $r_z = 0.188$ mm

*Exterior orientation parameters:

$$X_0 = -29.36 \ mm; \quad Y_0 = -132.84 \ mm; \quad Z_0 = 3032.79 \ mm; \quad \omega = -4.26 \cdot 10^{-3} rad;$$

$$\phi = 2.25 \cdot 10^{-3} rad \ ; \kappa = 38.88 \cdot 10^{-3} rad.$$ This values were determined after 8 iterations.

*Interior orientation parameters:

$$\xi_0 = -57.1 \cdot 10^{-3} \ mm; \quad \eta_0 = -106.2 \cdot 10^{-3} \ mm; \quad c = 7.66 \ mm$$

• **Results:**

The following object-coordinates were calculated for the reference points used as control points using the general method:

	x (mm)	y (mm)	z (mm)	d (mm)	d_z (mm)	d_{xy} (mm)	d_x (mm)	d_y (mm)
P10	-989.02	453.22	-147.69	9.08	3.31	8.459	6.98	-4.78
P20	-117.18	529.97	-165.34	3.50	0.66	3.44	2.82	1.97
P30	841.07	574.49	-174.04	4.67	-2.04	4.20	-3.93	1.49
P40	-1031.15	11.34	-10.26	2.64	0.74	2.53	-2.15	1.34
P50	3.95	5.45	-0.37	6.74	-0.37	6.73	3.95	5.45
P60	853.55	48.78	-5.11	4.10	1.89	3.63	3.55	0.78
P70	-993.08	-577.12	174.37	4.28	-0.62	4.23	-4.08	-1.12
P80	-83.51	-750.65	232.25	7.99	-1.75	7.79	1.49	-7.65
P90	854.37	-727.92	237.38	6.03	-0.62	6.00	-5.62	2.08

Table 40: Object-coordinates and deviations calculated for the plate in position 1, using the general method described in Chapter 4

	$\varphi^{measured}$ [rad]	$\varphi^{calculated}$ [rad]	$d\varphi$ [rad]
P10	-16.076	-15.803	0.273
P20	87.351	87.220	-0.131
P30	230.072	229.999	-0.073
P40	-60.010	-59.578	0.431
P50	49.774	49.173	-0.601
P60	173.106	173.250	0.143
P70	-110.570	-110.402	0.168
P80	-37.699	-38.504	-0.804
P90	82.466	83.080	0.614

Table 41: Phase calculated for the plate in position 1, using the first equation of the set of Equations (4.3)

	x (mm)	y (mm)	d_{xy} (mm)	d_x (mm)	d_y (mm)
P10	-990.02	453.83	7.29	5.98	-4.17
P20	-117.20	530.11	3.50	2.80	2.11
P30	840.51	574.04	4.60	-4.49	1.04
P40	-1031.39	11.38	2.76	-2.39	1.38
P50	3.95	5.43	6.72	3.95	5.43
P60	854.10	48.90	4.19	4.10	0.90
P70	-992.87	-577.02	4.00	-3.87	-1.02
P80	-83.47	-750.26	7.42	1.53	-7.26
P90	854.18	-727.79	6.23	-5.82	2.21

Table 42: Planimetric object-coordinates calculated for the plate in position 1, using the two last equations of the set of Equations (4.3)

1. 7.   Appendix G: Different measurements done with the general method

1. 7. 1.   Shape measurement of different objects

1. 7. 1. a.   The windsurf board

The interferometric parameters were tested according to the same method described in Chapter 4, Section 4.2.5 and gave the following results:

	$\varphi_{measured}$ (rad)	$\varphi_{calculated}$ (rad)	$d\varphi$ (rad)
P10	815.652	815.933	0.282
P20	794.323	793.683	-0.640
P30	792.728	793.002	0.275
P40	823.727	823.840	0.113
P50	979.579	979.547	-0.033
P60	955.575	955.939	0.364
P70	968.215	967.675	-0.540
P80	988.636	988.779	0.144

Table 43: Windsurf board. Measured and calculated phase at the reference point, using the first Equation in (4.3)

The central perspective parameters were tested according to the same method described in Chapter 4; Section 4.2.5 and gave the following results

	$x_{calculated}$ (mm)	$y_{calculated}$ (mm)	d_{xy} (mm)	d_x (mm)	d_y (mm)
P10	-433.20	330.22	1.23	-1.20	-0.27
P20	-425.12	188.91	1.92	1.88	0.41
P30	-428.09	-44.25	2.50	-1.09	2.25
P40	-416.56	-318.14	1.70	0.44	-1.64
P50	428.79	278.14	0.67	-0.21	0.64
P60	421.22	33.78	2.47	-1.78	-1.71
P70	428.81	-209.69	3.29	0.81	-3.19
P80	425.21	-319.92	3.77	1.21	3.57

Table 44: Windsurf board. Planimetric object-coordinates as calculated using the central perspective equations.

1. 7. 1. b.   Car part

The interferometric parameters were tested according to the same method described in Chapter 4, Section 4.2.5 and gave the following results:

	$\varphi_{measured}$ (rad)	$\varphi_{calculated}$ (rad)	$d\varphi$ (rad)
P10	-24.721	-11.311	13.409
P20	148.969	148.874	-0.095
P30	33.689	33.836	0.147
P40	-60.801	-60.816	-0.015
P50	160.259	160.419	0.160
P60	1.589	1.283	-0.306
P70	-91.511	-91.363	0.148
P80	91.219	91.181	-0.038

Table 45: Car part. Measured and calculated phase at the control points, and their difference.

The central perspective parameters were tested according to the same method described in Chapter 4; Section 4.2.5 and gave the following results:

	$x_{calculated}$ (mm)	$y_{calculated}$ (mm)	d_{xy} (mm)
P10	-431.77	551.07	57.82
P20	391.56	541.4	2.55
P30	-39.765	265.83	3.42
P40	-455.38	19.76	1.32
P50	456.98	-18.17	2.00
P60	-74.126	-242.18	3.68
P70	-540.01	-547.75	1.24
P80	376.79	-548.29	0.29

Table 46: Car part. Planimetric object-coordinates as calculated using the central perspective equations.

1. 7. 2. Measurement with different configurations of the set-up.

1. 7. 2. a.   Configuration 1

The interferometric parameters were tested according to the same method described in Chapter 4, Section 4.2.5 and gave the following results

	Point 1	Point 2	Point 3	Point 4	Point 5
Measured phase (rad)	-274.97	38.28	-116.44	-256.59	73.60
Calculated phase (rad)	-275.29	38.47	-116.43	-256.28	73.41
Phase difference (rad)	-0.32	0.19	0.01	0.31	-0.19

Table 47: Configuration 1.   Measured and calculated phase at the control points, and their difference.

The central perspective parameters were tested according to the same method described in Chapter 4; Section 4.2.5 and gave the following results:

Planimetric object-coordinates...	**Point 1**	**Point 2**	**Point 3**	**Point 4**	**Point 5**
... as measured using the theodolite (mm)	X = -1000 Y = 472	X = 841 Y = 605	X = 0 Y = 0	X = -983 Y = -610	X = 867 Y = -761
... as calculated using the central perspective equations (mm)	X = -998.14 Y = 471.59	X = 840.96 Y = 607.05	X = 1.6914 Y = 1.0201	X = -984.12 Y = -611.95	X = 864.65 Y = -761.82
Planimetric deviation (mm)	d_{xy} = 1.91	d_{xy} =2.05	d_{xy} =1.97	d_{xy} = 2.24	d_{xy} = 2.49

Table 48: Configuration 1. Planimetric object-coordinates as calculated using the central perspective equations

1. 7. 2. b.   Configuration 2

The interferometric parameters were tested according to the same method described in Chapter 4, Section 4.2.5 and gave the following results:

	Point 1	**Point 2**	**Point 3**	**Point 4**	**Point 5**
Measured phase (rad)	-257.54	55.05	-99.16	-239.28	91.67
Calculated phase (rad)	-258.19	55.43	-99.14	-238.64	91.28
Phase difference (rad)	-0.65	0.39	0.02	0.64	-0.39

Table 49: Configuration 2.   Measured and calculated phase at the control points, and their difference.

The central perspective parameters were tested according to the same method described in Chapter 4; Section 4.2.5 and gave the following results:

Planimetric object-coordinates...	**Point 1**	**Point 2**	**Point 3**	**Point 4**	**Point 5**
... as measured using the theodolite (mm)	x = -1000 y = 473	x = 841 y = 605	x = 0 y = 0	x = -983 y = -610	x = 867 y = -761
... as calculated using the central perspective equations (mm)	x = -998.22 y = 470.04	x = 840.57 y = 604.19	x = 4.8589 y = 4.6882	x = -987.3 y = -610.59	x = 865.8 y = -759.67
Planimetric deviation (mm)	$d_{xy} = 3.45$	$d_{xy} = 0.92$	$d_{xy} = 6.75$	$d_{xy} = 4.33$	$d_{xy} = 1.79$

Table 50: Configuration 2. Planimetric object- coordinates as calculated using the central perspective equations

1. 7. 2. c.   Configuration 3

The interferometric parameters were tested according to the same method described in Chapter 4, Section 4.2.5 and gave the following results:

	Point 1	Point 2	Point 3	Point 4	Point 5
Measured phase (rad)	-237.15	74.53	-78.47	-217.93	111.57
Calculated phase (rad)	-237.25	75.21	-78.07	-217.50	111.72
Phase difference (rad)	-0.10	0.68	0.40	0.43	0.15

Table 51: Configuration 3.   Measured and calculated phase at the control points, and their difference.

The central perspective parameters were tested according to the same method described in Chapter 4; Section 4.2.5 and gave the following results:

Planimetric object-coordinates...	Point 1	Point 2	Point 3	Point 4	Point 5
... as measured (mm)	x = -1000 y = 473	x = 841 y = 606	x = 0 y = 0	x = -983 y = -610	x = 866 y = -761
... as calculated (mm)	x = -1000.2 y = 472.82	x = 835.66 y = 597.18	x = 11.945 y = 3.0229	x = -987.51 y = -610.89	x = 867.52 y = -753.02
Planimetric deviation (mm)	d_{xy} = 0.30	d_{xy} = 10.31	d_{xy} = 12.32	d_{xy} = 4.60	d_{xy} = 8.13

Table 52: Configuration 3. Planimetric object- coordinates as calculated using the central perspective equations

1. 7. 2. d. Configuration 4

The interferometric parameters were tested according to the same method described in Chapter 4, Section 4.2.5 and gave the following results:

	Point 1	Point 2	Point 3	Point 4	Point 5
Measured phase (rad)	-178.45	201.04	12.69	-157.42	242.98
Calculated phase (rad)	-178.84	200.81	12.70	-157.04	242.31
Phase difference (rad)	-0.38	-0.22	0.01	0.38	-0.68

Table 53: Aluminium plate, Configuration 4. Measured and calculated phase at the control points, and their difference.

The central perspective parameters were tested according to the same method described in Chapter 4; Section 4.2.5 and gave the following results:

Planimetric object-coordinates...	Point 1	Point 2	Point 3	Point 4	Point 5
... as measured (mm)	x = -1000 y = 474	x = 841 y = 605	x = 0 y = 0	x = -984 y = -609	x = 866 y = -761
... as calculated (mm)	x = -1002.2 y = 475.65	x = 839.26 y = 603.84	x = 3.7236 y = 4.1582	x = -987.24 y = -611.65	x = -866.71 y = 763.02
Planimetric deviation (mm)	$d_{xy} = 3.4688$	$d_{xy} = 2.7768$	$d_{xy} = 5.5818$	$d_{xy} = 4.547$	$d_{xy} = 2.15$

Table 54: Aluminium plate, Configuration 4. Planimetric object- coordinates as calculated using the central perspective equations

1. 8.   Static out-of-plane deformation measurement

1. 8. 1.   Position 0

Object-coordinates...	Point1	Point 2	Point 3	Point 4	Point 5	Point6
... as measured with the theodolite (mm)	x = -374.4 y = 657.5 z = 1141	x = 391.55 y = 667.5 z = 426.05	x = 1073.6 y = 704.5 z = -381	x = 173.55 y = 303.5 z = 665.05	x = 622.55 y = 316.5 z = 192.05	x = -356.4 y = -28.5 z = 1108
... as calculated (mm)	x = -370.83 y = 653.4 z = 1141.20	x = 393.21 y = 672.51 z = 426.65	x = 1067.8 y = 702.27 z = -383.76	x = 169.93 y = 305.81 z = 665.43	x = 628.94 y = 319.91 z = 193.18	x = -364.66 y = -27.80 z = 1106.60
Deviations (mm)	d = 5.44 d_z = 0.21	d = 5.31 d_z = 0.60	d = 6.81 d_z = 2.76	d = 4.32 d_z = 0.38	d = 7.33 d_z = 1.13	d = 8.41 d_z = 1.40
Object-coordinates....	Point 7	Point 8	Point 9	Point 10	Point 11	Point 12
.... as measured with the theodolite (mm)	x = 1063.6 y = 28.5 z = -401	x = 189.55 y = -267.5 z = 604.05	x = 591.55 y = -253.5 z = 176.05	x = -397.4 y = -704.5 z = 1057	x = 239.55 y = -704.5 z = 201.05	x = 1020.6 y = -643.5 z = -463
.... as calculated (mm)	x = 1064.7 y = 25.35 z = -398.15	x = 185.42 y = -274.22 z = 603.76	x = 598.84 y = -257.48 z = 175.11	x = -393.61 y = -700.08 z = 1058.2	x = 597.22 y = -677.24 z = 76.363	x = 1018.6 y = -638.8 z = -463.91
Deviations (mm)	d = 4.38 d_z = 2.85	d = 7.90 d_z = 0.29	d = 8.36 d_z = 0.94	d = 5.9284 d_z = 1.15	d = 379.76 d_z = 124.69	d = 5.19 d_z = 0.90

Table 55: Beach Umbrella; Configuration 0. Object- coordinates as measured with the theodolite and calculated using the method described in Chapter 4

	Point1	Point 2	Point 3	Point 4	Point 5	Point6
Measured phase (rad)	44.53	265.89	541.91	184.92	340.60	45.24
Calculated phase (rad)	44.58	265.93	541.55	185.11	340.56	44.98
Phase difference (rad)	0.05	0.047	-0.35	0.19	-0.045	-0.26
	Point 7	Point 8	Point 9	Point 10	Point 11	Point 12
Measured phase (rad)	538.76	195.21	336.58	49.02	358.64	543.95
Calculated phase (rad)	539.55	195.36	335.99	49.21	304.98	543.75
Phase difference (rad)	0.80	0.15	-0.59	0.19	-53.66	-0.20

Table 56: Beach umbrella, Configuration 0.   Measured and calculated phase at the control points, and their difference.

Planimetric object-coordinates...	Point1	Point 2	Point 3	Point 4	Point 5	Point6
...as measured using the theodolite (mm)	X = -374.4 Y = 657.5	X = 391.55 Y = 667.5	X = 1073.6 Y = 704.5	X = 173.55 Y = 303.5	X = 622.55 Y = 316.5	X = -356.4 Y = -28.5
...as calculated (mm)	X = -371.03 Y = 653.49	X = 392.97 Y = 672.67	X = 1068.1 Y = 701.67	X = 169.72 Y = 305.87	X = 628.62 Y = 320.06	X = -363.35 Y = -27.812
Planimetric Deviation (mm)	d_{xy} = 5.2389	d_{xy} = 5.3623	d_{xy} = 6.2087	d_{xy} = 4.499	d_{xy} = 7.0357	d_{xy} = 6.9802
Planimetric object-coordinates...	Point 7	Point 8	Point 9	Point 10	Point 11	Point 12
...as measured using the theodolite (mm)	X = 1063.6 Y = 28.5	X = 189.55 Y = -267.5	X = 591.55 Y = -253.5	X = -397.4 Y = -704.5	X = 239.55 Y = -704.5	X = 1020.6 Y = -643.5
...as calculated (mm)	X = 1064.4 Y = 25.41	X = 185.57 Y = -274.2	X = 599.11 Y = -257.41	X = -394.68 Y = -700.47	X = 632.25 Y = -650.2	X = 1018.7 Y = -638.64
Planimetric Deviation (mm))	d_{xy} = 3.1944	d_{xy} = 7.7916	d_{xy} = 8.5117	d_{xy} = 4.8581	d_{xy} = 396.44	d_{xy} = 5.2189

Table 57: Beach umbrella, Configuration 0. Planimetric object- coordinates as calculated using the central perspective equations

1. 8. 2. Position 2

Object-coordinates...	Point1	Point 2	Point 3	Point 4	Point 5	Point6
... as measured with the theodolite (mm)	x = -547.45 y = 595.5 z = 952.05	x = 283.55 y = 643.50 z = 329.05	x = 867.55 y = 654.50 z = -542.95	x = 112.55 y = 287.50 z = 602.05	x = 556.55 y = 304.50 z = 136.05	x = -471.45 y = -86.50 z = 936.05
... as calculated (mm)	x = -543.83 y = 592.89 z = 944.16	x = 278.74 y = 648.57 z = 323.96	x = 867.96 y = 649.79 z = 529.71	x = 107.96 y = 294.17 z = 602.65	x = 560.66 y = 308.19 z = 134.00	x = -470.97 y = -87.951 z = 939.96
Deviations (mm)	d = 9.07 d_z = 7.89	d = 8.65 d_z =5.09	d = 14.05 d_z = 13.24	d = 8.12 d_z = 0.60	d = 5.89 d_z = 2.05	d = 4.20 d_z = 3.91
Object-coordinates....	Point 7	Point 8	Point 9	Point 10	Point 11	Point 12
.... as measured with the theodolite (mm)	x = 880.55 y = -20.50 z = -509.95	x = 158.55 y = -274.50 z = 532.05	x = 519.55 y = -256.50 z = 149.05	n.m.	x = 447.55 y = -657.50 z = 29.05	x = 784.55 y = -686.50 z = -546.95
.... as calculated (mm)	x = 876.57 y = -19.277 z = -521.00	x = 157.76 y = -276.24 z = 540.90	x = 526.98 y = -260.67 z = 150.75	n.m.	x = 448.91 y = -662.72 z = 30.139	x = 777.88 y = -683.72 z = -552.12
Deviations (mm)	d = 11.81 d_z = 11.05	d = 9.06 d_z = 8.85	d = 8.69 d_z = 1.70	n.m.	d = 5.50 d_z = 1.09	d = 8.88 d_z = 5.17

Table 58: Beach Umbrella; Configuration 2. Object- coordinates as measured with the theodolite and calculated using the method described in Chapter 4; *n.m. = not measured*

	Point1	Point 2	Point 3	Point 4	Point 5	Point6
Measured phase (rad)	796.68	993.64	1266.12	906.63	1059.59	793.85
Calculated phase (rad)	794.49	992.40	1269.71	906.90	1058.77	794.92
Phase difference (rad)	-2.19	-1.24	3.59	0.28	-0.82	1.07
	Point 7	Point 8	Point 9	Point 10	Point 11	Point 12
Measured phase (rad)	1261.418	919.94	1047.32	n.m.	1070.73	1251.99
Calculated phase (rad)	1258.64	922.50	1047.49	n.m.	1071.07	1250.99
Phase difference (rad)	-2.77	2.57	0.17	n.m.	0.34	-0.99

Table 59: Beach umbrella, Configuration 2.   Measured and calculated phase at the control points, and their difference.

Planimetric object-coordinates...	Point1	Point 2	Point 3	Point 4	Point 5	Point6
...as measured using the theodolite (mm)	X =-547.45 Y = 595.5	X =283.55 Y =643.5	X =867.55 Y =654.5	X =112.55 Y =287.5	X =556.55 Y = 304.5	X =-471.45 Y =-86.5
...as calculated (mm)	X = -536.28 Y= 590.45	X = 280.91 Y = 647.26	X =865.87 Y =652.39	X = 107.63 Y = 294.26	X = 561.28 Y = 307.94	X = -474.56 Y = -88.034
Planimetric deviation (mm)	d_{xy} =12.257	d_{xy} = 4.5909	d_{xy} = 2.6977	d_{xy} = 8.3587	d_{xy} = 5.8494	d_{xy} = 3.468
Planimetric object-coordinates...	Point 7	Point 8	Point 9	Point 10	Point 11	Point 12
...as measured using the theodolite (mm)	X = 880.55 Y = -20.50	X =158.55 Y =-274.50	X =519.55 Y =-256.50	n.m.	X =447.55 Y = -657.50	X =784.55 Y =-686.50
...as calculated (mm)	X = 878.29 Y =-19.354	X = 153.2 Y =-277.08	X1 = 526.44 Y1 = -260.8	n.m.	X = 448.56 Y = -662.95	X = 778.82 Y =-682.79
Planimetric deviation (mm)	d_{xy} = 2.5348	d_{xy} = 5.9349	d_{xy} = 8.1229	n.m.	d_{xy} = 5.539	d_{xy} = 6.8232

Table 60: Beach umbrella, Configuration 2. Planimetric object- coordinates as calculated using the central perspective equations

The bad deviations found for point P11 in Table 58 is probably due to an error when reading the image-coordinates of that reference point. This is also the reason why the phase and planimetric deviation for the same point in Tables 59 and 60.

1. 8. 3. Position 4

Object-coordinates...	Point1	Point 2	Point 3	Point 4	Point 5	Point6
... as measured with the theodolite (mm)	x = -679.45 y = 485.50 z = 760.05	x = 193.55 y = 587.50 z = 229.05	x =683.55 y =512.50 z =-680.95	x =60.55 y =252.50 z =534.05	x =496.55 y =260.50 z = 81.05	x =-538.45 y =-183.50 z =742.05
... as calculated (mm)	x = -669.97 y = 483.53 z = 762.41	x = 193.05 y = 591.33 z = 229.04	x = 718.67 y = 481.46 z = -498.21	x = 57.27 y = 255.14 z = 533.92	x = 499.13 y = 264.19 z = 80.34	x = -542.82 y = -185.37 z = 738.82
Deviations (mm)	d = 9.97 d_z = 2.36	d = 3.86 d_z = 0.01	d = 188.66 d_z =182.74	d = 4.21 d_z = 0.13	d = 4.56 d_z = 0.70	d = 5.74 d_z = 3.22
Object-coordinates....	Point 7	Point 8	Point 9	Point 10	Point 11	Point 12
.... as measured with the theodolite (mm)	x = 684.55 y = -152.50 z = -565.95	x = 171.55 y = -297.50 z = 463.05	x = 461.55 y = -288.50 z = 172.05	n.m.	n.m.	x = 482.55 y = -788.50 z = -526.95
.... as calculated (mm)	x = 703.34 y = -148.15 z = -481.42	x = 170.28 y = -300.81 z = 464.23	x = 462.99 y = -292.28 z = 172.90	n.m.	n.m.	x = 474.43 y = -792.09 z = -553.45
Deviations (mm)	d = 86.70 d_z = 84.53	d = 3.74 d_z = 1.18	d = 4.14 d_z = 0.85	n.m.	n.m.	d = 27.95 d_z = 26.50

Table 61: Beach Umbrella; Configuration 4. Object-image-interferometric coordinates as measured with the theodolite and calculated using the method described in Chapter 4; *n.m. = not measured*

	Point1	Point 2	Point 3	Point 4	Point 5	Point6
Measured phase (rad)	353.35	529.00	762.44	434.07	582.36	353.76
Calculated phase (rad)	353.76	528.98	810.52	434.11	581.97	353.07
Phase difference (rad)	0.41	-0.02	48.08	0.04	-0.39	-0.72
	Point 7	Point 8	Point 9	Point 10	Point 11	Point 12
Measured phase (rad)	748.52	449.53	545.55	n.m.	n.m.	740.01
Calculated phase (rad)	770.63	449.96	545.78	n.m.	n.m.	733.42
Phase difference (rad)	22.11	0.44	0.24	n.m.	n.m.	-6.58

Table 62: Beach umbrella, Configuration 4. Measured and calculated phase at the control points, and their difference.

Planimetric object-coordinates...	Point1	Point 2	Point 3	Point 4	Point 5	Point6
...as measured using the theodolite (mm)	X =-679.45 Y =485.5	X =193.55 Y =587.5	X =683.55 Y =512.5	X =60.55 Y =252.5	X =496.55 Y =260.5	X =-538.45 Y =-183.5
...as calculated (mm)	X =-672.21 Y = 484.09	X = 193.06 Y = 591.33	X = 680.41 Y = 508.97	X = 57.342 Y = 255.13	X = 499.36 Y = 264.12	X = -539.97 Y = -185.17
Planimetric deviation (mm)	d_{xy} = 7.38	d_{xy} = 3.86	d_{xy} = 4.73	d_{xy} = 4.15	d_{xy}= 4.59	d_{xy} = 2.26
Planimetric object-coordinates...	Point 7	Point 8	Point 9	Point 10	Point 11	Point 12
...as measured using the theodolite (mm)	X =684.55 Y =-152.5	X =171.55 Y =-297.5	X =461.55 Y =-288.5	n.m.	n.m.	X = 482.55 Y =-788.5
...as calculated (mm)	X = 685.19 Y =-150.66	X = 169.68 Y =-300.93	X = 462.7 Y =-292.36	n.m.	n.m.	X = 481.72 Y = -786.51
Planimetric deviation (mm)	d_{xy} = 1.95	d_{xy} = 3.91	d_{xy} =4.03	n.m.	n.m.	d_{xy} = 2.15

Table 63: Beach umbrella, Configuration 4. Planimetric object-coordinates as calculated using the central perspective equations

The bad deviations found for point P3 in table 61 is probably due to a local error in the phase at that reference point. This is further confirmed by the phase deviation for the same point in Table 62.

1. 9.   References

1. Anonyme, *Numérisation 3D, technologies et besoins.* Contrôle industriel, 1999 (no 217), p. 22-49.
2. Piazzini C., Plisson A., and Dennes S., *http://www.bordeaux.ensam.fr/enseignement/initiale/appro/proj31_99/projet5.html#deux*, 1999.
3. *http://www.renishaw.com*, . 2001-2002, Renishaw.
4. *http://www.romer.com*, . 2002, Romer.
5. *http://www.faro.com*, . 2001, Faro.
6. *http://www.mensi.com/*, . 1987-2002, Mensi.
7. Steinbichler Optotechnik GmbH, *www.steinbichler.de*, .
8. *http://www.leica-geosystems.com*, , Leica.
9. *http://www.aracor.com*, . 2002, ARACOR.
10. *Imetric SA,Technopole, CH-2900 Porrentruy, http:\\www.imetric.com*, .
11. GOM, *http://www.gom.com/*, .
12. *Marktanalyse 1D-3D optischer Sensoren*, NTB, Interstaatliche Hochschule für Technik Buchs, 2003, Switzerland.

CURRICULUM VITAE

Name:	Anne-Isabelle Desmangles
Born:	March 4th, 1971 in Port-au-Prince, Haïti (W.I.)
Nationality:	Swiss
Address:	4, Ch. du Bois de la Fontaine, 1007 Lausanne, Switzerland
Telephone:	+41 (0)21 626 50 58
Email:	Anne-Isabelle.Desmangles@epfl.ch

EDUCATION

December 1999	PhD registration at the Swiss Institute of Technology Lausanne
July 1996	Master of Science, Condensed Matter Physics Department, University of Geneva.
December 1994	Bachelor's Degree in Science, Group of Applied Physics, University of Geneva.
June 1989	High school Diploma with merit (Mathematics and Physics option) at Lycée A. Dumas (French school) in Port-au-Prince, Haïti (W.I.)

SCIENTIFIC WORK EXPERIENCE

Since February 1999	Research associate at the Institute for Stress Analysis (IMAC), Civil Engineering Department, and then at the Laboratory of Metrology (MET), Department of Electricity (group transfer), Swiss Institute of Technology Lausanne (EPFL). **Topic:** 3-D shape and deformation measurements of large objects; Elaboration of a prototype allowing such measurements (from theory to application)
August 96-January 99	Research associate at the Institute of Applied Optics (IOA), Department of Microengineering, Swiss Institute of Technology Lausanne (EPFL). **Topic:** Bioartificial pancreas; Synthesis and characterization of photosensitive polymer gels used for cells microencapsulation by chemical and optical techniques.
September 95-June 96	Research work for the Master of Science, Condensed Matter Physics Department, University of Geneva **Topic:** Superconductivity; Synthesis and characterization of low critical temperature superconductors (Niobium) thin films.
August-November 94	Diploma work for the Bachelor Degree, Group of Applied Physics, University of Geneva **Topic:** Biomedical prosthesis; Study of Titanium (orthopedic prosthesis) corrosion by Atomic Force Microscopy).
November 93-April 94	Training at the Romand Center for Cochlear Implants, Hospital of Geneva. **Topic:** Biomedical prosthesis; Treatment of quality tests of the cochlear implant by computer.

OTHER WORK EXPERIENCE

1996-2001	Teaching assistant of optics laboratory for students at IOA, IMAC and MET, Swiss Institute of Technology Lausanne (EPFL)
1993-1996	Teaching assistant of physics laboratory for High School students at Collège Calvin, Geneva.

TECHNOLOGICAL COMPETENCES

Biomedical field: Cell microencapsulation; Grafts; Titanium orthopedic implants; Cochlear implants

Polymers and Gels: Photopolymerization, Electrophoresis

Analysis and Characterization Tools: fluorescence, absorption and transmission spectrometry, Nomarski and confocal microscopy, AFM, SEM, EDX, X-rays cristallography

Optics: Lasers, Interferometry, CCD cameras, Holography, Speckle interferometry, OLC tomography

Thin Film Technologies: Sputtering and Electron beam deposition

Vacuum Technologies: Primary, turbomolecular and titanium-sublimation pumps, Vacuum chambers

Cryogenics and Superconductivity: Cooling samples to almost 0 K in special dewars, using liquid nitrogen and helium; behavior of low critical temperature superconductors under magnetic field

LANGUAGES

French: mother tongue.

English: fluently written and spoken (Cambridge Certificate of Advanced English).

Spanish: basic knowledge, written and spoken.

German: basic knowledge, written and spoken.

COMPUTER SKILLS

Programming Pascal, LabView, LabView IMAQ vision, Visual Basic and basic skills in Fortran.

Good knowledge of various software packages (Word, Excel, Matlab, Adobe PhotoShop, Adobe Illustrator, Kaleidagraph, PowerPoint, Claris draw).

OTHER ACTIVITIES

2000-2001	Representative of the Scientific Staff at the School Assembly of the Swiss Institute of Technology Lausanne (EPFL)
1994-1996	Representative of the Students in Physics at the Council of the Sciences Department of the University of Geneva.
1992-1993	Representative of the Geneva Association of the Students in Physics at the University Conference of the Students Associations.

PUBLICATIONS

A.-I. Desmangles, P. Jacquot, *Large object shape measurement using coherent light fringe projection: a new approach for calibration*, Proceedings of ODIMAP III, 3rd Topical Meeting on Optoelectronic Distance Measurement and Applications, September 20-22, 2001, Pavia (Italy).

A.-I. Desmangles, O. Jordan, F. Marquis-Weible, *Interfacial Photopolymerization of β-Cell Clusters : Approaches to Reduce Coating Thickness Using Ionic and Lipophilic Dyes*, Biotechnology and Bioengineering, Vol.72, No. 6, March 20, 2001.

A.-I. Desmangles, M. Facchini, P. Jacquot, *Large surface Contouring by fringe projection method using coherent light*, Berichtsband 70, Fachtagung Optische Formerfassung, Messen in der Fertigung: 3D-Messtechnik in Produktion und Entwicklung, Oktober 5-6, 1999, Stuttgart.

PRESENTATIONS

A.-I. Desmangles, P. Jacquot, *Large object shape measurement using coherent light fringe projection: a new approach for calibration*, ODIMAP III, 3rd Topical Meeting on Optoelectronic Distance Measurement and Applications, September 20-22, 2001, Pavia (Italy).

A.-I. Desmangles, M. Facchini, P. Jacquot, *Large surface Contouring by fringe projection method using coherent light*, Berichtsband 70, Fachtagung Optische Formerfassung, Messen in der Fertigung: 3D-Messtechnik in Produktion und Entwicklung, Oktober 5-6, 1999, Stuttgart.